

University of Alberta

X-ray Spectroscopic Studies of Intermetallic Compounds

by

Andrew P. Grosvenor



A thesis submitted to the Faculty of Graduate Studies and Research
in partial fulfillment of the requirements for the degree of

Doctor of Philosophy

Department of Chemistry

Edmonton, Alberta
Spring, 2008



Library and
Archives Canada

Bibliothèque et
Archives Canada

Published Heritage
Branch

Direction du
Patrimoine de l'édition

395 Wellington Street
Ottawa ON K1A 0N4
Canada

395, rue Wellington
Ottawa ON K1A 0N4
Canada

Your file *Votre référence*
ISBN: 978-0-494-45440-4
Our file *Notre référence*
ISBN: 978-0-494-45440-4

NOTICE:

The author has granted a non-exclusive license allowing Library and Archives Canada to reproduce, publish, archive, preserve, conserve, communicate to the public by telecommunication or on the Internet, loan, distribute and sell theses worldwide, for commercial or non-commercial purposes, in microform, paper, electronic and/or any other formats.

The author retains copyright ownership and moral rights in this thesis. Neither the thesis nor substantial extracts from it may be printed or otherwise reproduced without the author's permission.

AVIS:

L'auteur a accordé une licence non exclusive permettant à la Bibliothèque et Archives Canada de reproduire, publier, archiver, sauvegarder, conserver, transmettre au public par télécommunication ou par l'Internet, prêter, distribuer et vendre des thèses partout dans le monde, à des fins commerciales ou autres, sur support microforme, papier, électronique et/ou autres formats.

L'auteur conserve la propriété du droit d'auteur et des droits moraux qui protègent cette thèse. Ni la thèse ni des extraits substantiels de celle-ci ne doivent être imprimés ou autrement reproduits sans son autorisation.

In compliance with the Canadian Privacy Act some supporting forms may have been removed from this thesis.

Conformément à la loi canadienne sur la protection de la vie privée, quelques formulaires secondaires ont été enlevés de cette thèse.

While these forms may be included in the document page count, their removal does not represent any loss of content from the thesis.

Bien que ces formulaires aient inclus dans la pagination, il n'y aura aucun contenu manquant.


Canada

Abstract

Intermetallic compounds, containing metals or metalloids in definite ratios, are a broad class of materials with a wide range of properties, structures, and applications. X-ray photoelectron spectroscopy (XPS), photoemission spectroscopy (PES), and X-ray absorption near-edge spectroscopy (XANES) were used to investigate the electronic structure of several transition-metal pnictides ($Pn = P, As, Sb$).

Monophosphides, MP , having the MnP-type structure were examined by XPS. The charges were found to be closer to $M^{1+}P^{1-}$ than $M^{3+}P^{3-}$ and the P 2p XPS binding energies decrease linearly because the M -P bond becomes more ionic as M is changed from Co to Cr. In contrast, the mixed-metal phosphides $M_{1-x}M'_xP$ (M is more electronegative than M') and mixed arsenide phosphides $MAs_{1-y}P_y$ do not interpolate with the linear trend seen for MP , with the P 2p binding energies being lower than expected. These shifts were found by XANES to result from a next-nearest neighbour effect involving $M' \rightarrow M$ charge transfer in $M_{1-x}M'_xP$ and $As \rightarrow P$ charge transfer in $MAs_{1-y}P_y$, lowering the Madelung potential operating on the P site and thus the P 2p binding energy.

$CoAs_3$ -type (skutterudite) compounds of the form $REFe_4Pn_{12}$ ($RE = La, Ce$) and $CoPn_3$ were also examined by XPS. Analysis of the spectra of the RE members led to the charge formulation $RE^{3+}(Fe^{2+})_4(Pn^{1-})_{12}$. The Ce charge was confirmed by the presence of a Ce 4f peak in the valence band spectrum. The Co 2p spectra of $CoPn_3$ showed no appreciable shift in energy relative to Co metal because of the delocalized valence electronic structure. However, the higher binding energy plasmon loss satellite peak observed in the Co 2p spectra was informative. In the series $CoPn_3$, CoP, and Co

metal, this satellite peak intensifies as the Co-*Pn* bond becomes more covalent and as the Co charge decreases.

A new metallic compound, Hf(Si_{0.5}As_{0.5})As, having the ZrSiS-type structure was identified. The atomic charges are not as extreme as those predicted from an ionic model. Using XPS and PES, the charge formulation was revealed to be Hf²⁺[(Si_{0.5}As_{0.5})As]²⁻. These charges were determined by fitting the valence band spectrum, allowing for the number of valence electrons per atom to be extracted.

Acknowledgement

Throughout my Ph.D. studies I have had the pleasure and honour to work for Professor A. Mar and Professor R. Cavell. I would not be the chemist that I am today without their teachings, guidance and encouragement. I am grateful for everything they have done for me. The work presented in this thesis was performed and written by myself, except when stated otherwise (see below), with Profs. Mar and Cavell acting as editors, for which they are thanked. The past and present members of the Mar and Cavell groups are thanked for their help in synthesizing and characterizing the materials discussed in this thesis. My family, friends, and Erika are thanked for all of the support that they have given me throughout my university career.

The Natural Sciences and Engineering Research Council (NSERC) of Canada supported this work through Discovery Grants to Professors Mar and Cavell. Access to the Kratos XPS instruments used in this research was kindly provided by the Alberta Centre for Surface Engineering and Science (ACSES) at the University of Alberta. ACSES was established with capital funding from the Canada Foundation for Innovation (CFI) and Alberta Innovation and Science. I would like to extend my thanks to the staff members of ACSES, particularly Dr. D. Karpuzov, for all of their help over the last few years in collecting the XPS data presented in this thesis as well as for the fruitful conversations that we have had. Dr. S. Ramamurthy (Surface Science Western, University of Western Ontario) is thanked for performing the REELS analysis of Co metal. Dr. R. McDonald and Dr. M. J. Ferguson (X-ray Crystallography Laboratory) are acknowledged for collecting single-crystal X-ray diffraction data, and Ms. C. Barker (Department of Chemical and Materials Engineering) is thanked for her help with SEM-

EDX analysis. Dr. R. Blyth, Dr. J. Thompson, and Mr. T. Regier of the Canadian Light Source (CLS) are thanked for help in carrying out the XANES and PES measurements at 11-ID.1 at the CLS. Dr. Blyth collected the valence band photoemission spectra (PES) presented in Chapter 8 and is also thanked for help in writing the description of resonant PES. The Canadian Light Source is supported by NSERC, NRC, CIHR, and the University of Saskatchewan. Dr. Robert Gordon and the staff of PNC-XOR are thanked for help in carrying out the XANES experiments at PNC/XOR-CAT, sector 20 at the Advanced Photon Source (APS). PNC/XOR facilities at the APS, and research at these facilities, are supported by the US Department of Energy - Basic Energy Sciences, a major research support grant (MRS) from NSERC, the University of Washington, Simon Fraser University, and the Advanced Photon Source. Use of the APS is also supported by the U. S. Department of Energy, Office of Science, Office of Basic Energy Sciences, under Contract DE-AC02-06CH11357. Lastly, I would like to thank NSERC, Alberta Ingenuity and the University of Alberta for financial support.

Table of Contents

Chapter 1: Introduction	1
1.1 Intermetallic Compounds	1
1.2 Applications	2
1.2.1 MnP-type Compounds	2
1.2.2 Skutterudites.....	4
1.3 Bonding in Extended Solids.....	7
1.4 Structure and Bonding in MnP-type, CoAs ₃ -type, and ZrSiS-type Compounds	9
1.4.1 MnP-type Structure	9
1.4.2 CoAs ₃ -type Structure	19
1.4.3 ZrSiS-type Structure.....	21
1.5 Spectroscopy	24
1.6 Overview	25
Chapter 2: X-ray Spectroscopy	27
2.1 Introduction.....	27
2.2 X-ray Photoelectron Spectroscopy (XPS).....	27
2.3 Synchrotron Radiation	43
2.4 X-ray Absorption Spectroscopy (XAS)	48
2.5 Photoemission Spectroscopy (PES).....	54

Chapter 3: An Examination of the Bonding in Binary Transition-Metal Monophosphides MP ($M = \text{Cr, Mn, Fe, Co}$) by X-ray Photoelectron Spectroscopy	57
3.1 Introduction.....	57
3.2 Experimental	59
3.2.1 Synthesis	59
3.2.2 XPS Analysis	59
3.2.3 REELS Analysis	61
3.2.4 Band Structure Calculations.....	61
3.3 Results and Discussion.....	62
3.3.1 Phosphorus 2p High-Resolution X-ray Photoelectron Spectra.....	62
3.3.2 Metal 2p _{3/2} High-Resolution X-ray Photoelectron Spectra.....	66
3.3.3 Satellite Structure in Co Metal and CoP Co 2p _{3/2} Spectra	69
3.3.4 Valence Band Spectra	75
3.4 Conclusions.....	87
Chapter 4: Next-Nearest Neighbour Contributions to P 2p_{3/2} X-ray Photoelectron Binding Energy Shifts of Mixed Transition-Metal Phosphides $M_{1-x}M'_xP$ with the MnP-Type Structure.....	90
4.1 Introduction.....	90
4.2 Experimental	94
4.2.1 Synthesis	94
4.2.2 XPS Analysis	95
4.2.3 P K-edge XANES Analysis	96

4.2.4	Mn K-edge XANES Analysis	97
4.3	Results and Discussion.....	97
4.3.1	P 2p XPS Spectra	97
4.3.2	Metal 2p XPS Spectra	108
4.3.3	Mn K-edge XANES	113
4.4	Conclusions	116
Chapter 5:	Next-Nearest Neighbour Contributions to the XPS Binding Energies and XANES Absorption Energies of P and As in Transition-Metal Arsenide Phosphides $MA_{s_{1-y}}P_y$ Having the MnP-Type Structure	117
5.1	Introduction	117
5.2	Experimental	120
5.2.1	Synthesis	120
5.2.2	XPS Analysis	121
5.2.3	P K-edge, As L-edge, and <i>M</i> L-edge XANES Analysis	123
5.2.4	As K- and <i>M</i> K-edge XANES Analysis.....	124
5.2.5	Band Structure Calculations.....	125
5.3	Results.....	125
5.3.1	Is As less Electronegative than P?	125
5.3.2	P 2p XPS and P K-edge XANES Spectra.....	126
5.3.3	As L- and K-edge XANES Spectra.....	128
5.3.4	<i>M</i> 2p XPS Spectra	135
5.3.5	<i>M</i> L- and K-edge XANES Spectra.....	137
5.4	Discussion	140

5.4.1	Shifts in P 2p _{3/2} BEs and P K-edge Absorption Energies	140
5.4.2	Shifts in As L ₃ - and K-edge Absorption Energies	143
5.5	Conclusions.....	144
Chapter 6:	X-ray Photoelectron Spectroscopy Study of Rare-Earth Filled Transition-metal Phosphide Skutterudites LaFe₄P₁₂ and CeFe₄P₁₂.....	146
6.1	Introduction.....	146
6.2	Experimental	149
6.2.1	Synthesis	149
6.2.2	XPS Analysis	150
6.2.3	Band Structure Calculations.....	151
6.3	Results and Discussion.....	152
6.3.1	High-Resolution P 2p Spectra.....	152
6.3.2	High-Resolution Fe 2p Spectra	154
6.3.3	High-Resolution RE 3d Spectra	156
6.3.4	Valence Band Spectra	162
6.4	Conclusions.....	171
Chapter 7:	Electronic Structure of the Antimonide and Phosphide Skutterudites LaFe₄Sb₁₂, CeFe₄Sb₁₂, CoSb₃ and CoP₃ Probed by X-ray Photoelectron Spectroscopy.....	173
7.1	Introduction.....	173
7.2	Experimental	176
7.2.1	Synthesis	176
7.2.2	XPS Analysis	176

7.2.3	Band Structure Calculations.....	178
7.3	Results and Discussion.....	178
7.3.1	High-Resolution Sb 3d and P 2p Spectra.....	178
7.3.2	High-Resolution Fe and Co 2p Spectra.....	180
7.3.3	Co 2p Satellite Structure	183
7.3.4	High-Resolution Rare-Earth 3d Spectra.....	185
7.3.5	Valence Band Spectra	190
7.4	Conclusions.....	197
Chapter 8:	Analysis of the Electronic Structure of Hf(Si_{0.5}As_{0.5})As by X-ray Photoelectron and Photoemission Spectroscopy	199
8.1	Introduction.....	199
8.2	Experimental	201
8.2.1	Synthesis	201
8.2.2	Structure Determination.....	202
8.2.3	Property Measurements.....	205
8.2.4	X-ray Photoelectron Spectroscopy (XPS).....	205
8.2.5	Photoemission Spectroscopy (PES).....	207
8.2.6	Band Structure Calculations.....	208
8.3	Results and Discussion.....	208
8.3.1	Synthesis and Crystal Structure	208
8.3.2	Electrical and Magnetic Properties	212
8.3.3	Electronic Structure.....	212
8.3.3.1	As 3d and Si 2p XPS Spectra.....	214

8.3.3.2	Hf 4f XPS Spectra.....	217
8.3.3.3	Valence Band XPS Spectra and LMTO Band Structure Calculations	219
8.3.3.4	Photoemission Spectroscopy (PES).....	221
8.3.3.5	Fitting of the Valence Band Spectrum.....	225
8.4	Conclusions.....	229
Chapter 9:	Summary and Conclusions.....	231
9.1	X-ray Spectroscopy of Intermetallic Compounds.....	231
9.1.1	MnP-type Compounds	232
9.1.2	CoAs ₃ -type Compounds (Skutterudites).....	235
9.1.3	Hf(Si _{0.5} As _{0.5})As.....	236
9.1.4	Charges of Anions Involved in Homo- or Hetero-Atomic Anion-Anion Bonds	238
9.2	Metal Spectra in MnP-type and CoAs ₃ -type Compounds	240
9.3	XPS and XANES Results for Intermetallic Compounds	242
9.4	Future Spectroscopic Examinations of Intermetallic Compounds.....	244
References	247
Appendix 1:	Supplementary Data for Chapter 4.....	262
Appendix 2:	Supplementary Data for Chapter 5.....	264
Appendix 3:	ARXPS Study of the Ion Mobility Through (HfO₂)_x(SiO₂)_{1-x} Formed on Air-Exposed Hf(Si_{0.5}As_{0.5})As	265
A3.1	Introduction.....	265

A3.2 Experimental	266
A3.3 Results and Discussion.....	268
A3.4 Conclusions.....	275

List of Tables

Table 3-1	Binding Energies (eV) of Core Photoelectron Peaks in Transition-Metal Monophosphides MP ($M = \text{Cr, Mn, Fe, Co}$) and Metal Standards.....	63
Table 3-2	Bulk Plasmon Loss Peak Energies (eV) in Co Metal	73
Table 3-3	Binding Energies (eV) of Component Peaks in Valence Band Spectra of MP ($M = \text{Cr, Mn, Fe, Co}$)	81
Table 3-4	Corrections Applied to Intensities of Peaks in Valence Band Spectra of MP ($M = \text{Cr, Mn, Fe, Co}$)	84
Table 3-5	Electron Populations in MP ($M = \text{Cr, Mn, Fe, Co}$)	85
Table 4-1	Phosphorus $2p_{3/2}$ binding energies, P K-edge absorption energies, and metal $2p_{3/2}$ binding energies for metals, binary phosphides MP , and mixed phosphides $M_{1-x}M'_xP$	101
Table 5-1	P $2p_{3/2}$ and $M 2p_{3/2}$ XPS binding energies (eV) and P K-, As L_{3-} , and As K-edge absorption energies (eV) in MP , $MA_{S_{1-y}}P_y$, and MAs	129
Table 6-1	Binding Energies (eV) of Component Peaks in Valence Band Spectra of $LaFe_4P_{12}$ and $CeFe_4P_{12}$	166
Table 6-2	Corrections Applied to Peak Intensities in Valence Band Spectra of $LaFe_4P_{12}$ and $CeFe_4P_{12}$	170
Table 6-3	Electron Populations in $LaFe_4P_{12}$ and $CeFe_4P_{12}$	170
Table 7-1	Binding energies (eV) of component peaks in valence band spectra of $CoSb_3$, CoP_3 , $LaFe_4Sb_{12}$, and $CeFe_4Sb_{12}$	194
Table 7-2	Corrections applied to peak intensities in valence band spectra of CoP_3 , $CoSb_3$, $LaFe_4Sb_{12}$, and $CeFe_4Sb_{12}$	195
Table 7-3	Electron populations in $CoSb_3$, CoP_3 , $LaFe_4Sb_{12}$ and $CeFe_4Sb_{12}$	196
Table 8-1	Crystallographic data for $Hf(Si_{0.5}As_{0.5})As$	203
Table 8-2	Atomic coordinates and equivalent isotropic displacement parameters for $Hf(Si_{0.5}As_{0.5})As$	204

Table 8-3	Selected interatomic distances (\AA) in $\text{Hf}(\text{Si}_{0.5}\text{As}_{0.5})\text{As}$	204
Table 8-4	Atomic photoelectron cross-sections (σ)	226
Table 8-5	Electron population of valence states in $\text{Hf}(\text{Si}_{0.5}\text{As}_{0.5})\text{As}$ calculated using Eq 8-2 and a total valence electron population of $13.5 e^-$	228
Table 9-1	Information obtained from intermetallic compounds using XPS and XANES.....	243
Table A1-1	Full width at half maximum (FWHM), in degrees, for strongest reflections in $\text{Mn}_{1-x}\text{V}_x\text{P}$ and MnP	262
Table A1-2	P $2p_{3/2}$ binding energies (eV) from measurements for separate $\text{Mn}_{1-x}\text{V}_x\text{P}$ samples or at separate times for $\text{Co}_{1-x}\text{V}_x\text{P}$ and $\text{Co}_{1-x}\text{Mn}_x\text{P}$ samples.....	262
Table A2-1	P $2p_{3/2}$ binding energies (eV) from measurements for separate $\text{MAS}_{1-y}\text{P}_y$ samples or for the same $\text{MAS}_{1-y}\text{P}_y$ sample but collected at different times.....	264
Table A3-1	Binding energy values for the spin-up component peaks of the fitted Hf 4f, Si 2p, and As 3d spectra from air-exposed $\text{Hf}(\text{Si}_{0.5}\text{As}_{0.5})\text{As}$. The binding energies from standard compounds are provided for reference.....	270

List of Figures

Figure 1-1	Schematic of a thermoelectric device used for either power generation (a) or refrigeration (b)	5
Figure 1-2	Octahedral ML_6 molecule (lower) and the corresponding molecular orbital (MO) diagram (upper)	8
Figure 1-3	Graph of the P-P and M - M distances in the first row transition-metal phosphides (ScP – NiP).....	11
Figure 1-4	Distortion of M atom positions that occur as a NiAs-type structure evolves to a MnP-type structure with chains of bonded M - M atoms being developed	11
Figure 1-5	MnP-type crystal structure of MP viewed down the b axis	13
Figure 1-6	Molecular orbital representation of the bonding relationships present in MnP	14
Figure 1-7	Chain of P atoms (a) separated by a distance a with each having a basis function χ_n . A schematic representation of the Bloch function when 3s orbitals are considered is shown in (b) and when 3p orbitals are considered in (c).....	16
Figure 1-8	The unit cell of MnP is presented in (a) with its reciprocal space analogue (Brillouin zone or Wigner-Seitz cell) being shown in (b). The band structure going from Γ to X, Y, and Z is shown in (c) and the total density of states (DOS) and partial DOS for the Mn 3d, P 3p and P 3s states are shown in (d).....	18
Figure 1-9	Filled skutterudite-type structure of ternary rare-earth transition-metal pnictides REM_4Pn_{12}	20
Figure 1-10	Structure of ZrSiS viewed down the a direction.....	23
Figure 2-1	Excitation of a P atom leading to the ejection of a photoelectron from the 2p orbital.....	30
Figure 2-2	Schematic representation of a modern XPS instrument having a monochromatic X-ray source	30
Figure 2-3	Diagram of the Ar^+ ion sputtering of a surface, which removes contaminate/oxide layers, exposing a clean surface for analysis	35
Figure 2-4	Survey spectrum of sputter cleaned Hf metal	35

Figure 2-5	High resolution P 2p XPS spectrum from FeP.....	40
Figure 2-6	Plot of the Fe 2p _{3/2} binding energy (BE) vs. nominal Fe charge for a series of Fe oxides and halides	40
Figure 2-7	Difference in brightness between a synchrotron radiation source and other light sources.....	44
Figure 2-8	Layout of a synchrotron radiation source.....	46
Figure 2-9	Schematic representation of (a) wiggler and (b) undulator insertion devices.....	46
Figure 2-10	Co K-edge XAS spectrum from CoP collected in transmission mode.....	50
Figure 2-11	Schematic diagram of a single scattering event causing the EXAFS phenomena.....	52
Figure 2-12	Typical set-up of a hard X-ray XAS experiment	52
Figure 2-13	Calculated As 4p photoelectron cross-section with varying excitation energy from 0 to 1400 eV.....	56
Figure 3-1	High-resolution P 2p XPS spectra of (a) CrP, (b) MnP, (c) FeP, and (d) CoP	63
Figure 3-2	Plot of P 2p _{3/2} binding energies, BE, versus the difference in electronegativity (Allred-Rochow) between the phosphorus and metal atoms, $\Delta\chi$, for several first-row transition-metal monophosphides.....	65
Figure 3-3	Plot of the charge on P atoms (estimated from binding energy values) versus the difference in electronegativity, $\Delta\chi$, for CrP, MnP, FeP and CoP	65
Figure 3-4	High-resolution metal 2p _{3/2} XPS spectra for (a) CrP, (b) MnP, (c) FeP, and (d) CoP.....	67
Figure 3-5	High-resolution 2p _{3/2} XPS spectra of clean samples of (a) Cr, (b) Mn, (c) Fe, and (d) Co metal	67
Figure 3-6	REELS spectrum of Co metal taken at 0.3 keV.....	72

Figure 3-7	Fitted valence band spectra of sputter-cleaned samples of (a) Cr, (b) Mn, (c) Fe, and (d) Co metal	76
Figure 3-8	Fitted valence band spectra of sputter-cleaned samples of (a) CrP, (b) MnP, (c) FeP, and (d) CoP	78
Figure 3-9	(a) Valence band spectrum of MnP compared to the calculated projections of the density of states for (b) P 3s, (c) P 3p, and (d) Mn 3d orbitals	79
Figure 3-10	Energy level diagrams for (a) CrP, (b) MnP, (c) FeP, and (d) CoP	88
Figure 4-1	High-resolution P 2p spectra for MnP and $Mn_{0.85}V_{0.15}P$	98
Figure 4-2	Dependence of (a–b) P $2p_{3/2}$ binding energy and (c–d) P K-edge absorption energy on electronegativity difference $\Delta\chi$ for binary phosphides MP and ternary phosphides	100
Figure 4-3	P K-edge XANES spectra for CoP and $Co_{0.80}V_{0.20}P$ representing P $1s \rightarrow np$ transitions	106
Figure 4-4	Representative metal $2p_{3/2}$ spectra for $Mn_{1-x}V_xP$, $Co_{1-x}Mn_xP$, $Co_{1-x}V_xP$, and the parent binary phosphides	109
Figure 4-5	Plot showing the variation in the normalized plasmon intensity vs. the difference in electronegativity between the two dissimilar metals ($\chi_M - \chi_{M'}$) in the Co 2p spectrum of CoP, $Co_{1-x}Mn_xP$, and $Co_{1-x}V_xP$	112
Figure 4-6	Mn K-edge XANES spectra of (a) $Mn_{0.95}V_{0.05}P$ and (b) $Co_{0.10}Mn_{0.90}P$	115
Figure 5-1	Plot of orthorhombic cell parameters vs. y for the $CoAs_{1-y}P_y$ series, which adopts the MnP-type structure	122
Figure 5-2	High-resolution P 2p XPS spectra for FeP and $FeAs_{0.10}P_{0.90}$, with $2p_{3/2}$ and $2p_{1/2}$ component peaks labelled	127
Figure 5-3	Dependence of (a) P $2p_{3/2}$ BE, (b) P K-edge absorption energy, and (c) As L_3 -edge absorption energy on electronegativity difference ($\Delta\chi = \chi_{Pn} - \chi_M$) for binary pnictides MP or MAs and ternary mixed pnictides	130
Figure 5-4	(a) P K-edge XANES spectrum for $CoAs_{0.10}P_{0.90}$ and (b) As L_3 -edge XANES spectrum for CrAs	131

Figure 5-5	(a) Normalized As K-edge absorption spectra, collected in transmission mode, for FeAs and some FeAs _{1-y} P _y compounds. (b) Orbital projections of the calculated conduction states of FeAs and FeAs _{0.50} P _{0.50}	133
Figure 5-6	Representative metal 2p _{3/2} XPS spectra for (a) CrAs _{1-y} P _y , (b) FeAs _{1-y} P _y , and (c) CoAs _{1-y} P _y , compared to the parent binary phosphides and arsenides	136
Figure 5-7	Plot showing the variation in the normalized plasmon intensity vs <i>y</i> in the Co 2p spectra for CoAs _{1-y} P _y	136
Figure 5-8	Normalized total electron yield Fe L _{2,3} -edge XANES spectra for FeAs and some FeAs _{1-y} P _y compounds	138
Figure 5-9	Normalized Cr K-edge XANES spectra, collected in transmission mode, for CrAs _{1-y} P _y	138
Figure 5-10	Schematic representation of the dependence of <i>M</i> and <i>P_n</i> charges on <i>y</i> in MAs _{1-y} P _y	142
Figure 6-1	High-resolution P 2p XPS spectra of LaFe ₄ P ₁₂ and CeFe ₄ P ₁₂	153
Figure 6-2	High-resolution Fe 2p XPS spectra of LaFe ₄ P ₁₂ and CeFe ₄ P ₁₂	155
Figure 6-3	(a) High-resolution La 3d XPS spectrum of LaFe ₄ P ₁₂ and (b) Ce 3d XPS spectrum of CeFe ₄ P ₁₂	157
Figure 6-4	High-resolution La 3d XPS spectrum of LaP	159
Figure 6-5	High-resolution Ce 3d XPS spectra of CeF ₃ and CeF ₄ , showing the difference between the Ce ³⁺ and Ce ⁴⁺ lineshapes	159
Figure 6-6	(a) Valence band spectrum of LaFe ₄ P ₁₂ . (b) Contributions of P 3s, P 3p, and Fe 3d orbitals (shaded regions) to the total density of states (line) for LaFe ₄ P ₁₂	163
Figure 6-7	(a) Fitted valence band spectra of LaFe ₄ P ₁₂ and CeFe ₄ P ₁₂ . (b) Valence band spectra from CeFe ₄ P ₁₂ and LaFe ₄ P ₁₂ overlaid on each other	165
Figure 6-8	Valence band spectra of LaF ₃ and CeF ₃	168
Figure 7-1	High-resolution Sb 3d spectra of (a) LaFe ₄ Sb ₁₂ , (b) CeFe ₄ Sb ₁₂ , (c) CoSb ₃ , and (d) P 2p spectrum of CoP ₃	179

Figure 7-2	High-resolution Fe 2p spectra of (a) LaFe ₄ Sb ₁₂ and (b) CeFe ₄ Sb ₁₂ ; and Co 2p spectra of (c) CoSb ₃ and (d) CoP ₃	181
Figure 7-3	Correlation between Co charge and relative intensity of the Co 2p satellite in Co, CoSb ₃ , CoP, and CoP ₃	186
Figure 7-4	High-resolution rare-earth 3d spectra of (a) LaFe ₄ Sb ₁₂ and (b) CeFe ₄ Sb ₁₂ , (c) CeF ₃ , and (d) CeF ₄	187
Figure 7-5	Valence band spectrum of CoP ₃ compared with the Co 3d, P 3p, and P 3s projections of the density of states	191
Figure 7-6	Fitted valence band spectra of (a) CoSb ₃ , (b) CoP ₃ , (c) LaFe ₄ Sb ₁₂ , and (d) CeFe ₄ Sb ₁₂	192
Figure 7-7	Overlapped valence band spectra of LaFe ₄ Sb ₁₂ and CeFe ₄ Sb ₁₂ showing the position of the Ce 4f ¹ state.....	194
Figure 8-1	Structure of Hf(Si _{0.5} As _{0.5})As viewed down the <i>a</i> direction	210
Figure 8-2	(a) Electrical resistivity (within the <i>ab</i> plane) and (b) magnetic susceptibility of Hf(Si _{0.5} As _{0.5})As	213
Figure 8-3	(a) As 3d and (b) Si 2p core-line spectra of Hf(Si _{0.5} As _{0.5})As	215
Figure 8-4	Hf 4f core-line spectra of (a) Hf(Si _{0.5} As _{0.5})As and (b) Hf metal.....	218
Figure 8-5	XPS valence band spectrum of Hf(Si _{0.5} As _{0.5})As.....	220
Figure 8-6	Band structures of (a) HfAs ₂ , (b) HfSiAs, and (c) Hf(Si _{0.5} As _{0.5})As.....	220
Figure 8-7	Resonant PES spectra of Hf(Si _{0.5} As _{0.5})As collected using an excitation energy equal to the Hf N ₃ (4p _{3/2}) absorption edge (384 eV) and one just below the absorption edge (360 eV).....	223
Figure 8-8	(a) Variation in the Hf 5d, As 4p, and Si 3p photoionization cross-sections from 250 eV to 500 eV and (b) PES valence band spectra collected using excitation energies equal to 255 eV, 360 eV, and 500 eV	223
Figure 8-9	Fitted XPS valence band spectrum of Hf(Si _{0.5} As _{0.5})As	226

Figure 9-1 Lewis dot diagrams of the P-P bonding network present in MnP-type (a) and CoAs ₃ -type (b) compounds. The anion-anion bonding environment in Hf(Si _{0.5} As _{0.5})As is presented in (c)	239
Figure A1-1 Plot of cell parameters vs. <i>x</i> for MnP-type phases observed in reactions with nominal composition (a) Co _{1-x} Mn _x P, (b) Mn _{1-x} V _x P, and (c) Co _{1-x} V _x P	263
Figure A3-1 Core-line spectra of the Hf 4f, Si 2p, and As 3d components from clean Hf(Si _{0.5} As _{0.5})As after Ar ⁺ sputter-cleaning (a–c), and after exposure to the atmosphere at a take-off angle of 90° (d–f) or 15° (g–i)	269
Figure A3-2 (a) O 1s spectrum from air-exposed Hf(Si _{0.5} As _{0.5})As surface at a take-off angle of 15°. (b) Plot of O 1s component peak intensities versus take-off angle	272
Figure A3-3 Schematic representation of the oxide film formed on Hf(Si _{0.5} As _{0.5})As after exposure to the ambient atmosphere for 60 minutes at room temperature	274
Figure A3-4 Logarithmic kinetics of the oxidation of Hf(Si _{0.5} As _{0.5})As after exposure to the atmosphere for 1, 5, and 60 minutes	274

List of Symbols and Abbreviations

$2c-2e^-$	2 centre – 2 electron bond
$10Dq$	Crystal field splitting energy
α	Seebeck coefficient
δ	Phase shift
ζ_i	Orbital exponents
θ	Take-off angle (angle between the XPS detector and sample)
λ	Inelastic mean free path (IMFP)
λ	Magnetic period
λ	Total thermal conductivity
λ	Wavelength
μ	Absorption coefficient
$\mu(E)$	Intensity of EXAFS oscillations
$\mu_0(E)$	Background function describing what X-ray absorption would look like for an isolated atom
ρ	Density
ρ	Electrical resistivity
σ	Electrical conductivity
σ	Photoionization (or photoelectron) cross-section
σ	Single (sigma) bond
σ^2	Describes effects associated with thermal atom-atom oscillation
χ	Extended X-ray absorption fine structure (EXAFS) function
χ	Magnetic susceptibility
χ_n	Basis function

ψ	Wave function
Δ	Electron deficiency of an atoms valence states with respect to attaining a filled octet
$\Delta\chi$	Difference in electronegativity (χ)
ΔE_i	Total binding energy shift
Δl	Change in angular momentum (l)
ΔT	Change in temperature
$\Delta\mu_o(E_o)$	Absorption edge step height
ΔV	Change in voltage
Φ	Work function
a, b, c	Lengths of unit cell edges
AFM	Atomic Force Microscopy
APS	Advanced Photon Source
ARXPS	Angle-resolved XPS
b	Barn (unit of photoionization cross-section, σ)
B	Magnetic field strength in units of Tesla (T)
BE	Binding Energy
C	Atomic concentration
CHA	Concentric hemispherical analyzer
CLS	Canadian Light Source
COOP	Crystal Orbital Overlap Population
CN	Coordination Number
DFSO	Differential Fractional Site Occupancy
DOS	Density of States

e^-	Electron
eV	Electron volt
E	Energy
EDX	Energy Dispersive X-ray Spectroscopy
E_F	Fermi energy
E_i	Measured binding energy of the atom of interest
E_i^0	Reference binding energy
E_o	Absorption edge threshold energy
Eq	Equation
ESCA	Electron Spectroscopy for Chemical Analysis
E_v	Vacuum energy
EXAFS	Extended X-ray Absorption Fine Structure
f_j	Scattering amplitude of surrounding atoms
F_o	Structure factor
FLY	Fluorescence Yield
FWHM	Full Width at Half Maximum
g	Gap distance between magnetic poles in an insertion device
hcp	hexagonal close-packed
$h\nu$	Excitation (or photon) energy
H	Applied magnetic field
H	Hamiltonian
HDN	Hydrodenitrogenation
HDS	Hydrodesulfurization

H_{ii}	Valence shell ionization potentials
I	Peak intensity (peak height or area) from a XPS spectrum
I	Intensity of transmitted radiation
I_f	Intensity of radiation produced by fluorescence
I_o	Intensity of exciting radiation
I_{Ref}	Intensity of radiation transmitted through a reference sample
j	Coupled angular momentum and spin quantum number
k	Factor describing the interaction between valence and core electrons
k	wave vector
K	XPS spectrometer related peak intensity correction factors
KE	Kinetic Energy
L	Ligand
m	Electron mass
M	Magnetization
M	Metal
MO	Molecular orbital
n	Principal quantum number
N_j	Coordination number of neighbouring atoms
N	Volume density of a particular element in a material
p	Function that accounts for systematic instrumental (XRD) errors
PES	Photoemission Spectroscopy
Pn	Pnicogen or Pnictides (e.g., P, As, Sb)
$q_{i(j)}$	Charge of atom i (or j)

r	Orbital radius
r_{ij}	Distance between atom i and atom j
R	Scattering path length of a photoelectron (or atom-atom distance)
RE	Rare-earth
REELS	Reflection Electron Energy Loss Spectroscopy
RF	Radio Frequency
$R_w(F_o^2)$	Residual that is weighted by the square of the structure factor (F_o)
RSD	Residual Standard Deviation
s	Spin quantum number
SEM	Scanning Electron Microscopy
S_o^2	Amplitude reduction term resulting from multi-electron excitations of the absorbing atom
SR	Synchrotron Radiation
t	Sample thickness
TEY	Total Electron Yield
U_{eq}	Equivalent isotropic displacement parameters
x, y, z	Location of an atom expressed in units of $a, b,$ and c
XANES	X-ray Absorption Near-edge Spectroscopy
XAS	X-ray Absorption Spectroscopy
XPS	X-ray Photoelectron Spectroscopy
XRD	X-ray Diffraction
Z	Atomic number
Z	Number of formula units per unit cell
Z	Thermoelectric figure of merit

Chapter 1

Introduction

1.1 Intermetallic Compounds

Intermetallic compounds can be defined as those containing several metals in relatively fixed compositions,¹ distinguishing them from metal alloys, which show extensive solid solubility of the component metals. In the Fe-Ni system, FeNi₃ is an intermetallic compound² whereas Fe_{1-x}Ni_x (kamacite, $x < 0.07$) is an alloy that has been observed in meteorites.^{3, 4} This definition has conventionally been extended to include metalloids and even some of the less electronegative nonmetals, such as Si, P, As, Sb, and Te.¹ Since the electronegativities of constituent elements in intermetallics differ only slightly, the bonding character is more covalent or polar-covalent than ionic. Thus, electron-counting formalisms often used to estimate charge distributions are problematic. In this thesis, X-ray photoelectron spectroscopy (XPS) and X-ray absorption near edge spectroscopy (XANES) have been employed to examine charge distributions and bonding in intermetallic compounds.

Compounds adopting three crystal structure types, MnP, CoAs₃, and ZrSiS, will be discussed in this thesis. Many binary metal phosphides and arsenides, as well as several mixed metal phosphide and mixed arsenide phosphide systems are known to

adopt the MnP-type structure. Of these compounds, CoP has been suggested as a catalyst for the removal of N and S from petrochemicals.⁵ The CoAs₃-type structure is adopted by a diverse set of binary metal phosphides, arsenides, and antimonides.⁶ There are also some rare-earth containing ternary members having this structure type, which have been proposed for use in thermoelectric applications including power generation and refrigeration.⁶ Some intermetallic thermoelectric materials (e.g., Bi₂Te₃) are currently being used for refrigeration applications in portable coolers.⁷ Although applications of compounds which possess either the MnP-type or CoAs₃-type structure have been extensively developed, as will be described in the following section, less effort has been applied to understanding their electronic structure. The ZrSiS-type structure represents a case wherein the metal atoms have a coordination environment that is different than that which exists in either the MnP-type or CoAs₃-type structures and this class has not been examined by X-ray spectroscopy. The examination of this structure type allows for a novel study of the differences between the charges determined through electron counting and those found experimentally.

1.2 Applications

Descriptions of some of the applications of MnP-type and CoAs₃-type compounds will be provided before further examining the different structure types investigated.

1.2.1 MnP-type Compounds

Many petroleum sources, such as the Alberta oil sands, contain high levels of S that must be removed, so much current work has been focussed on finding catalysts with high activity for removing S from petrochemicals. Transition metal phosphides, particularly Ni₂P (Fe₂P-type structure) and CoP (MnP-type structure), have been found to

be useful as hydrodesulfurization (HDS) and hydrodenitrogenation (HDN) catalysts for the removal of S and N from petroleum feedstocks.^{5, 8-10} Although some work has already been done to determine the efficiency of these compounds for S removal from model compounds such as thiophene (C_4H_4S),^{5, 9} significantly less effort has been applied to examine the overall electronic structure (in terms of atomic charge and bonding) although some studies do exist.¹¹⁻¹⁵ X-ray spectroscopy is quite useful in this respect and has been used herein to study the simpler of the two compounds listed above, CoP, as well as related compounds.

In terms of catalytic activity, CoP has been found to remove ~30-40 % of the S found in a model feedstock (dibenzothiophene, $C_{12}H_8S$) and ~30-40 % of the N found in quinoline (C_9H_7N).⁵ Although it is much less active than the common commercial catalyst (Ni-Mo-S supported on Al_2O_3) for HDS (77 %), its HDN conversion is very similar (38 %).⁵ Ni_2P , on the other hand, has significantly higher HDS and HDN conversion ratios of 98 % and 90 %, respectively (compared to either CoP or Ni-Mo-S).⁵ Although there has been some speculation on the mechanism for HDS/HDN catalysis by Ni_2P , at present, the mechanistic process for removal of S or N from organic compounds by CoP has not been examined. To increase the performance of these catalysts in bulk form, they are dispersed on a support material (e.g., SiO_2 , Al_2O_3) which increases the surface area of the catalyst.⁸ The catalytic activity may also be increased if nanocrystals of these compounds are used and some investigations in this direction have been undertaken with the preparation of “nano” transition metal phosphides, such as MnP, FeP, CoP, Cu_3P , and Ni_2P , being a topic of current interest.¹⁶⁻¹⁹ As indicated above, mixed metal and mixed arsenide phosphides can also be prepared having the MnP-type

structure. To further evaluate the application of transition metal phosphides for the catalytic removal of S from petroleum sources, it is important to determine how the electronic structure of these compounds compare to that of the known catalyst, CoP, and whether the properties of these compounds can be modified through substitution.

1.2.2 Skutterudites

The rare earth containing skutterudites (compounds that adopt the CoAs_3 -type structure) have been studied for thermoelectric power generation and refrigeration.⁶ Thermoelectric power generation is based on the observations made by Seebeck that when two dissimilar materials are joined and the two ends held at different temperatures, a potential is developed.²⁰ This voltage was found to be proportional to the temperature gradient applied across the two materials. The potential difference arising from an applied temperature gradient across the two joined materials is defined by the Seebeck coefficient, α , and is equal to $\Delta V/\Delta T$.²⁰ A thermoelectric power generation device is shown in Figure 1-1a. Two dissimilar semiconductors (one being a p-type and the other being an n-type) are connected together via a solid metal block at the hot end ($T + \Delta T$) and are connected independently to the colder end (T). The temperature gradient creates electrical carriers in the two materials (holes in the p-type material and electrons in the n-type material) which travel from the cold end towards the hot end.²⁰ These carriers also transport heat.²⁰ The effect is the production of a current which can be used as a power source following Ohm's law ($V = IR$).

Besides power generation, thermoelectric materials can also be used for refrigeration applications. A schematic of this setup is shown in Figure 1-1b. Applying

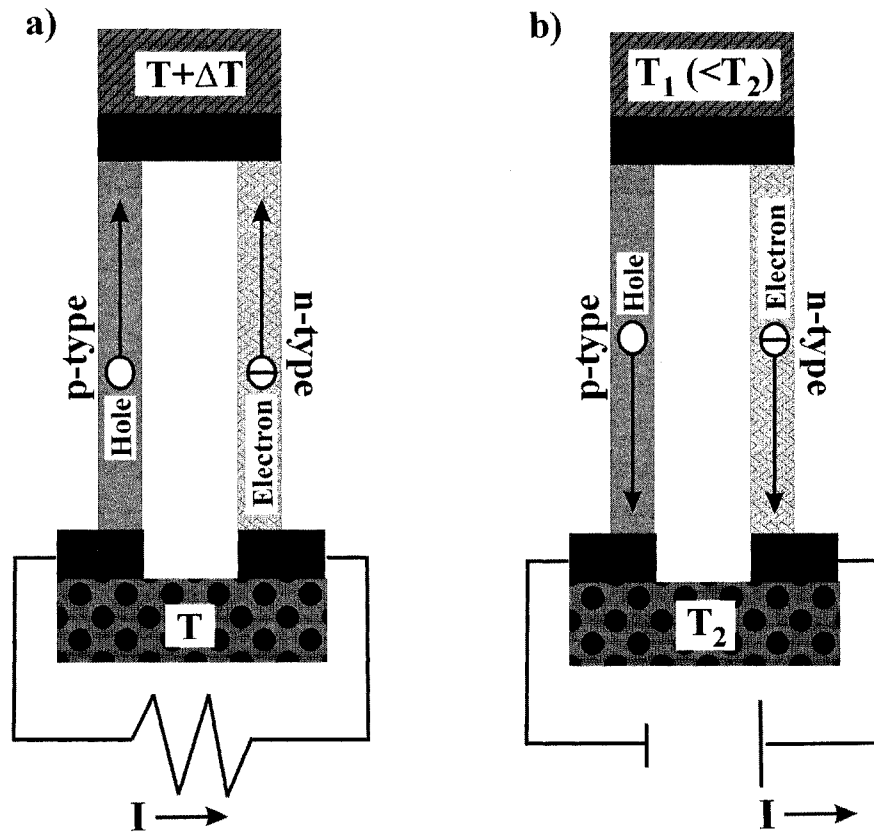


Figure 1-1 Schematic of a thermoelectric device used for either power generation (a) or refrigeration (b).

an electrical power source, the heat carrying holes and electrons can be driven from the heat source (labelled as T_1) to the heat sink (labelled as T_2). This process produces active cooling at the heat source and is referred to as the Peltier effect.²⁰

Various materials have been found to be useful for thermoelectric applications and their performance is described by the figure of merit, $Z = \frac{\alpha^2 \sigma}{\lambda}$, where σ is the electrical conductivity and λ is the total thermal conductivity (which includes both lattice and electronic contributions).²⁰ A high value of Z is desirable for thermoelectric applications. An important aspect that emerges from the equation for Z is that if the total thermal conductivity (λ) can be reduced, Z is increased. Rare earth skutterudites have been found to be good thermoelectrics because of the presence of a rare earth atom in a large dodecahedral cage of pnictogen (P, Sb) atoms. It has been suggested that the rare earth atom may “rattle” within the cage causing phonon scattering, which reduces the lattice thermal conductivity contribution to the λ parameter and therefore should increase Z .²⁰ For this reason, these materials have been described as being “phonon-glass-electron crystals” because they have low thermal conductivity but considerable electron conduction as most are small band-gap semiconductors or metallic.²⁰ The Fe-containing materials examined in this thesis are considered p-type (i.e., a hole is present in the valence band) but n-type skutterudites can also be produced by substitution of some Co atoms for Fe atoms (e.g., $REFe_3CoSb_{12}$).²⁰ Although much effort has been spent on examining these materials, there are still some lingering questions regarding the electronic structure of different skutterudite compounds. Here, X-ray spectroscopy has

been used to try to answer these questions to more fully understand these materials and their applicability as thermoelectrics.

1.3 Bonding in Extended Solids

The extended structures of intermetallic compounds, which will be discussed in the next section, create bonding environments which may be unfamiliar to conventional chemists more familiar with molecular systems. We shall here describe a simple molecular bonding picture and then transform the environment to describe extended intermetallic compounds containing not only metal-anion bonding but also metal-metal bonding and anion-anion bonding.

To begin, consider a simple isolated metal-centred octahedral complex (ML_6). This local coordination geometry is found in two of the three structure types discussed later. If we start with a metal (M) ion such as Fe^{2+} and bring six ligand (L) atoms close, as shown in Figure 1-2, then the atomic orbitals, having the appropriate symmetry, can mix to form molecular orbitals (MO). The extent of the interaction (the “bonding”) is described by the amount of “overlap” which represents the concentration of electron distribution that is established between the atoms. On the Fe atom, the five 3d, three 4p and one 4s orbitals may contribute to the bonding. For simplicity, only sigma (σ) bonds forming between the M and L atoms involving a p orbital from each L atom, containing two electrons (i.e., σ -donor ligands), will be considered.²¹ In this octahedral environment, only the Fe 4p, 4s, $3d_{x^2-y^2}$, and $3d_{z^2}$ orbitals are properly oriented to interact strongly with the L p orbitals. Essentially, the Fe $3d_{xy}$, $3d_{yz}$, and $3d_{xz}$ orbitals are non-bonding. With this information, a molecular orbital (MO) diagram can be fashioned and is shown in Figure 1-2. Such a diagram shows the atomic orbitals involved in making

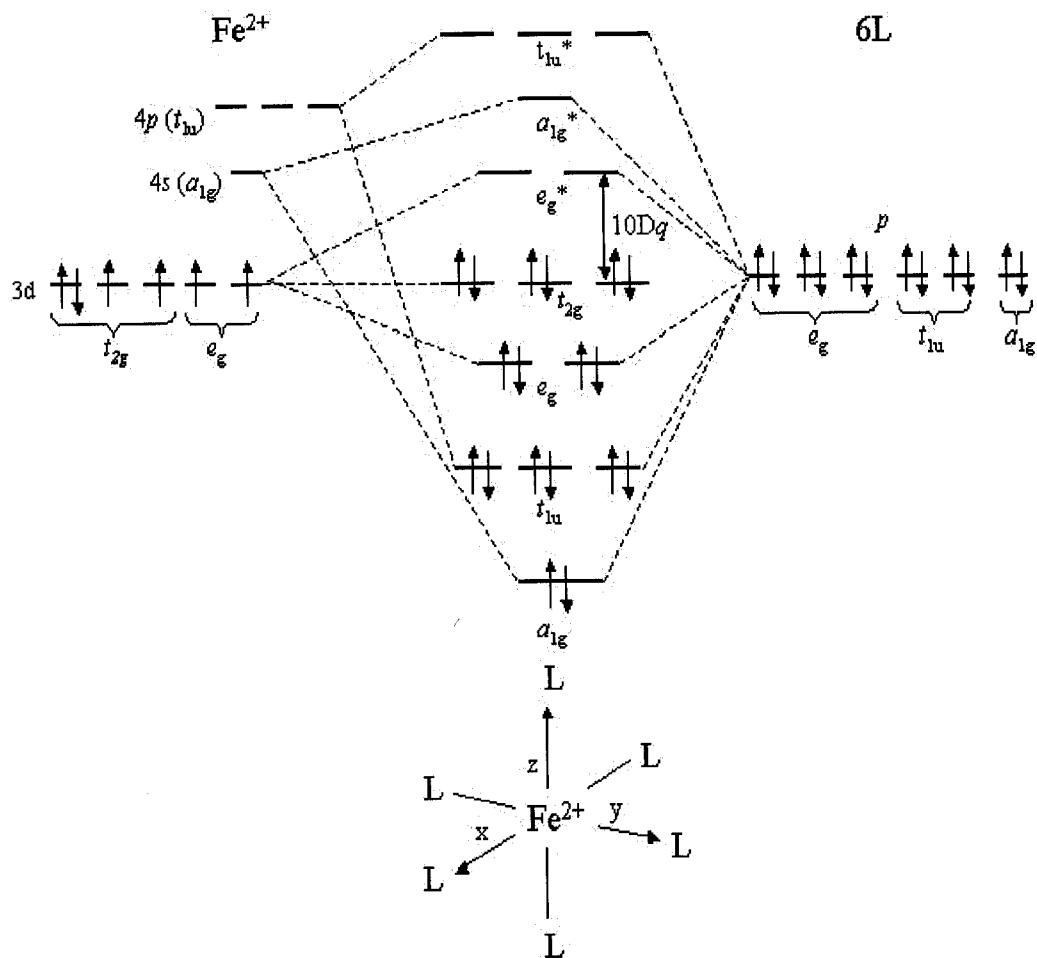


Figure 1-2 Octahedral ML_6 molecule (lower) and the corresponding molecular orbital (MO) diagram (upper). In the upper orbital diagram, the symmetry labels are given for the atomic and molecular orbitals. The low spin case for $M = Fe^{2+}$ is indicated ($10Dq$ is large). This diagram has been compiled using references 21 and 22.

certain molecular orbitals having discrete energies, which can be described using symmetry labels.²² In this diagram, the bonding molecular orbitals are filled by the total of 12 electrons that the six L atoms contribute.

Depending on the oxidation state of the *M* atom, the non-bonding t_{2g} and anti-bonding e_g^* levels may also contain electrons. The energy separation between the t_{2g} and e_g^* states is called $10Dq$ and varies depending on the ligand and metal.²¹ The value of $10Dq$ is larger with strong field ligands (e.g., CN^{1-}) than with weak field ligands (e.g., F^{1-}). If the d orbitals on the metal atom contain 6 electrons as is the case for Fe^{2+} , and $10Dq$ is greater than the electron-electron repulsion energy, then all six electrons will occupy the three t_{2g} states and the *M* ion will be in a low spin state. If, however, a weak field ligand is used then the electron-electron repulsion energy is greater than $10Dq$ and the six d electrons will be distributed between the t_{2g} and e_g^* states creating a high spin configuration.²¹ Before examining how bonding differs in intermetallic compounds, compared to that of the ML_6 example discussed above, the structures must first be examined.

1.4 Structure and Bonding in MnP-type, CoAs₃-type, and ZrSiS-type Compounds

1.4.1 MnP-type Structure

The first row transition metals form a series of monophosphides, MP ($M = Sc-Ni$), whose structures progress from NaCl-type (ScP) to TiAs-type (TiP), NiAs-type (VP), MnP-type (CrP, MnP, FeP, CoP), and NiP-type.²³ The different structure types result from successive distortions arising from the interplay of metal-metal and phosphorus-phosphorus bonding.²³ As the structure changes from ScP to NiP, so does the coordination environment around P. In ScP, P has octahedral symmetry, whereas in TiP

there are two inequivalent P atoms with octahedral and trigonal prismatic coordination. From VP through to NiP, all the P atoms have a trigonal prismatic coordination.²⁴ This trend in coordination environment is in accordance with good space-filling and is consistent with the variation in size of the metal atoms although electronic effects also play a role.²⁴ Along with strong *M*-P bonding, which is found in all of these structures, *M*-*M* bonding is prevalent in the MnP-type and NiP-type structures. As well, a trend in the P-P distances is observed going from ScP to NiP with a P-P distance of >3 Å in ScP to VP and decreasing to ~ 2.6 - 2.7 Å in CrP to CoP and ~ 2.4 Å in NiP.²³ With the shorter distances, uniform P-P bonding in the form of zigzag chains is observed in the MnP-type compounds.²³ At the end of the series P-P dimers are observed in NiP.²³ This P-P bonding can only be considered weak because the distances are longer than the normal P-P single bond distance observed in the molecule, P₄ (~ 2.2 Å).²⁵ A graph showing the P-P and *M*-*M* interactions in the first row transition-metal phosphides is presented in Figure 1-3.

The transformation from NiAs-type (VP) to MnP-type (CrP, MnP, FeP, and CoP) is related to an electronically driven distortion of triangular nets in which the metal atoms approach each other along the *b* and *c* directions.²⁵ A schematic representation of this distortion is shown in Figure 1-4. The occurrence of the NiAs- or MnP-type structures has been related to the overall valence electron count, with the transition from NiAs to MnP occurring when the electron count exceeds 10 electrons but is less than 14, at which point the NiP-type structure is preferred.²⁵ The distortion of the NiAs- to the MnP-type structure can be associated with the presence of *M*-*M* bonding in the latter, a result of the increased occupation of *M* 3d orbitals.²⁵ Other non-first row transition metal phosphides,

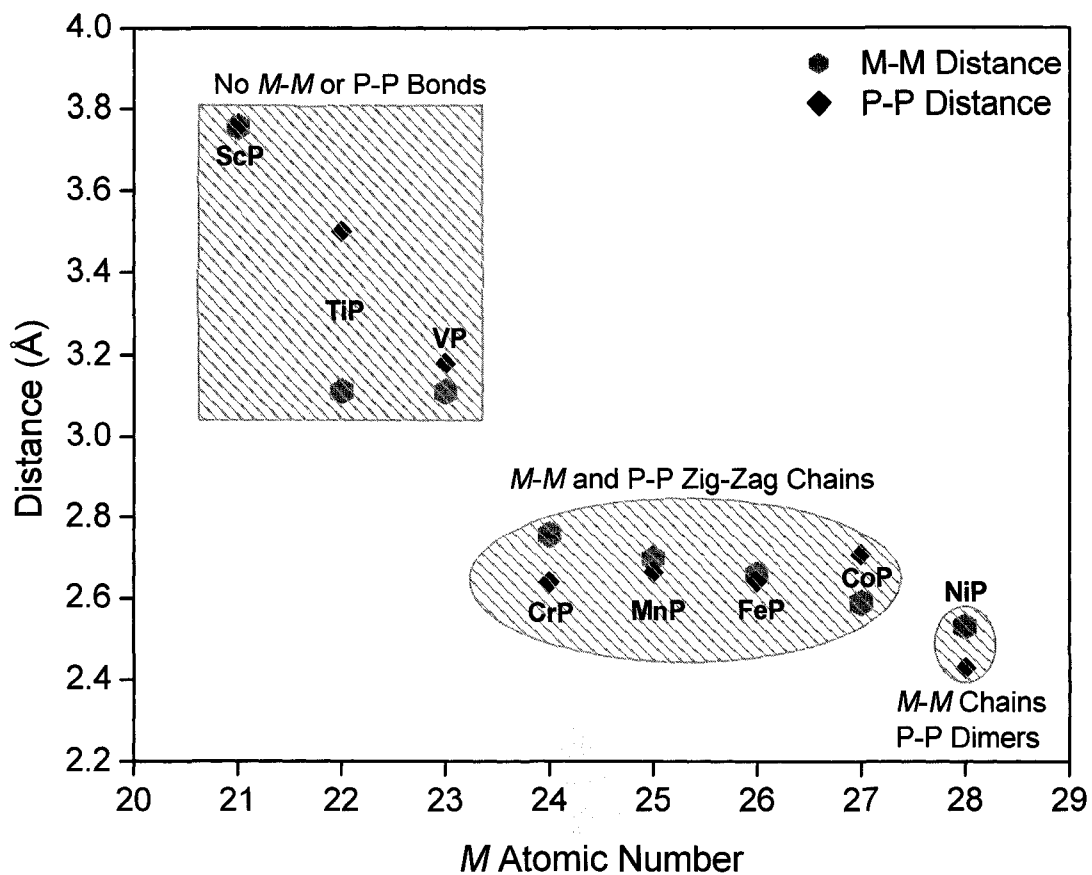


Figure 1-3 Graph of the P-P and *M-M* distances in the first row transition-metal phosphides (ScP – NiP).

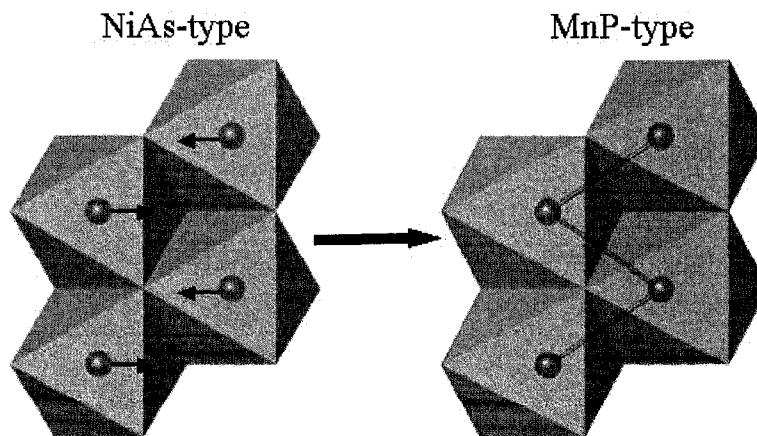


Figure 1-4 Distortion of *M* atom positions that occur as a NiAs-type structure evolves to a MnP-type structure with chains of bonded *M-M* atoms being developed.²⁵ The coordinating *P_n* atoms have been represented as polyhedra.

MoP and WP, as well as transition metal arsenides (CrAs, FeAs, and CoAs) adopt the MnP-type structure. Pseudo binary compounds $M_{1-x}M'_xP$ where $M \neq M'$ ($M = V, Cr, Mn, Fe, Co$),^{26, 27} $MAs_{1-y}P_y$,^{28, 29} and $Mn_{1-x}Cr_xAs_{1-y}P_y$ ^{30, 31} can also adopt this structure type. In these compounds, the substituted atoms are randomly distributed and both X-ray and neutron diffraction indicate no development of a super structure.²⁶⁻²⁸

The MnP-type structure is shown in Figure 1-5. The metal atoms occupy all the octahedral sites between hexagonal close-packed (hcp) layers of phosphorus atoms so that columns of face-sharing distorted metal-centred octahedra develop along the stacking axis (a). The P atoms lie in a trigonal prismatic coordination environment. The electronic structure of these compounds consists of bands that arise from the interaction of metal 3d, 4s, and 4p orbitals with the phosphorus 3s and 3p orbitals. The result is a filled, lower energy, set of $M-P$ bonding levels, a partially filled set of mostly metal-based d levels (split into t_{2g} and e_g components), and an empty, higher energy, set of $M-P$ antibonding levels.^{25, 32, 33} Metal-metal bonding is present not only along the columns of face-sharing octahedra along the a -direction, but also between the columns in the form of zigzag chains running along the b -direction. The metal-metal bonding network originates from the interaction between the metal-based t_{2g} orbitals, whose lobes are directed away from the metal-phosphorus bonds. These metal-metal interactions are quite strong as indicated by bond lengths of 2.6–2.8 Å.³⁴ A result of these metal-metal bonds is that the t_{2g} -based bands are broad and overlap significantly with the e_g -based bands leaving no gap between them in agreement with the metallic character of these compounds.^{35, 36} These structural distortions also generate zigzag chains of phosphorus atoms running along the b -direction, but at distances (2.6–2.7 Å)³⁴ that are somewhat longer than the

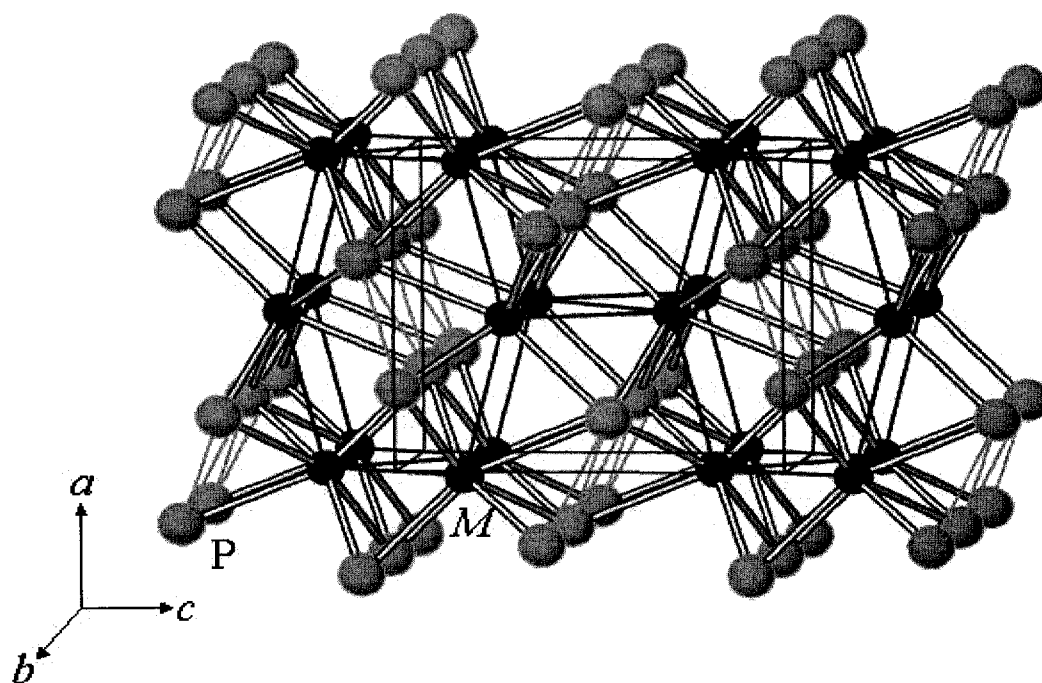


Figure 1-5 MnP-type crystal structure of *MP* viewed down the *b* axis. The small black spheres are *M* atoms and the large grey spheres are *P* atoms. The thin black lines indicate the metal-metal bonding network present along the *a* and *b* directions while the thin grey lines indicate the P-P bonding present along the *b*-direction.

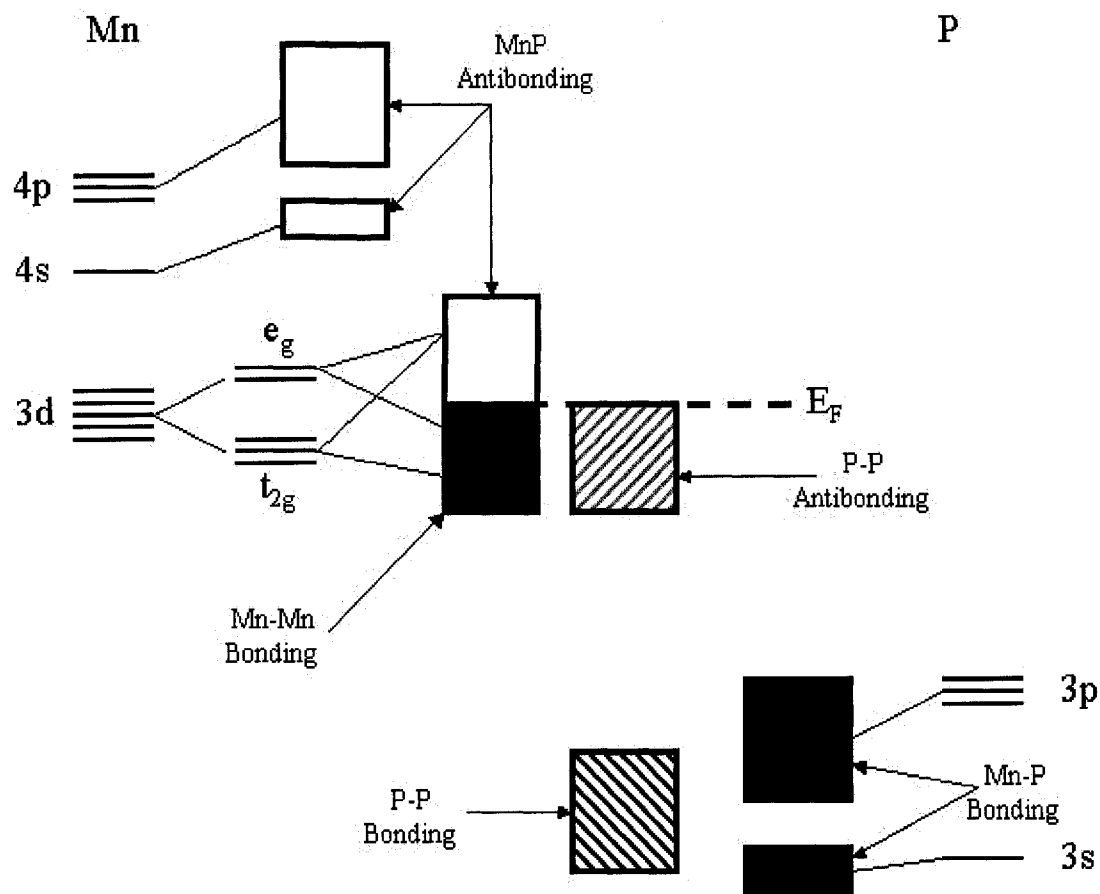


Figure 1-6 Molecular orbital representation of the bonding relationships present in MnP. The filled or hatched boxes represent bands of states occupied with electron density while the empty boxes (above E_F) are unoccupied. The dimensions of the bands are arbitrary. The e_g and t_{2g} originating components overlap resulting in this material being metallic. This diagram has been compiled using information provided in reference 25.

typical single P–P covalent bond length of 2.2 Å.^{25, 37} If the P–P interactions are assumed to be 2 centre-2 electron bonds, only six electrons are required in the valence states for P to attain a closed shell octet with the P charge being 1- but a charge of 3- has also been suggested.²⁵ A MO picture of the bonding found in compounds having this structure type is presented in Figure 1-6.

A description of the density of states and the bonding involved within an extended crystal lattice can also be developed using Bloch functions. Within this formalism, the energies of states are plotted as a function of k (wave vector) in reciprocal space. For a 1-D chain of atoms having a unit cell spacing of a in real space, the wave vector can be represented as $\frac{2\pi}{a}$. In a one dimensional chain of P atoms (Figure 1-7a), similar to that found in MnP, the bonding may incorporate 3s orbital interactions. To solve the Schrödinger equation, $H\psi_k = E\psi_k$, the P 3s orbitals are assigned basis functions, χ_n , and the wavefunction can be written as $\psi_k = \sum_n e^{ikna} \chi_n$.³⁸ Because the energies are symmetrical around the Brillouin zone centre ($k = 0$), we can focus our analysis on one half of the first Brillouin zone ($-\frac{\pi}{a} \leq k \leq \frac{\pi}{a}$) which represents the smallest unit of the reciprocal lattice.³⁸ At $k = 0$, the wavefunction

$$\psi_k = \sum_n e^{ikna} \chi_n = \sum_n e^0 \chi_n = \chi_0 + \chi_1 + \chi_2 \dots$$

leads to the P 3s orbitals participating in only bonding (in-phase) interactions, corresponding to the lowest energy. At the zone edge, $k = \pi/a$, the wavefunction

$$\psi_k = \sum_n e^{im} \chi_n = \sum_n (-1)^n \chi_n = \chi_0 - \chi_1 + \chi_2 - \chi_3 \dots$$

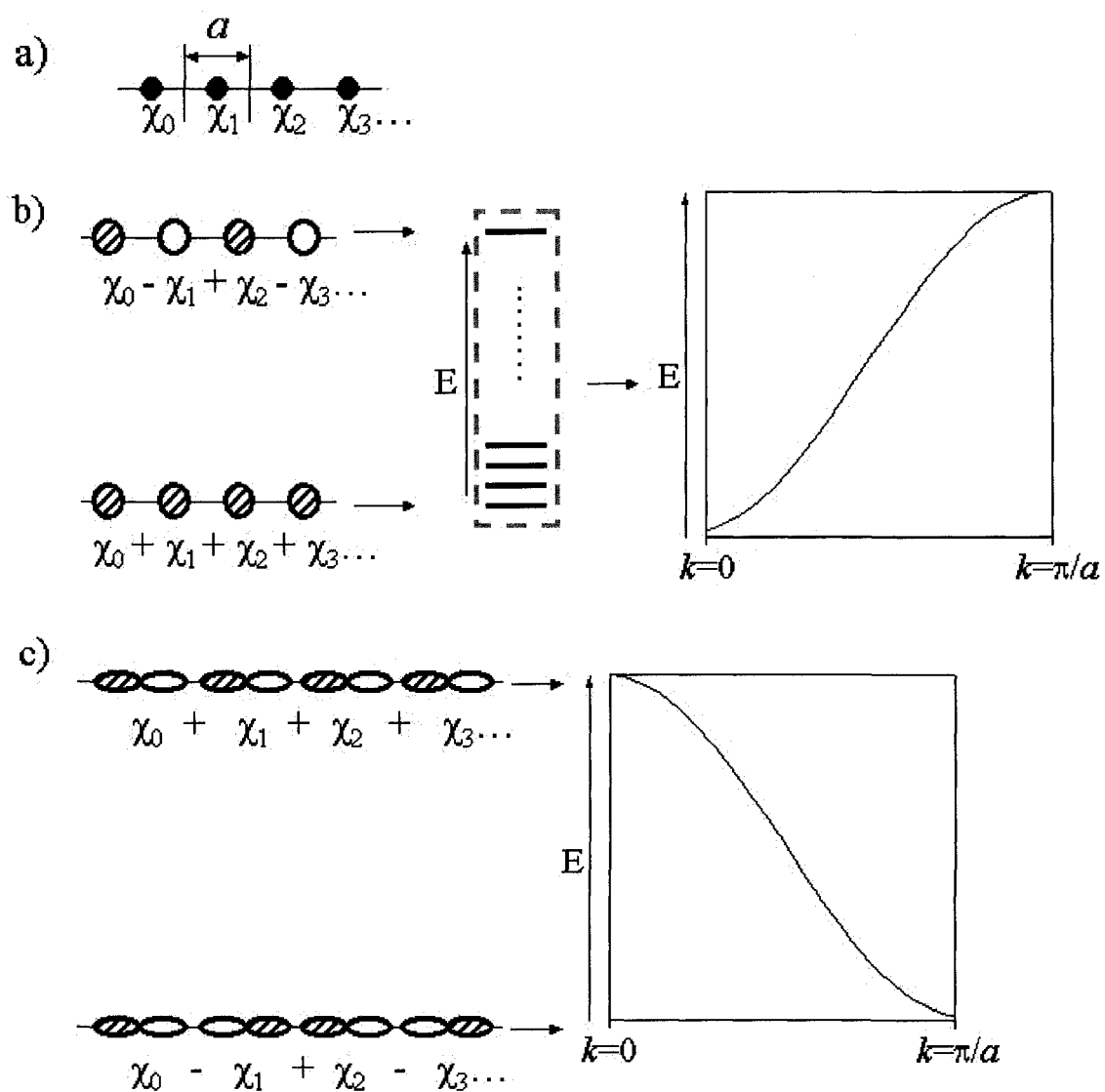


Figure 1-7 Chain of P atoms (a) separated by a distance a with each having a basis function χ_n . A schematic representation of the Bloch function when 3s orbitals are considered is shown in (b) and when 3p orbitals are considered in (c).

leads to the P 3s orbitals participating in only anti-bonding (out-of-phase) interactions, corresponding to the highest energy (Figure 1-7b). Between the two most extreme values of k there are intermediate states containing combinations of both bonding and antibonding interactions. The energies of these states can be plotted vs. k , or they can be portrayed as a “block” of energies as in Figure 1-7b.³⁸ Because of the enormous number of k points, a band is often drawn instead of many closely spaced points when energy is plotted vs. k .

Because the P-P distances within the MnP-type structure are longer than expected for a normal P-P single bond, one might expect that the greatest contribution to the bonding is from P 3p orbitals. If the band structure for a linear chain of P 3p orbitals is examined (Figure 1-7c), the most anti-bonding (highest energy) interaction lies at the zone centre ($k = 0$) while the lowest energy bonding interaction lies at the zone edge, $k = \pi/a$.

The unit cell and corresponding reciprocal space representation (Brillouin zone or Wigner-Seitz cell) for MnP is shown in Figures 1-8a,b with special k vectors marked (Γ , X, Y, Z). These vectors map out the 3 dimensional reciprocal space. The band structure of MnP is shown in Figure 1-8c. The total density of states, DOS, is proportional to the inverse of the slope of E vs. k . The total DOS for MnP as well as the partial DOS for the contributing Mn and P valence orbitals is shown in Figure 1-8d. This representation resembles the molecular orbital diagram described above and presented in Figure 1-6. The Fermi energy (E_F) cuts through the DOS with no gap because MnP is metallic.^{35, 36} Both representations of the valence states shown in Figures 1-8d and 1-6 for MnP contain

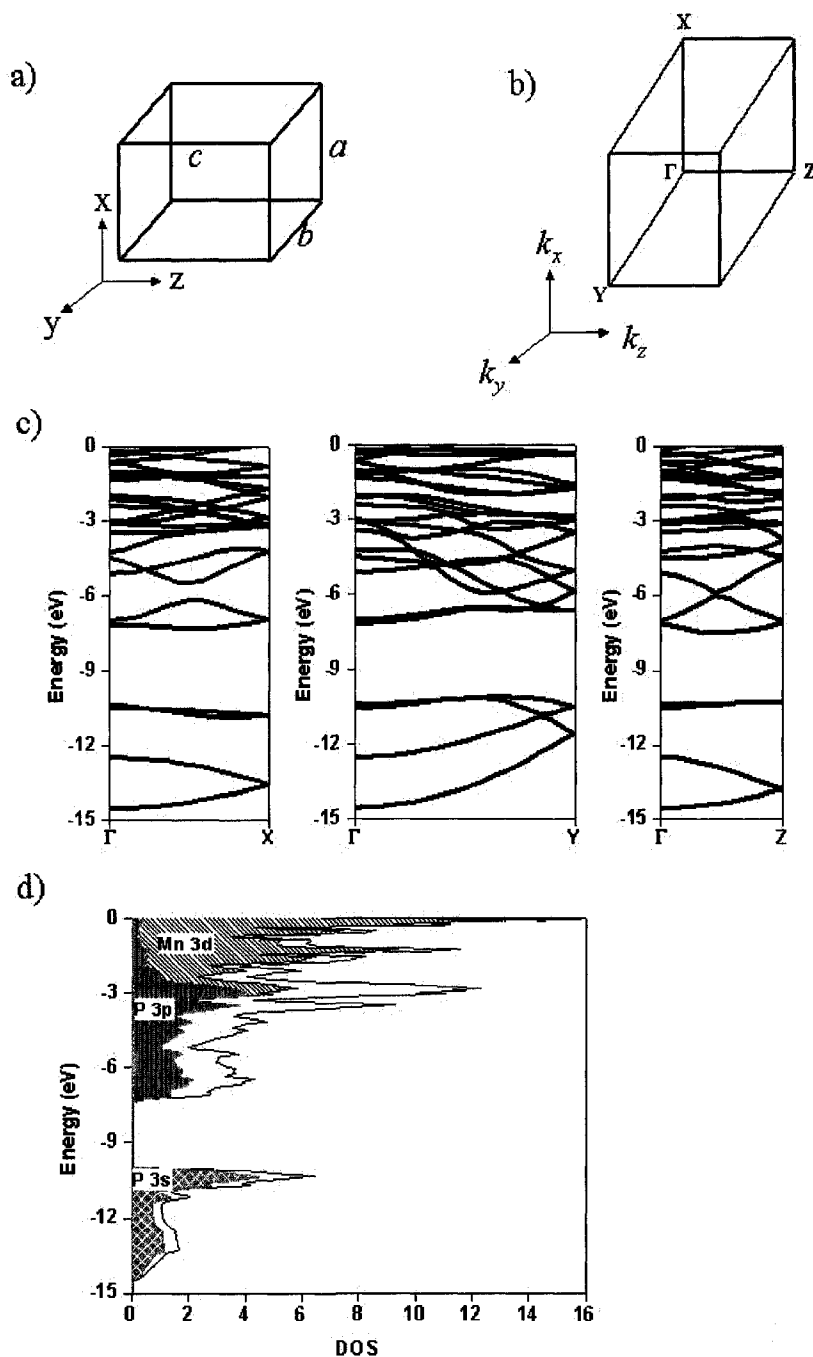


Figure 1-8 The unit cell of MnP is presented in (a) with its reciprocal space analogue (Brillouin zone or Wigner-Seitz cell) being shown in (b). The band structure going from Γ to X, Y, and Z is shown in (c) and the total density of states (DOS) and partial DOS for the Mn 3d, P 3p and P 3s states are shown in (d). In (c) and (d), the Fermi edge (E_F) has been set to 0 eV. The band structure was calculated using a tight-binding linear muffin tin orbital package using the atomic spheres approximation.⁴⁰

broad bonding and antibonding states. This is quite different from the narrow bonding states expected for isolated systems such as ML_6 discussed above.

1.4.2 CoAs₃-type Structure

Since their initial discovery by Jeitschko and Braun,³⁹ the ternary rare-earth (RE) transition-metal pnictides, REM_4Pn_{12} ($RE=La, Ce, Pr, Nd, Sm, Eu, Gd, Tb, Yb; M=Fe, Ru, Os; Pn=P, As, Sb$),⁶ particularly the antimonide members, have received considerable attention because of their potential as thermoelectric materials at high temperatures.²⁰ All of these compounds have a cubic structure related to that of the parent mineral CoAs₃, called skutterudite.⁴¹ Many other binary transition metal pnictides MPn_3 ($M=Co, Rh, Ir; Pn=P, As, Sb$) adopt the same structure.^{42, 43} The crystal structure, presented in Figure 1-9, consists of a network of corner-sharing metal-centred octahedra, which are tilted to form nearly square Pn_4 rings creating large voids in the form of dodecahedral cages of Pn atoms (two such voids are present per unit cell). In the MPn_3 versions, the M charge is considered to be 3+ (i.e., the metals are d^6) with the Pn atoms having a charge of 1- owing to 2 centre – 2 electron ($2c-2e^-$) $Pn-Pn$ bonding. If Group 9 metals are exchanged for Group 8 metals, the M charge is reduced from 3+ to 2+, and a RE atom such as La, with a charge of 3+ can occupy the dodecahedral cage formed by the Pn atoms (e.g., LaFe₄P₁₂ – see Figure 1-9). With these charges and the chemical formula as written above, it can be seen that the valence states are not fully occupied, leaving a hole. The presence of a hole in the valence states has been observed⁴⁴ (i.e., these compounds are p-type) with the hole being suggested to reside on the Fe or P atoms.⁴⁵ The rare-earth atoms that reside within the dodecahedral cage have been observed, by

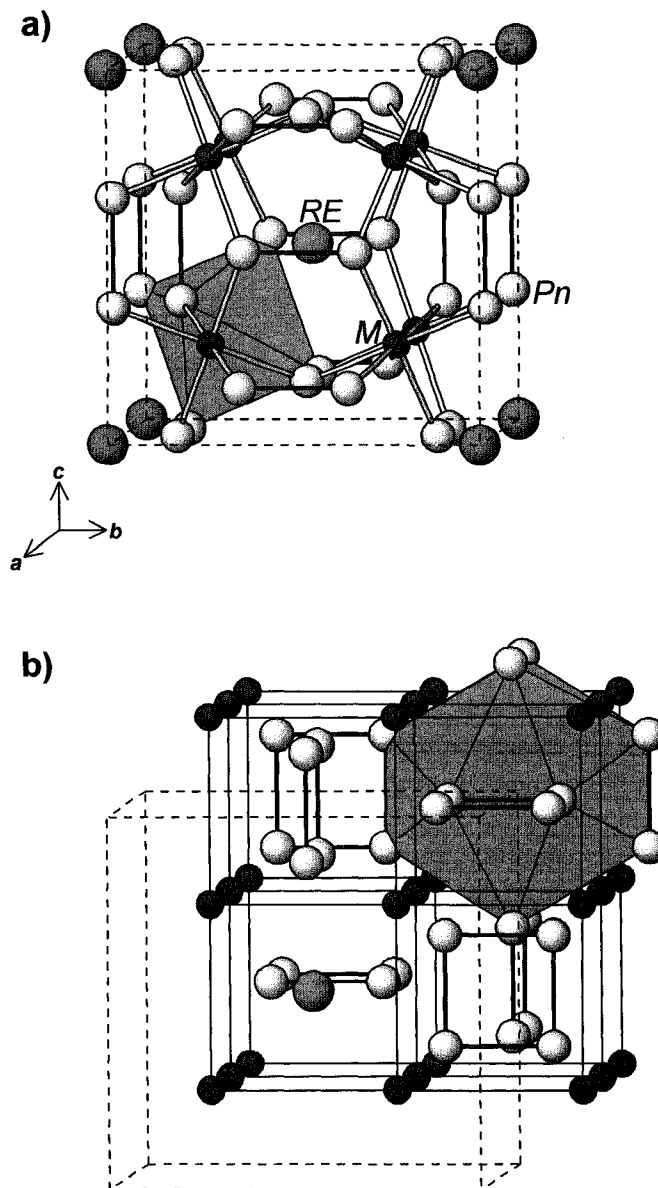


Figure 1-9 Filled skutterudite-type structure of ternary rare-earth transition-metal pnictides REM_4Pn_{12} , with the body-centred cubic unit cell outlined in dashed lines. The large grey spheres are RE atoms, the small solid spheres are M atoms, and the medium lightly-shaded spheres are Pn atoms. (a) The framework of M -centred octahedra is emphasized. (b) An alternative representation highlights the cubic arrangement of M atoms enclosing the RE atoms (centred in a dodecahedral cage) and Pn_4 rings.

X-ray diffraction, to have large displacement parameters,⁴⁶ which suggests that these atoms “rattle” within the cage.

In binary skutterudites such as CoP_3 , an electron-counting scheme is easily derived by applying the Zintl concept.⁶ In this model, the more electropositive Co atoms are assumed to transfer a sufficient number of valence electrons so the P atoms attain closed-shell configurations. An assignment of the resultant low-spin Co^{3+} ($t_{2g}^6 e_g^0$) accounts for the octahedral metal coordination and the observed diamagnetism.⁴⁷ An assignment of P^{1-} is consistent with the presence of P_4 rings with each P atom engaged in two $2c-2e^-$ P–P bonds. Extrapolated to a band picture in which the metal 3d, 4s, and 4p orbitals and the phosphorus 3s and 3p orbitals interact with each other within the extended structure, the electronic structure of the solid consists of filled M –P bonding and metal-based t_{2g} levels lying at lower energy, and empty metal-based e_g and M –P antibonding levels lying at higher energy.⁴⁵ Overlaid on this energy-level diagram are filled P–P bonding and empty P–P antibonding levels. Although an energy gap is expected between the filled t_{2g} and empty e_g bands, more subtle effects conspire to close this gap so that most binary skutterudites are narrow or zero band-gap semiconductors, as has been predicted by calculations and confirmed by experiments.⁴⁸⁻⁵² The closing of the gap can be related to hybridization between the M nd states and Pn np states.⁴⁹ The related ternary compounds have RE atoms which may bond through hybridization of their 4f states with Pn np and M nd states.⁵³

1.4.3 ZrSiS-type Structure

Many metalloid-rich compounds having the formula MAB crystallize in the tetragonal structure type known most commonly as the PbFCl- or ZrSiS-type, an ordered

ternary variant of the Cu_2Sb -type adopted by metal-rich compounds.^{54, 55} They can be distinguished by the quantity Δ , the electron deficiency attributed to A and B (after full electron transfer from M) with respect to each attaining an octet.⁵⁶ In general, the PbFCl -type derives from normal valence compounds where M provides sufficient electrons so that A and B each have an octet ($\Delta = 0$) and form isolated anions, as in $\text{Pb}^{2+}\text{F}^{1-}\text{Cl}^{1-}$. In contrast, the anions in ZrSiS -type compounds must participate in homoatomic bonding to fulfill their octets, as in $\text{Zr}^{4+}\text{Si}^{2-}\text{S}^{2-}$ ($\Delta = 2$) where polyanionic Si–Si bonding is present.⁵⁷ Reflecting the more covalent bonding character, the ZrSiS -type structure is a robust one which is possessed by many MAB compounds. In these cases, M is an early transition metal or f-block element (e.g., Zr, Hf, La, Ce) and A and B are heavier p-block elements (e.g., Si, Ge, As, Sb, S, Se, Te).⁵⁴ The A and B sites are subject to substitutional disorder ($\text{Zr}(\text{Si}_{1-x}\text{As}_x)(\text{As}_y\text{Te}_{1-y})$,⁵⁴ $\text{Zr}(\text{Si}_{0.7}\text{Sb}_{0.3})\text{Sb}$ ⁵⁷) or partial occupancy ($\text{ZrAs}_{0.9}(\text{As}_{0.5}\text{Se}_{0.5})$ ⁵⁸).

The ZrSiS -type structure, adopted by MAB compounds, shown in Figure 1-10, can be described in terms of a stacking of square nets with those containing the A atoms (Si in ZrSiS) being twice as dense as those containing the M (Zr) or B (S) atoms. The Si–Si distances present in the A net in ZrSiS are longer than expected for a $2c-2e^-$ bond (2.51 Å compared to 2.34 Å³⁷), and, as such, only fractional Si–Si bonding can be suggested ($2c-1e^-$). The atomic charges in ZrSiS can be predicted by electron counting. The isolated S atoms accept two electrons from the less electronegative Zr atoms to achieve an octet. The Zr atom, which is coordinated to Si and S atoms in a 9-coordinate monocapped square antiprismatic geometry,⁵⁴ attains an octet and a charge of 4+ when it donates its two remaining 4d electrons to the Si atoms. As a result, the Si atoms should then have a charge of 2- with a total of 6 valence electrons on each Si atom. If we

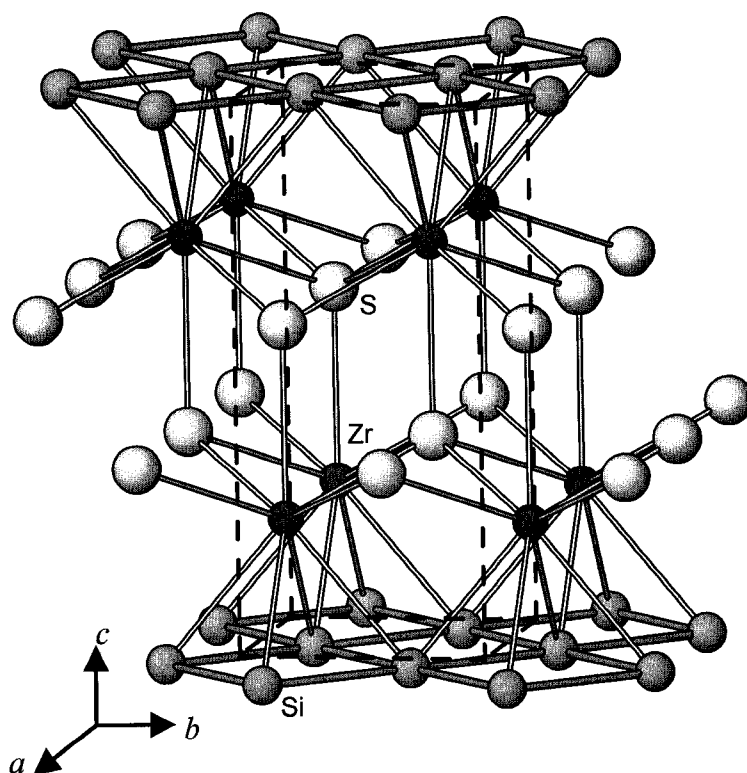


Figure 1-10 Structure of ZrSiS viewed down the *a* direction. Like other MAB compounds with the ZrSiS-type structure, it consists of a stacking of nets of M (Zr), A (Si), and B (S) atoms.

designate the square sheet of Si atoms as lying on the xy plane (ab plane in Figure 1-10), then placing 2 electrons each into the $3p_z$ and $3s$ orbitals leaves one electron each in the $3p_x$ and $3p_y$ orbitals. Because four Si-Si bonds are present in the xy plane per Si atom, with each bond donating $1/2$ of an electron to the Si atom, the Si atoms are, like the S and Zr atoms, able to attain a closed shell octet. Such an electron counting scheme suggests that the Si atoms follow the rule of 6 valence electrons per atom for those present in a square net.⁵⁹

1.5 Spectroscopy

In this thesis, X-ray photoelectron spectroscopy (XPS) and X-ray absorption spectroscopy (XAS) have been used to study various intermetallic compounds. The absorption of an X-ray, with appropriate energy, results in electrons being either fully ejected from atoms (XPS) or promoted to bound/continuum conduction states (XAS). By measuring the energy of the ejected electrons (photoelectrons) by kinetic energy analysis (XPS) or by observing the magnitude of X-ray absorption that occurs (XAS), information can be gained about the charge on the atom under study as well as variations in the local and extended chemical environment. XPS can also be used to directly examine the valence band and therefore the occupied bonding, antibonding, and nonbonding states found within a compound. Both XPS and XAS reveal the atomic charges and degree of ionic bonding present. This is very important in the case of intermetallic compounds where the bonding is rarely fully covalent or ionic and does not always follow simple electron counting rules. A more detailed description of these techniques will be provided in Chapter 2.

1.6 Overview

This thesis is devoted to the study of the electronic structure of various intermetallic compounds by applying XPS and XAS. The electronic structure of intermetallics has not been extensively studied spectroscopically so many unanswered questions persist. First, the charges of the constituent atoms in compounds having the MnP-type structure can be formulated as either $M^{1+}P^{1-}$ or $M^{3+}P^{3-}$ depending on whether or not the weak P-P bonds are considered. XPS has been used to examine the charges in CrP, MnP, FeP, and CoP not only by an analysis of the core-line binding energies but also the valence band spectra. This study will be described in Chapter 3. In Chapters 4 and 5, the variation in atomic charges in M or Pn substituted MnP-type compounds has been investigated by XPS and XAS in both mixed metal, $M_{1-x}M'_xP$ (Chapter 4), and mixed pnictogen, $MA_{1-y}P_y$ (Chapter 5), systems. Both studies show how charge transfer between the M atoms via $M-M$ bonding and between Pn atoms via $Pn-Pn$ bonding can affect the atomic charges, which is revealed by the resulting photoelectron binding energies. In Chapters 6 and 7, the charge environments of skutterudites will be discussed. Particular attention has been given to the charge of Ce in $CeFe_4P_{12}$ (Chapter 6) and $CeFe_4Sb_{12}$ (Chapter 7) because there is still considerable discussion in the literature as to whether the Ce charge is 4+ or 3+ and whether the hole present in the valence of the $REFe_4Pn_{12}$ compounds is located on the Fe or Pn atoms.⁴⁵ Besides the known compounds, the new phase $Hf(Si_xAs_{1-x})As$ ($0.5 \leq x \leq 0.7$) has been discovered which adopts the ZrSiS-type structure. The synthesis, structure and electronic structure, as determined by XPS and photoemission spectroscopy, of this material are described in Chapter 8. In this study (Chapter 8) we show that atomic charges predicted by electron

counting, using an ionic model, do not always correlate with the more realistic charges deduced for intermetallic compounds by spectroscopic analysis. We have also been able to examine how the charge environments on the anions changes when proceeding from systems with weak *Pn-Pn* bonding (MnP-type) to those where strong *Pn-Pn* bonding (CoAs₃-type) occurs and finally to cases of heteroatomic anion-anion bonding (Hf(Si_xAs_{1-x})As). These comparisons will be discussed in Chapter 9.

Chapter 2

X-ray Spectroscopy

2.1 Introduction

In this thesis, X-ray spectroscopy in the form of X-ray photoelectron spectroscopy (XPS), X-ray absorption spectroscopy (XAS), and photoemission spectroscopy (PES) has been used to study the electronic structure of various intermetallic compounds. The last two techniques (XAS and PES) require the use of synchrotron radiation whereas XPS is most commonly a laboratory-based technique using a conventional X-ray source. All these spectroscopic techniques involve the absorption of X-ray energy by an atom but differ in how the resulting excitation is analysed.

2.2 X-ray Photoelectron Spectroscopy (XPS)

X-ray photoelectron spectroscopy (XPS or ESCA – Electron Spectroscopy for Chemical Analysis) is a surface sensitive technique that is widely used to study the composition of surface layers (e.g., oxide films formed on transition metals).⁶⁰ XPS can also be used to study the bulk electronic structure of materials when the surface is properly prepared. This technique is capable of detecting all of the elements in the periodic table except H and He, which lack core electrons.⁶¹ Developed by Kai Siegbahn and co-workers in the 1950s, this technique is an application of the photoelectric effect,⁶¹

which was discovered by Hertz and later developed by Einstein who won the Nobel Prize in physics for this work in 1921.^{60, 62} The photoelectric effect describes the phenomenon wherein, if the radiation energy is sufficient, an atom can absorb the energy and the resulting excitation can lead to the emission of an electron (termed a photoelectron).⁶¹ This description can be represented by the following model;



where M is the atom in its ground state (containing n electrons), $h\nu$ is the excitation energy, M^+ is the atom in its final excited state after being photoionized (containing $n-1$ electrons), and e^- is the photoelectron. A soft X-ray source is typically used ($E < 2$ keV), but ultraviolet and hard X-ray radiation experiments can also be performed. When X-rays (either monochromatic or achromatic) are focused onto a surface, this effect can be used to determine the elements present by analyzing the energy of the ejected photoelectrons.⁶⁰ The energy of the photoelectron depends on the element from which it originated, the oxidation state of that element, the identity of its nearest and next-nearest neighbours, and the ground state orbital in which the electron resided.^{60, 61} The energies associated with the excitation, described by the photoelectric effect, can be represented as:

$$h\nu = KE + BE + \Phi_{Sample} \quad (2-2)$$

where $h\nu$ is the energy of the absorbed X-ray, KE is the kinetic energy of the photoelectron after it has been ejected from the atom, BE is the binding energy of the electron, and Φ_{Sample} is the work function of the surface (i.e., the energy required to transport the electron from its original depth to a distance outside of the surface, $\Phi_{Sample} =$

$E_{\text{vacuum}(v)} - E_{\text{Fermi}(F)}$).⁶⁰ The BE can be defined as the energy required to remove the electron from its ground state orbital to just above the Fermi edge (E_F), or as the difference in energy between the ground state containing n electrons and the final state, after photoionization, containing $n-1$ electrons.^{60, 63} A scheme for the excitation of a P atom leading to the production of a 2p photoelectron is presented in Figure 2-1. The resulting peak intensities are proportional to the element concentration, hence composition information can be obtained (this will be discussed in more detail later).

A schematic diagram of an XPS instrument is shown in Figure 2-2. The excitation is initiated by bombarding the surface with photons. Typical sources include achromatic and monochromatic Al and Mg X-ray tubes, He ultraviolet sources and synchrotron radiation.^{60, 64, 65} Although the incident photon flux is lower, monochromatic sources are preferred because they give better resolution than achromatic sources. After the photoelectron is ejected from the surface, it is transported within a vacuum environment to an analysis system where its energy is measured. The angle between the X-ray source and the detector system is typically fixed at 54.7° , which reduces the orbital orientation dependence of the excitation.^{66, 67} A concentric hemispherical analyzer (CHA) is used to direct the photoelectrons to a detector.⁶⁰ The photoelectron enters the transfer lens (entrance slit) of the CHA where its kinetic energy is reduced by an aperture having a retarding electric field. The retarding energy is stepped across a range of energies so that all photoelectrons have the same energy (pass energy) after they enter the CHA.⁶⁰ The lower the pass energy, the higher the resulting spectral resolution. Within the vacuum chamber, electrostatic or magnetic fields, or both, are applied to collect and focus electrons to increase the flux of photoelectrons

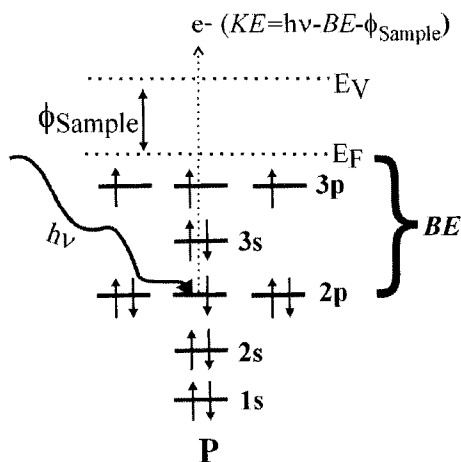


Figure 2-1 Excitation of a P atom leading to the ejection of a photoelectron from the 2p orbital.

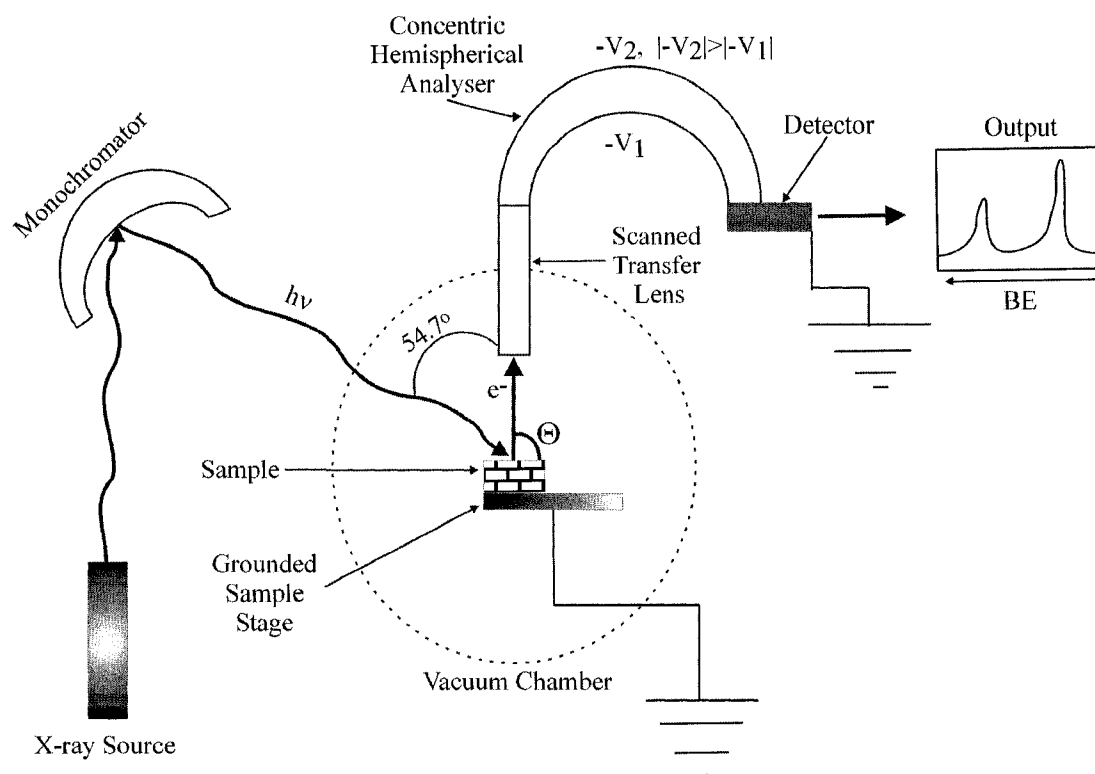


Figure 2-2 Schematic representation of a modern XPS instrument having a monochromatic X-ray source.

entering the CHA.

In the CHA, photoelectrons are focussed at the exit slit by opposing electric fields (negative potentials, V) on each hemisphere of the analyser.⁶⁰ The potential on the upper hemisphere is more negative than that on the lower hemisphere. Photoelectrons that enter the CHA with energies greater than or less than the pass energy are unable to successfully travel through the analyser and collide with the walls and are absorbed. In the XPS instruments used in this work (Kratos AXIS 165 and Kratos AXIS ULTRA), the energy filtered photoelectrons enter a channeltron detector which amplifies the electrons to a magnified pulse current which is then counted leading to an increased signal-to-noise ratio. By scanning the retarding energy in the transfer lense, a spectrum is recorded as intensity (counts per second, cps) vs. either the total kinetic energy of the photoelectron (i.e., its original energy before being reduced to the pass energy) or its calculated binding energy (BE).⁶⁰ In Eq 2-2, the work function term, Φ_{Sample} , is an energy specifically related to the sample. However, in XPS, by pinning the Fermi level of the sample and spectrometer to the same energy through grounding, the work function (Φ) is transformed to:

$$\Phi = (\Phi_{\text{Spectrometer}} + \Phi_{\text{Sample}}) - \Phi_{\text{Sample}} = \Phi_{\text{Spectrometer}} \quad (2-3).^{60}$$

This new work function, $\Phi_{\text{Spectrometer}}$, is a constant value that can be measured allowing for Eq 2-2 to be simplified to:

$$h\nu = KE + BE \quad (2-4).$$

During the XPS experiment, as electrons are being actively removed from the sample under study, charging may occur. The effect of charging is it tends to raise the measured BE of all the photoelectron peaks.⁶⁰ In modern instruments, the sample stage

is grounded. Through proper preparation, the sample is placed in electrical contact with the stage. If the sample is a metal or small band-gap semiconductor, the effect of charging is significantly reduced through grounding of the stage (i.e., the sample is able to recover the electrons that it has lost). For larger band-gap semiconductors and insulators, the effects of charging cannot be eliminated entirely by grounding. In such cases, the BE of a peak can be calibrated to a known value. Often the 1s signal from adventitious C deposited on the sample surface that is desorbed from the walls of the vacuum chamber is used for charge referencing by calibrating it to the known value of 284.8 ± 0.2 eV.⁶⁰ In the case of insulators, charging is often so severe that the resulting spectrum is very broad and difficult or impossible to interpret. Low energy electrons (e.g., from a tungsten filament) can be used to “bathe” the surface and compensate for charging, allowing well-resolved spectra to be obtained.⁶⁰ This process is referred to as charge neutralization.

XPS is a surface-sensitive technique with a maximum analysis depth of nearly 10 nm depending on the X-ray energy used (~5 nm is a more typical analysis depth).⁶⁰ Although X-rays can readily penetrate solids, the surface sensitivity of XPS arises from the numerous interactions that an ejected photoelectron suffers as it travels through the surface. The photoelectron may collide with other electrons, either elastically so that its trajectory changes, or inelastically so that its kinetic energy decreases (~10 - 40 eV/collision).^{60, 68, 69} The distance that a photoelectron can travel between inelastic collisions is called the inelastic mean free path (IMFP, λ). This value depends on the sample and can be estimated from calculations.⁷⁰ The IMFP generally becomes longer as

the kinetic energy of the exiting photoelectron increases,⁶⁰ and is typically in the range of $\sim 10 - 30 \text{ \AA}$.⁷⁰

Electrons traveling from deep within the sample are more likely to undergo multiple scattering events, losing enough kinetic energy to the point that they cannot penetrate the surface and be detected.⁶⁸ The maximum depth from which electrons can travel successfully through the material and be detected depends on the photoelectron kinetic energy and the angle (relative to the surface) of the exiting photoelectrons (take-off angle, Θ – See Figure 2-2).⁶⁰ (In an XPS instrument, the take-off angle is defined as the angle between the sample surface and the detector.) The sampling depth is maximized when the kinetic energy of the photoelectron is the highest and when the take-off angle is 90° . An XPS peak is considered to contain information from a depth, d , equal to $3\lambda \sin\Theta$.⁶⁰ This equation indicates that a photoelectron can only travel a maximum distance of 3λ (when $\Theta = 90^\circ$) before it becomes $>95\%$ probable that it will undergo an inelastic collision and lose energy. With the IMFP values indicated above, an XPS peak contains information from a maximum sample depth of $\sim 3-9 \text{ nm}$. Those electrons that have lost energy but are capable of breaching the surface make up the intense stepped background observed in all XPS spectra.⁶⁰ The intensity of the background increases with decreasing kinetic energy (increasing BE). As the take-off angle decreases (from 90° to 0°), the amount of material that the photoelectrons have to travel through before breaching the surface increases. This enhances the probability that the photoelectrons will undergo inelastic electron scattering and lose energy and therefore the observed spectral peaks (formed from photoelectrons that did not lose energy) are

more surface sensitive. This effect of varying the surface sensitivity of XPS by changing the take-off angle forms the basis of angle-resolved XPS (ARXPS), to be described later.

To examine the electronic structure of a compound by XPS, the surface must be free of surface oxides (formed by reaction with the atmosphere) or contaminants. There are several ways to produce clean surfaces. Single crystal or polycrystalline samples can be cleaved in vacuum to produce a fresh surface but samples must be fairly large to produce surfaces that are larger than the spot size of the instrument ($\sim 400 \mu\text{m} \times 700 \mu\text{m}$ in Kratos spectrometers). If this is not possible, clean, oxide-free surfaces can be obtained by grinding small crystals under an inert atmosphere in a glove box directly attached to the vacuum chamber of the instrument.

A widely used alternative method for preparing samples is to sputter-clean the surface in vacuum with a beam of energetic Ar^+ ions.⁶⁰ The ion impact removes contaminant or oxide layers, exposing a clean surface for analysis. A scheme of the sputtering process is shown in Figure 2-3. A drawback of this technique is that lighter atoms may be preferentially removed, rendering the composition of the surface layer different from that of the bulk.⁶⁰ Defects can also be introduced into the structure and atoms may undergo reduction,⁶⁰ which is very common when sputtering ionic oxides such as CeO_2 .^{71, 72} Although annealing in vacuum can often heal the surface, this is not always appropriate and depends on the sample. To overcome these possible side effects, the user must carefully compare the spectra of the sputter-cleaned surface to those from the “as received” surface, to determine whether or not the surface has been changed adversely.

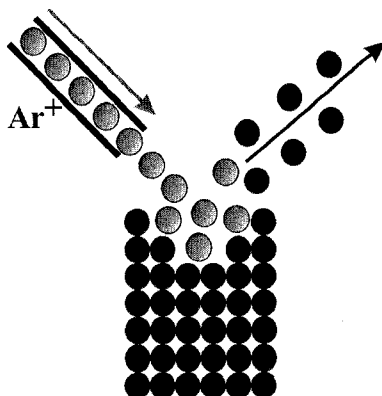


Figure 2-3 Diagram of the Ar^+ ion sputtering of a surface, which removes contaminate/oxide layers, exposing a clean surface for analysis.

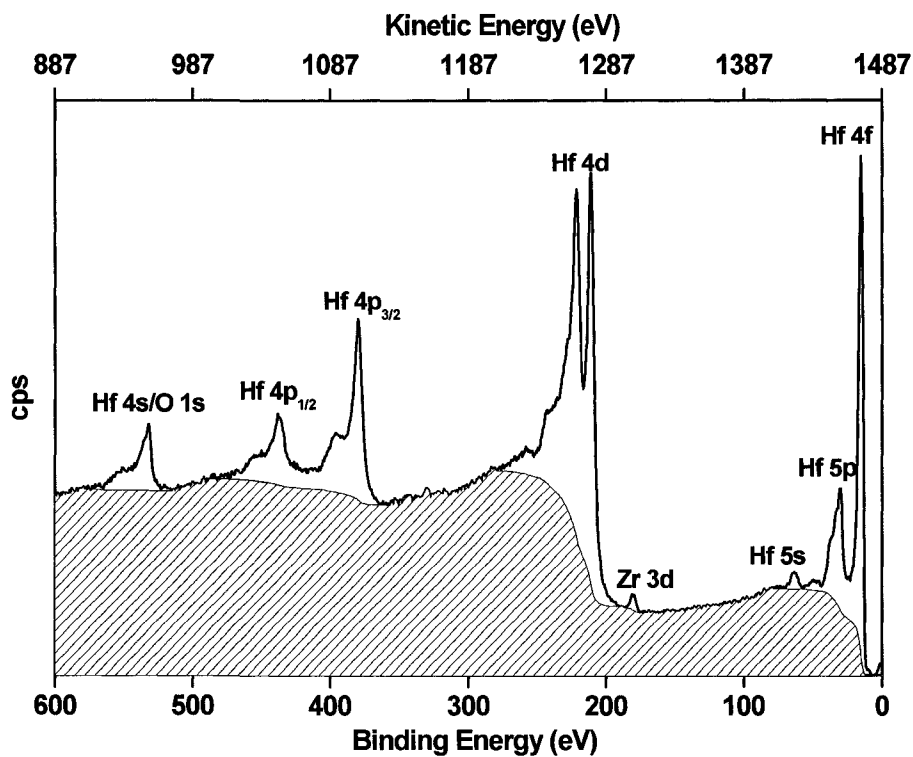


Figure 2-4 Survey spectrum of sputter cleaned Hf metal containing ~3% Zr impurity. All of the visible core-line peaks have been labelled. The hatched part of the spectrum represents the stepped background found in all XPS spectra resulting from photoelectrons losing kinetic energy by inelastic electron scattering as they travel through the surface and into vacuum. This spectrum was collected using a monochromatic Al $K\alpha$ X-ray source (1486.7 eV).

As discussed above, XPS can differentiate between atoms of the same elements in different chemical environments. Small differences may be revealed with high-resolution spectra which are collected using a low pass energy, a small energy step (~ 0.1 eV) and an energy envelope of only a few tens of eV. To determine the concentrations of different species on a surface, survey spectra are collected using a high pass energy (reduced resolution), a large energy step (0.7 eV) and a large energy envelope (> 1000 eV) allowing collection of all peaks that can be excited using the available X-ray source. When examining survey (or high resolution) spectra, the peaks resulting from the excitation of photoelectrons from particular orbitals sit on top of the stepped background, which arises from inelastic electron scattering. A representative survey spectrum of Hf metal is shown in Figure 2-4 with the different core-line peaks and energy loss background labelled.

The concentration of different species in a survey spectrum can be calculated by first subtracting the energy loss background resulting from inelastic electron scattering and dividing the peak area by the probability (cross-section, σ) that a photoelectron will be excited from a particular orbital. The photoelectron cross-sections for most elements in the periodic table, for a range of excitation energies, have been calculated.^{73, 74} The peak intensities must also be corrected for various spectrometer related factors (K).⁷⁵ These can include the efficiency of the detector, the presence of stray magnetic fields which affect transmission of low energy electrons, and the transmission function of the instrument.⁷⁵ The spectrometer transmission function depends on the photoelectron kinetic energy while the other factors may be influenced by the instrument and its location. The transmission function corrects for the fact that not all of the photoelectrons

that are emitted from the surface with a particular energy are detected. The final correction factor required is the inelastic mean free path (IMFP, λ). When inelastic collisions occur, the photoelectrons lose considerable amounts of kinetic energy and no longer contribute to the XPS peak which has a defined energy width. Thus, the peak intensity arising from a particular species is lower, implying a smaller concentration than the true value.⁶⁸ The percent concentration (C_i) of species on a surface can be calculated as follows:

$$C_i = \frac{I_i / (\sigma_i K_i \lambda_i)}{\sum_{j=1}^n I_j / (\sigma_j K_j \lambda_j)} \quad (2-5)$$

where $I_i / (\sigma_i K_i \lambda_i)$ is the corrected intensity of the species under consideration and $\sum_{j=1}^n I_j / (\sigma_j K_j \lambda_j)$ is the sum of the corrected intensities from all of the species present in the material.⁷⁵ Such an analysis allows for the detection of concentrations of elements that are greater than ~0.1 atomic percent.⁶⁰ Lower concentrations of elements are difficult to determine because of the presence of the intense energy loss background over the entire spectrum. When determining the concentration of species present in the same sample matrix that have peaks that are relatively close in binding energy, the values of K and λ are likely to be similar and can therefore be removed from the equation.

As stated above, the BE can be described as the energy difference between the initial state and the final state after the atom has been photoionized. In the 1930s (before the development of XPS but after the discovery of the photoelectric effect), Koopmans suggested that the final state(s), produced after removal of an electron, could be represented by a single wave function (i.e., a single energy).⁷⁶ This approximation is

referred to as Koopmans' theorem and was initially employed to interpret XPS spectra. In early work, this theorem proved sufficient because spectral resolution was low. When higher resolution spectrometers became available, however, spectral fine structures were observed. This suggested that Koopmans's theorem oversimplified the photoemission process and new theories were developed that allowed for different final states to be recognized with the differences in final state energy accounting for the observed fine structure.

When spectra are examined that result from the excitation of an orbital having a non-zero angular momentum, two peaks are observed.⁶⁰ These peaks are a result of final state configurations which have either a spin-up or spin-down electron left in the core-orbital after removal of a photoelectron. The difference in final state energy depending on if a spin-up or spin-down unpaired electron is left in the excited core-orbital is a result of spin-orbit coupling – the vector coupling of the spin angular momentum with the orbital angular momentum of the unpaired electron. The spin-up (parallel) peak is always lower in BE than the spin-down (anti-parallel) peak.^{60, 77} The difference in energy between the two final states, referred to as the exchange or spin-orbit splitting energy, is dependant on the orbital angular momentum, and is proportional to the inverse of the cube of the orbital radius ($1/r^3$) as well as the atomic number (Z).⁶⁰ The labels used to describe these peaks are represented as $nl_{j=l\pm s}$ where n is the principal quantum number of the excited orbital, l is the angular orbital momentum, and s is the spin quantum number of the unpaired electron remaining in the orbital after photoionization.⁶⁰ For example, if a P 2p orbital is excited then two final states are produced: $2p_{3/2}$ and $2p_{1/2}$ where the former is lower in energy than the latter. The intensity ratio of these peaks

is related to the degeneracy of the two final states and is equal to $(2j_1+1)/(2j_2+1)$ where j_1 is the coupled angular momentum (l) and spin (s) quantum numbers from the spin-up core electron and j_2 is the coupled momentum and spin quantum numbers from the spin-down core electron.⁶⁰ In the case of a 2p orbital, the $2p_{3/2}:2p_{1/2}$ intensity ratio is 2:1. An example of this splitting can be observed in the P 2p spectrum of FeP (Figure 2-5). When $l = 0$, as is the case for an s orbital, the final states are degenerate, regardless of the spin of the electron left in the orbital after removal of a photoelectron, and no spin-orbit splitting is observed.

Besides spin-orbit coupling, metal and rare-earth atoms having partly occupied d and/or f valence orbitals can show significant final state fine-structure.^{78, 79} When a photoelectron is removed from a core orbital of a metal atom containing spin-unpaired valence electrons, these electrons can undergo spin-orbit coupling with the unpaired core electron (or hole) producing multiple non-degenerate final states which yield broad photoelectron peaks.^{60, 78} This process is referred to as multiplet splitting.^{60, 78} If no spin-unpaired valence electrons are available, then this process does not occur and only a single symmetric peak is found which is similar to those observed for main group elements. Metal atoms found in metallic systems (or low to nearly zero bandgap semiconductors) show spectra that have an asymmetric lineshape to higher BE.^{79, 80} The reason for this lineshape will be discussed in the forthcoming chapters.

Apart from lineshape, detailed information about the system can be obtained from the binding energy (BE). As was indicated above, shifts in BE depend on the charge of the atom under study as well as the nature of the coordination environment.^{60, 61} Shifts can also be related to the degree of ionic character of the bonding between the excited

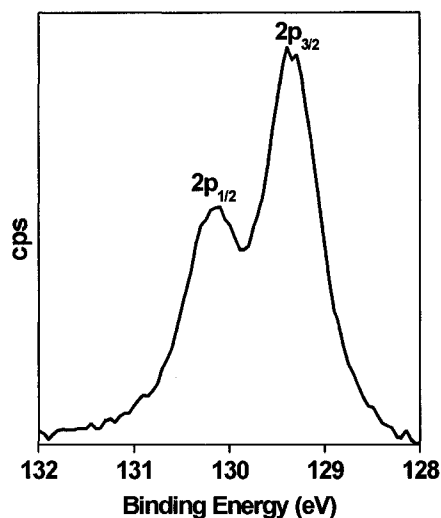


Figure 2-5 High resolution P 2p XPS spectrum from FeP. The two distinct spin-orbit coupled final states ($2p_{3/2}$, $2p_{1/2}$) have been labelled.

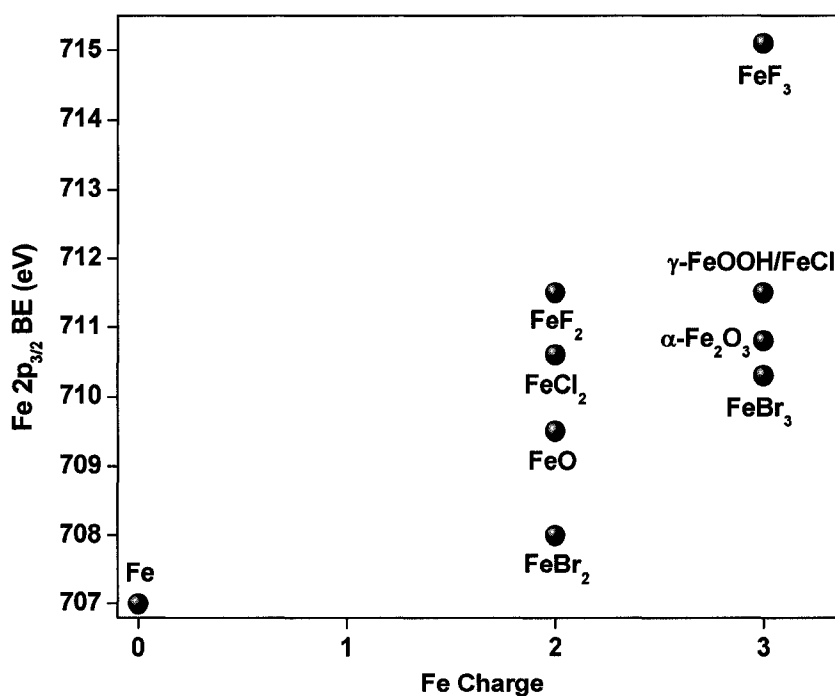


Figure 2-6 Plot of the Fe $2p_{3/2}$ binding energy (BE) vs. nominal Fe charge for a series of Fe oxides and halides.⁸¹ Although the BE increases with Fe charge from 0 to +3, the BE also varies between compounds having identical charges. This shift results from variations in the bonding environment and screening of the Fe nuclear charge provided by the different ligands.

atom and the coordinating ligands.^{60, 61} The shifts in BE can be described by the ability of electrons to screen the nuclear charge on the atom. Generally, the more electrons available, the easier it is to remove a photoelectron and therefore a lower BE is observed. Although the atomic charge tends to have the greatest effect on the BE, the other effects listed above can have a substantial influence.⁶⁰ An example of this is the variation of the Fe $2p_{3/2}$ BE for the element, and its various oxides and halides with the nominal Fe charge, which is illustrated in Figure 2-6.⁸¹ Although substantial shifts are observed between Fe⁰, Fe²⁺, and Fe³⁺, BE shifts are also observed between compounds having the same nominal Fe charge. These latter BE shifts can be related to the difference in screening of the Fe nuclear charge provided by the neighbouring atoms.⁸¹ In the intermetallic compounds discussed in this thesis, the bonding is much more covalent than it is in the more ionic Fe compounds discussed above and the shifts in BE between similar compounds can be fairly small. In these cases, the entire system must be considered when analyzing BE shifts from a particular atom.

In addition to characteristic core orbital excitations, valence band spectra can also be measured in an XPS spectrometer.¹ Such spectra probe the fully or partially occupied bonding, nonbonding or antibonding levels of the system and can be used to deduce atomic charge by fitting the spectrum with component peaks. This fitting method will be discussed in later chapters. One advantage of collecting valence band spectra is they can be directly compared to the calculated density of states to determine the validity of these calculations. To properly compare the valence spectrum of a compound with the calculated density of states, the spectral peak intensities need to be corrected for differences in photoelectron cross-section arising from different orbital components.

A typical use of XPS is to examine not only the thickness, but also the composition of surface layers such as oxides formed on metals. Although XPS has been used in this thesis to analyze the bulk electronic structure of intermetallic compounds, some of the methods used to examine surface layers will be discussed here. As was discussed above, XPS analysis becomes more surface sensitive as the take-off angle is lowered from 90° to 15° .⁶⁰ By collecting spectra, both high resolution and survey, at different take-off angles, the changes in intensity of the components of the spectra can give a qualitative picture of the surface in terms of depth and composition. Such an analysis is referred to as angle resolved XPS (ARXPS). A typical method used for examining thick films is depth profiling.⁶⁰ Using an Ar^+ sputter beam to remove surface material, spectra can be collected from different depths after sputtering for different amounts of time. Repeated sputtering followed by spectral measurement allows examination of the composition of very thick films such as oxide layers formed on steels during high temperature annealing.⁸² The thickness of these layers can be estimated by calibrating the sputtering rate of the Ar^+ source using a standard material. Because sputtering rates differ from material to material, the standard needs to be chemically similar to that of the surface to be examined. Calibration can be performed by determining the thickness of the sputter crater formed over a specific period of time by use of atomic force microscopy (AFM).⁶⁰ A disadvantage of this technique is that it is destructive, making it inappropriate when examining heritage samples such as artefacts. Non-destructive, quantitative techniques have also been developed that determine the film thickness through direct analysis of high resolution and survey spectra.⁸³⁻⁸⁵

2.3 Synchrotron Radiation

When relativistic electrons (or positrons) travelling near the speed of light are forced to move in a circular orbit by the application of a magnetic field, electromagnetic radiation is released in the forward direction of motion at a tangent to the orbit.⁸⁶ This “synchrotron radiation” (SR) was originally observed in particle accelerators and was considered problematic because its release caused the particles to lose energy.^{87, 88} Later it was realised that this radiation could be exploited to examine materials and dedicated systems were constructed to perform many different types of experiments, including spectroscopy and diffraction.^{86, 89, 90} Synchrotron radiation is characterized by three attributes: (i) it is a tuneable radiation source, as will be discussed below, (ii) the radiation is plane polarized, and (iii) the radiation is highly intense and focussed.⁸⁶ The intensity can be quantified in terms of flux (photons/second) or brightness (photons/second/area (mm²)). The brightness of synchrotron radiation is compared to that of some typical sources in Figure 2-7.

To produce synchrotron radiation, high energy electrons are confined in a storage ring (held under ultra-high vacuum) with magnetic fields being used to accelerate them around the orbit of the ring.⁸⁶ As the electrons are accelerated around the radius of the storage ring, a fan of polychromatic radiation is released that spans a wide energy range extending from IR through ultraviolet to soft (<2 keV) and hard (>2 keV) X-ray radiation.⁹¹ The released radiation is directed down a beamline, a vacuum pipe installed tangent to the ring. Within this pipe, monochromators or diffraction gratings (for hard or soft X-rays, respectively) are installed to select the wavelength of light to be used for the experiment and mirrors can be positioned to control the size of the beam.^{86, 91} At the end

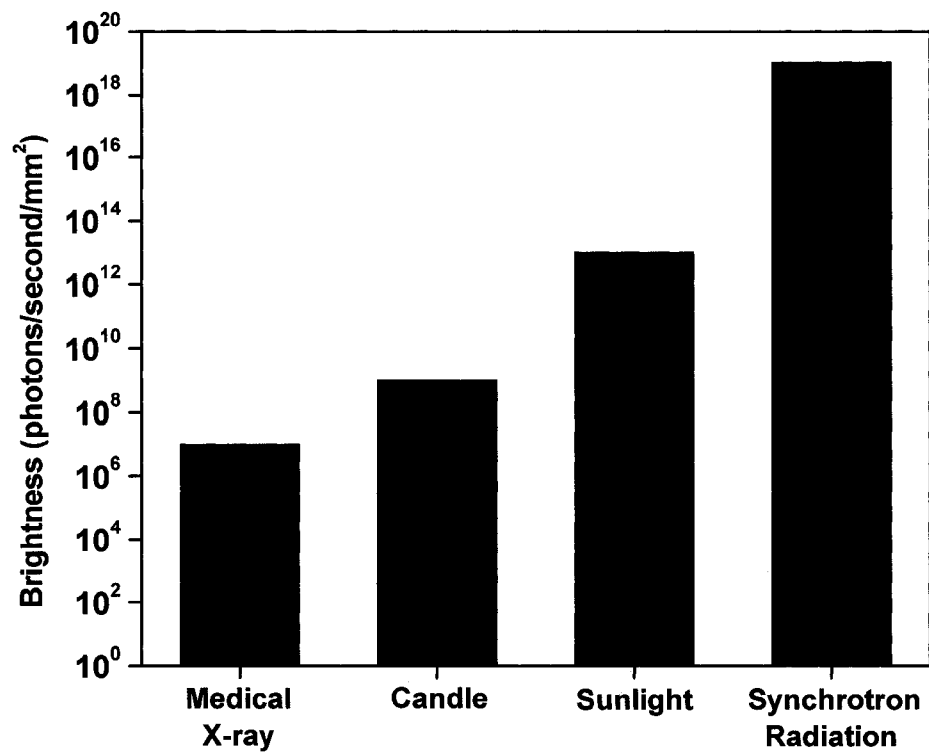


Figure 2-7 Difference in brightness between a synchrotron radiation source and other light sources.

of the beamline is the endstation where the experiment is performed. The brightness of this light, compared to other sources, allows very dilute samples to be examined that one may not be able to study by other techniques.

A diagram of a synchrotron is shown in Figure 2-8. Electrons from a linear accelerator are ramped up to the appropriate energy in a booster ring and injected into the storage ring where they are accelerated around the circumference by dipole magnets (bending magnets, $B \sim 1.35$ T (CLS)) to release synchrotron radiation, which travels down the beamline to the endstation.⁹¹ The radiation produced is polarized in the plane of the storage ring (horizontally polarized). To keep the electrons travelling in the storage ring without hitting the walls, the focus and orbit is maintained by use of quadrupole and sextupole magnets.⁹¹ The energy that the electrons have lost through the process of releasing electromagnetic radiation is recovered by the application of radio frequency (RF) radiation by means of a cavity within the vacuum ring.⁹² The RF radiation field causes the electrons to be bunched, which lowers the emittance (a product of the horizontal and vertical standard deviation and divergence of the electron beam) and increases the brightness of the synchrotron radiation.⁸⁶ This bunching also introduces a time structure to the emitted radiation which can be used to study dynamic processes. The maximum energy of the released synchrotron radiation depends on the energy of the electrons in the storage ring. The radius of the ring is also important as it becomes significantly more difficult to change the path of electrons as their energy increases. For example, the Canadian Light Source (CLS) uses electrons with an energy of 2.9 GeV and the storage ring radius is ~ 27 m, whereas the radius of the storage ring at the Advanced Photon Source (APS) is ~ 176 m for electrons having an energy of 7 GeV. The energy

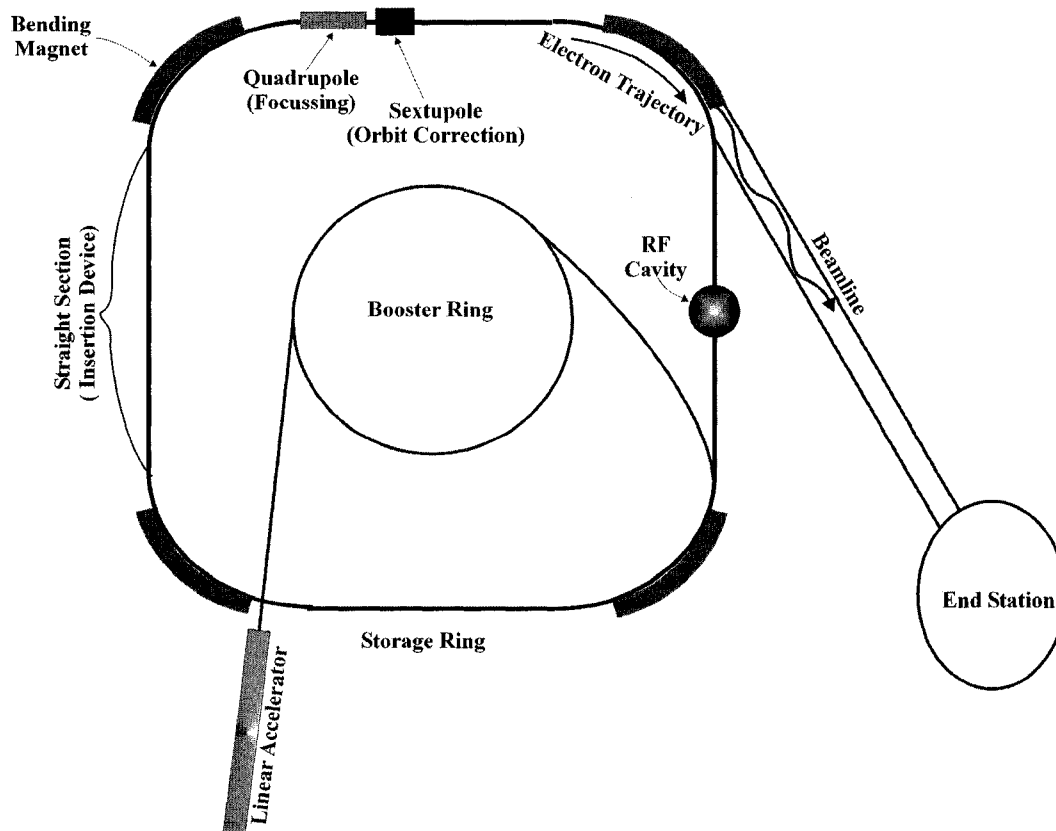


Figure 2-8 Layout of a synchrotron radiation source. For the purposes of simplification, only a few of the magnetic structures (quadrupoles and sextapoles) have been drawn.

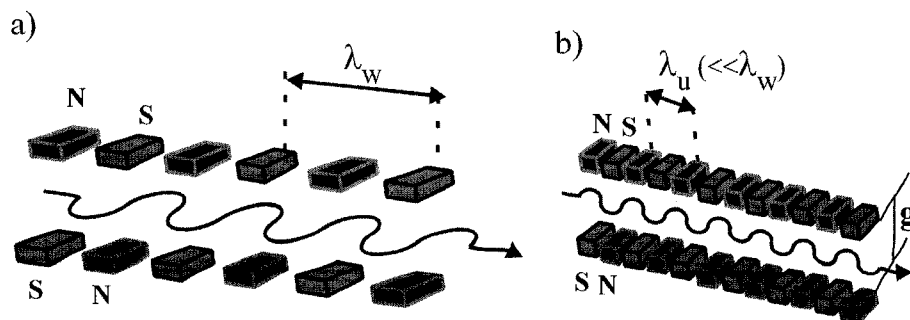


Figure 2-9 Schematic representation of (a) wiggler and (b) undulator insertion devices. Both the magnetic field strength and magnetic period ($\lambda_{w,u}$) of an undulator are less than that for a wiggler. The curved solid line represents the path of the electrons as they travel through the insertion devices.

lost to the production of synchrotron radiation by electrons traveling in a storage ring when accelerated by a single bending magnet can be expressed as

$$\Delta E = 88.5 \frac{E^4}{\rho} = 26.6 E^3 B \quad (2-6)$$

where ΔE is the range of SR energies produced in keV, E is the energy of electrons traveling in the storage ring in GeV, ρ (in m) is the radius of the orbit of electrons when deflected by the bending magnet (this value is not necessarily the same as the radius of the storage ring), and B is the magnetic field strength in tesla (T).⁸⁶

Besides bending magnets, insertion devices located in the straight sections of the storage ring (Figure 2-8) can also be used to produce synchrotron radiation. Insertion devices can be characterized as structures of multiple magnets having alternating poles. These devices can be separated into two categories: wigglers and undulators. In wigglers (Figure 2-9a), magnets having high magnetic fields (B up to 4 T (CLS)) are spaced apart so that the electrons travel in long magnetic periods ($\lambda_{\text{wiggler}(w)}$).⁸⁶ The effect of this insertion device is to increase the brightness of the radiation produced compared to a bending magnet. If a wiggler has N magnetic periods, then the brightness of the radiation is comparable to $2N$ bending magnets.⁸⁶ As well, the magnetic field strengths in wigglers are often higher than those of bending magnets which increases the maximum obtainable photon energy (Eq 2-6). Like bending magnets, wigglers also produce horizontally polarized radiation.⁸⁶ Undulators (Figure 2-9b) typically provide weaker magnetic fields and shorter periods ($\lambda_{\text{undulator}(u)}$) and the pulses of radiation generated as the electrons traverse each magnetic period are out of phase with the next pulse.⁸⁶ Pulses having wavelengths (λ) equal to this phase difference (or a subharmonic (λ/n)) add,

creating radiation profiles wherein the energies correspond to the harmonic wavelengths rather than the “white line” spectrum that is produced by either bending magnets or wigglers.⁸⁶ The brightness of the radiation produced by undulators is greater than that produced by wigglers or bending magnets but the maximum X-ray energy obtained is generally less. The wavelength of the photons released by the undulator can be adjusted by changing the magnetic field (accomplished by changing the gap distance, g , between poles – see Figure 2-9).⁸⁶ Although horizontally polarized radiation is normally produced, the polarization of undulator radiation can be varied by changing the orientation of the magnetic fields so that circularly or elliptically polarized radiation can be produced.⁸⁶

2.4 X-ray Absorption Spectroscopy (XAS)

The most prevalent spectroscopic technique utilizing synchrotron radiation to study materials is X-ray absorption spectroscopy (also referred to as X-ray absorption fine structure (XAFS)). This technique can be subdivided into two separate but intertwined techniques: X-ray absorption near-edge spectroscopy (XANES) and extended X-ray absorption fine structure (EXAFS).⁹³ XAS follows the well known “Beer-Lambert” law

$$I = I_0 e^{-\mu t} \quad (2-7)$$

where I_0 is the intensity of the exciting radiation (X-rays in the case of this thesis), I is the intensity of the transmitted radiation after interacting with the sample, μ is the absorption coefficient, and t is the sample thickness.^{94, 95} As X-rays with increasing energy are passed through the sample, absorption will occur for each atom at a specific energy (threshold) through the process of exciting a core electron into an unoccupied bound

(bonding) or continuum state.⁹⁶ This sharp increase in absorption probability is called an “edge”. These XANES (edge) spectra are characteristic of the atom and can provide information on atomic charge and ligand effects by analysis of shifts in the absorption energies (similar to analysis of XPS BEs) and can also provide information on the coordination environment of the atom under study through analysis of the lineshape.⁹⁷ The excitation normally follows dipole selection rules, i.e., $\Delta l = \pm 1$, (e.g., Co 1s \rightarrow Co 4p or P 3p in CoP) but quadrupolar excitations can also occur (e.g., Co 1s \rightarrow Co 3d), as shown in Figure 2-10a for the Co K-edge spectrum from CoP.^{93, 97} These quadrupolar peaks are often observed below the absorption threshold and are referred to as pre-edge peaks. The pre-edge peak intensity can provide information on the coordination environment and charge of transition metal atoms as will be discussed in Chapters 4 and 5.⁹⁷

As the excitation energy increases past the absorption edge (threshold energy), core electrons are ejected from the atom producing photoelectrons. This can be envisioned in a similar manner to that shown in Eq 2-1. The photoelectron can travel through and out of the surface of the material but if it interacts with other atoms within the sample it may be backscattered toward the atom from which it was initially excited (this is referred to as single scattering, see Figure 2-11).⁹⁵ Treating this photoelectron as a wave with a wavelength of $\lambda = 2\pi/k$ (k = wave vector), the wave front of the backscattered photoelectron can interfere constructively or destructively with the outgoing photoelectron.⁹⁵ This interference results in a modification of the absorption coefficient, μ , which appears as oscillations in the spectrum above the absorption edge. These features are known as the EXAFS (Figure 2-10a). The oscillations can be

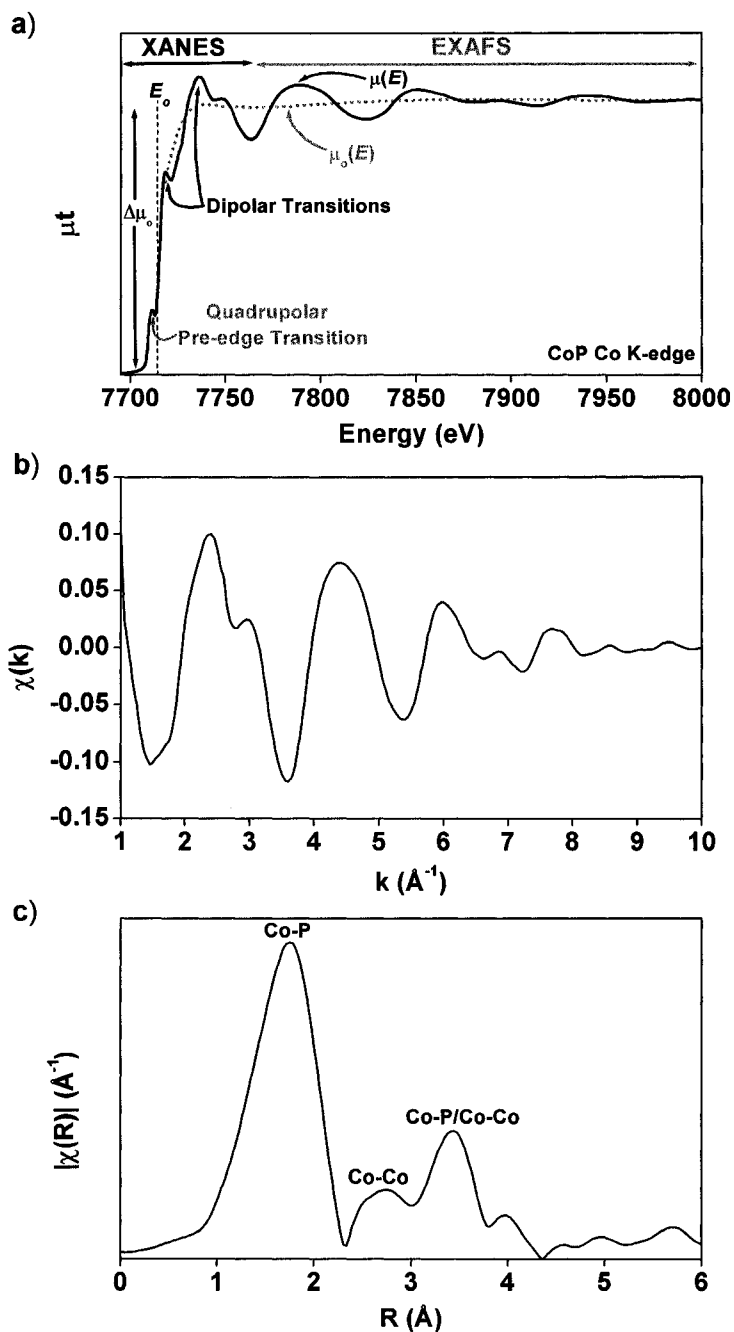


Figure 2-10 (a) Co K-edge XAS spectrum from CoP collected in transmission mode. The parameters found in Eq 2-9 are labelled as well as the quadrupolar pre-edge peak and the peaks resulting from dipolar transitions. The identity of the quadrupolar and dipolar transitions will be discussed in Chapters 4 and 5. The energy at which the XAS spectrum is separated into XANES or EXAFS is approximate. The EXAFS (χ) vs. k is shown in (b) while the magnitude of the χ vs. R after being Fourier transformed is shown in (c) with the identities of the main peaks being labelled.

represented vs. k (Figure 2-10b) by application of the equation

$$k = \sqrt{\frac{2m(E - E_o)}{\hbar^2}} \quad (2-8)$$

where m is the electron mass, E is the energy where the oscillation is observed, E_o is the absorption edge threshold energy, and \hbar is the reduced Planck's constant.^{93, 94} The intensity of these peaks is described by the function

$$\chi(E) = \frac{\mu(E) - \mu_o(E)}{\Delta\mu_o(E_o)} \quad (2-9)$$

where $\mu(E)$ is the intensity of the oscillation resulting from the EXAFS phenomenon, $\mu_o(E)$ is a background function that describes what the absorption would look like for an isolated atom, and $\Delta\mu_o(E_o)$ is the absorption edge step height.^{93, 94} Fourier transforming this spectrum replaces the oscillations with peaks at specific values of R which relate to the scattering path length. These peaks can provide information on atom-atom distances and, by analysis of the peak amplitude, the coordination environment surrounding the atom.^{93, 95} A representative EXAFS spectrum for CoP is displayed in Figure 2-10c.

The EXAFS function, χ , can be modelled by

$$\chi(k) = \sum_j \frac{N_j f_j S_0^2 e^{-2k^2 \sigma_j^2}}{k R_j^2} \sin[2kR_j + \delta_j(k)] \quad (2-10).^{94}$$

In this simplified model, the different variables take into account variations in the scattering amplitude of the surrounding atoms (f_j), the coordination number of neighbouring atoms (N_j), the distance between the absorbing and scattering atom (R_j), effects of disorder within the system resulting from thermal atom-atom oscillations (σ^2) and a phase shift $\delta_j(k)$.⁹⁴ The photoelectron wave vector (k) and an amplitude reduction

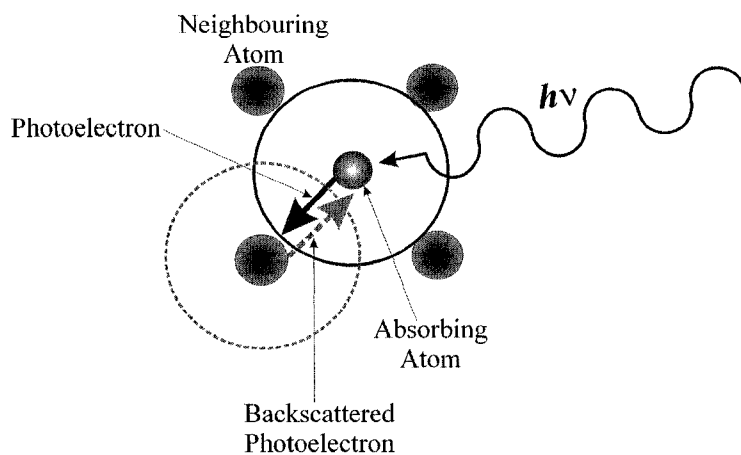


Figure 2-11 Schematic diagram of a single scattering event causing the EXAFS phenomena. The backscatter of a photoelectron from a neighbouring atom creates constructive or destructive interference and is shown by the arrows when the electron is treated as a particle or by circles when the electron is treated as a wave.

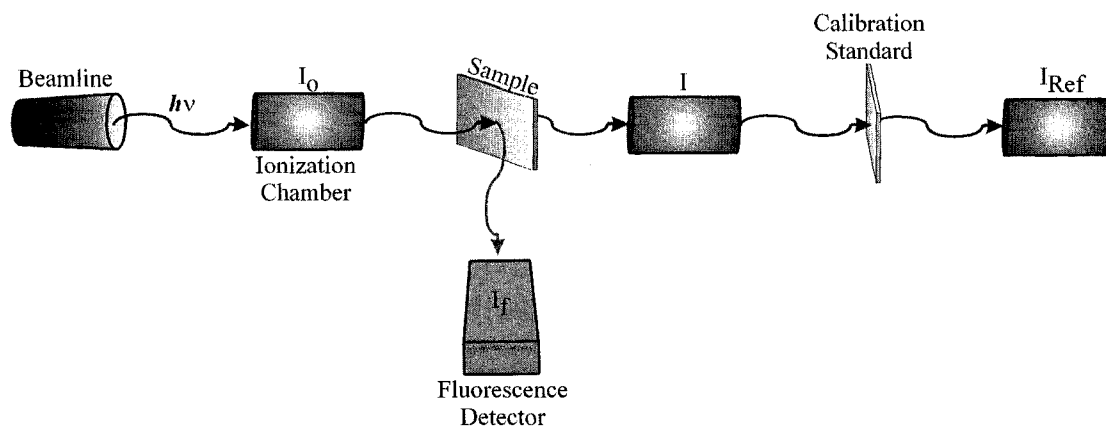


Figure 2-12 Typical set-up of a hard X-ray XAS experiment.

term (S_0^2) are also included.^{93, 94} The value of S_0^2 accounts for energy loss of the photoelectron from multi-electron excitations of the absorbing atom.⁹³ EXAFS is a local probe of the structure around an absorbing atom providing information on two to three coordination shells. Besides single scattering, multiple scattering can also occur in which the photoelectron is scattered by two or more atoms before returning to the excited atom. Because these path lengths are often long and since k is inversely related to R ,⁹⁸ oscillations resulting from multiple scattering can have energies, E , that are similar to E_0 (i.e., they can overlap the XANES portion of the spectrum – See Eq 2-8).⁹⁹⁻¹⁰¹ Consequently, quantitative analysis of XANES spectra is difficult.

A scheme of a hard X-ray XAS experiment is presented in Figure 2-12. X-rays with a particular energy, which is selected by a monochromator, first enter an ionization chamber (labelled in Figure 2-12) containing an inert gas (e.g., N_2 or He).^{94, 100} The incident X-ray photon flux (I_0) is determined by measuring the ionization current. The X-rays that exit through this chamber are focussed onto the sample where absorption occurs as the X-ray energy is scanned through and above the absorption edge energy. The flux of X-rays that are transmitted through the sample is measured using an ionization chamber placed directly behind the sample (I). In this way, a spectrum of absorption intensity (μt) vs. energy is collected where $\mu t = -\ln[I / I_0]$. The sample thickness, t , is often not known so absorption is represented as μt rather than μ . Alternatively, the absorption spectrum can also be collected by detecting the X-ray fluorescence (Figure 2-12) that results when the excited atom (having a core-hole vacancy) decays to a more stable (less energetic) state by filling the core-hole with an outer shell electron.⁹⁴ The absorption coefficient, μ , for a fluorescence experiment is

represented by the ratio, I_f/I_o .^{94, 100} To calibrate the recorded spectra, a reference sample is typically placed between the sample ionization chamber (I) and the reference ionization chamber (I_{Ref}) with the spectrum being collected concurrently (Figure 2-12).

In addition to hard X-ray spectroscopy, soft X-ray XAS experiments have also been performed in this thesis to examine the P K-, As L-, and ML-edges. To reduce the absorption of X-rays by air, soft X-ray XAS experiments are performed in vacuum. Fluorescence yield (FLY) or total electron yield detectors are employed because soft X-rays are not well transmitted except through the thinnest samples. Besides fluorescence, the final excited state of an atom can also decay through an interactive process wherein a higher energy electron drops down to fill the core-hole and gives its extra energy to another electron, which can be excited out of the atom.¹⁰² This process is referred to as Auger emission.¹⁰² Auger processes are also observed in XPS spectra.⁶⁰ An absorption spectrum can be obtained by scanning the X-ray energy through the absorption edge and detecting the Auger electrons as well as secondary electrons and photoelectrons that are emitted by measuring the drain current from the sample.¹⁰² This is referred to as a total electron yield (TEY) experiment. Spectra collected in this way tend to be more surface sensitive than those collected by fluorescence.¹⁰²

2.5 Photoemission Spectroscopy (PES)

Photoemission spectroscopy is very similar to XPS except that synchrotron radiation rather than a fixed energy X-ray source is used. Using synchrotron radiation, two types of selected energy analysis become available that cannot be easily performed using normal laboratory based XPS. When the X-ray energy is changed, only the kinetic energy of the photoelectron is changed because the binding energy is fixed. As was

discussed in the XPS section, the IMFP generally increases with the kinetic energy of the photoelectron.⁶⁰ Therefore by smoothly changing the excitation energy, the surface sensitivity of the measurement can be varied. Along with altering the IMFP, varying the excitation energy also changes the cross-section for producing a photoelectron from a specific atomic orbital which can affect the peak intensity (see Eq 2-5).^{74, 103} The calculated atomic photoelectron cross-sections (σ) for electrons from an As 4p orbital as the excitation energy is changed are presented in Figure 2-13.⁷⁴ As can be seen, σ increases as the excitation energy is lowered and approaches the As 4p ionization threshold energy (~ 7.9 eV).^{74, 103} Electrons cannot be excited when the energy is below the ionization threshold. The atomic orbital contributions to valence band spectra can therefore be determined by examining the variation in peak intensity with excitation energy, as the values for σ are different for dissimilar atomic orbitals.⁷⁴ This type of analysis, as well as resonant PES which will be described in Chapter 8, has been applied to aid in the identification of the Hf 5d valence states in the valence band spectrum of $\text{Hf}(\text{Si}_{0.5}\text{As}_{0.5})\text{As}$.

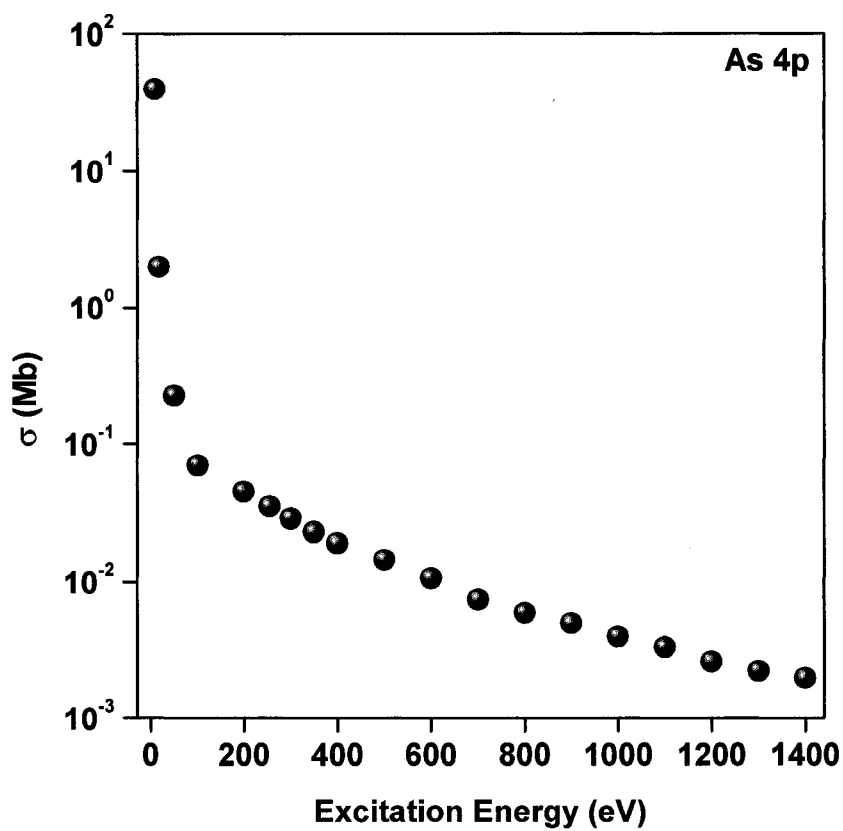


Figure 2-13 Calculated As 4p photoelectron cross-section with varying excitation energy from 0 to 1400 eV.⁷⁴ The cross-sections are presented in units of mega barns (Mb, 1 b=10⁻²⁴ cm²).

Chapter 3

An Examination of the Bonding in Binary Transition-Metal Monophosphides MP ($M = \text{Cr, Mn, Fe, Co}$) by X-ray Photoelectron Spectroscopy*

3.1 Introduction

The first-row transition metals form a series of monophosphides, MP ($M = \text{Sc-Ni}$), whose structures and properties have been extensively investigated. There is a progression of structure types, from NaCl-type (ScP) to TiAs-type (TiP), NiAs-type (VP), MnP-type (CrP, MnP, FeP, CoP), and NiP-type (NiP), in which successive distortions arise from the interplay of metal-metal and phosphorus-phosphorus bonding.²³ These compounds exhibit a wealth of interesting physical properties; they are all metallic and many display unusual magnetic ordering transitions.³⁵ For example, a large body of work is available on MnP alone, which undergoes transitions to ferromagnetic and helimagnetic phases.^{104, 105} Study of the size-dependent properties of MnP and FeP nanoparticles has now begun.^{16, 17} CoP and other transition-metal phosphides may have applications as hydrodesulphurization and hydrodenitrogenation catalysts.⁵

To analyze the bonding in these monophosphides in more detail, it is desirable to focus on a series of isostructural members. Here we select the four MnP-type members: CrP, MnP, FeP, and CoP.^{34, 106} This structure, shown in Figure 1-5 and described in Section 1.4.1 of Chapter 1, is based on a distortion of the NiAs-type, one of the most

**A version of this chapter has been published. Reproduced with permission from Grosvenor, A. P.; Wik, S. D.; Cavell, R. G.; Mar, A. Inorg. Chem. 2005, 44, 8988-8998. Copyright (2005) by the American Chemical Society.*

celebrated structure types in intermetallic chemistry.¹⁰⁷ To a first approximation, the electronic structure of these compounds consists of bands that arise from the interaction of metal 3d, 4s, and 4p orbitals with the phosphorus 3s and 3p orbitals. The result is a filled, lower energy, set of M -P bonding levels, a partially filled set of mostly metal-based d levels (split into t_{2g} and e_g components), and an empty, higher energy, set of M -P antibonding levels.^{25, 32, 33} In the orthorhombic MnP-type structure, there is metal-metal bonding not only along the columns of face-sharing octahedra along the a -direction, but also between the columns in the form of zigzag chains running along the b -direction. The metal-metal bonding network originates from the interaction between the metal-based t_{2g} orbitals, whose lobes are directed away from the metal-phosphorus bonds. These metal-metal interactions are quite strong as indicated by bond lengths of 2.6–2.8 Å.³⁴ Zigzag chains of phosphorus atoms running along the b -direction are also present, but at distances (2.6–2.7 Å)³⁴ that are somewhat longer than the typical single P–P covalent bond length of 2.2 Å.³⁷ Several questions arise: To what extent does electron transfer occur from metal to phosphorus atoms? How reasonable are formulations such as $M^{3+}P^{3-}$ (which assumes isolated P anions) or $M^{1+}P^{1-}$ (which assumes 2 centre–2e⁻ bonds in the zigzag chains of P atoms)? How closely does the metal-metal bonding character in these compounds resemble that in the elemental metals?

The electronic structure of some first-row transition-metal monophosphides has been previously investigated with both experimental X-ray photoelectron spectroscopy (XPS) studies¹¹⁻¹⁴ and theoretical calculations.^{25, 32, 33, 108, 109} Here we describe new high-resolution XPS measurements of CrP, MnP, FeP, and CoP, with the goal of clarifying the electronic structure and bonding in these important compounds. In

particular, the metal 2p and phosphorus 2p binding energies have been measured, and the trends in these energies have been related to the degree of covalency in the metal-phosphorus bonds. For the first time, the metal $2p_{3/2}$ peak shapes in these monophosphides have been analyzed in detail and compared to those in clean samples of the parent transition metal. The origin of the satellite structure found in the Co $2p_{3/2}$ spectra in Co metal and in CoP will also be discussed. Valence orbital electron populations in these compounds were extracted, for the purpose of bonding analyses, from peak fitting deconvolution of the valence band spectra.

3.2 Experimental

3.2.1 Synthesis

The monophosphides were prepared from stoichiometric reaction of Cr (99.95%, Alfa-Aesar), Mn (99.95%, Cerac), Fe (99.9%, Cerac), or Co (99.999%, Spex) metal powder with red P (99.995%, Cerac), placed in evacuated fused-silica tubes. The tubes were heated to 1323 K over a 36-h period and maintained at this temperature for 4 d before being cooled over 12 h to room temperature. The products were isolated and stored in a glove box under argon to limit exposure to air. The powder X-ray diffraction patterns, obtained on an Inel powder diffractometer equipped with a CPS 120 detector, were in good agreement with those calculated from the literature crystallographic data and revealed that the samples represented pure phases.

3.2.2 XPS Analysis

All measurements were performed on a Kratos AXIS Ultra spectrometer equipped with a monochromatic Al $K\alpha$ X-ray source. The analysis chamber was maintained at a

pressure of 10^{-6} – 10^{-7} Pa throughout the measurements. The resolution function for this instrument has been determined to be 0.4 eV by analysis of the cobalt Fermi edge.

Samples were finely ground in a glove box and pressed into 0.5-mm thick In foil (Alfa-Aesar) before being placed on a Cu sample holder and transferred to the XPS instrument in a sealed container to reduce exposure to air during transport. After being loaded into the instrument, the samples were sputter-cleaned with an Ar^+ ion beam (4 kV, 10 mA) to remove any surface oxide or phosphate which had formed. The time required for sputter-cleaning depended on the degree of oxidation present (as ascertained by initial survey spectra of the as-received samples), and ranged from 10 min (CoP) to 45 min (MnP). After the samples were sufficiently clean, both survey (broad range) and high-resolution spectra were obtained. Survey spectra were collected with a binding energy (BE) range of 0–1100 eV, a pass energy of 160 eV, a step size of 0.7 eV, a sweep time of 180 s, and a spot size of $700 \times 400 \mu\text{m}$. High-resolution spectra were collected with an energy envelope of 20–45 eV (depending on the peak being examined (phosphorus 2p, metal $2p_{3/2}$, or valence band)), a pass energy of 20 eV, and a step size of 0.05 eV. All of the XPS spectra reported in this thesis represent the average of multiple sweeps, which improves the statistics of the binding energy measurements. The results were analysed with use of the CasaXPS software package.¹¹⁰ During this study, it was found that charge correction was not required, most likely because of the metallic nature of these compounds. To fit the high-resolution spectra, a Shirley-type function was first used to remove the background arising from energy loss. The extracted spectra were then fitted with a combined Gaussian (70%) and Lorentzian (30%) line profile to account for spectrometer and life-time broadening, respectively. The chemical compositions of the

samples were determined from both these XPS survey spectra and independent EDX analysis (Hitachi S-2700 SEM; 20 kV beam voltage). Within experimental accuracy, all samples were essentially stoichiometric ($50\pm 5\%$ M; $50\pm 5\%$ P).

XPS spectra of metal standards were also collected. Samples (in the form of foils or pieces) of Cr (Fisher Scientific), Mn (99.98%, Alfa-Aesar), Fe (99.995%, Alfa-Aesar), and Co (99.0%, British Drug House) metal were sputter-cleaned to remove any surface oxide present and analyzed using similar parameters as above. Both survey and high resolution spectra (metal $2p_{3/2}$ and valence band) were obtained.

3.2.3 REELS Analysis

To examine the nature of the satellite peaks observed in the XPS spectrum of Co metal (99.995%, Alfa-Aesar), reflection electron energy loss spectroscopy (REELS) was performed on a PHI 660 scanning Auger microprobe with electron beam energies of 3 to 0.2 keV. In EELS, an electron energy loss spectrum is obtained which can contain peaks resulting from core-electron ionization (similar to XAS) as well as plasmon loss.¹¹¹ Before analysis, the sample was cleaned *in situ* by Ar^+ ion-beam sputtering at 3 kV. The sample was considered suitably clean when no O KLL line was observed in the Auger spectra. This analysis was performed at Surface Science Western (SSW) at the University of Western Ontario (UWO).

3.2.4 Band Structure Calculations

Although theoretical calculations have been previously performed on some MnP-type compounds, it was desirable to extract partial density of states profiles for the metal and phosphorus valence states to illustrate the fitting of the experimental valence band spectra here. A tight-binding extended Hückel band structure calculation on MnP was

performed with 96 k points in the irreducible portion of the Brillouin zone, with use of the EHMAcc suite of programs,^{112, 113} The atomic parameters (valence shell ionization potentials H_{ii} (eV) and orbital exponents ζ_i) were as follows: for Mn 4s, $H_{ii} = -9.8$, $\zeta_i = 1.80$; for Mn 4p, $H_{ii} = -5.9$, $\zeta_i = 1.80$; for Mn 3d, $H_{ii} = -11.7$, $\zeta_{i1} = 5.15$, $c_1 = 0.514$, $\zeta_{i2} = 1.70$, $c_2 = 0.693$; for P 3s, $H_{ii} = -18.6$, $\zeta_i = 1.84$; for P 3p, $H_{ii} = -14.0$, $\zeta_i = 1.45$.

3.3 Results and Discussion

3.3.1 Phosphorus 2p High-Resolution X-ray Photoelectron Spectra

Figure 3-1 shows the high-resolution phosphorus 2p XPS spectra collected for CrP, MnP, FeP, and CoP. Each spectrum shows two peaks corresponding to the P 2p_{3/2} (low binding energy) and P 2p_{1/2} (high binding energy) states. Sharp lineshapes were observed which could be fitted with component peaks having a FWHM as small as 0.7 eV. In all cases, the intensity ratio of the P 2p_{3/2} and 2p_{1/2} peaks was 2:1, which is consistent with the expected ratio of $(2j_1+1)/(2j_2+1)$, where j_1 and j_2 represent the coupled orbital (l) and spin (s) angular momentum quantum numbers from respective spin-up and spin-down states of the unpaired core electron which remains after photoionization.⁶⁰ On progressing through the series CrP to CoP, the P 2p_{3/2} and 2p_{1/2} binding energies gradually increase (Table 3-1). On the high-binding energy side in all spectra, there is a small peak which is attributed to the P 2p_{1/2} signal from some remaining unreacted phosphorus; the corresponding P 2p_{3/2} peak is not indicated as it would be buried under the main P 2p_{1/2} peak from the transition-metal monophosphide. The precision in the BEs listed in Table 3-1 is estimated to be ± 0.1 eV, but it may be better because each BE is obtained from the average of several sweeps (e.g., 6 – 20 sweeps per P 2p spectrum).

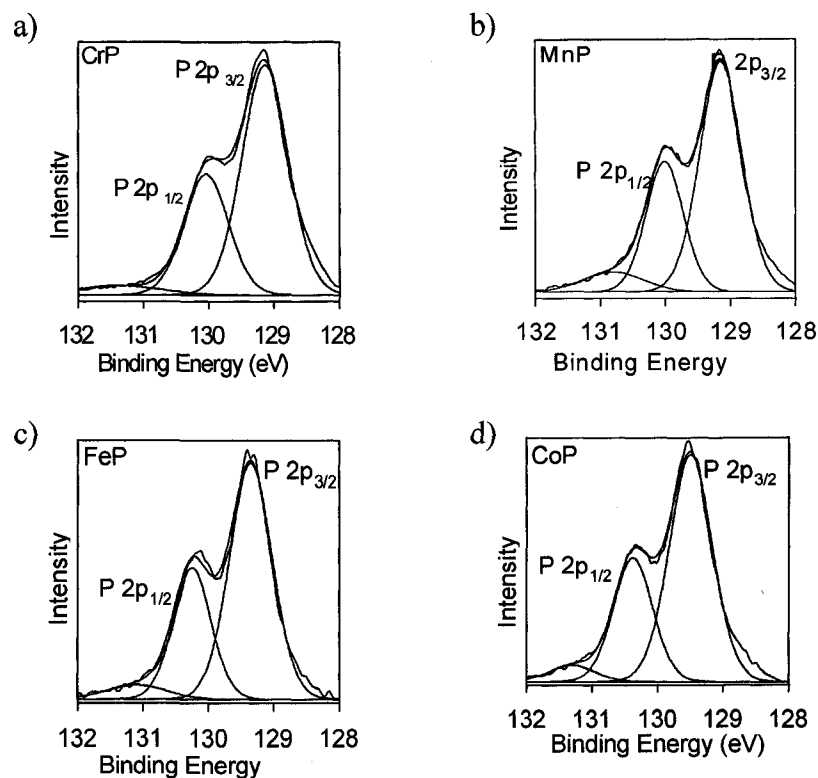


Figure 3-1 High-resolution P 2p XPS spectra of (a) CrP, (b) MnP, (c) FeP, and (d) CoP.

Table 3-1 Binding Energies (eV) of Core Photoelectron Peaks in Transition-Metal Monophosphides MP ($M = \text{Cr, Mn, Fe, Co}$) and Metal Standards.^a

	CrP	MnP	FeP	CoP
P 2p _{1/2}	130.0	130.2	130.2	130.4
P 2p _{3/2}	129.1	129.2	129.3	129.5
M 2p _{3/2}	573.9	638.7	706.9	778.3
				(781.4, 783.0) ^b
	Cr	Mn	Fe	Co
M 2p _{3/2}	574.1	638.7	707.0	778.1
				(781.1, 783.1) ^b

^a The BEs were obtained from spectra scanned multiple times to improve statistics.

^b Satellite peaks arising from plasmon loss processes.

For the MP ($M = \text{Cr, Mn, Fe, Co}$) compounds studied here, the small variation in BE from CoP to CrP (0.4 eV) is significant as it exceeds the precision of the measurement.

Figure 3-2 shows a plot of the P $2p_{3/2}$ binding energies versus the difference in electronegativity (Allred-Rochow)¹¹⁴ between the phosphorus and metal atoms for these and other first-row transition-metal monophosphides. The binding energies are lower in the monophosphides than in elemental phosphorus, indicating the presence of anionic phosphorus in these compounds. The trend of increasing phosphorus binding energy through the series from CrP to CoP clearly confirms our expectation of decreasing ionic character in the metal-phosphorus bonding as the electronegativity difference between the elements decreases. Interestingly, theoretical studies on the diatomic gas-phase molecules MP ($M = \text{Sc-Cu}$) also show the same general trend of decreasing ionic character.¹¹⁵

Since core-level binding energies are affected by the chemical environment, the charge on the phosphorus atoms in these compounds may be estimated from the P $2p_{3/2}$ binding energies. Binding energies for a large number of compounds containing the same transition metals and phosphorus in a variety of oxidation states (as well as that of elemental phosphorus) are available from the NIST XPS database.¹¹⁶ If a linear relationship is assumed between the P $2p_{3/2}$ binding energy and the oxidation state, an interpolation of the binding energies for the transition-metal monophosphides suggests P charges of -1.4 in CrP, -1.1 in MnP, -1.0 in FeP, and -0.7 in CoP. A plot of these values versus the electronegativity difference is shown in Figure 3-3, consistent with the decreasing ionicity of the metal-phosphorus bond through the sequence from CrP to CoP. These values also suggest that the formulation $M^{3+}P^{3-}$ is untenable, and in fact, they are

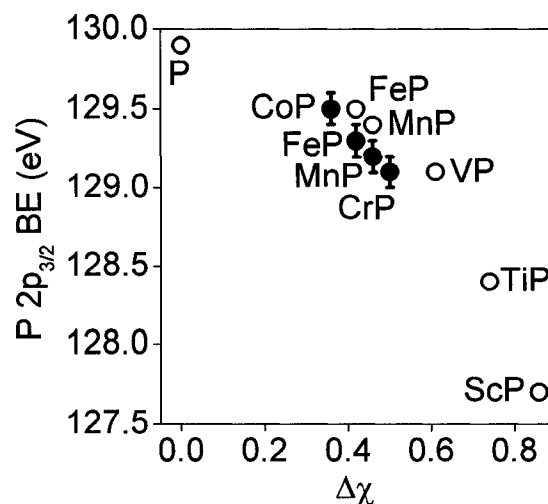


Figure 3-2 Plot of P $2p_{3/2}$ binding energies, BE, versus the difference in electronegativity (Allred-Rochow) between the phosphorus and metal atoms, $\Delta\chi$,¹¹⁴ for several first-row transition-metal monophosphides. Values indicated by solid circles (●) are from this work, and those by open circles (○) are from Reference 12. Error bars for the samples examined in this thesis represent the instrumental precision of ± 0.1 eV. The variations in BE from CoP to CrP, although small, are significant.

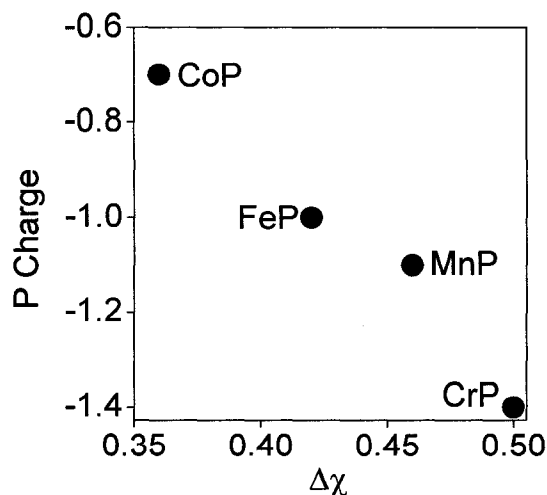


Figure 3-3 Plot of the charge on P atoms (estimated from binding energy values) versus the difference in electronegativity, $\Delta\chi$, for CrP, MnP, FeP and CoP.

remarkably consistent with the formulation $M^{1+}P^{1-}$ mentioned earlier in which some P–P bonding is implicated. However, caution must be applied because it is difficult to separate the effect of electron count, which modifies the degree of P–P bonding, and the effect of decreased ionicity in the metal-phosphorus bond on the ultimate charge adopted by the phosphorus atoms. Indeed, the trend in P–P bond lengths through the series CrP (2.644 Å) to CoP (2.701 Å),³⁴ as well as charges calculated in theoretical studies,²⁵ is opposite to that suggested here, implying that decreased metal-to-phosphorus electron transfer (from CrP to CoP) is the more important effect in determining the binding energies observed.

3.3.2 Metal $2p_{3/2}$ High-Resolution X-ray Photoelectron Spectra

Figure 3-4 shows the high-resolution metal $2p_{3/2}$ spectra for CrP, MnP, FeP, and CoP. The binding energies (Table 3-1) are similar to those found for the elemental metal (within 0.1–0.2 eV) and to values previously reported by Myers *et al.*¹² However, the high-resolution spectra presented here show a distinct asymmetric line shape that, to our knowledge, has not been previously reported for these compounds. This feature is characteristic of significant metal-metal bonding such as has been proposed for MnP-type structures.²⁵

To substantiate the inference of metal-metal bonding, we have collected high-resolution $2p_{3/2}$ spectra for the elemental metals Cr, Mn, Fe, and Co, which are shown in Figure 3-5. Each spectrum shows an asymmetric lineshape skewed to higher binding energy. According to Doniach and Šunjić,¹¹⁷ this type of lineshape arises when valence electrons, interacting with the core hole (produced after photoionization), are excited and scattered from filled states below the Fermi edge to empty conduction states above.

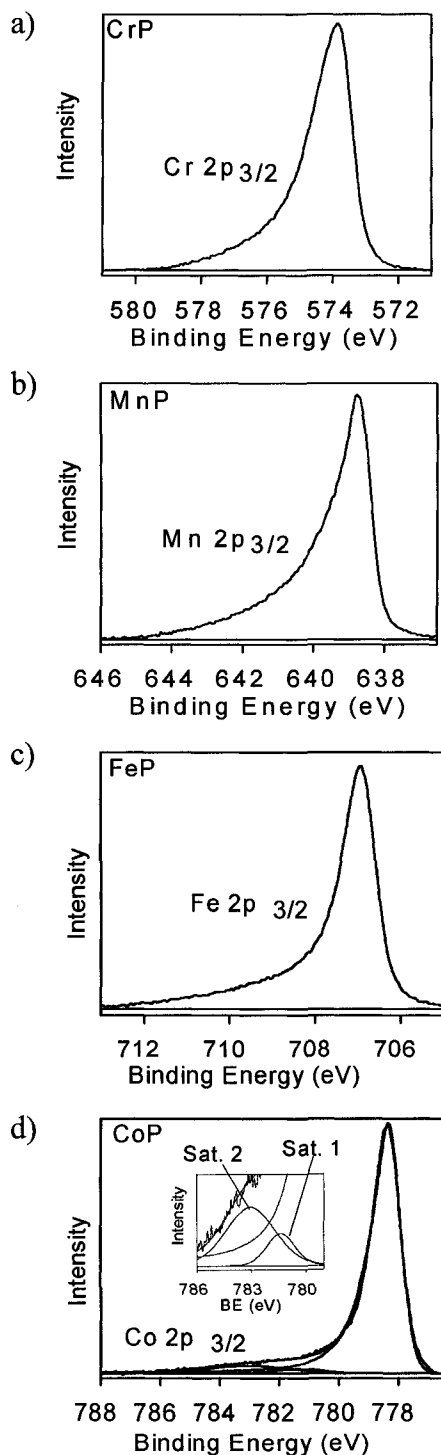


Figure 3-4 High-resolution metal 2p_{3/2} XPS spectra for (a) CrP, (b) MnP, (c) FeP, and (d) CoP. The inset in Figure 4d shows the observed low intensity satellite structure for CoP.

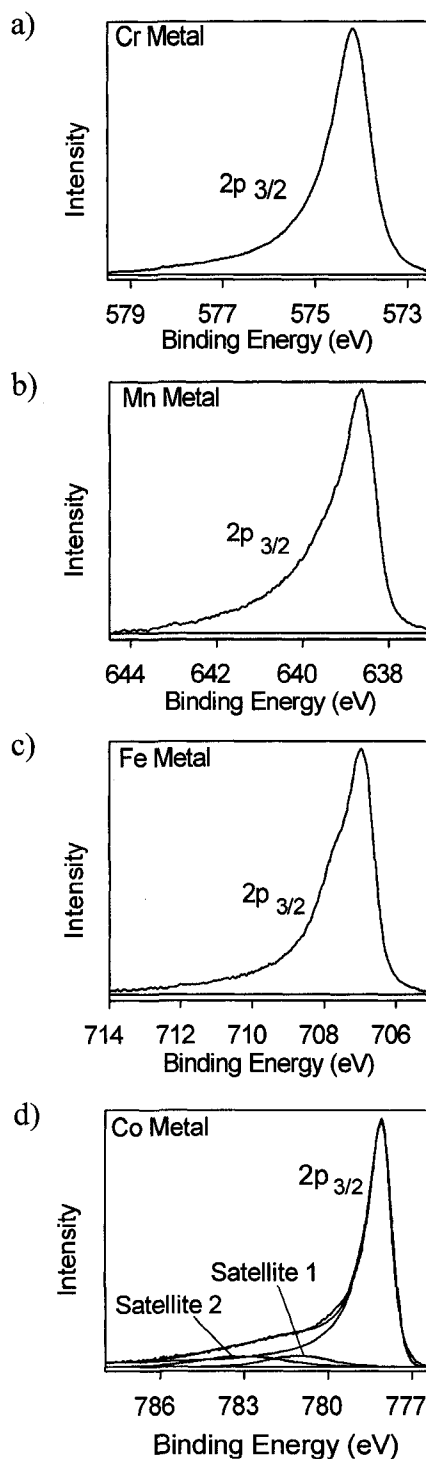


Figure 3-5 High-resolution 2p_{3/2} XPS spectra of clean samples of (a) Cr, (b) Mn, (c) Fe, and (d) Co metal.

Since there is a continuum of states above the Fermi edge in a metal, an asymmetric tail comprising many closely spaced states is observed instead of a few distinct satellite peaks.¹¹⁸ The spectrum for Co metal, however, reveals not only an asymmetric line shape, but also a distinct satellite structure (Figure 3-5d) which has been observed before.^{119, 120} To properly fit the spectrum, two satellite peaks centred at 5.0 and 3.0 eV away from the main core line were required. Note that the spectrum for CoP also shows two satellite peaks at similar energies as in Co metal, but with much lower intensities (Figure 3-4d). A detailed interpretation of these satellite peaks is important but is deferred to Section 3.3.3.

The similarity in the binding energies and lineshapes of the metal $2p_{3/2}$ spectra for both the transition-metal monophosphides and the elemental metals argues for the presence of metal atoms with nearly zero charge and substantial metal-metal bonding in the monophosphides. Relative to a metal atom in a cationic state with a localized electronic structure, photoelectrons from a metal atom participating in extended metal-metal bonding may have a lower binding energy because of the delocalization of electrons in conduction states allowing the atom to experience, on average, greater nuclear screening. As well, the strong hybridization of metal- and phosphorus-based states arising from the primarily covalent nature of the bonding interactions reduces the difference in binding energy of the metal atoms in the monophosphides versus in the elemental metals.⁸⁰ In contrast, the difference in binding energy observed for the P atoms in the monophosphides compared to elemental phosphorus suggests that the electrons in the monophosphide P atoms are localized and any bonding within the anionic P substructure is also localized. At first glance, these binding energy results seem to

imply a problem with charge neutrality in these transition-metal monophosphides, as the metal atoms are assigned charges of nearly 0 whereas the phosphorus atoms are assigned charges of nearly -1 . It is interesting to note that a similar problem was encountered in an earlier band structure calculation, which revealed that the clear presence of some P–P bonding (as evaluated by overlap populations) was not reflected correctly in the charges borne by the phosphorus atoms.²⁵ Resolving this problem involves a more sophisticated interpretation of the XPS spectra, given below.

3.3.3 Satellite Structure in Co Metal and CoP Co $2p_{3/2}$ Spectra

The satellite structure in the Co $2p_{3/2}$ spectra of Co metal and CoP noted above is also observed in the spectrum of Ni metal, which has received considerable attention in the past.¹²¹⁻¹²³ Two explanations have been developed to account for this satellite structure: plasmon loss (loss of kinetic energy of the photoelectron when it interacts with bound valence electrons, causing them to oscillate)¹¹¹ and the “two core hole” theory.¹²¹ The former was initially abandoned when no evidence of plasmon loss was found in optical or electron energy loss spectra.¹²¹ Instead, it was suggested that the satellite structure found at 6 eV above the core line in the XPS spectrum of Ni metal could arise from final state effects,¹²¹ similar to those proposed by Kotani and Toyozawa.¹²⁴ After photoionization, the resulting core hole increases the effective charge operating on the remaining electrons. This increased charge pulls conduction states below the Fermi energy. If the conduction state is empty, then the satellite peak is observed because of a final state containing two holes (one in the core level present after photoionization and one in the valence band). If a filled conduction state is pulled below the Fermi energy,

then this final state represents the observed core line.¹²¹ The same description has been applied to describe the satellite peak observed in the spectrum of Co metal.¹¹⁹

Although the “two core hole” theory has been widely accepted, there is evidence that the plasmon loss explanation deserves further consideration. Previous electron energy loss studies of the first-row transition metals have revealed the presence of two peaks at <10 eV below the main elastic line for Co and Ni metal.^{125, 126} These peaks were attributed to plasmon loss as well as to $M_{4,5}$ ionization.¹²⁵ It should be noted that these results were not specifically used to rationalize the nature of the satellite peak found in the XPS spectrum of Ni metal during the period in which the “two core hole” theory was developed. Recently, a careful re-examination of REELS data for Ni metal has revealed peaks at a similar energy separation from the main elastic line as is found for the satellite peak from the core line observed in the Ni $2p_{3/2}$ XPS spectrum.¹²⁷ These features were attributed to both bulk and surface plasmon structures. Plasmon loss events occurring by interaction of the exiting photoelectrons with valence electrons of atoms located closest to the surface (surface plasmon loss) are lower in energy than those occurring by interaction with valence electrons of atoms located below the surface (bulk plasmon loss).¹²⁸ If the presence of the satellite peak in the XPS spectrum were really due to the process involved in the “two core hole” theory, then no corresponding transitions should be observed in the REELS spectrum because photoionization does not occur in this experiment.¹²⁷ The fact that these features were indeed observed in the REELS data militates against the “two core hole” explanation and instead favours the plasmon loss explanation.

Further, REELS analysis of NiO showed no such similar peaks, as expected since no low energy plasmon loss satellite structures are observed in its corresponding Ni 2p_{3/2} XPS spectrum.¹²⁷ This confirms that the peaks observed for Ni metal are real and not due to noise or other associated spectrometer effects. Plasmon loss peaks normally occur at much higher energy than was observed during this study of Ni metal (typically ~20 eV as determined by EELS).^{125, 126} However, similar low energy plasmon loss has been observed by EELS of Mo (110) after deposition of two monolayers of Ba onto the surface.¹²⁸ The surface plasmon peak found at 2.6 eV was proposed to arise from interaction of the exiting electrons with the layer of Ba atoms located closest to the surface, whereas the bulk plasmon peak found at 6.7 eV was attributed to interactions of the exiting electrons with the layer of Ba atoms beneath it.¹²⁸ These observations imply that the interaction of electrons with atoms found within the uppermost region of a surface result in a much lower energy plasmon loss than is the case deeper within the surface. Moreover, in the initial reports that suggested the presence of lower energy surface plasmon peaks, it was observed that although these losses were found during experiments using EELS in reflection mode, they were not specifically observed when transmission EELS was used.¹²⁶

To understand the nature of the satellite peaks observed in the XPS spectra of Co metal and CoP, a REELS analysis was performed on Co metal (Figure 3-6). The overall spectrum, taken at 0.3 keV (Figure 3-6a), compares well with that obtained by Robins and Swan.¹²⁵ In the energy loss region at ~10 eV below the elastic line, five low intensity peaks were observed (Figure 3-6b). The positions of these peaks, which are attributed to plasmon loss, were located more precisely by analyzing a plot of the first

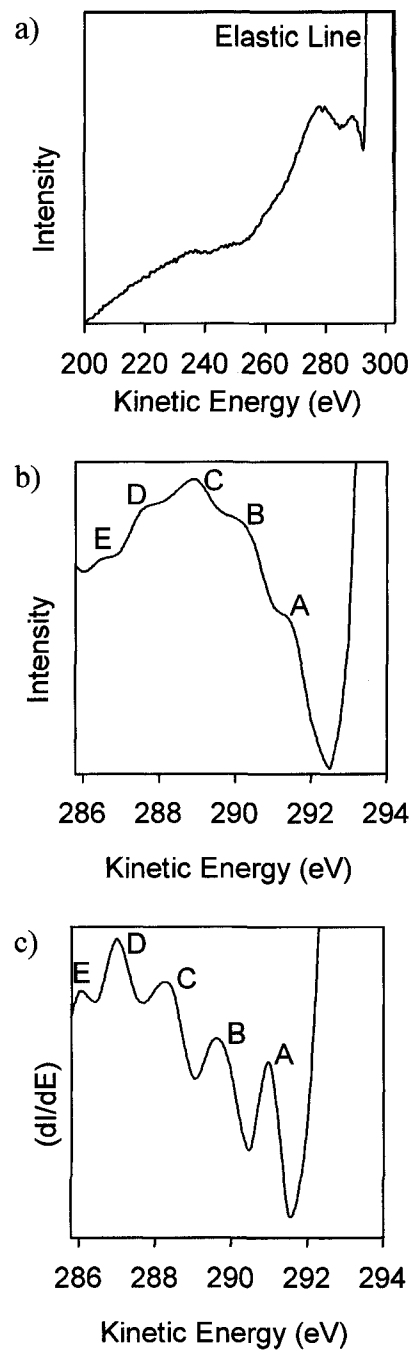


Figure 3-6 (a) REELS spectrum of Co metal taken at 0.3 keV. (b) Expanded spectrum showing the plasmon loss region located just below the main elastic line. (c) First derivative of the expanded spectrum.

Table 3-2 Bulk Plasmon Loss Peak Energies (eV) in Co Metal ^a

Line	Peak Energy (eV)	Energy separation from elastic peak
elastic peak	295.5	
A	291.5	4.0
B	290.0	5.5
C	289.0	6.5
D	287.5	8.0
E	286.0	9.5

^a Energies were determined from the first derivative of the REELS spectrum (Figure 3-6c) taken using a beam energy of 0.3 keV. Surface plasmon loss peaks were also observed in spectra taken at 0.2 keV with energies of 2 and 3 eV from the main elastic line.

derivative of the intensity (Figure 3-6c) and are listed in Table 3-2. The peaks labelled A and B are the most intense (after subtraction of the background due to inelastic electron scattering); they are believed to represent bulk plasmon loss and also appear in the corresponding XPS spectrum as a broad peak centred at 5 eV above the main $2p_{3/2}$ core line (satellite 2 in Figure 3-5d). The bulk plasmon event might be represented by two peaks rather than one because of interactions with different valence states, i.e., Co 3d and Co 4s states. Peaks C, D, and E may represent higher energy plasmon loss or multiple plasmon loss events. The broad satellite peak centred at 3.0 eV above the core line in the XPS spectrum of Co (labelled as satellite 1 in Figure 3-5d) was not observed in the REELS data taken at 0.3 keV, likely because it is overlapped by the intense and broad elastic peak. A REELS spectrum was also taken at a lower beam energy of 0.2 keV (not shown). Intense peaks separated only slightly from the elastic line, at 2 and 3 eV away, were observed and attributed to surface plasmon loss since such peaks were not observed in spectra taken using higher energy and thus less surface sensitive electron beams. Thus, it appears that satellite 1 arises from surface plasmon loss and satellite 2 arises from bulk plasmon loss in the XPS spectra of Co metal (Figure 3-5d) and CoP (Figure 3-4d). As pointed out earlier, these losses most likely arise from interactions of the exiting photoelectrons and valence electrons of atoms located within the uppermost region of the surface. It should also be noted that as the electron beam energy was increased, the higher energy loss peaks were consistently observed, indicating that these are real transitions and not noise.

The Co $2p_{3/2}$ XPS spectra of Co metal and CoP could be fitted with individual peaks representing the different plasmon loss structures observed in the REELS data, but

it was found to be much simpler to model these loss events using two broad peaks (FWHM > 2 eV). The observation of the plasmon loss peaks in CoP at similar energy separations as those found in Co metal (Table 3-1) indicates that similar valence electrons are involved in the plasmon loss process (most likely Co 3d and 4s electrons). However, the lower intensity of the satellite peaks in CoP suggests that there are fewer valence electrons around the Co atoms in CoP than in Co metal. That is, analysis of the satellite structure points strongly to the conclusion that, despite their similar binding energies, the Co atoms in CoP are definitely cationic relative to the elemental metal. By analogy, we assert that this argument can be extended to the other monophosphides studied as well.

3.3.4 Valence Band Spectra

Comparing the valence band spectra of the elemental metals and the metal phosphides provides further insight into the bonding interactions present in these compounds. The valence band spectra of the metals (Figure 3-7) show a broad peak located at the Fermi edge which can be fitted by two peaks representing $3d_{5/2}$ and $3d_{3/2}$ states with a fixed intensity ratio of 3:2. As was earlier observed in the metal $2p_{3/2}$ spectra (Figure 3-5), it was important to model these peaks as asymmetric to higher binding energy to properly fit the spectra, indicating that Doniach-Šunjić processes also occur during excitation of the 3d valence electrons.¹¹⁸ No attempt was made to include a peak representing 4s states since it would be broad and have an energy similar to the 3d states with a lower intensity due to a low electron population.^{25, 121} In principle, the d orbitals are not quite degenerate and the fit could be improved by employing multiple 3d peak sets, but the two peaks used here were deemed sufficient to give a reasonable fit.

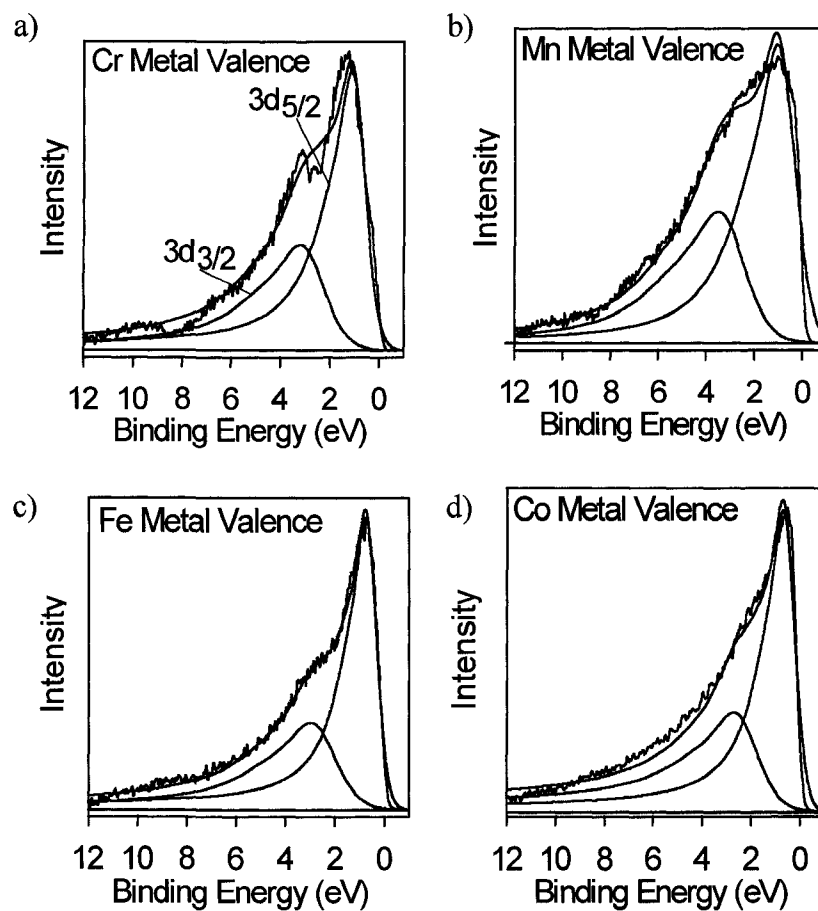


Figure 3-7 Fitted valence band spectra of sputter-cleaned samples of (a) Cr, (b) Mn, (c) Fe, and (d) Co metal. The spectra have been fitted using two peaks representing $3d_{5/2}$ and $3d_{3/2}$ states with a fixed intensity ratio of 3:2. As these samples are metals, 0 BE can be described as the Fermi edge (E_F).

The fitted valence band spectra of the transition-metal monophosphides are shown in Figure 3-8. In general terms, the measured valence band spectra are in excellent qualitative agreement with calculated band structures, which show a sharp Fermi edge and a narrow, metal-based, d-band with a high density of states superimposed partially on a broader, largely phosphorus-based p-band.^{13, 14, 25, 32, 33} They also resemble spectra previously reported for MnP,^{12, 13, 105} FeP,^{12, 14} and CoSb,¹²⁹ but the use of different excitation energies in different studies affects the photoionization cross-sections and thus modifies the peak intensities.⁷³

To fit the spectra presented in Figure 3-8 with both transition-metal and phosphorus states, they were compared to previously reported band structure calculations and XPS results. The region 15–10 eV below E_F has been attributed to P 3s states¹¹ whereas the broad region above it (8–3 eV) has been attributed to P 3p bonding states.¹⁴ The transition-metal 3d states (containing both t_{2g} and e_g components) have been suggested to lie close to E_F along with P 3p nonbonding states having a similar to slightly lower binding energy.¹⁴ The position of the P 3p nonbonding states lying above the transition-metal 3d states has been implied previously in band structure calculations of transition-metal monophosphides¹⁴ as well as in the valence band spectrum of Ni₂P.¹⁵ As an example, the unfitted valence band spectrum for MnP can be compared to the P 3s, P 3p, and Mn 3d projections of the density of states, as determined from an extended Hückel calculation (Figure 3-9). The highest BE region can be assigned to P 3s states, the region above it to P 3p states, followed by Mn 3d states; there is also a small contribution of P 3p nonbonding states closest to the Fermi edge. Guided in this manner,

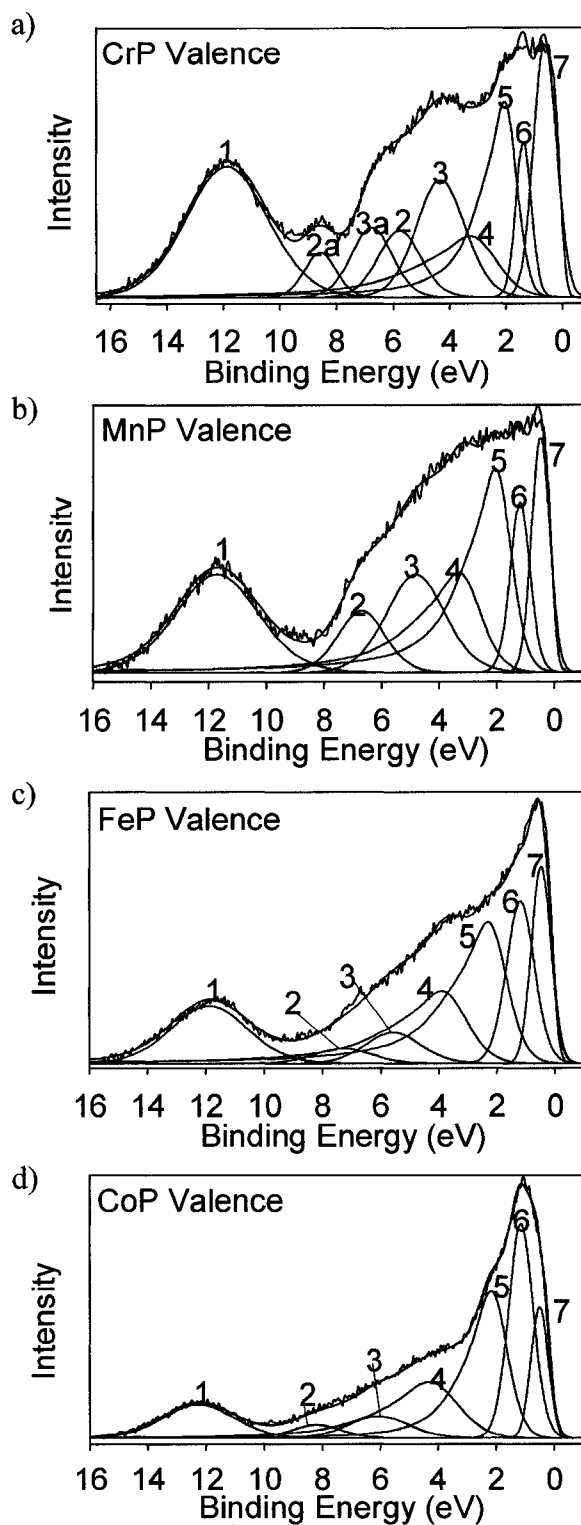


Figure 3-8 Fitted valence band spectra of sputter-cleaned samples of (a) CrP, (b) MnP, (c) FeP, and (d) CoP.

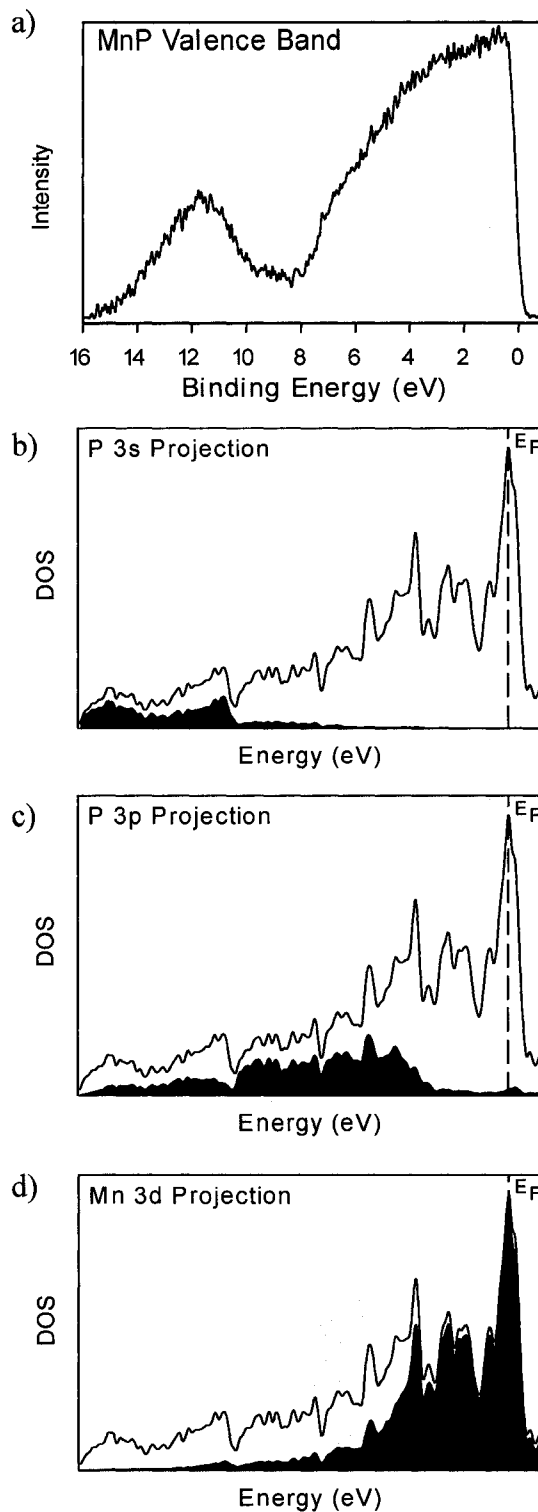


Figure 3-9 (a) Valence band spectrum of MnP compared to the calculated projections of the density of states for (b) P 3s, (c) P 3p, and (d) Mn 3d orbitals. The shaded regions represent the projections whereas the solid line represents the total density of states. The dashed line marks the Fermi level.

we have developed a fitting methodology for the valence spectra of all four compounds, described below.

The superior resolution of the spectra obtained here allows deconvolution into components, labelled from 1 to 7 (Figure 3-8), in an attempt to separate individual valence states. Although there is some degree of overlap, each of the peaks shown is required to optimize the fit to the spectrum, especially the shoulder features, which appear reproducibly. Consistent with calculated band structures and previously reported XPS results, the following assignments are proposed. Peak 1 represents P 3s states, and peaks 2 and 3 represent P 3p_{1/2} and 3p_{3/2} states, respectively, with a fixed intensity ratio of 1:2. Peaks 4 and 5 represent the t_{2g} set of the metal 3d states and were fitted with an asymmetric lineshape profile (as was observed in the valence band spectra of the elemental metals, discussed above) with a fixed intensity ratio of 3:2 (3d_{5/2}:3d_{3/2}). Peak 6 represents the e_g set (M–P antibonding) of the metal 3d states and was fitted with a single profile constrained to represent spin-up electrons. Peak 7 likely represents essentially nonbonding P 3p states. To properly fit this state, only a Gaussian lineshape was required, suggesting that spectrometer effects are dominant; lifetime effects are probably small, given the low energy of this feature, which appears just below the Fermi edge. The identity of peaks 2a and 3a found in the spectrum of CrP is discussed below. The binding energies, FWHM values, and peak areas of the component peaks used to fit the valence band spectra are listed in Table 3-3 and were optimized to provide the best fit. The goodness of fit was judged from the standard deviation of the difference between the simulated and experimental spectra, called the residual standard deviation (RSD). A low RSD (e.g., 2.0 for CoP) implies a good fit. After a preliminary fitting was performed by

Table 3-3 Binding Energies (eV) of Component Peaks in Valence Band Spectra of *MP* (*M* = Cr, Mn, Fe, Co)^a

Peak	Assignment	CrP	MnP	FeP	CoP
1	P 3s	11.8 (3.4)[27.0]	11.7 (3.4)[23.3]	11.9 (3.1)[18.5]	12.3 (2.9)[12.3]
2	P 3p _{1/2}	8.6 (1.3)[3.6], ^b 5.8 (1.8)[7.3]	6.7 (1.9)[8.3]	7.3 (2.4)[3.6]	8.2 (2.0)[3.4]
3	P 3p _{3/2}	6.8 (1.7)[7.3], ^b 4.3 (2.0)[14.5]	4.8 (2.4)[16.6]	5.6 (2.2)[7.2]	6.1 (2.5)[6.8]
4	<i>M</i> 3d _{3/2} t _{2g}	3.2 (2.2)[7.8]	3.3 (1.8)[12.0]	3.9 (2.0)[14.4]	4.3 (2.3)[15.7]
5	<i>M</i> 3d _{5/2} t _{2g}	2.0 (1.0)[11.7]	2.0 (1.3)[17.8]	2.3 (1.5)[21.5]	2.2 (1.3)[23.5]
6	<i>M</i> 3d _{5/2} e _g	1.4 (0.7)[6.1]	1.2 (0.8)[9.7]	1.2 (1.1)[19.0]	1.1 (1.0)[26.9]
7	P 3p	0.6 (1.0)[14.6]	0.5 (0.8)[12.2]	0.5 (0.8)[15.7]	0.5 (0.7)[11.4]

^a FWHM values (eV) are indicated in parentheses while the peak areas, in percent, are indicated in square brackets.

^b A second set of higher binding energy P 3p_{1/2} and P 3p_{3/2} peaks, labelled respectively as peaks 2a and 3a in Figure 3-8a, is present in the spectrum of CrP.

inspection, the component peak widths and energies were constrained such that they could only shift from their initial values by 2 eV or less. Within the CasaXPS software, the widths, energies, and intensities of the different component peaks were allowed to vary until the RSD converged to within ± 0.1 . Similar constraints and fitting procedures were applied to the valence band spectra discussed in Chapters 6 to 8.

Consistent with the expectation that the major orbital interactions should be between the metal 3d and P 3p states, these peaks show considerable overlap in energy. In this analysis, we have made a distinction for the phosphorus 3p states, which are dispersed over a very wide energy range according to band structure calculations (Figure 3-9c), into those that are clearly bonding in character (near 5–7 eV) and those that are essentially nonbonding in character (close to the Fermi edge). Justifying this analysis, we note that the P 3p bonding peaks are wide and their binding energies show a significant shift through the series CrP to CoP (Table 3-3), which is to be expected if they are truly involved in bonding interactions. In contrast, the P 3p nonbonding peaks are narrow and their binding energies show little change. Interestingly, the binding energies of the P 3s states (near 12 eV) show only a slight shift on going from CrP to CoP similar to that observed for the obviously nonbonding P 2p states, implying that they are less important than the 3p states in bonding interactions as has been suggested previously.¹⁵ The metal 3d states, split into t_{2g} and e_g components, have similar energies as those in the valence band spectra of the pure metals. This verifies our earlier conclusion derived from analysis of the satellite structure in the metal $2p_{3/2}$ core spectra of Co metal and CoP which showed that during the plasmon loss process in which the exiting photoelectrons interacted with the valence electrons of the metal atoms in the pure metal and in the

monophosphide, the photoelectrons lost similar amounts of energy. The general increase in the binding energies of the metal $3d_{3/2} t_{2g}$ peak with a concomitant increase in the energy separation between this peak and the corresponding $3d_{5/2} t_{2g}$ peak as the atomic number of the metal increases is normally observed in XPS spectra.⁶⁰

The electron populations of the different orbital states in the valence band spectra were extracted from normalized peak intensities, C_i , according to Eq 3-1.⁷⁵

$$C_i = \frac{I_i / (\sigma_i \lambda_i)}{\sum_{j=1}^n I_j / (\sigma_j \lambda_j)} \quad (3-1)$$

In this equation, $I_i / (\sigma_i \lambda_i)$ represents the corrected intensity of the peak under consideration and $\sum_{j=1}^n I_j / (\sigma_j \lambda_j)$ represents the sum of the corrected intensities from all of the peaks present in the valence band spectrum. The values of the photoionization cross-section (σ) and inelastic mean free path (IMFP, λ) corrections are listed in Table 3-4. Much of the variation in the shapes of the valence band spectra shown in Figure 3-8 arises from the different cross-sections for the metal 3d states. The number of electrons in each state was then calculated assuming a total of 11, 12, 13, and 14 electrons in the valence band of CrP, MnP, FeP, and CoP, respectively. The results of these calculations are summarized in Table 3-5.

From the total electron populations, a charge of about +0.7 for the metal and about -0.7 for the phosphorus atoms in each of these compounds was deduced, providing further support for the approximate formulation $M^{1+}P^{1-}$ described earlier. The electron populations of individual states also correlate with some of the general trends seen in the

Table 3-4 Corrections Applied to Intensities of Peaks in Valence Band Spectra of *MP* (*M* = Cr, Mn, Fe, Co) ^a

Atom	State	Photoionization cross-section, σ	IMFP, λ (Å)
Cr	3d _{3/2}	0.0264	26.2
	3d _{5/2}	0.0387	
Mn	3d _{3/2}	0.0424	25.9
	3d _{5/2}	0.0622	
Fe	3d _{3/2}	0.0694	25.9
	3d _{5/2}	0.1017	
Co	3d _{3/2}	0.1082	24.0
	3d _{5/2}	0.1582	
P	3s	0.1116	33.9
	3p _{1/2}	0.0354	
	3p _{3/2}	0.0708	

^a The P 3p_{1/2} and 3p_{3/2} cross-sections were corrected on the basis of comparison of experimental cross-sections determined by Brillson and Ceasar¹³⁰ to those calculated by Scofield.⁷³ All other cross-sections listed are those calculated by Scofield.⁷³ These cross-sections were determined for an excitation energy equal to that of Al K α X-rays.⁷³ The IMFP values were determined using the QUASESTM IMFP calculator.¹³¹

Table 3-5 Electron Populations in *MP* (*M* = Cr, Mn, Fe, Co).

State	CrP	MnP	FeP	CoP
P 3s nonbonding	1.3	1.4	1.6	1.4
P 3p bonding	3.3 ^a	3.1	1.9	2.4
<i>M</i> 3d t _{2g}	4.2	5.0	5.2	5.2
<i>M</i> 3d e _g antibonding	1.1	1.4	2.3	3.0
P 3p nonbonding	1.1	1.1	2.1	2.0
Total P	5.7	5.7	5.6	5.8
Total <i>M</i>	5.3	6.3	7.4	8.2
Total number of e ⁻	11.0	12.0	13.0	14.0

^a 1.1 e⁻ in P–P bonding states (peaks 2a and 3a in Figure 3-8a) and 2.2 e⁻ in Cr–P bonding states (peaks 2 and 3 in Figure 3-8a).

crystal structures. The population of the metal t_{2g} states, which are involved in metal-metal bonding, increases through the series CrP ($4.2 e^-$) to CoP ($5.2 e^-$), consistent with the shortening of the average metal-metal bond lengths (2.782 to 2.678 \AA),³⁴ if contacts less than 3.0 \AA are considered significant. The population of the phosphorus $3p$ bonding states, which are involved in both metal-P and possibly P-P bonding, decreases on going from CrP ($3.3 e^-$) to CoP ($2.4 e^-$), consistent with the lengthening of P-P bond lengths (2.644 to 2.701 \AA).³⁴ Given that these are weak interactions at best, any manifestation of P-P bonding states should be most prominent in CrP. Indeed, the valence band spectrum of CrP (Figure 3-8a) reveals extra shoulders that can be fit by invoking a second set of higher binding energy P $3p$ states (peaks 2a and 3a in Figure 3-8a) which result from P-P bonding, in addition to the first set of P $3p$ states (peaks 2 and 3 in Figure 3-8a) at lower binding energy which are due to Cr-P bonding. Table 3-5 shows that the electron population in the P-P bonding states is only half as large as in the Cr-P bonding states. On progressing to the other transition-metal monophosphides of the series, a trend towards populating the nonbonding P $3p$ states, at the expense of the bonding P $3p$ states is observed which is consistent with the gradual disappearance of the already weak P-P bonds. In the case of FeP and CoP, the values of the electron populations of the phosphorus-based states suggest that there is negligible P-P bonding. Size effects cannot be ruled out as being responsible for these trends in both metal-metal and phosphorus-phosphorus bonding behaviour. Progressing along the first-row transition metal series, we see a contraction of the structure, which may serve as the true driving force for the observed trends. The occurrence of ferromagnetism in some of these compounds also complicates the interpretation of the electronic structure.

From the above analysis of the electron populations deduced from the valence band spectra, experimental energy level diagrams for these four monophosphides can be constructed. Figure 3-10 presents plots of the electron population versus energy. These diagrams are consistent with theoretical band structure calculations. Band dispersion and electron populations of different metal- and phosphorus-based states agree well with partial density of states curves and the bonding, nonbonding, or antibonding character of states agrees well with crystal orbital overlap population curves.²⁵

3.4 Conclusions

Core and valence-band X-ray photoelectron spectra have been obtained for the series of isostructural MnP-type transition-metal monophosphides CrP, MnP, FeP, and CoP. The high-resolution phosphorus 2p spectra indicated that the charge of the P atoms is close to -1 , as determined from their binding energies. The increase in the phosphorus 2p binding energies through the sequence CrP to CoP confirms the decrease in ionicity of the metal-phosphorus bond as the difference in electronegativity between the atoms diminishes.

The high-resolution metal $2p_{3/2}$ spectra of the monophosphides closely resemble those of the parent transition metals in terms of both binding energy and lineshape. The metal atoms in the monophosphides possess a delocalized electronic structure arising from the presence of extended metal-metal bonding, which provides greater nuclear shielding than for isolated atoms. The satellite structure observed in the Co $2p_{3/2}$ spectra of both Co metal and CoP was confirmed by REELS analysis of Co metal. This feature arises from plasmon loss and not as the result of a "two core hole" final state effect. The common satellite structure for both Co metal and CoP implies that the Co valence

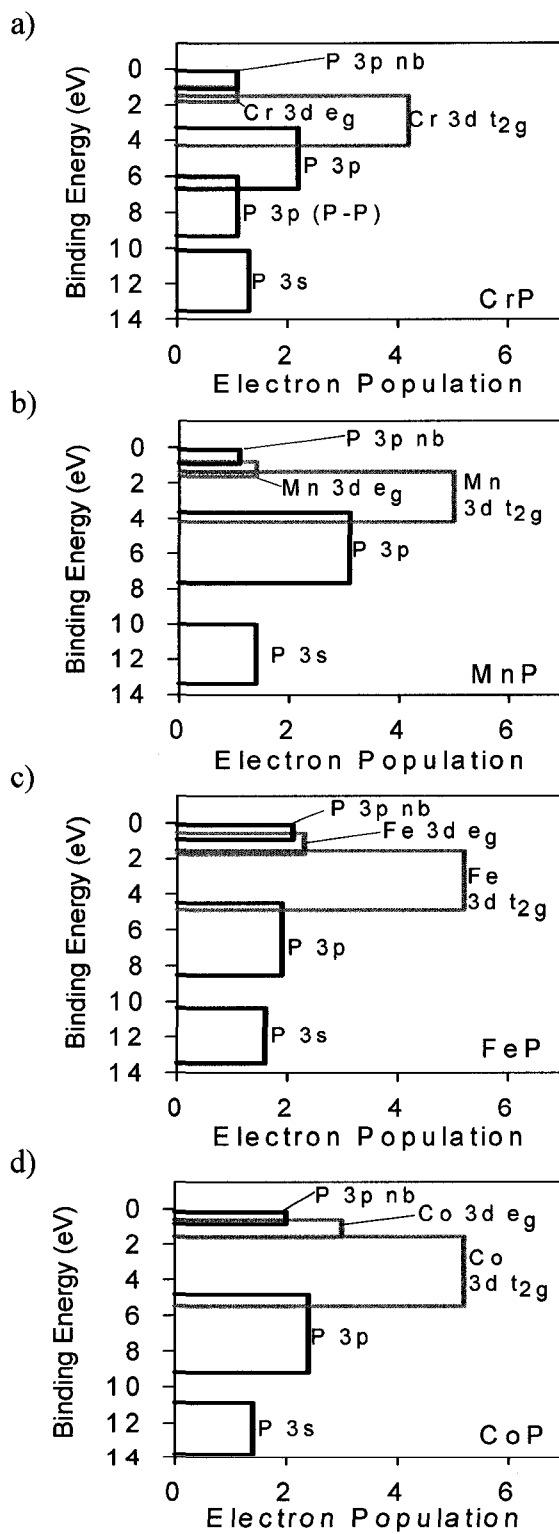


Figure 3-10 Energy level diagrams for (a) CrP, (b) MnP, (c) FeP, and (d) CoP. (Non-bonding states are indicated as nb.)

electrons have similar energies, as was confirmed by analysis of the valence band spectra. However, there are fewer valence electrons around the Co atoms in CoP than in Co metal, implying a cationic state which is consistent with the anionic state of the phosphorus atoms.

The valence band spectra agree well with calculated band structures. We demonstrate a useful approach for analyzing the valence band spectra by fitting these bands with component peaks representing electronic states and their populations. The major orbital interactions arise between the metal 3d and phosphorus 3p states. The electron count for the metal and phosphorus atoms, extracted from the corrected intensities of these component peaks, favours the formulation $M^{1+}P^{1-}$ in which both metal-metal and phosphorus-phosphorus bonding are present. The metal-metal bonding network involves highly delocalized states, similar in character to those of the pure metal, whereas the phosphorus-phosphorus bonding network, which is already weak for CrP and MnP and probably negligible for FeP and CoP, involves localized covalent bonding. Energy level diagrams were constructed from the valence band spectra and extracted electron populations, which compare well to calculated band structures. This type of bonding analysis derived from XPS spectra is complementary to theoretical calculations and may be generalized to study the bonding interactions involved in other inorganic solids.

Chapter 4

Next-Nearest Neighbour Contributions to P 2p_{3/2} X-ray Photoelectron Binding Energy Shifts of Mixed Transition-Metal Phosphides $M_{1-x}M'_xP$ with the MnP-Type Structure*

4.1 Introduction

In the previous chapter, the XPS spectra of binary transition-metal phosphides MP ($M = \text{Cr, Mn, Fe, Co}$) with the MnP-type structure were examined. The MnP-type structure was described in Chapter 1. In this structure, the metal atoms are coordinated to P atoms in a distorted octahedral geometry and establish metal-metal bonding ($< 3 \text{ \AA}$) through zigzag chains along the a and b directions (Figure 1-5).³⁴ Mixed transition-metal phosphides $M_{1-x}M'_xP$ with the same structure type can also be prepared in which M and M' are randomly distributed in the metal sublattice, as indicated by the presence of sharp reflections and the absence of superstructure reflections in the X-ray and neutron diffraction patterns.^{26, 27} In these mixed-metal systems, M is designated to be more electronegative than M' . Both the binary and pseudobinary phosphides are metallic and display interesting magnetic properties.^{26, 27, 35, 104, 105, 132, 133} Here, XPS and XANES have been used to study how metal substitution affects the energies and lineshapes of the spectra from mixed transition-metal phosphides compared to those for the binary compounds.

*A version of this chapter has been published. Reproduced with permission from Grosvenor, A. P.; Cavell, R. G.; Mar, A. *J. Solid State Chem.* **2007**, *180*, 2702-2712. Copyright (2007) by Elsevier.

X-ray photoelectron spectroscopy (XPS) has not been applied extensively to the study of intermetallic compounds, where the interpretation of binding energy shifts is difficult. In general, variations in core-line XPS binding energies (BE) are related to the interactions between an atom of interest and its nearest immediate neighbours, an effect known as the primary substituent shift.¹³⁴ Longer-range interactions with more distant atoms in secondary coordination shells may also exert an influence on these binding energies, an effect known as the secondary substituent shift (also called β -shift or next-nearest neighbour shift).¹³⁴

Like XPS, X-ray absorption spectroscopy (XAS), which can be subdivided into XANES (X-ray absorption near-edge spectroscopy) and EXAFS (extended X-ray absorption fine structure), also provides information about the electronic structure of materials. The XANES absorption energy shifts as the local chemical environment is altered^{97, 99} and the lineshape reveals valuable information about the composition of the valence and conduction states.⁹⁷ Next-nearest neighbour effects have also been implicated in XANES spectra.¹³⁵

The next-nearest neighbour effect, examined by XPS, has been identified in a few specific cases. The clearest examples occur in halogenated hydrocarbons.^{134, 136-138} In fluorinated aromatic hydrocarbons, substitution of H by F induces a positive shift in the C 1s XPS spectrum by as much as 3 eV for the α -C atoms (bound directly to F) and by ~ 1 eV for the β -C atoms (those bound to the α -C). Molecular orbital calculations revealed that the binding energies of the β -C atoms shift not only because of the change in electronegativity of the substituent F vs. H, but also because of the change in the charge developed on the α -C atoms.¹³⁶ The magnitude of this shift is thus expected to be less

pronounced as the electronegativity of the substituent decreases, as has been observed in Cl-, Br-, O-, and N-containing polymers.¹³⁹⁻¹⁴² The source of the shifts can be identified using a simple model that describes the binding energy shifts arising from ground state effects. This model, called the charge potential model, is defined by the equation:

$$\Delta E_i = E_i - E_i^{\circ} = k\Delta q_i + \Delta \sum_{j \neq i} q_j / r_{ij} . \quad (4-1)$$

The total binding energy shift, ΔE_i , which is the difference between the measured binding energy of the atom of interest, E_i , and a reference binding energy, E_i° , consists of two contributions. The $k\Delta q_i$ term describes intraatomic effects involving the change in charge Δq_i on atom i multiplied by a constant k which is related to the interaction between valence and core electrons.^{143, 144} The $\Delta \sum_{j \neq i} q_j / r_{ij}$ term describes interatomic effects involving how the charges of coordinating atoms, q_j , surrounding the photoemission site influence the BE of the resulting photoelectron and, because of its similarity to the Madelung potential, is often referred to as such.^{143, 144} The charge potential model explains the binding energy shifts in the example above. When H is substituted by the more electronegative F atom, the α -C atom has a higher binding energy because its apparent positive charge q_i is increased. In turn, the increase in the apparent charge on the α -C atom induces a more positive Madelung potential felt by the β -C atom, whose binding energy also becomes higher.¹³⁶ This analysis indicates that intraatomic effects (i.e., change in charge) have a greater influence on the magnitude of the binding energy shift than do interatomic effects (i.e., change in Madelung potential).

Next-nearest neighbour effects have also been observed in the XPS spectra for a few inorganic substances. In nitrated silicon dioxide and silicon oxynitride thin films,

the N 1s binding energies shift by ~ 0.1 eV upon substitution of the next nearest neighbours (O for Si).^{145, 146} The P 2p binding energies of transition-metal substituted phosphate (P_2O_5) glasses decrease when the next nearest neighbour is replaced by a metal (i.e., P–O–P to P–O–*M*).^{147, 148} The magnitude of the shift (1–2 eV) diminishes as the electronegativity of the metal increases.¹⁴⁷⁻¹⁵⁰ According to the charge potential model, when P is substituted by the more electropositive *M* atom, the apparent negative charge on the O atom increases not only because of a change in its formal charge but also in the degree of ionic bonding. This induces a more negative Madelung potential felt by the (unsubstituted) P atom, whose 2p binding energy becomes lower. Quantum chemical calculations for several sulphide minerals showed that the S 2p binding energies depend on interactions with next nearest neighbours when they are sufficiently close to the S atom.⁶³ For example, in MoS_2 (molybdenite), the calculated S 2p binding energy is 161.7 eV when only nearest neighbours are considered, but is 162.5 eV when next-nearest neighbours are included, in excellent agreement with the range of experimentally reported values (162.0–162.8 eV).⁶³ These observed differences in binding energy can be related to the expected change in the magnitude of the Madelung potential when both nearest and next-nearest neighbours are included in the calculation in contrast to the underestimate when only nearest neighbours are considered.

In this chapter, the XPS spectra of several series of mixed phosphides ($Co_{1-x}Mn_xP$, $Mn_{1-x}V_xP$, and $Co_{1-x}V_xP$) are reported, demonstrating how next-nearest neighbour contributions resulting from $M' \rightarrow M$ charge transfer via metal-metal bonds can influence the P 2p binding energies. The observed shifts in energies are described in terms of the charge potential model and electronegativity of the metals. An empirical

model that combines both nearest and next-nearest neighbour contributions derived from electronegativity differences allows estimation of the magnitude of the shifts. Metal XPS and XANES spectra were also analyzed as well as the P K-edge XANES spectra.

4.2 Experimental

4.2.1 Synthesis

Starting materials were powders of the metals (Ti, 99.98%, Cerac; V, 99.5%, Alfa-Aesar; Mn, 99.95%, Cerac; Co, 99.999%, Spex) and red P (99%, Alfa-Aesar). Products were identified by their powder X-ray diffraction patterns obtained on an Inel powder diffractometer equipped with a CPS 120 detector. All samples were manipulated and stored in a glove box under Ar to limit exposure to air.

The parent binary monophosphides (CoP, MnP, and VP) were prepared through stoichiometric reaction of metal powders with red P confined in evacuated fused-silica tubes. The tubes were heated up to 1323 K over 48 h and held at this temperature for one week before being cooled slowly over 24 h to room temperature. The end member, TiP, was similarly prepared through reaction of Ti powder and red P in an evacuated fused-silica tube heated to 1173 K over 36 h and held at this temperature for one week before being quenched in water.

The mixed metal phosphides ($\text{Co}_{1-x}\text{Mn}_x\text{P}$, $\text{Mn}_{1-x}\text{V}_x\text{P}$, and $\text{Co}_{1-x}\text{V}_x\text{P}$) were prepared from stoichiometric reaction of the binary phosphides. The mixed materials were ground together in a glove box under dry Ar and sealed in evacuated fused-silica tubes. The tubes were heated up to 1273 K over 20 h, held at this temperature for ~5 d, and then quenched in water. This heating and grinding process was repeated for a total of three 5-d heat treatments at 1273 K to improve the homogeneity of each sample. The

following samples were examined by XPS and XANES analyses: $\text{Co}_{0.10}\text{Mn}_{0.90}\text{P}$, $\text{Co}_{0.30}\text{Mn}_{0.70}\text{P}$, $\text{Co}_{0.40}\text{Mn}_{0.60}\text{P}$, $\text{Mn}_{0.95}\text{V}_{0.05}\text{P}$, $\text{Mn}_{0.85}\text{V}_{0.15}\text{P}$, $\text{Mn}_{0.75}\text{V}_{0.25}\text{P}$, $\text{Mn}_{0.60}\text{V}_{0.40}\text{P}$, $\text{Co}_{0.90}\text{V}_{0.10}\text{P}$, and $\text{Co}_{0.80}\text{V}_{0.20}\text{P}$. Powder X-ray diffraction confirmed that these samples were single-phase and that all adopt the MnP-type structure. The $\text{Co}_{1-x}\text{Mn}_x\text{P}$ and $\text{Mn}_{1-x}\text{V}_x\text{P}$ series have been reported previously.^{26, 27} The $\text{Co}_{1-x}\text{V}_x\text{P}$ series is new (although the corresponding arsenide series, $\text{Co}_{1-x}\text{V}_x\text{As}$, is known¹⁵¹), and the two members prepared have cell parameters ($a = 5.095(3) \text{ \AA}$, $b = 3.268(3) \text{ \AA}$, $c = 5.629(4) \text{ \AA}$ for $\text{Co}_{0.90}\text{V}_{0.10}\text{P}$ and $a = 5.106(3) \text{ \AA}$, $b = 3.262(3) \text{ \AA}$, $c = 5.658(4) \text{ \AA}$ for $\text{Co}_{0.80}\text{V}_{0.20}\text{P}$) that extrapolate smoothly from those of CoP ($a = 5.077 \text{ \AA}$, $b = 3.281 \text{ \AA}$, $c = 5.587 \text{ \AA}$) in accordance with Vegard's law.¹⁵² The smooth variation in cell parameters vs. x (Figure A1-1 in Appendix 1) and the lack of peak broadening in the powder diffraction patterns (Table A1-1 in Appendix 1) for the mixed-metal phosphides strongly support the presence of single-phase samples.

4.2.2 XPS Analysis

Measurements were performed on a Kratos AXIS 165 spectrometer using either Mg K or Al K X-rays. The resolution function for this instrument has been determined to be 0.4 eV when monochromatic Al $K\alpha$ X-rays are used based on analysis of the Co Fermi edge. Analysis of multiple Cu $2p_{3/2}$ spectra yielded a binding energy of $932.59 \pm 0.03 \text{ eV}$ indicating that the second decimal place is significant. This value agrees with those previously reported.¹¹⁶

After the samples were finely ground in a glove box under Ar, they were pressed onto In foil (Alfa-Aesar) or C tape, and placed on a Cu sample holder. The samples were then transported to the XPS instrument under Ar to reduce the possibility of surface

oxidation. After being loaded into the spectrometer, samples were sputter-cleaned for 30–60 min. by means of Ar^+ ion sputtering (4 kV, 10 mA) to remove any surface oxide or phosphate formed. Analysis of the survey spectra collected indicated that only a small amount of phosphate remained after this procedure. Preferential sputtering of the light elements was not observed. High-resolution spectra of the P 2p, metal 2p, and C 1s core lines were collected with a pass energy of 20–40 eV, a step size of 0.05 eV, a sweep time of 180 s, and an energy envelope of 20–40 eV. Spectra were analysed with the aid of the CasaXPS software program.¹¹⁰ During data analysis, the samples were calibrated using the C 1s line arising from adventitious C with a fixed value of 284.80 eV, although this was rarely required because the samples studied are metallic. To remove the background arising from energy loss, a Shirley-type function was applied.

4.2.3 P K-edge XANES Analysis

XANES spectra of the P K-edge were collected at the Canadian Light Source (CLS), Saskatoon, Saskatchewan, using the spherical grating monochromator (SGM) undulator beamline, 11-ID.1.¹⁵³ Although the P K edge is outside the design range of the beamline, good quality spectra were still obtained. At this energy, the monochromatized photon flux is $\sim 10^9$ photons/second, with an estimated resolution of ~ 1 eV and a beam size of approximately $50 \times 100 \mu\text{m}$. Powdered samples were mounted on carbon tape and inserted in the vacuum chamber via a load lock. Total electron yield and total X-ray fluorescence yield spectra were measured from 10 eV below the edge to ~ 35 eV above the edge at 0.1 eV per step. The spectra were calibrated against a sample of $\text{Na}_4\text{P}_2\text{O}_7$, with the peak maximum of the P K-edge set to 2152.4 eV.¹⁵⁴ The P edge values reported herein represent the maximum of the first-derivative peak of each spectrum which

removes the influence of higher energy surface phosphates. A precision of ± 0.1 eV was estimated through comparison of multiple analyses of the compounds studied.

4.2.4 Mn K-edge XANES Analysis

XANES spectra of the Mn K-edge were collected at Pacific Northwest Consortium/X-ray Operations and Research Collaborative Access Team (PNC/XOR-CAT), Sector 20 at the Advanced Photon Source (APS), Argonne National Laboratory with the bending magnet (20BM) beamline. A silicon (111) double crystal monochromator was used to provide a monochromatic photon flux of $\sim 10^{11}$ photons/second, with a resolution of 1.4 eV at 10 KeV and a beam size of approximately 1×5.5 mm. Powdered samples were ground, sandwiched between Kapton tape, and positioned 45° to the X-ray beam. The fluorescence spectrum was measured with a Lytle-type fluorescence ionization chamber detector positioned at 90° relative to the X-ray beam.¹⁵⁵ Through the absorption edge, the X-ray energy was increased by 0.25 eV per step. A Mn metal standard was positioned behind the sample and analyzed concurrently in transmission mode using N_2 -filled ionization chambers. The resulting K-edge was calibrated to the accepted value of 6539 eV.¹⁵⁶ All XANES spectra were analyzed using the Athena software program.¹⁵⁷

4.3 Results and Discussion

4.3.1 P 2p XPS Spectra

P 2p spectra were collected for several binary (MnP, CoP) and pseudobinary mixed ($Co_{1-x}Mn_xP$, $Mn_{1-x}V_xP$, and $Co_{1-x}V_xP$) phosphides with the MnP-type structure, as well as for TiP (TiAs-type) and VP (NiAs-type). These structure types are closely related and differ only in the extent of small structural distortions.²³ Because the P 2p spectra

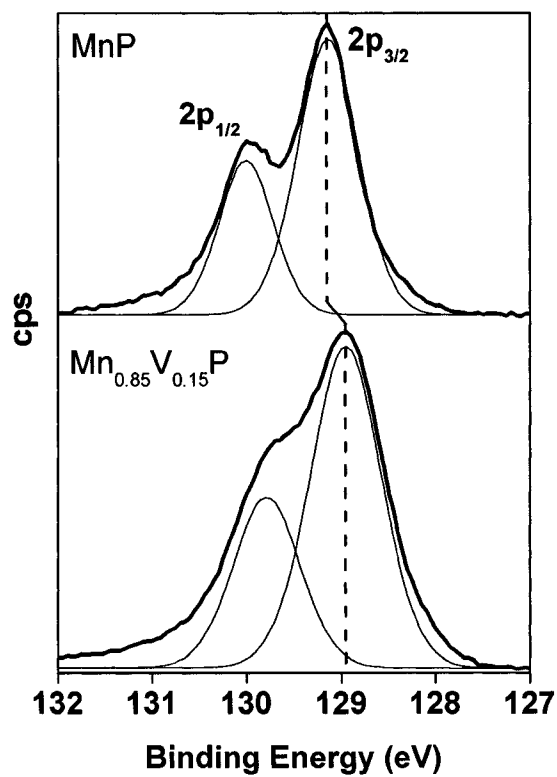


Figure 4-1 High-resolution P 2p spectra for MnP and $Mn_{0.85}V_{0.15}P$. Each spectrum has been fitted with two peaks representing the $2p_{3/2}$ and $2p_{1/2}$ spin-orbit final states in a 2:1 intensity ratio and the background has been subtracted using a Shirley-type function. The $2p_{3/2}$ binding energies are indicated by vertical dashed lines and are also provided in Table 4-1.

for all samples are similar, it suffices to show representative examples, such as MnP and $\text{Mn}_{0.85}\text{V}_{0.15}\text{P}$, as presented in Figure 4-1. In general, the separation between the $2p_{3/2}$ and $2p_{1/2}$ peaks for the parent binary phosphide (MnP) is clear, but it is less obvious for the mixed phosphide ($\text{Mn}_{0.85}\text{V}_{0.15}\text{P}$). The FWHM of the component peaks required to fit the spectra increases from 0.7 eV for MnP to 0.9 eV for $\text{Mn}_{0.85}\text{V}_{0.15}\text{P}$. The line broadening in $\text{Mn}_{0.85}\text{V}_{0.15}\text{P}$ can be ascribed to the superposition of multiple signals arising from the presence of different local distributions of metal atoms around each P atom. Nevertheless, it is still a reasonable approximation to fit the spectra of the mixed phosphides with single $2p_{3/2}$ and $2p_{1/2}$ component peaks to determine average binding energies.

Figure 4-2a shows a plot of the P $2p_{3/2}$ binding energies (also listed in Table 4-1) for various binary (MP) and mixed ($M_{1-x}M'_xP$) phosphides. The binding energies are reported to two decimal places with a reliability of better than ± 0.10 eV based on multiple analyses of separately synthesized samples or the same sample examined at different times (Table A1-2 in Appendix 1). The horizontal axis represents the difference in Allred-Rochow electronegativity between phosphorus and the metal ($\chi_P - \chi_M$).¹¹⁴ In the case of the mixed phosphides, χ_M is replaced by the weighted average electronegativity of the two metals, $(1-x)\chi_M + x\chi_{M'}$. This type of plot was applied in Chapter 3 as well as in previous reports to examine trends in bonding character as the electronegativity difference between the metal and ligand is altered in a series of related compounds.^{81, 158} For the binary phosphides MP , the P $2p_{3/2}$ binding energies decrease linearly on progressing from CoP to TiP. This trend is consistent with expectations: as M becomes more electropositive, the greater ionic character of the M -P bonds induces a

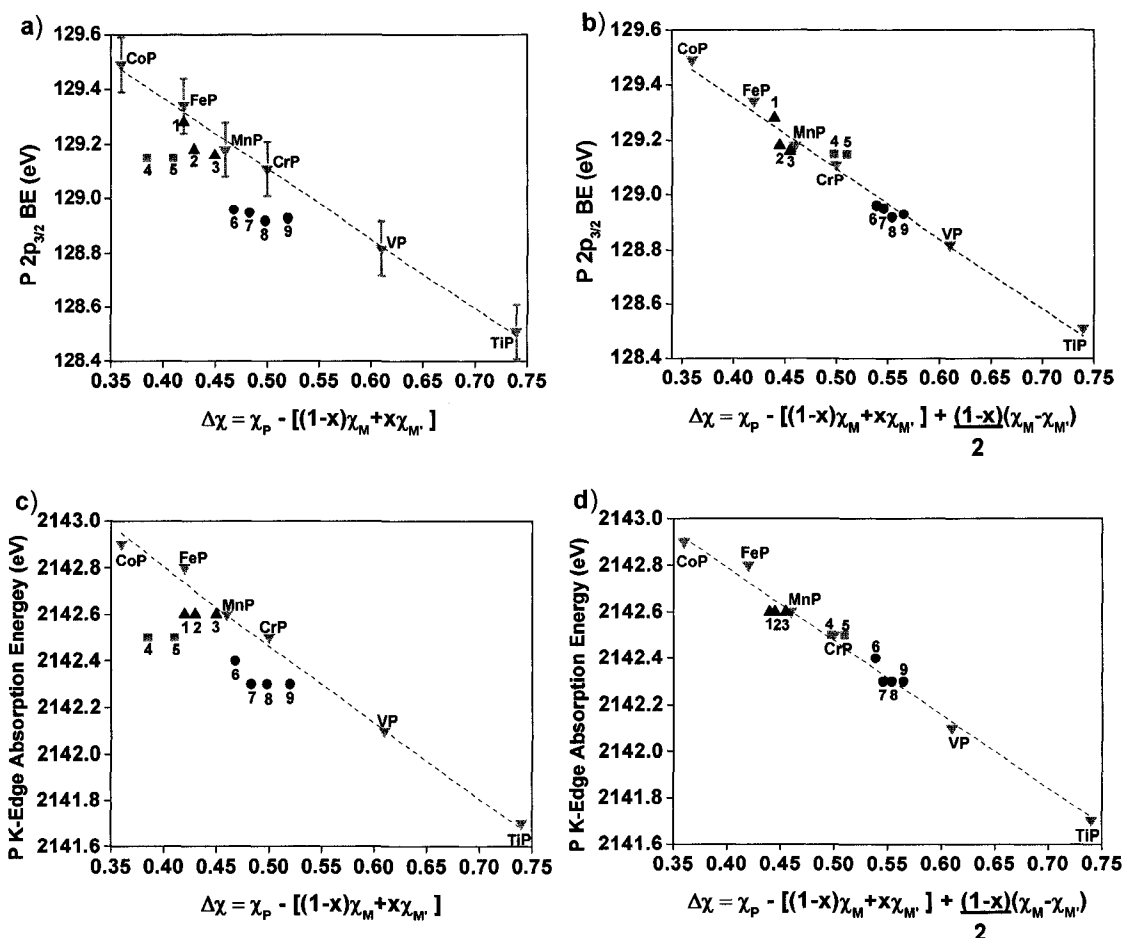


Figure 4-2 Dependence of (a–b) P 2p_{3/2} binding energy and (c–d) P K-edge absorption energy on electronegativity difference $\Delta\chi$ for binary phosphides MP (▼) and ternary phosphides Co_{1-x}Mn_xP (▲) (1 = Co_{0.40}Mn_{0.60}P, 2 = Co_{0.30}Mn_{0.70}P, 3 = Co_{0.10}Mn_{0.90}P), Co_{1-x}V_xP (■) (4 = Co_{0.90}V_{0.10}P, 5 = Co_{0.80}V_{0.20}P), and Mn_{1-x}V_xP (●) (6 = Mn_{0.95}V_{0.05}P, 7 = Mn_{0.85}V_{0.15}P, 8 = Mn_{0.75}V_{0.25}P, 9 = Mn_{0.60}V_{0.40}P). The expression for $\Delta\chi$ incorporates only nearest neighbour contributions (Eq 4-2) in (a) and (c), but also includes next-nearest neighbour contributions (Eq 4-3) in (b) and (d), leading to improved correlations as seen by the linear fits to the data (dashed lines) with $R^2 = 0.971$ and 0.982, respectively. Error bars for the binary MP compounds have been included in (a) to illustrate that the BE shift exhibited by most of the M_{1-x}M'_xP compounds compared to MP is greater than the precision of the measurement.

Table 4-1 Phosphorus 2p_{3/2} binding energies, P K-edge absorption energies, and metal 2p_{3/2} binding energies for metals, binary phosphides MP, and mixed phosphides M_{1-x}M_xP.

Compound	P 2p _{3/2} BE (eV)	P K-edge absorption energy (eV)	Co 2p _{3/2} BE (eV)	Mn 2p _{3/2} BE (eV)	V 2p _{3/2} BE (eV)
Co			778.10		
Mn				638.66	
V					512.3±0.1 ^a
CoP	129.49	2142.9	778.33		
FeP	129.34	2142.8			
MnP	129.18	2142.6		638.73	
CrP	129.11	2142.5			
VP	128.82	2142.1			512.50
TiP	128.51	2141.7			
Co _{0.10} Mn _{0.90} P	129.16	2142.6	778.49	638.78	
Co _{0.30} Mn _{0.70} P	129.18	2142.6	778.41	638.78	
Co _{0.40} Mn _{0.60} P	129.28	2142.6	778.35	638.78	
Co _{0.90} V _{0.10} P	129.15	2142.5	778.10		512.48
Co _{0.80} V _{0.20} P	129.15	2142.5	778.15		512.54
Mn _{0.95} V _{0.05} P	128.96	2142.4		638.72	512.55
Mn _{0.85} V _{0.15} P	128.95	2142.3		638.63	512.49
Mn _{0.75} V _{0.25} P	128.92	2142.3		638.65	512.47
Mn _{0.60} V _{0.40} P	128.93	2142.3		638.70	512.50

^aThe V metal 2p_{3/2} binding energy was taken from reference 116.

more pronounced electron transfer to P, which gains more electron density. If Eq 4-1 is applied to the binary phosphides MP , the charge potential model predicts that the phosphorus binding energy will be lowered by the enhanced negative charge q_i on P, but raised by the more positive Madelung potential arising from the enhanced positive charge on the surrounding metal atoms. The observed trend of an overall linear decrease in binding energy from CoP to TiP confirms that intraatomic effects tend to dominate over interatomic effects, as asserted earlier. In contrast, however, the binding energies for the mixed phosphides $M_{1-x}M'_xP$ do not follow this linear trend, and instead are lower than expected relative to those of the binary phosphides MP even when the precision of the measurement (better than ± 0.10 eV) is taken into consideration.

To understand why the mixed phosphides $M_{1-x}M'_xP$ behave differently, we must consider the complete crystal structure. In the MnP-type structure, adopted by the compounds studied here, each metal atom is surrounded by six nearest-neighbour P atoms at distances of 2.2–2.4 Å which define the immediate first coordination shell.³⁴ There are, however, four other metal atoms in the coordination environment, at slightly longer distances of 2.6–2.8 Å.³⁴ These form part of a metal-metal bonding network which must also be considered. In the binary phosphides MP , all the metal atoms are the same, but in the mixed phosphides $M_{1-x}M'_xP$, it is possible for an M atom to be surrounded locally not only by other M atoms but also by M' atoms, particularly when x is large. As a result, a polarization develops between the two different metals. If M is designated as the more electronegative metal and M' as the more electropositive metal in the formula $M_{1-x}M'_xP$, then M' will donate electron density not only to the P atoms but also to the M atoms. The M atoms in $M_{1-x}M'_xP$ then acquire more electron density than

they possess in the parent binary compound MP . The apparent charge of the M atoms decreases as a result of this charge transfer. Within the charge potential model, this will affect the P 2p binding energies by altering the Madelung potential term ($\Delta\Sigma_{j\neq I} q_j/r_{ij}$). If the P 2p_{3/2} binding energies of the mixed metal phosphides are compared to the line of best fit presented in Figure 4-2a for the binary phosphides, it can be seen that the deviation in binding energy tends to become more negative with increasing concentration of M atoms. This can be ascribed to an overall decrease in Madelung potential owing to the $M \rightarrow M$ charge transfer (i.e., q_M decreases which lowers $\Delta\Sigma_{j\neq I} q_j/r_{ij}$ at high concentrations of M). In this series, there is also a change in the average M -P bond lengths, ranging from 2.304 Å in CoP to 2.358 Å in MnP.³⁴ As a result of the $1/r_{ij}$ dependence, the charge on the smaller, more electronegative M atoms has a greater influence than the larger, more electropositive atoms M' in the Madelung potential term.

The next-nearest neighbour effect described here can be compared with those described in the introduction. It is similar to the case of phosphate glasses in which substitution of P with a metal (with O located between the P atom under examination and the substituted atom; i.e., P-O-M) causes a decrease in the P 2p binding energy.¹⁴⁷⁻¹⁵⁰ In these phosphate glasses, the substitution of P with M alters the Madelung potential component of the P 2p binding energy causing it to be lower than it is in the unsubstituted case. In this example and those presented in the introduction, the *identity* of the nearest neighbour is important in describing the shift in binding energy (in terms of both magnitude and direction) experienced because of next-nearest neighbour effects.

To improve the correlation of the P 2p binding energy shift trends with atomic properties for the $M_{1-x}M'_xP$ system, we have extended the model to include next-nearest

neighbour contributions employing a simple electronegativity analysis. To derive Figure 4-2a we had assumed that, as in the binary phosphides MP , the magnitude of the ground state transfer of electron density from the metal to the P atoms in the first coordination shell was related to the difference in electronegativity of P and of the weighted average of the metals:

$$\Delta\chi = \chi_P - [(1-x)\chi_M + x\chi_{M'}] \quad (4-2)$$

In the context of the charge potential model, Eq 4-2 incorporates the change in the apparent charge on the P atoms (Δq_i) because of the substitution of one metal for another. Much of the change can be related to the variation in degree of ionic bonding present as a metal of different electronegativity is substituted for the original. The lower than expected P $2p_{3/2}$ BE values for $M_{1-x}M'_xP$ relative to those for MP (Figure 4-2a) and the fact that these shifts do not fall on the line connecting the simple binaries suggest that $\Delta\chi$ should be increased to achieve a linear correlation. Increasing $\Delta\chi$ results naturally when a term to represent the charge transfer occurring between M and M' , i.e., $\chi_M - \chi_{M'}$, is added to Eq 4-2. Introducing this next level of charge readjustment alters the Madelung potential term, which is $\Delta\Sigma_{j \neq i} q_j/r_{ij}$ in the charge potential model. Because the level of substitution, x , varies through a given $M_{1-x}M'_xP$ series, $\chi_M - \chi_{M'}$ must be multiplied by a scaling factor that reflects the proportionate degree of this additional charge transfer. It is the concentration of the more electronegative metal M that is most important because M receives electron density from M' , reducing the charge (q_j) on M , which results in an overall decrease in the Madelung potential and thus a lowering of the P $2p$ binding energy. As was indicated above, the magnitude of this shift increases with increasing concentration of M . The fractional concentration of M atoms is $(1-x)$ relative to all metal

atoms, but because only one out of every two atoms in the formula $M_{1-x}M_xP$ is a metal, this must be divided by two to give the concentration of M relative to all atoms. Thus, the final expression for the difference in electronegativity is:

$$\Delta\chi = \chi_P - [(1-x)\chi_M + x\chi_{M'}] + \frac{(1-x)}{2}(\chi_M - \chi_{M'}) \quad (4-3)$$

For the parent binary phosphides MP for which $x = 0$ and $M = M'$, the expression reduces to the simple difference in electronegativity between M and P . In those cases, the change in q_i (the charge on P) correlates directly with the magnitude of the P 2p binding energy shift.

Figure 4-2b shows a plot of the P 2p_{3/2} binding energies vs. the extended expression for the electronegativity difference for the MP and $M_{1-x}M_xP$ phosphides which takes next-nearest neighbour effects into consideration. The linear correlation ($R^2 = 0.971$) lends strong support to this model in which both nearest and next-nearest neighbour effects are included. Additional compelling evidence is provided by comparing the plots of the P K-edge absorption energies (Table 4-1) vs. the electronegativity difference calculated using either Eq 4-2 (Figure 4-2c) or Eq 4-3 (Figure 4-2d). Representative P K-edge XANES spectra from CoP and $Co_{0.80}V_{0.20}P$ are presented in Figure 4-3. Because XANES is a bulk-sensitive technique, the agreement between the XANES and XPS results indicates that the variations in P 2p BE observed between the binary and mixed-metal phosphides derive from a bulk rather than a surface electronic effect. The excellent correlation obtained when Eq 4-3 is applied to the P K-edge absorption energies reinforces the importance of next-nearest neighbour contributions when the second coordination shell has been modified by substitution.

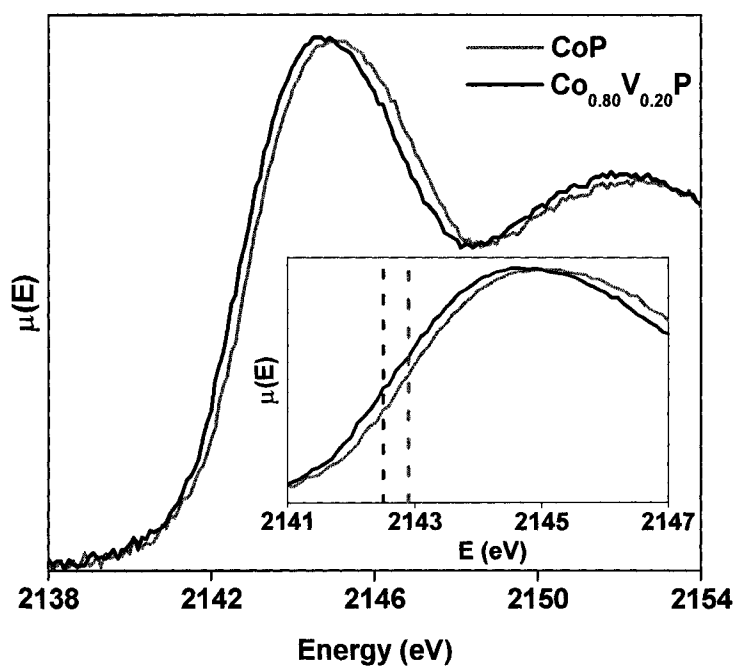


Figure 4-3 P K-edge XANES spectra for CoP and $\text{Co}_{0.80}\text{V}_{0.20}\text{P}$ representing P $1s \rightarrow np$ transitions. Inset: Absorption edges with the inflection points (Table 4-1) marked by vertical dashed lines.

Although the charge potential model describes the variations in P binding energy and absorption energy well in this system, it should be emphasized that this model is based only on changes in ground state energies. In reality, the binding energy of the X-ray excited photoelectron represents the difference in energy between the ground state of the atom having n electrons and the final state of the atom containing $n-1$ electrons.⁶³ As such, various processes can affect the final state energy and therefore alter the binding energy of the atom under study. The presence of a hole in the core electron states produced by the removal of a photoelectron can be thought to act like a positive charge. One of the effects of this added unit of positive charge is adiabatic relaxation of the electrons towards the nucleus which can be separated into inter- and intra-atomic contributions.¹³⁴ An increase of electron density flowing toward the atom due to the production of the core-hole acts to decrease the final state energy by increasing the screening of the nuclear charge; this results in a lowering of the binding energy of the atom under study.¹³⁴ The resulting reorganization of the distribution of electron density on the surrounding atoms will also alter the Madelung potential component of the final state.⁶³ Analysis of the relaxation energy of gas-phase P and S compounds suggests that when the coordination environment around a given atomic centre is fixed (as is the case in the metal phosphides discussed here), greater relaxation occurs as the electronegativity of the ligand decreases.^{159, 160} By comparison to the P 2p binding energies presented above, if relaxation was responsible for the shifts in energy observed in the $M_{1-x}M_xP$ compounds, then the magnitude of the shift would be expected to increase with increasing concentration of M (the more electropositive metal). However, the situation is reversed in that the magnitude of the shift decreases with increasing concentration of

M' . This suggests then that variations in adiabatic relaxation are not responsible for the shifts found in these mixed metal compounds compared to the binary phosphides. Given this conclusion, it is reasonable to use the charge potential model to describe the observed variations in the P 2p binding energies, particularly since it has been found that variations in the Madelung potential tend to have a larger influence on the binding energy than do changes in adiabatic relaxation.^{161, 162}

4.3.2 Metal 2p XPS Spectra

Figure 4-4 shows a collection of metal 2p_{3/2} spectra for the parent binary phosphides MP and several representative members of the $M_{1-x}M'_xP$ series. All spectra exhibit an asymmetric lineshape, which is characteristic of an itinerant electronic structure and results from a final state effect first described by Doniach and Šunjić.¹¹⁷ This lineshape was described in Chapter 3 (Section 3.3.2). As previously observed in the parent binary compounds (Chapter 3), the delocalized electronic structure of the metal atoms arises from the strong metal-metal bonds found in phosphides with the MnP-type structure. Table 4-1 lists the metal 2p_{3/2} binding energies for the elemental metals, the binary phosphides MP , and the mixed phosphides $M_{1-x}M'_xP$. In contrast to the P spectra, the metal 2p_{3/2} binding energies generally do not shift appreciably in $M_{1-x}M'_xP$ relative to those in the parent binary phosphides. The electronic delocalization arising from metal-metal bonding in $M_{1-x}M'_xP$ leads to both a well-screened ground state and final state that is produced after photoionization (as is found in the parent compounds as well as in the elemental metals), so that little variation in the metal 2p_{3/2} binding energies is observed. This is a situation where the charge potential model is unable to describe the metal

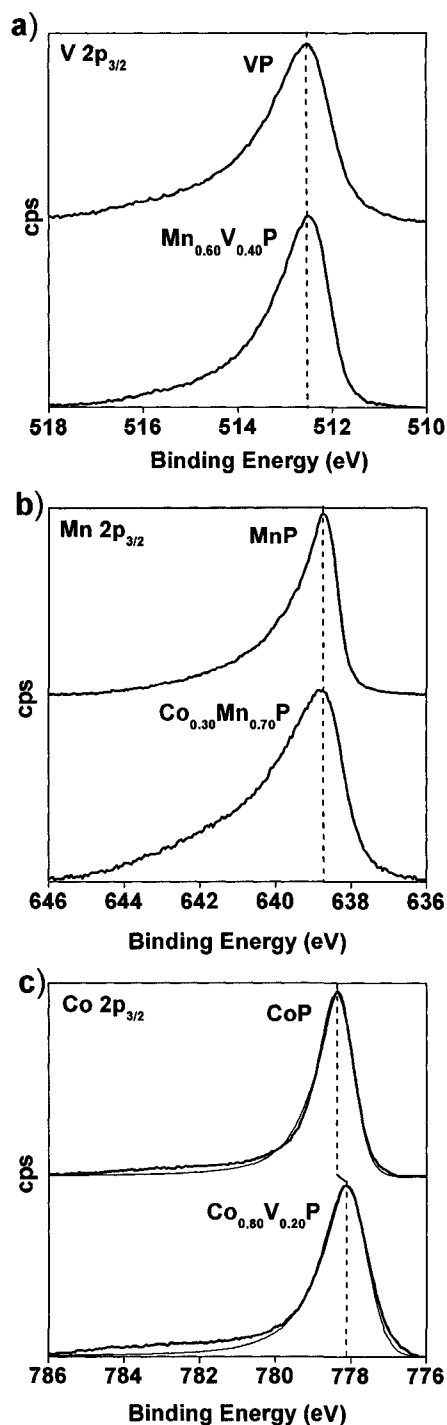


Figure 4-4 Representative metal $2p_{3/2}$ spectra for $Mn_{1-x}V_xP$, $Co_{1-x}Mn_xP$, $Co_{1-x}V_xP$, and the parent binary phosphides. An asymmetric peak (thin solid line) has been used to fit the $Co 2p_{3/2}$ spectra of CoP and $Co_{0.80}V_{0.20}P$, revealing the superimposed high binding energy satellite peak. The $2p_{3/2}$ binding energies, which are listed in Table 4-1, are marked by vertical dashed lines.

binding energy shifts properly, because final state effects such as those described above and in Chapter 3 are not incorporated into Eq 4-1.

Unlike the other mixed phosphides, the $\text{Co}_{1-x}\text{V}_x\text{P}$ series appears to be anomalous in displaying perceptible differences in the Co $2p_{3/2}$ binding energies relative to those in CoP (see Table 4-1 and Figure 4-4). In $\text{Co}_{0.90}\text{V}_{0.10}\text{P}$ and $\text{Co}_{0.80}\text{V}_{0.20}\text{P}$, the Co $2p_{3/2}$ binding energy is ~ 0.2 eV lower than in CoP, whereas the V $2p_{3/2}$ binding energy is nearly identical to that in VP. The appearance of a shift in the case of the Co $2p$ binding energies of $\text{Co}_{1-x}\text{V}_x\text{P}$ compared to CoP, in contrast to the constancy of metal $2p$ binding energies throughout the parent and mixed metal phosphides, can be ascribed to the magnitude of the differences in metal electronegativities, $\chi_M - \chi_{M'}$. As indicated above, this quantity relates directly to the change in charge experienced by M . The electronegativity difference between Co and V is the largest ($\chi_{\text{Co}} - \chi_{\text{V}} = 0.25$); in the other cases, the differences are smaller ($\chi_{\text{Mn}} - \chi_{\text{V}} = 0.15$ and $\chi_{\text{Co}} - \chi_{\text{Mn}} = 0.10$).¹¹⁴ The downward shift in binding energy observed for the Co $2p$ spectrum of $\text{Co}_{1-x}\text{V}_x\text{P}$ compared to CoP confirms the charge transfer model above. This result shows how substitution of V (M') for Co (M) can cause a decrease in the Madelung potential term of the local environment around the P atoms through a reduction of the charge on the M atoms.

The satellite peak observed in the Co $2p_{3/2}$ spectra at an energy slightly higher than the main core-line (Figure 4-4c) also provides support for the proposed charge transfer that occurs from $M' \rightarrow M$ in the mixed metal phosphides as a result of the metal-metal bonding framework. In Chapter 3, we attributed this satellite peak to plasmon loss. Plasmon loss can be described as the loss of kinetic energy of the photoelectron (increase

in binding energy) arising from an oscillation of bound valence electrons.¹¹¹ This assignment has been corroborated by identifying the occurrence of the same phenomenon in most of the first-row transition metals (Sc–Ni).^{127, 163-166} Note that no such plasmon loss peak is observed in the Mn or V $2p_{3/2}$ spectra, likely because it is overlapped by the significantly more intense core-line. The amplitude of the plasmon loss peak observed in the Co $2p_{3/2}$ spectra has been found to vary greatly with only a slight change in the occupancy of the Co valence states as was indicated in Chapter 3. This behaviour will be further discussed in Chapter 7. Analysis of the 1s XPS peak of Sc–Co using a Cu $K\alpha$ X-ray source also revealed that the plasmon loss peak intensifies with greater number of spin-unpaired electrons, and that the energy separation between the plasmon loss peak and the core-line increases with greater concentration of 3d valence electrons.¹⁶⁶ The intensity of the plasmon loss peak is more sensitive than the energy of the plasmon loss peak or the $2p_{3/2}$ core-line binding energy to changes in the occupancy of the valence states. For example, the plasmon peak is considerably more intense but is only 0.3 eV higher in energy in the Co $2p_{3/2}$ spectrum for Co metal vs. that in CoP (Table 3-1 in Chapter 3), and the Co $2p_{3/2}$ BE differs by only 0.2 eV on progressing from Co to CoP (see Table 4-1) owing to electronic delocalization.

In comparison to CoP and $\text{Co}_{1-x}\text{Mn}_x\text{P}$, the satellite peak for $\text{Co}_{1-x}\text{V}_x\text{P}$ is significantly more intense. To quantify this observation, Figure 4-5 shows a plot of the normalized intensity of the plasmon loss peak ($I_{\text{plasmon}}/I_{\text{core-line}}$) vs. the difference in electronegativity between the metals ($\chi_M - \chi_{M'}$). For reference, the normalized intensity of the plasmon loss peak for Co metal is shown as a dashed line. As the electronegativity difference increases, the plasmon loss peak intensifies. The plot reveals that Co atoms in

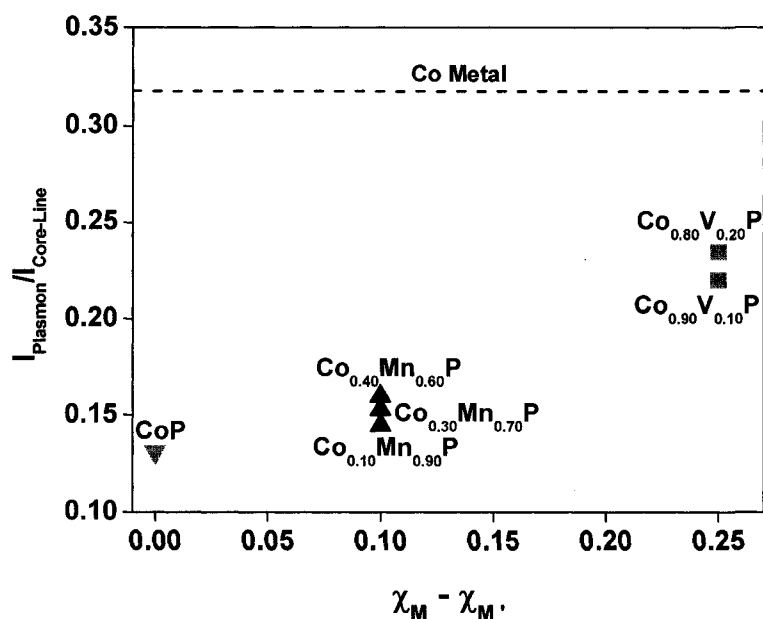


Figure 4-5 Plot showing the variation in the normalized plasmon intensity vs. the difference in electronegativity between the two dissimilar metals ($\chi_M - \chi_{M'}$) in the Co 2p spectrum of CoP, Co_{1-x}Mn_xP, and Co_{1-x}V_xP. The value for Co metal is represented as a dashed line.

$\text{Co}_{1-x}\text{V}_x\text{P}$ contain significantly more electron density in their valence states than is the case for CoP . An increase in occupation of the Co valence states is also observed within the $\text{Co}_{1-x}\text{Mn}_x\text{P}$ series. These results further support the argument that as Co is substituted for a more electropositive metal, the positive charge on Co decreases, thereby reducing the Madelung potential term operating on the P 2p binding energy which is lowered compared to the binary phosphides. The intensity of the plasmon loss peak can also be related to the deviation of the P 2p_{3/2} (Figure 4-2a) or P K-edge absorption energies (Figure 4-2c) for $\text{Co}_{1-x}\text{V}_x\text{P}$ and $\text{Co}_{1-x}\text{Mn}_x\text{P}$. The more intense plasmon loss peak in $\text{Co}_{1-x}\text{V}_x\text{P}$ suggests a greater occupancy of Co valence states and lower Co charge than in $\text{Co}_{1-x}\text{Mn}_x\text{P}$. This is consistent with the more pronounced negative deviations of the P 2p_{3/2} and P K-edge absorption energies in $\text{Co}_{1-x}\text{V}_x\text{P}$ than in $\text{Co}_{1-x}\text{Mn}_x\text{P}$, as a result of the lowered Madelung potential in the case of the former.

4.3.3 Mn K-edge XANES

Because the Mn 2p XPS spectrum does not contain an observable plasmon loss peak, other methods must be used to interrogate the change in occupation of the Mn valence states in the $\text{Mn}_{1-x}\text{V}_x\text{P}$ and $\text{Co}_{1-x}\text{Mn}_x\text{P}$ series compared to MnP . The Mn K-edge XANES spectrum of MnP has been shown previously to contain a pre-edge peak arising from the excitation of 1s electrons into 3d states.¹⁶⁷ Among other factors, the intensity of this peak decreases with increasing occupancy of the metal 3d valence states.¹⁶⁸ Although the pre-edge peak is primarily assigned to a (1s → 3d) transition, the distorted octahedral coordination of the metal atoms in the MnP -type structure introduces some participation of 4p orbitals in the metal-phosphorus bonding³³ adding a small dipolar component (1s → 4p) to this peak. As such, only compounds that are very similar to the

parent binary can be compared, because any significant change in the P–M–P bond angles may alter the contribution of 4p orbitals involved in bonding and hence the intensity of the pre-edge peak. Moreover, quadrupolar $1s \rightarrow 3d$ transitions are already considerably weaker than dipolar ($1s \rightarrow 4p$) transitions.¹⁶⁹ For this reason, only the least substituted members where the structures are minimally perturbed ($\text{Mn}_{0.95}\text{V}_{0.05}\text{P}$ and $\text{Co}_{0.10}\text{Mn}_{0.90}\text{P}$) were examined, and their Mn K-edge XANES spectra are shown normalized in comparison to MnP in Figure 4-6.

In $\text{Mn}_{0.95}\text{V}_{0.05}\text{P}$, the pre-edge peak (labelled A) is slightly less intense than in MnP (Figure 4-6a). This indicates an increased occupancy of the Mn valence states in $\text{Mn}_{0.95}\text{V}_{0.05}\text{P}$ relative to MnP, providing further evidence for the occurrence of a secondary charge transfer from V to the more electronegative Mn atoms. In $\text{Co}_{0.10}\text{Mn}_{0.90}\text{P}$, the roles of the metal atoms are reversed relative to $\text{Mn}_{0.95}\text{V}_{0.05}\text{P}$, and charge transfer from the more electropositive Mn atoms to Co is now operative. The Mn K-edge spectra of $\text{Co}_{0.10}\text{Mn}_{0.90}\text{P}$ and MnP overlap well except for the region near the pre-edge peak (Figure 4-6b). The slightly more intense pre-edge peak in $\text{Co}_{0.10}\text{Mn}_{0.90}\text{P}$ indicates decreased electron density of the Mn valence states compared to MnP. This observation agrees with the earlier conclusion that the Co valence states experience a slight increase in electron density, which manifests itself as an enhancement of the Co 2p plasmon loss peak in the $\text{Co}_{1-x}\text{Mn}_x\text{P}$ series (Figure 4-5). That is, the charge transfer from Mn to Co is confirmed. This result is also consistent with the improved fitting of the P energies when Eq 4-3 is used instead of Eq 4-2 for the electronegativity expression, supporting the importance of next-nearest neighbour contributions to alteration of the Madelung potential of the chemical environment surrounding the P atoms.

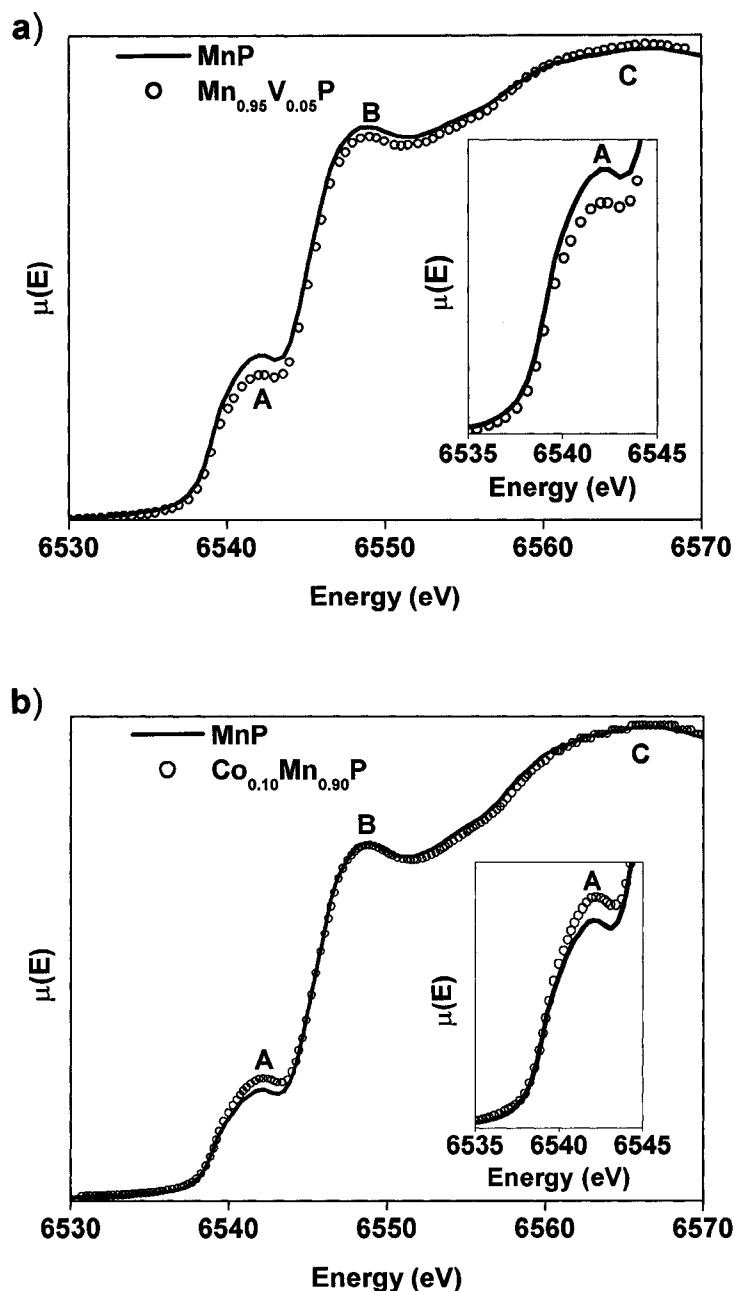


Figure 4-6 Mn K-edge XANES spectra of (a) $\text{Mn}_{0.95}\text{V}_{0.05}\text{P}$ and (b) $\text{Co}_{0.10}\text{Mn}_{0.90}\text{P}$. Included for comparison, the spectrum of MnP matches that reported previously.¹⁶⁷ Peak **A** represents the pre-edge peak originating from $1s \rightarrow 3d$ and $1s \rightarrow 4p$ transitions, peak **B** represents the excitation of Mn $1s$ electrons into P $3p$ antibonding states, and peak **C** represents the Mn $1s \rightarrow 4p$ transition.¹⁶⁷ The insets highlight details near peak **A**. The linewidths of the spectra are all broader than the standard deviation of the measurement.

4.4 Conclusions

P $2p_{3/2}$ binding energies and P K-edge absorption energies in mixed transition-metal phosphides $M_{1-x}M'_xP$ with the MnP-type structure are shifted down relative to those in the parent binary phosphides MP . These shifts arise from a next-nearest neighbour contribution which modifies the charge distribution. Charge transfer between the two dissimilar metals in $M_{1-x}M'_xP$ through a metal-metal bonding framework enables the more electronegative metal M atoms to acquire more electron density than is present in the parent binary compound MP . In terms of the charge potential model (Eq 4-1), this decreased positive charge on M acts to lower the Madelung potential of the environment around the P atoms, which is manifested by a lower P $2p_{3/2}$ binding energy and P K-edge absorption energy. The observed P shifts, which increase with increasing concentration of M , arises from both nearest and next-nearest neighbour interactions and can be modeled through an enhanced expression for the electronegativity difference (Eq 4-3) which necessarily must include the next-nearest neighbour contributions in differentially substituted systems. The modified electronegativity difference model correlates well with observed binding energies.

Chapter 5

Next-Nearest Neighbour Contributions to the XPS Binding Energies and XANES Absorption Energies of P and As in Transition-Metal Arsenide Phosphides $MAs_{1-y}P_y$ Having the MnP-Type Structure*

5.1 Introduction

In Chapters 3 and 4, XPS and XANES were used to examine binary and pseudobinary transition-metal phosphides MP and $M_{1-x}M'_xP$, the majority of which possess the MnP-type structure. These materials are of interest because of their magnetic properties and catalytic activity.^{5, 170} As was described in Chapter 1, the MnP-type structure consists of an arrangement of metal-centred distorted octahedra (Figure 1-5), which form networks of strong metal-metal and weak P–P bonds,³⁴ consistent with the charge formulation $M^{1+}P^{1-}$. Compounds of this structure type are metallic.¹⁷⁰ Throughout the series of binary phosphides MP , the P $2p_{3/2}$ XPS binding energies (BEs) and P K-edge absorption energies decrease linearly as the difference in electronegativity between M and P increases as we progress from CoP to CrP (all MnP-type), to VP (NiAs-type), and finally to TiP (TiAs-type). These shifts arise because as M becomes more electropositive, P becomes more negatively charged. In contrast, in the pseudobinary phosphides $M_{1-x}M'_xP$, the P XPS BEs and absorption energies do not follow this linear trend and the shifts are lower than expected. Here, the presence of two different metals interacting through the metal-metal bonding network induces a charge redistribution, the

*A version of this chapter has been submitted for publication. Reproduced with permission from Grosvenor, A. P.; Cavell, R. G.; Mar, A. J. *Solid State Chem.* 2008, submitted. Copyright (2008) by Elsevier.

more electropositive metal M' donating electron density not only to P but also to the more electronegative metal M . This next-nearest neighbour effect reduces the Madelung potential operating on the P photoemission or absorption site, lowering its energy, especially when the concentration of the more electronegative metal M is high. Because the next-nearest neighbour effect has been demonstrated to be important in mixed-metal phosphides, it is of interest to determine if it also applies to mixed-anion systems. Several metal arsenide phosphide series $MA_{1-y}P_y$, with the MnP-type structure are known, wherein As and P atoms are randomly distributed within the anion sites,^{28, 29} and have been investigated in this chapter by XPS and XANES.

In Chapter 4, the charge potential model was introduced to describe the P 2p BE shifts observed for $M_{1-x}M'_xP$ vs. MP in terms of ground state effects:^{63, 143, 144}

$$\Delta E = E_i - E_i^{\circ} = k\Delta q_i + \Delta \sum_{j \neq i}^n q_j / r_{ij} . \quad (5-1)$$

Within different compounds, an atom i acquires a BE (E_i) that is shifted relative to a reference energy E_i° because of variations in two possible factors: (i) the atomic charge (q_i in $k\Delta q_i$, where k is a constant representing interactions between valence and core electrons), and (ii) the chemical environment ($\Delta \sum_{j \neq i} q_j / r_{ij}$), where r_{ij} is the distance to neighbouring atoms j .^{143, 144} The second term, often called the Madelung or crystal potential because of its equivalence to the same concept in ionic solids, describes how the charges of coordinating atoms, q_j , surrounding the photoemission site influence the BE of the resulting photoelectron.^{61, 143} Effectively, how well the nuclear charge is screened within the atom of interest depends on the magnitudes of these intraatomic ($k\Delta q_i$) and interatomic ($\Delta \sum_{j \neq i} q_j / r_{ij}$) terms, the latter usually playing a less significant role. Although

the immediate coordination environment (the nearest neighbours around an atom) constitutes the most important contribution to the interatomic term, the more extended environment (the *next*-nearest neighbours) may also affect the BEs, as was discussed in Chapter 4. In addition to ground state effects, after an electron is excited, the production of a core hole causes electrons to relax towards the atom because of the decreased screening of the nuclear charge, modifying the final state energy and thereby the photoelectron BE.¹³⁴ These final state effects can be added to the ground state effects described by Eq 5-1 through additional terms, $-(\Delta E_i^{IA1} + \Delta E_i^{IA2})$, that represent intraatomic (IA1) and interatomic (IA2) relaxation, the former usually being negligible.¹³⁴

The electronic structure of solids can also be analyzed by X-ray absorption spectroscopy (XAS), which can be subdivided into X-ray absorption near-edge spectroscopy (XANES) and extended X-ray absorption fine structure (EXAFS).^{97, 99} XANES probes the absorption edge wherein core electrons are excited into bound or continuum states, thereby giving information about atomic charge and coordination environment.⁹⁷ As explained in Chapter 2 (Section 2.4), EXAFS oscillations (resulting from multiple scattering of the photoelectron) superimposed near the absorption edge often render quantitative analysis of XANES spectra difficult. As is the case for XPS BEs, X-ray absorption threshold energies depend on similar factors to those described by Eq 5-1.¹⁷¹ However, because electrons are now promoted into bound or continuum states, they will still provide partial screening to the excited atom. This implies that absorption energies are less sensitive to relaxation effects than are XPS BEs. For example, in the series of compounds MnO, LaMnO₃, and CaMnO₃, the calculated Mn

K-edge absorption threshold energies increase as the occupancy of the Mn 3d band and the Madelung potential change.¹⁷¹ The shifts in these Mn K-edge absorption energies are much larger than the shifts in the Mn 1s XPS BEs because the absorption energies are not dampened by relaxation effects.¹⁷¹ Next-nearest neighbour effects have also been identified in XANES.¹³⁵

As a continuation of our investigation of the electronic structure of transition-metal pnictides having the MnP-type structure, we report here XPS and XANES spectra of $\text{CrAs}_{1-y}\text{P}_y$, $\text{FeAs}_{1-y}\text{P}_y$, and the new series $\text{CoAs}_{1-y}\text{P}_y$. The charge potential model (Eq 5-1) has been applied to explain shifts in their P 2p XPS BEs and P K-edge and As L_{3-} and K-edge absorption energies. The metal 2p XPS and L- and K-edge absorption spectra are also presented.

5.2 Experimental

5.2.1 Synthesis

Starting materials were metal powders (Cr, 99.8%, Alfa-Aesar; Fe, 99.9%, Cerac; Co, 99.8%, Cerac; V, 99.5%, Alfa-Aesar), red P powder (99%, Alfa-Aesar), and ground As pieces (99.9998%, Alfa Inorganics). Products were identified by their powder X-ray diffraction (XRD) patterns collected on an Inel powder diffractometer equipped with a CPS 120 detector. All samples were stored in a glove box under Ar to limit exposure to air.

Binary monpnictides (CrP, FeP, CoP; CrAs, FeAs, CoAs, VAs) were prepared through stoichiometric reaction of M with P or As in sealed and evacuated fused-silica tubes. The tubes were heated to 1323 K (for MP) or 1073 K (for MAs) over 2 days and held at this temperature for at least 5 days before being quenched in water. For MAs ,

addition of small amounts of I_2 (Anachemica) improved crystallinity of the products. Ternary pnictides $MAs_{1-y}P_y$ ($M = Cr, Fe, Co$; $y = 0.10, 0.25, 0.50, 0.75, 0.90$) were prepared through stoichiometric reaction of $(1-y)$ MAs and y MP in sealed and evacuated fused-silica tubes. The tubes were heated to 1173 K over 24 h and held at this temperature for 5 days before being quenched in water. To improve homogeneity, the samples were reground under Ar, resealed in fused-silica tubes, and reheated with the same heating profile; this procedure was repeated over three ($FeAs_{1-y}P_y$, $CoAs_{1-y}P_y$) or four ($CrAs_{1-y}P_y$) cycles. Powder XRD confirmed that all samples were single-phase and had adopted the MnP-type structure. Cell parameters for $CrAs_{1-y}P_y$ and $FeAs_{1-y}P_y$ agree with literature values,^{28, 29} and those for the new series $CoAs_{1-y}P_y$ interpolate smoothly from the end members (Figure 5-1), in accordance with Vegard's law.¹⁵²

5.2.2 XPS analysis

Measurements were performed on a Kratos AXIS 165 spectrometer using monochromatic Al $K\alpha$ X-rays. The resolution function for this instrument with this X-ray source is 0.4 eV, based on analysis of the Co Fermi edge, and the BEs are significant to two decimal places. Samples were finely ground under Ar, pressed onto In foil (Alfa-Aesar), and mounted on a Cu sample holder. They were transported and inserted into the introduction chamber of the spectrometer under Ar to reduce the possibility of extensive surface oxidation. Samples were sputter-cleaned *in situ* with an Ar^+ ion beam (4 kV, 10 mA) to remove any surface oxides or contaminants (e.g., C, I) formed. This sputtering process causes slight reduction of As, manifested by a low-binding energy shoulder in the As 3d spectrum, but no effects were observed in the P or M spectra. Annealing the samples in vacuum using temperatures as high as 700 K for ~30 minutes or lowering the

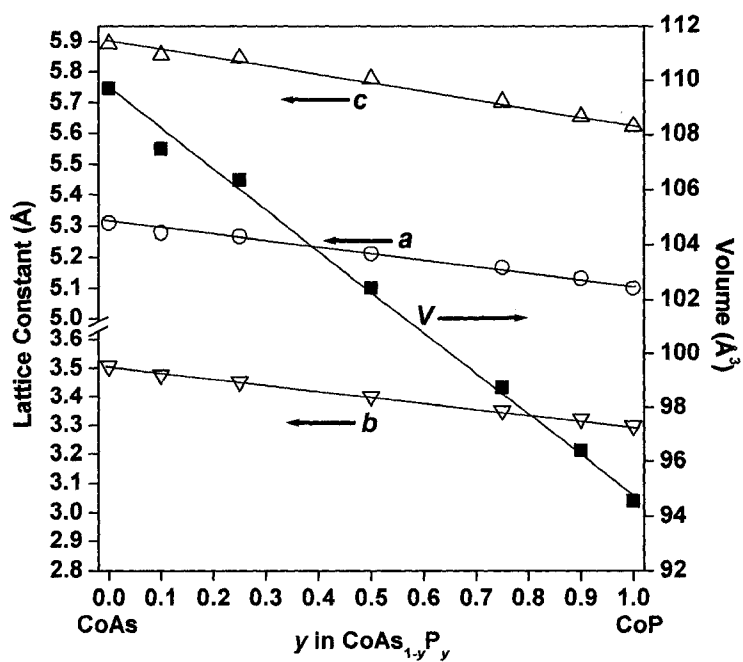


Figure 5-1 Plot of orthorhombic cell parameters vs. y for the $\text{CoAs}_{1-y}\text{P}_y$ series, which adopts the MnP-type structure.

Ar^+ ion sputtering current (1 mA) did not eliminate this As reduction. Survey spectra revealed that preferential sputtering of light elements did not occur and that the surface and bulk compositions are similar. For example, different batches of $\text{FeAs}_{0.10}\text{P}_{0.90}$ (nominal) had a composition of $\text{FeAs}_{0.1(1)}\text{P}_{1.0(1)}$. High-resolution spectra of the *M* 2p, P 2p, As 3d, and C 1s core lines were collected with a pass energy of 20 eV, a step size of 0.05 eV, a sweep time of 180 s, and an energy envelope of 20–40 eV. Spectra were analyzed with the aid of the CasaXPS software program.¹¹⁰ During data analysis, the samples were calibrated using the C 1s line arising from adventitious C with a fixed value of 284.80 eV, although this was rarely required because the samples studied are metallic. To remove the background arising from energy loss, a Shirley-type function was applied.

5.2.3 P K-edge, As L-edge, and *ML*-edge XANES analysis

P K-, As L-, and *ML*-edge XANES spectra were collected at the Canadian Light Source (CLS), Saskatoon, Saskatchewan, using the spherical grating monochromator (SGM) undulator beamline, 11-ID.1.¹⁵³ The flux is $\sim 10^9$ photons/second at energies near the P K-edge (~ 2150 eV) and increases to $\sim 10^{11}$ photons/second below this energy (1900 eV). The estimated resolution is ~ 1 eV and a beam size of approximately $50 \times 100 \mu\text{m}$ was used. Powdered samples were mounted on carbon tape and inserted in the vacuum chamber via a load lock. Total electron yield (TEY) and X-ray fluorescence yield (FLY) spectra were measured from 30–10 eV below the edge to ~ 35 eV (P), 50 eV (*M*), or 75 eV (As) above the edge at 0.1 eV per step. The P K-edge spectra were calibrated against a sample of $\text{Na}_4\text{P}_2\text{O}_7$, with the peak maximum of the P K-edge set to 2152.4 eV.¹⁵⁴ The As L-edge spectra were calibrated against a sample of Ge with the first derivative of the

L_3 edge set to 1217 eV.¹⁵⁶ The $M L$ -edge spectra were calibrated against the first derivative of the L_3 edge of the corresponding pure metal with energies of 574.1 eV (Cr), 706.8 eV (Fe), and 778.1 eV (Co).¹⁵⁶ The absorption edge values reported herein represent the maximum of the first derivative peak, to remove the influence of surface phosphates or arsenates formed. A precision of ± 0.1 eV was estimated through comparison of multiple analyses of the compounds studied.

5.2.4 As K- and $M K$ -edge XANES Analysis

XANES spectra of the As and $M K$ -edges were collected at Pacific Northwest Consortium/X-ray Operations and Research Collaborative Access Team (PNC/XOR-CAT), Sector 20 at the Advanced Photon Source (APS), Argonne National Laboratory with the bending magnet (20BM) beamline. A silicon (111) double crystal monochromator was used to provide a monochromatic photon flux of $\sim 10^{11}$ photons/second, with a resolution of 1.4 eV at 10 keV and a beam size of approximately 1×4.5 mm. Finely ground samples were sandwiched between Kapton tape, and positioned 45° to the X-ray beam. The fluorescence spectra were measured with a Canberra 13-element fluorescence detector and transmission spectra were measured with N_2 -filled ionization chambers (the I_0 ionization chamber contained a 50:50 mixture of He and N_2). Through the absorption edge, the X-ray energy was increased by 0.15 eV per step. For the $M K$ -edge spectra, a standard of the elemental metal was positioned behind the sample and analyzed concurrently in transmission mode with N_2 -filled ionization chambers, and the peak maximum of the first derivative was calibrated to the accepted values of 5989 eV (Cr), 7112 eV (Fe), or 7709 eV (Co).¹⁵⁶ The As K-edge spectra were calibrated by collecting the Au L_3 spectrum and setting the first derivative to 11919

eV.¹⁵⁶ The precision of the measurements was estimated to be ± 0.1 eV based on multiple analyses of the compounds and the absorption energies reported herein represent the maximum of the first derivative peak. All XANES spectra were analyzed using the Athena software program.¹⁵⁷

5.2.5 Band Structure Calculations

To interpret the As and *M*K-edge XANES spectra, tight-binding linear muffin-tin orbital band structure calculations were performed on FeAs and FeAs_{0.50}P_{0.50} within the atomic spheres approximation (TB-LMTO ASA).⁴⁰ Contributions from the Fe 4p, Fe 3d, As 4p, and P 3p orbitals to the density of states were extracted. Although FeAs and FeAs_{0.50}P_{0.50} adopt the MnP-type structure (space group *Pnma* (No. 62)), mixed occupancy of the As and P atoms in the latter is difficult to treat. Instead, an ordered model of FeAs_{0.50}P_{0.50} was considered, with reduced symmetry in space group *Pcm2₁* (No. 26). The calculations were performed with 432 *k* points in the irreducible portion of the Brillouin zone.

5.3 Results

5.3.1 Is As less Electronegative than P?

In this report, electronegativity differences are identified as a major factor influencing the shifts in energy and variations in lineshape in the spectra of *MP*, *MAs_{1-y}P_y*, and *MAs*. However, the relative electronegativities of P and As on different electronegativity scales are inconsistent (cf., Allred-Rochow, $\chi_P = 2.06$, $\chi_{As} = 2.20$ vs Pauling, $\chi_P = 2.2$, $\chi_{As} = 2.1$).^{37, 114, 172} In Chapters 3 and 4, we preferred to use Allred-Rochow electronegativities because they are derived from atomic properties and thus more closely linked to binding and absorption energies, instead of Pauling

electronegativities, which are derived from thermodynamic data.^{37, 114} Alternatively, we can examine the experimental XPS BE values to determine the electronegativity of As. For example, the skutterudites CoPn_3 are known for $\text{Pn} = \text{P}, \text{As}, \text{Sb}$, and Co XPS spectra have been measured for CoP_3 and CoSb_3 as will be described in Chapter 7. The Co $2p_{3/2}$ BE decreases from 778.5 eV in CoP_3 to 778.1 eV in CoSb_3 because the more covalent character in the Co–Sb bonds leads to better screening of the Co nuclear charge. We have prepared CoAs_3 (in a similar manner as CoP_3 and CoSb_3) and found that the Co $2p_{3/2}$ BE is 778.3 eV, between those of CoP_3 and CoSb_3 . This implies that the electronegativity of As is intermediate between P and Sb. If Allred-Rochow electronegativities are chosen for Co ($\chi = 1.70$), P, and Sb ($\chi = 1.82$) and if the Co $2p_{3/2}$ BE shifts are assumed to be linearly proportional to the difference in electronegativity in the Co– Pn bond ($\Delta\chi = \chi_{\text{Pn}} - \chi_{\text{Co}}$), then a revised value of $\chi_{\text{As}} = 1.94$ (vs. 2.20 as above) is obtained. The interpretation of spectra in the $\text{MAS}_{1-y}\text{P}_y$ compounds below will thus be based on the revised value which makes As less electronegative than P.

5.3.2 P 2p XPS and P K-edge XANES Spectra

The spectra of FeP and $\text{FeAs}_{0.10}\text{P}_{0.90}$ (Figure 5-2) reveal a distinct separation between the $2p_{3/2}$ and $2p_{1/2}$ spin-orbit coupled final states, which can be fitted by component peaks having a full width at half maximum (FWHM) of $\sim 0.7\text{--}0.8$ eV with an intensity ratio of 2:1 ($2p_{3/2}:2p_{1/2}$), equal to the theoretical value.¹³⁴ In the mixed-metal phosphides $\text{M}_{1-x}\text{M}'_x\text{P}$ examined in Chapter 4, the component peaks were much broader than those in the binary phosphides because different local distributions of M and M' atoms are present in the first coordination shell around the P photoemission site. No such broadening is observed in $\text{FeAs}_{0.10}\text{P}_{0.90}$ relative to FeP , probably because the different

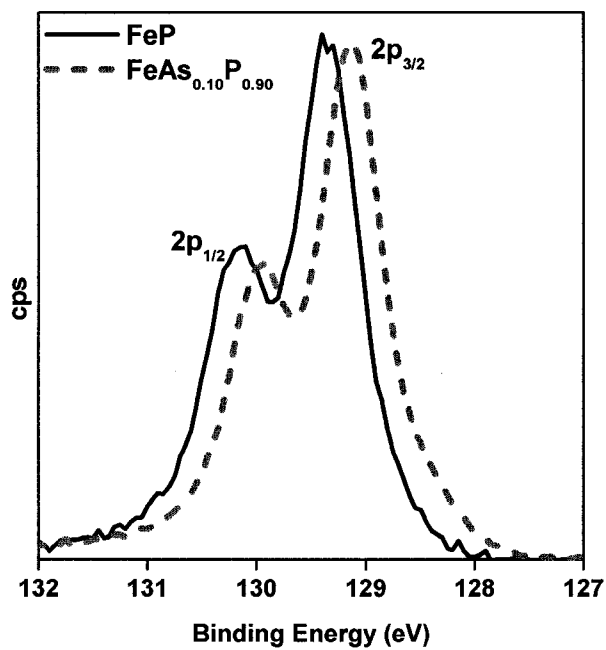


Figure 5-2 High-resolution P 2p XPS spectra for FeP and FeAs_{0.10}P_{0.90}, with 2p_{3/2} and 2p_{1/2} component peaks labelled.

local distributions of P and As atoms in the second coordination shell around the P photoemission site are further away.

Table 5-1 lists P $2p_{3/2}$ BEs for various MP and $MAs_{1-y}P_y$ compounds. From multiple measurements on separately synthesized samples or of the same sample examined at different times, we deduce that the precision of these BEs is better than ± 0.10 eV and in fact closer to ± 0.05 eV (Table A2-1 in Appendix 2). Figure 5-3a shows a plot of BE vs difference in electronegativity ($\Delta\chi = \chi_P - \chi_M$). Although the P $2p_{3/2}$ BEs decrease linearly through the binary phosphide MP series from CoP to TiP, as discussed in Chapter 4, they do not follow this trend in the mixed pnictides $MAs_{1-y}P_y$, with the BEs being lower than expected, even when the precision of the measurement is taken into consideration. Within a given $MAs_{1-y}P_y$ series, the P $2p_{3/2}$ BEs actually deviate more with *increasing* P concentration. Table 5-1 also lists P K-edge absorption energies from XANES, a bulk-sensitive technique. A representative P K-edge spectrum for $CoAs_{0.10}P_{0.90}$ is shown in Figure 5-4a. A similar behaviour to that observed by analysis of the P 2p BEs is revealed in a plot of P K-edge absorption energies vs $\Delta\chi$ (Figure 5-3b), confirming that these shifts arise from a bulk rather than a surface electronic effect.

5.3.3 As L- and K-edge XANES Spectra

Although As 3d XPS spectra were also collected, their analysis was complicated by the presence of a low-binding energy shoulder (arising from slight reduction of As atoms during Ar^+ ion sputtering, as noted in Section 5.2.2) and by the partial overlap with Cr 3p signals in CrAs and $CrAs_{1-y}P_y$. To circumvent these difficulties, As L- and K-edge XANES spectra were investigated. A representative As L_3 -edge spectrum for CrAs, resulting from excitation of As 2p electrons into either As 4s or 4d states, is shown in

Table 5-1 P 2p_{3/2} and M 2p_{3/2} XPS binding energies (eV) and P K-, As L₃-, and As K-edge absorption energies (eV) in MP, MAs_{1-y}P_y, and MAs

Compound	P 2p _{3/2} BE	P K- edge	As L ₃ - edge	As K- edge ^a	Co 2p _{3/2} BE	Fe 2p _{3/2} BE	Cr 2p _{3/2} BE
CoP	129.49	2142.9			778.33		
FeP	129.34	2142.8				706.91	
MnP	129.18	2142.6					
CrP	129.11	2142.5					573.87
VP	128.82	2142.1					
TiP	128.51	2141.7					
CoAs			1322.1	11866.7	777.91		
FeAs			1322.0	11866.6		706.66	
CrAs			1321.7	11866.4			573.80
VAs			1321.5				
CoAs _{0.10} P _{0.90}	129.34	2142.7	1322.4	11866.9	778.22		
CoAs _{0.25} P _{0.75}	129.35	2142.7	1322.3	11866.9	778.20		
CoAs _{0.50} P _{0.50}	129.39	2142.8	1322.2	11866.9	778.16		
CoAs _{0.75} P _{0.25}	129.40	2142.9	1322.1	11866.7	778.11		
FeAs _{0.10} P _{0.90}	129.20	2142.6	1322.2	11866.9		706.81	
FeAs _{0.25} P _{0.75}	129.24	2142.6	1322.2	11866.8		706.85	
FeAs _{0.50} P _{0.50}	129.24	2142.7	1322.1	11866.6		706.77	
FeAs _{0.75} P _{0.25}	129.28			11866.6		706.76	
FeAs _{0.90} P _{0.10}	129.33			11866.6		706.76	
CrAs _{0.10} P _{0.90}	128.99	2142.4	1322.0	11867.1			573.81
CrAs _{0.75} P _{0.25}	129.06	2142.4	1321.8	11867.0			573.90

^aBecause the As K-edge absorption threshold energy is overlapped by the intense pre-edge peak and EXAFS peaks, as described in Section 5.3.3, caution must be applied when interpreting these values.

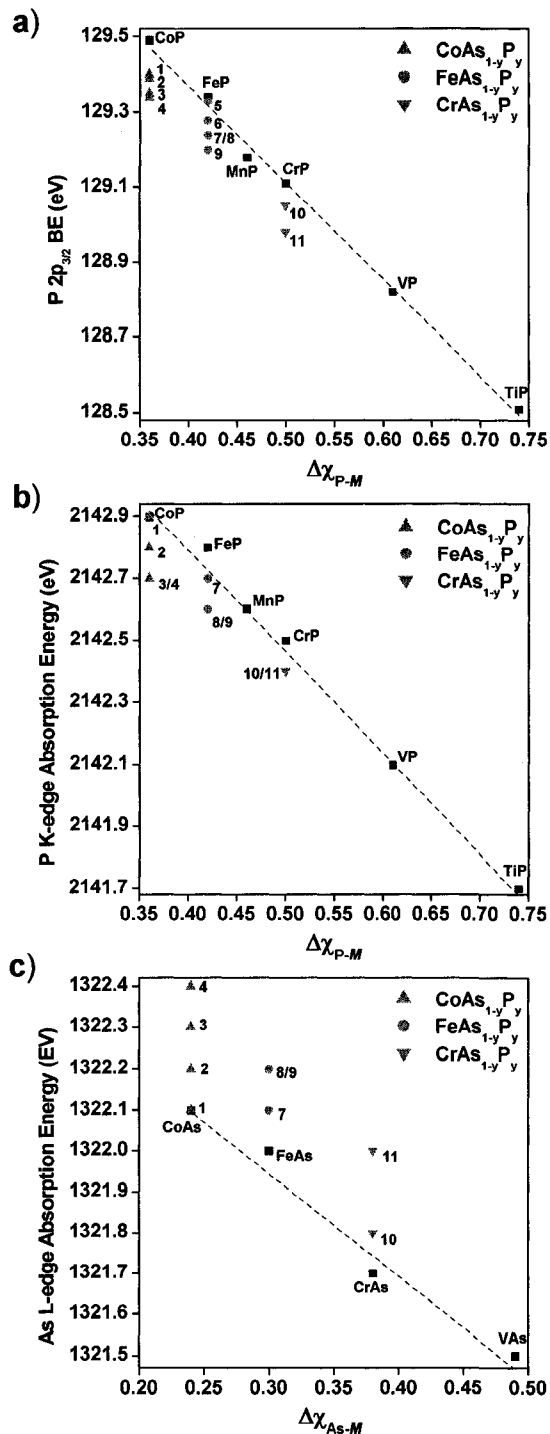


Figure 5-3 Dependence of (a) P 2p_{3/2} BE, (b) P K-edge absorption energy, and (c) As L₃-edge absorption energy on the electronegativity difference ($\Delta\chi = \chi_{Pn} - \chi_M$) for binary pnictides MP or MAs (■) and ternary mixed pnictides CoAs_{1-y}P_y (▲) (1 = CoAs_{0.75}P_{0.25}, 2 = CoAs_{0.50}P_{0.50}, 3 = CoAs_{0.25}P_{0.75}, 4 = CoAs_{0.10}P_{0.90}), FeAs_{1-y}P_y (●) (5 = FeAs_{0.90}P_{0.10}, 6 = FeAs_{0.75}P_{0.25}, 7 = FeAs_{0.50}P_{0.50}, 8 = FeAs_{0.25}P_{0.75}, 9 = FeAs_{0.20}P_{0.90}), and CrAs_{1-y}P_y (▼) (10 = CrAs_{0.75}P_{0.25}, 11 = CrAs_{0.10}P_{0.90}).

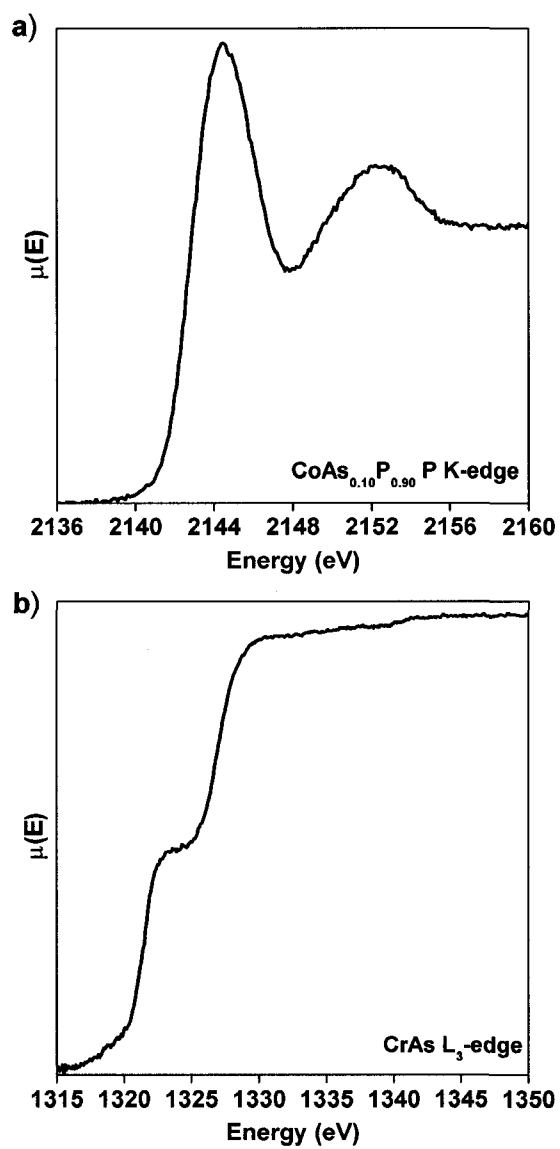


Figure 5-4 (a) P K-edge XANES spectrum for CoAs_{0.10}P_{0.90} and (b) As L₃-edge XANES spectrum for CrAs. All spectra were measured in fluorescence mode.

Figure 5-4b. Table 5-1 lists As L₃-edge absorption energies for various *MAs* and *MAs_{1-y}P_y* compounds, and Figure 5-3c shows a plot of these energies vs difference in electronegativity ($\Delta\chi = \chi_{\text{As}} - \chi_{\text{M}}$). Like the P energies in *MP* (Figure 5-3a and 5-3b), the As L₃-edge absorption energies decrease linearly in the binary arsenides *MAs* through the series from CoAs to VAs. The As L₃-edge absorption energies in the mixed pnictides *MAs_{1-y}P_y* deviate from this linear trend and, opposite to the behaviour of the P energies, they are *higher* than expected, with deviations which increase with the increase in P concentration in a given *MAs_{1-y}P_y* series. The largest deviations between the *MAs_{1-y}P_y* and *MAs* compounds are greater than the precision of the analysis (± 0.1 eV).

The As K-edge absorption spectra are more complex. Representative spectra for FeAs and some FeAs_{1-y}P_y members collected in transmission mode are shown in Figure 5-5a. On the basis of previous studies on other As-containing compounds, the low-energy white-line intensity (labeled A) is assigned to be a pre-edge peak.¹⁷³ By comparison of the spectra to the calculated conduction states (Figure 5-5b), this peak can be ascribed to a dipolar transition in which As 1s electrons are excited into bound As 4p states located below the continuum states (absorption threshold). Because As 4p states are involved in bonding, the intensity of this pre-edge peak can provide information on charge. This peak intensifies going from FeAs to FeAs_{0.10}P_{0.90}, implying that the As charge becomes less negative (more neutral) with increasing *y* (greater P concentration) in FeAs_{1-y}P_y. This trend is also observed in the CoAs_{1-y}P_y and CrAs_{1-y}P_y series. Moreover, this pre-edge peak becomes less intense through the sequence CoAs, FeAs, and CrAs, consistent with the decrease in As L₃-edge energy seen earlier in Figure 5-3c. In general, pre-edge intensities are quite sensitive to charge, as has been shown in studies

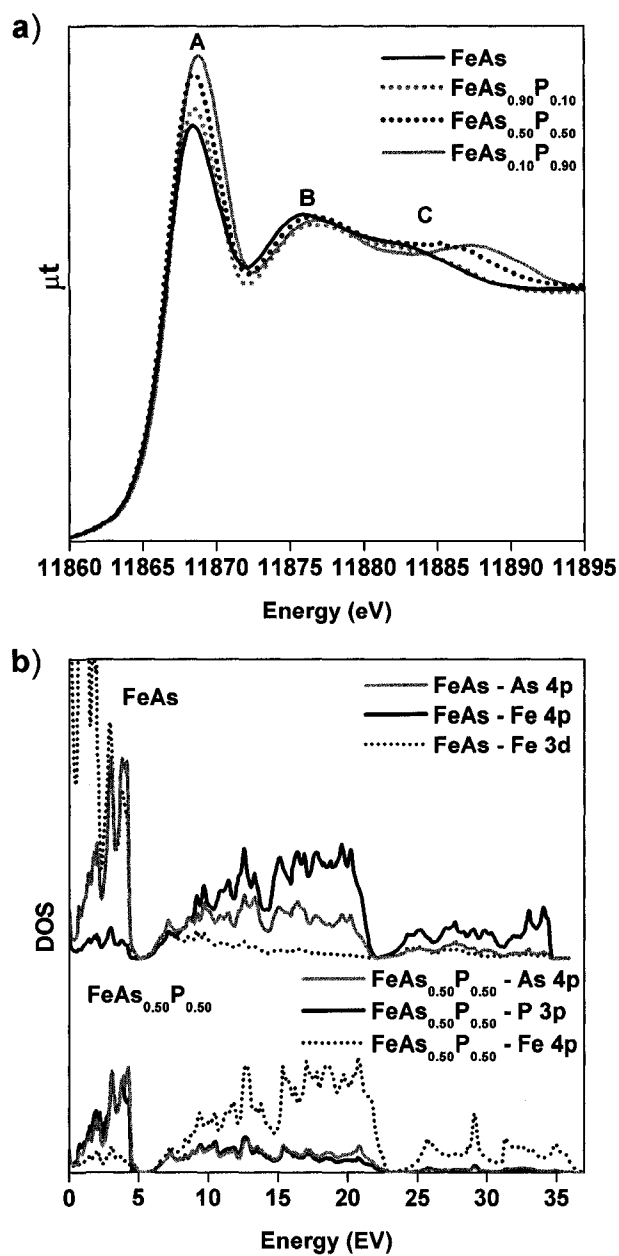


Figure 5-5 (a) Normalized As K-edge absorption spectra, collected in transmission mode, for FeAs and some FeAs_{1-y}P_y compounds. Identification of peaks A, B, and C is discussed in the text. (b) Orbital projections of the calculated conduction states of FeAs and FeAs_{0.50}P_{0.50}. The Fermi edge (E_F) is at 0 eV.

of the Au L₃-edge in a series of compounds where an increase in charge from 0 to 1+ causes the pre-edge peak to intensify by as much as ~40%.¹⁷⁴ Likewise, the As charge does not have to change much to produce substantial changes in the pre-edge peak intensity. Peak A is much less intense in *MAs* and *MAs_{1-y}P_y* (Figure 5-5a), where the As charge is near 1-, than in *As₂S₃*, where the As charge is nominally 3+.¹⁷³ (The lower energy P K-edge spectra could not be analyzed similarly because they were collected in fluorescence mode, where self-absorption effects in thick samples may appreciably affect peak intensities.¹⁷⁵)

Two higher-energy resonances (labelled B and C) are also present in Figure 5-5a. By comparison to the calculated conduction states (Figure 5-5b), they may be initially assigned as excitations from As 1s to As 4p, P 3p, or Fe 4p states. However, these peaks resemble those found in the As K-edge spectrum of *As₂S₃*, where they are attributed to EXAFS phenomena.¹⁷³ This alternative interpretation is supported by the observation that peaks B and C shift to higher energy with greater *y* in *FeAs_{1-y}P_y* (Figure 5-5a), consistent with the expectation that the energy is inverse proportional to the scattering path length⁹⁸ and that the average Fe-*Pn* bond distance shortens as the P concentration increases. The presence of a strong pre-edge peak (A) and intense EXAFS peaks (B and C) makes it difficult to track variations in the threshold energy, which is buried beneath these features. Nevertheless, there does appear to be a trend in the As K-edge energies (Table 5-1). Similar to the As L₃-edge absorption energies, the As K-edge energies decrease going from *CoAs* to *CrAs*. The absorption energies for the *MAs_{1-y}P_y* compounds are, in general, higher than those observed for *MAs* and increase with increasing *y*. For example, in the *FeAs_{1-y}P_y* series, the As K-edge absorption energies are

11866.6 eV for FeAs to FeAs_{0.50}P_{0.50}, and increase to 11866.8 eV for FeAs_{0.25}P_{0.75} and to 11866.9 eV for FeAs_{0.10}P_{0.90}. This agrees well with the trend in As L₃-edge energies (Figure 5-3c, Table 5-1).

5.3.4 *M* 2p XPS Spectra

Figure 5-6 shows *M* 2p XPS spectra for a representative member of each *M*As_{1-y}P_y (*M* = Cr, Fe, Co) series and for the parent binary pnictides *MP* and *MAs*. Table 5-1 lists the *M* 2p_{3/2} BEs. All spectra exhibit an asymmetric lineshape, which is characteristic of an itinerant electronic structure, first described by Doniach and Šunjić¹¹⁷ and discussed in Chapter 3 (Section 3.3.2). As in the binary and mixed-metal phosphides *MP* and *M*_{1-x}*M'*_xP investigated previously, this lineshape originates from the electronic delocalization associated with the metal-metal bonding network found in the MnP-type structure also adopted by *MAs* and *MAs*_{1-y}P_y.

Through the series from *MP* to *MAs*, the *M* 2p_{3/2} BE decreases slightly for *M* = Fe and Co, but hardly changes for *M* = Cr (Figure 5-6 and Table 5-1), when the precision of $\sim\pm 0.10$ eV is taken into consideration. The smaller BE in the metal arsenides *MAs* is consistent with the less positive *M* charge resulting from the presence of less electronegative As atoms and more covalent *M*-As bonds. The absence of a shift on going from CrP to CrAs probably reflects the diminishing magnitude of the relative electronegativity differences as *M* becomes less electronegative (cf., $\Delta\chi_{\text{Cr-P}}/\Delta\chi_{\text{Cr-As}} = 1.3$ vs. $\Delta\chi_{\text{Co-P}}/\Delta\chi_{\text{Co-As}} = 1.5$).¹¹⁴

The Co 2p_{3/2} spectra also exhibit a high BE satellite (Figure 5-6c), which was attributed to plasmon loss in Chapters 3 and 4, in which the kinetic energy of the photoelectron is reduced because of oscillations of bound valence electrons, leading to an

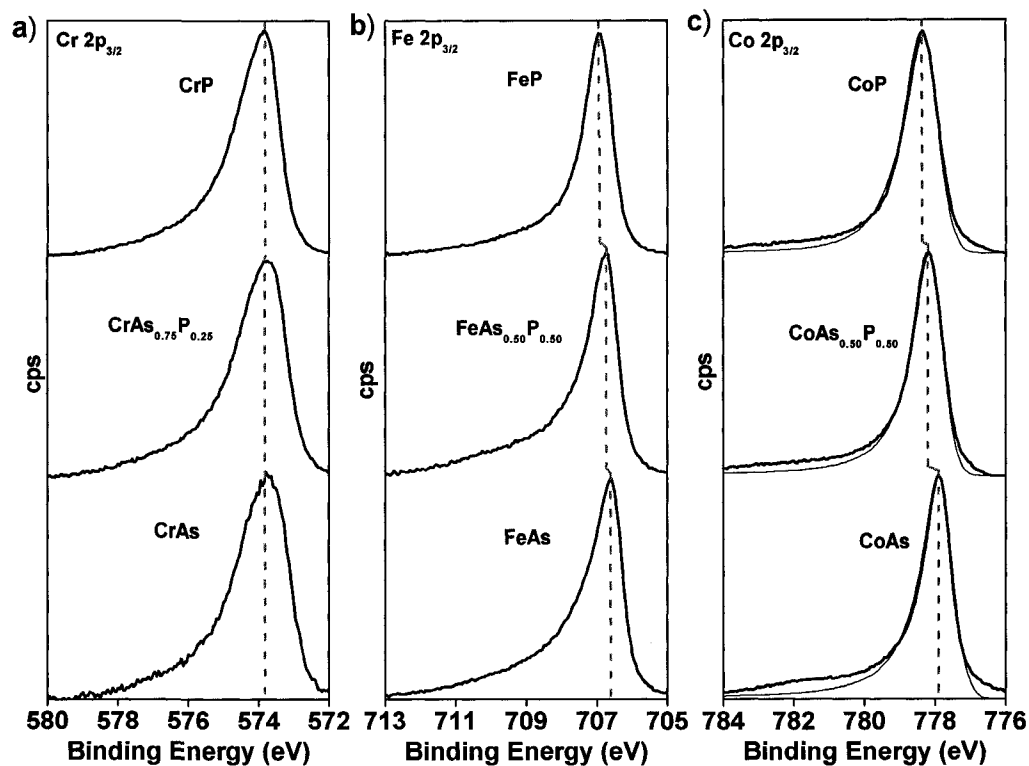


Figure 5-6 Representative metal $2p_{3/2}$ XPS spectra for (a) $\text{CrAs}_{1-y}\text{P}_y$, (b) $\text{FeAs}_{1-y}\text{P}_y$, and (c) $\text{CoAs}_{1-y}\text{P}_y$, compared to the parent binary phosphides and arsenides. The Co $2p_{3/2}$ spectra were fitted with an asymmetric peak (thin solid line), revealing the superimposed high-binding energy satellite peak. The $2p_{3/2}$ BEs, which are listed in Table 5-1, are marked by vertical dashed lines.

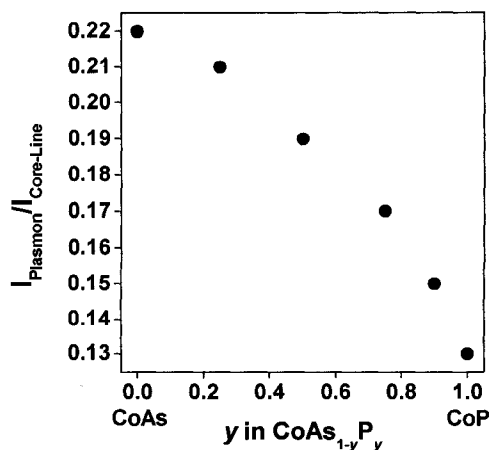


Figure 5-7 Plot showing the variation in the normalized plasmon intensity vs y in the Co $2p$ spectra for $\text{CoAs}_{1-y}\text{P}_y$.

apparent increase in BE.¹¹¹ This interpretation has been corroborated by identifying the occurrence of the same phenomenon in most of the first-row transition metals (Sc–Ni).^{127, 163-166} Note that no such plasmon loss peak is observed in the Fe or Cr 2p_{3/2} spectra, likely because it is overlapped by the much more intense core line. The plasmon loss peak weakens as Co becomes more positively charged, as seen in the Co 2p_{3/2} spectra for the series Co^{x+}P_x ($x = 0, 1, 3$) (see Chapter 7, Section 7.3.3). The plasmon loss peak may also become less intense as the number of spin-unpaired electrons decreases, as observed in the 1s XPS spectra of Sc–Co measured with a Cu K α X-ray source.¹⁶⁶ Figure 5-7 shows a plot of the Co 2p_{3/2} plasmon loss intensity (normalized to the core-line intensity) vs. y for the CoAs_{1-y}P_y series. As the P concentration (y) increases, the intensity of the plasmon loss peak diminishes, implying that Co becomes more positively charged as we progress from CoAs to CoP.

5.3.5 *M* L- and K-edge XANES Spectra

Further insight on the charges of *M* atoms in *M*As_{1-y}P_y can be provided by the *M* L- and K-edge XANES spectra. In the L-edge spectra, *M* 2p electrons are promoted into unoccupied *M* 3d and possibly *M* 4s states, so the intensity of the L₃ and L₂ peaks reveals information about the *M* charge. Figure 5-8 shows normalized Fe L-edge spectra for representative members of the FeAs_{1-y}P_y series. The two resolved L₃ peaks can be assigned to the 3d t_{2g} and e_g states of the Fe atoms, which are surrounded by pnictogen atoms in a distorted octahedral coordination. The L₂ peak is not resolved into distinct t_{2g} and e_g states because of spectral broadening resulting from a decreased lifetime of the final state. Both L₃ and L₂ peaks are more intense in FeAs_{0.10}P_{0.90} and FeAs_{0.50}P_{0.50} than in FeAs; in particular, the e_g portion of the L₃ peak is considerably enhanced in

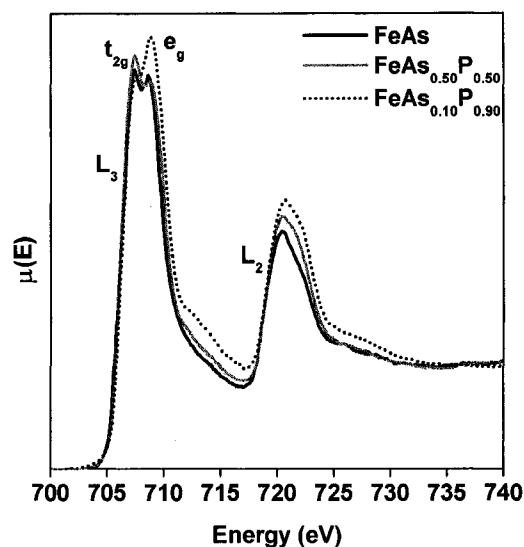


Figure 5-8 Normalized total electron yield Fe $L_{2,3}$ -edge XANES spectra for FeAs and some $\text{FeAs}_{1-y}\text{P}_y$ compounds. The small shoulders observed just above the L_3 and L_2 edges in the $\text{FeAs}_{0.10}\text{P}_{0.90}$ spectrum probably arise from some surface oxide formed.

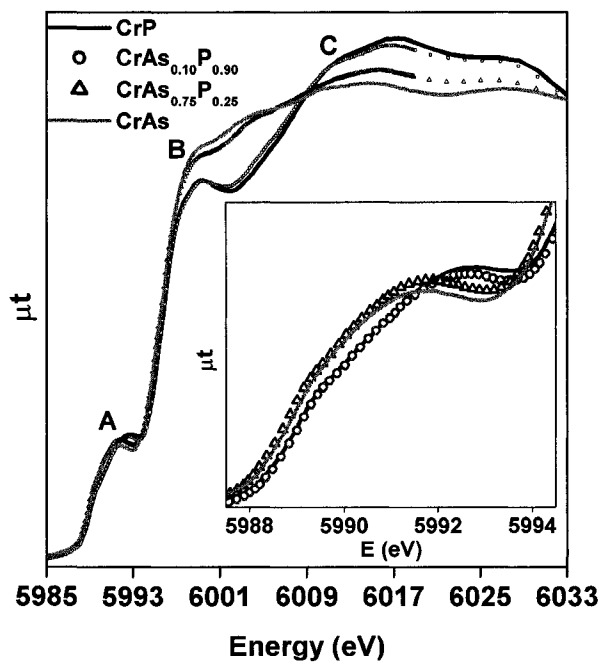


Figure 5-9 Normalized Cr K-edge XANES spectra, collected in transmission mode, for $\text{CrAs}_{1-y}\text{P}_y$. Peak A primarily represents a pre-edge Cr $1s \rightarrow \text{Cr } 3d$ transition. Based on comparison to the calculated conduction states of FeAs and $\text{FeAs}_{0.50}\text{P}_{0.50}$ (Figure 5-5b), peak B may represent a Cr $1s \rightarrow Pn np$ transition whereas peak C may represent a Cr $1s \rightarrow \text{Cr } 4p$ transition or an EXAFS feature (see text). The inset highlights the differences in pre-edge peak intensity among the four compounds.

$\text{FeAs}_{0.10}\text{P}_{0.90}$. These intensity changes imply that the 3d states are depopulated and thus the Fe charge becomes more positive as y increases in $\text{FeAs}_{1-y}\text{P}_y$. Similar results were obtained for the $\text{CoAs}_{1-y}\text{P}_y$ series, whereas difficulties in normalizing the spectra made such an analysis impossible for the $\text{CrAs}_{1-y}\text{P}_y$ series.

Cr K-edge spectra for the $\text{CrAs}_{1-y}\text{P}_y$ series (including the end-members CrP and CrAs) are shown in Figure 5-9. The lineshape for the spectrum of CrP is very similar to that observed in the Mn K-edge spectrum of MnP presented in Figure 4-6 (Chapter 4) and elsewhere.¹⁶⁷ The spectra contain three main excitations, labeled A, B, and C. Peak A is a pre-edge peak in which Cr 1s electrons are primarily excited into unoccupied Cr 3d states, or possibly also into Cr 4p and $Pn\ np$ states, from inspection of the calculated conduction states for CrAs, which resemble those for FeAs (Figure 5-5b). These states overlap near the Fermi edge because the distorted octahedral coordination around Cr atoms entails some participation of Cr 4p orbitals in bonding.³³ Peak A (Cr 1s \rightarrow Cr 3d) is a quadrupolar transition and therefore it is much weaker than peaks B (Cr 1s $\rightarrow Pn\ np$) and C (Cr 1s \rightarrow Cr 4p), which are dipolar transitions. Similar transitions have been identified in the Mn K-edge spectrum of MnP.¹⁶⁷ As in the argument pertaining to the M L-edge spectra above, the intensity of the pre-edge peak here reveals information about the M charge (when the coordination environment of M is fixed). The pre-edge peak intensifies on proceeding from CrAs, through $\text{CrAs}_{1-y}\text{P}_y$, to CrP (inset of Figure 5-9), indicating that the 3d states are gradually depopulated and the Cr charge becomes more positive as y increases in $\text{CrAs}_{1-y}\text{P}_y$. Also apparent from Figure 5-9, the Cr K-edges gradually shift to higher energy as we progress from CrAs to CrP, consistent with an increase in Cr charge. Although the energy shift of peak C (which affects the apparent

intensity of peak B) may be traced to the increase in energy of the M 4p states on going from MAs through $MAs_{1-y}P_y$ (Figure 5-5b), it can also be explained by a shift of the EXAFS, as proposed in the discussion of the As K-edge spectra (Section 5.3.3). Analysis of the $FeAs_{1-y}P_y$ and $CoAs_{1-y}P_y$ K-edge spectra gave similar conclusions to those above.

5.4 Discussion

5.4.1 Shifts in P $2p_{3/2}$ BEs and P K-edge Absorption Energies

The trend in P $2p_{3/2}$ BE within a given $MAs_{1-y}P_y$ series is unusual: the BE gradually decreases as the $MAs_{1-y}P_y$ series becomes more phosphorus rich (higher y) but the BE abruptly increases when the end-member binary phosphide MP itself is reached (Table 5-1 and Figure 5-3a). Relaxation effects may be considered first. Previous investigations in gas-phase molecules have shown that, as long as the coordination geometry is retained, substitution of more *electropositive* atoms in the coordination environment enhances relaxation towards the nucleus of the central atom under study, lowering its BE.¹⁵⁹ In the $MAs_{1-y}P_y$ series, a central P atom is surrounded by M atoms in the first coordination sphere and pnictogen (P or As) atoms in the second coordination sphere. Substitution of more *electronegative* P atoms in the coordination environment lowers the BE of the central P atom, opposite to expectations and an observation that rules out significant relaxation effects. Moreover, the trend in P K-edge absorption energies (Figure 5-3b) is consistent with the trend shown by phosphorus BEs. Absorption energies are less influenced by relaxation effects than are BEs, because of the greater screening that is maintained in the absorption process. An estimate of the ability of electrons to screen the nuclear charge can be made from the values of Z_{eff} which can be calculated with Slater's rules.¹⁷⁶ A neutral P atom yields a Z_{eff} value of 4.45, a

photoionized P atom with a 1s core-hole (i.e., P^{1+}) has a value of 5.45, and for the photoabsorption process, which can be modelled by promotion of a 1s electron into an empty 3p orbital (P^*), a value of 5.10 is determined.¹⁷⁶ The nuclear charge is thus better screened in P^* than in P^{1+} , implying that relaxation of electrons towards the nucleus will be less important in the absorption process compared to the photoemission process. The trends in P BEs and absorption energies (Figures 5-3a and 5-3b) are thus attributed to ground state effects as described by the charge potential model (Eq 5-1). Because these energy shifts are close to the limit of precision of the measurements, we offer only a qualitative analysis below.

The charges on M and As that are formed within a given $MAs_{1-y}P_y$ series can be deduced. As y increases, the As atoms become less negatively charged (from As K-edge spectra (Section 5.3.3)), not only because they give up electron density to the more electronegative P atoms via the weak $Pn-Pn$ bonding network, but also because they are less capable than the P atoms in competing for electron density donated by the M atoms. As y increases, the M atoms also become more positively charged (as derived from Co plasmon loss peak intensities (Section 5.3.4) and Fe $L_{2,3}$ -edge and Cr K-edge spectra (Section 5.3.5)), because the $M-Pn$ bond becomes more ionic, on average. Applying the constraints that (i) the average Pn charge balances the M charge in $MAs_{1-y}P_y$ (i.e., a concentration factor must be included) and (ii) the P charge in MP is more negative than the As charge in MAs , in agreement with relative electronegativities, we can deduce that the P atoms become less negatively charged as y increases in $MAs_{1-y}P_y$ (Figure 5-10). A physical interpretation of this trend is that as P atoms gradually substitute for As atoms in a $MAs_{1-y}P_y$ series, the required total negative charge can be distributed over a greater

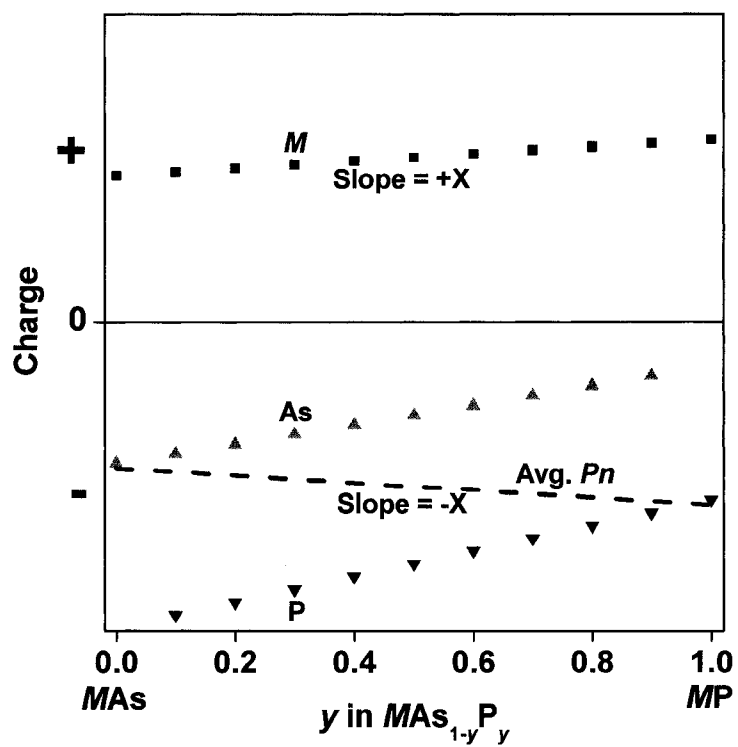


Figure 5-10 Schematic representation of the dependence of M (■) and Pn (P , ▼; As , ▲) charges on y in $MA_{s_{1-y}}P_y$. The average Pn charge ($q_{Pn} = yq_P + (1-y)q_{As}$), represented by the dashed line, balances the M charge in $MA_{s_{1-y}}P_y$.

number of the more electronegative P atoms, such that each P atom, on average, does not need to carry as high a negative charge.

According to Eq 5-1, the P $2p_{3/2}$ BEs and P K-edge absorption energies should both increase with increasing proportion of P atoms as we proceed from $MAs_{1-y}P_y$ ($y < 1$) to MP , because q_i becomes less negative (in $k\Delta q_i$) and the Madelung potential ($\Delta \sum_{j \neq i} q_j / r_{ij}$) becomes more positive, if only the first coordination shell containing the M atoms is considered. For very P-rich members (high y), however, the second coordination shell now contains many P atoms, which provide better screening to the photoemission or absorption site than the As atoms because they are more electronegative (more negative q_j values) and they are closer (smaller r_{ij} distances). Thus, next-nearest neighbour (interatomic) effects can become quite important in overcoming and reversing trends controlled by the atomic charge alone. In this present series, the P 2p BE and P K-edge absorption energy actually become lower as y increases in $MAs_{1-y}P_y$ ($0 < y < 1$), with an abrupt increase in the P 2p BE and K-edge absorption energy being observed for the pure MP end-member. This jump can be related to the reduced screening of the P photoemission or absorption site provided by the less negatively charged P atoms and the more positively charged M atoms present in the pure end members compared to the values found in the mixed $MAs_{1-y}P_y$ series.

5.4.2 Shifts in As L_{3-} and K-edge Absorption Energies

In the binary arsenides MAs , the As L_{3-} and K-edge absorption energies decrease as the difference in electronegativity ($\Delta\chi = \chi_{As} - \chi_M$) increases, consistent with the development of more negatively charged As atoms as the M -As bond becomes more ionic and consistent with a more negative $k\Delta q_i$ term in Eq 5-1. This trend is confirmed

by the attenuation of the pre-edge peak in the As K-edge spectra through the series from CoAs to CrAs (Section 5.3.3).

In the mixed pnictides $MAs_{1-y}P_y$, the As L_{3-} and K-edge absorption energies increase with y , opposite to the trend shown by the P energies. This occurs not only because the As atoms become less negatively charged (less negative $k\Delta q_i$ term), but also because the M atoms in the first coordination shell become more positively charged (more positive $\Delta\Sigma_{j\neq i} q_j/r_{ij}$ term). The next-nearest neighbour effects associated with the Pn atoms in the second coordination shell will not be as important because they are further away from the larger As atom.

5.5 Conclusions

Binary phosphides (MP) and arsenides (MAs) show a linear decrease in the P or As BEs and absorption energies with greater differences in electronegativity ($\Delta\chi = \chi_{Pn} - \chi_M$) because the pnictogen atoms become more negatively charged as the ionic character in the $M-Pn$ bond increases. However, mixed arsenide phosphides $MAs_{1-y}P_y$ with the MnP-type structure do not show this behaviour. As y increases, the P $2p_{3/2}$ XPS BEs and P K-edge absorption energies decrease and are always lower than those for the binary phosphides MP , whereas the As L_{3-} and K-edge absorption energies increase and are always higher than those for the binary arsenides MAs . These trends can be rationalized within the charge potential model, taking into consideration the contribution of next-nearest neighbour effects arising from the presence of a $Pn-Pn$ bonding network and the competition between the two different anions for electron density from the more electropositive M atoms. These effects can be related to the electronegativity difference

between P and As ($\chi_P = 2.06 > \chi_{As} = 1.94$) which was deduced here from analysis of the Co $2p_{3/2}$ BE shifts in the $CoPn_3$ ($Pn = P, As, Sb$) series.

With increasing y , the As atoms become less negatively charged in $MAs_{1-y}P_y$ than in MAs , consistent with an observed increase in the As L_{3-} and K-edge absorption energy. The P atoms are more negatively charged in $MAs_{1-y}P_y$ than in MP , consistent with observed decreases in the P $2p_{3/2}$ BE and P K-edge absorption energy. Lastly, the M atoms become more positively charged with increasing y in $MAs_{1-y}P_y$, consistent with the Co $2p$ XPS spectra and the M L_{-} and K-edge absorption spectra. Importantly, the metal atoms in the first coordination shell and the pnictogen atoms in the second coordination shell modify the Madelung potential operating on the pnictogen centres and thus affect their BE and absorption energies (particularly for P) indicating the importance of both near and next-nearest neighbour effects on these energies. The variation of the M , As, and P charges in the $MAs_{1-y}P_y$ series reflects a considerable tunability in the electronic structure of MnP-type compounds, which could prove useful in catalytic applications. This last statement can also be extended to the mixed-metal phosphides, $M_{1-x}M'_xP$, examined in Chapter 4.

Chapter 6

X-ray Photoelectron Spectroscopy Study of Rare-Earth Filled Transition-metal Phosphide Skutterudites $\text{LaFe}_4\text{P}_{12}$ and $\text{CeFe}_4\text{P}_{12}$ *

6.1 Introduction

In the previous chapters (3-5), the charges and bonding environment of binary and pseudo-binary transition-metal pnictides containing strong metal-metal bonds and weak *Pn-Pn* bonds were investigated by use of X-ray spectroscopy. Here, we extend this analysis to rare-earth containing transition-metal phosphides having the skutterudite structure which contains strong P-P bonds but no metal-metal bonds. Using XPS, this examination allows for a comparison of not only the binding energies but also the lineshapes, particularly for the metal atoms, between systems containing different degrees of homoatomic bonding.

The ternary rare-earth transition-metal pnictides $RE M_4 P n_{12}$ ($RE = \text{La, Ce, Pr, Nd, Sm, Eu, Gd, Tb, Yb}$; $M = \text{Fe, Ru, Os}$; $P n = \text{P, As, Sb}$),⁶ especially the antimonide members, have received considerable attention because of their potential as thermoelectric materials at high temperatures.²⁰ Their cubic structure is based on that of the parent mineral CoAs_3 , called skutterudite,⁴¹ which was described in Chapter 1 (Section 1.4.2). The crystal structure consists of a network of corner-sharing transition-metal-centred octahedra, which undergo a tilting distortion to form nearly square $P n_4$

*A version of this chapter has been published. Reproduced with permission from Grosvenor, A. P.; Cavell, R. G.; Mar, A. *Chem. Mater.* **2006**, *18*, 1650-1657. Copyright (2006) by the American Chemical Society.

rings and large voids in the form of dodecahedral cages that are filled by *RE* atoms in the ternary variants (Figure 1-9). As the displacement parameters of the *RE* atoms within these dodecahedral cages of pnictogen atoms are unusually large,⁴⁶ it has become fashionable to attribute the improved thermoelectric properties of these antimonides to a propitious combination of poor thermal conductivity (created by the “rattling” of the *RE* atoms, which scatters lattice vibrations) and good electrical conductivity -- a model known as a “phonon-glass electron-crystal”.¹⁷⁷ A detailed understanding of the electronic structure of these skutterudites is thus important for further development of these materials.

Although many experimental and theoretical studies have now been conducted on both the binary and ternary skutterudites, certain features of their electronic structure are still controversial. Some assertions derived from theoretical calculations^{45, 48-53} remain unconfirmed by experiment. In particular, there is conflicting evidence with regard to the valence state of specific atoms in these compounds. Although charge transfer is expected to be small in any of the rare-earth filled skutterudites, it will be most pronounced in the phosphides where electronegativity differences are the greatest and ambiguities in valence states are thereby more readily resolved.

To describe the bonding found in the *RE* containing skutterudites, a simple electron counting analysis can be performed for the binary skutterudite, CoP_3 . As was described in Chapter 1 (Section 1.4.2), by application of the Zintl concept, an assignment of low-spin $\text{Co}^{3+} (t_{2g}^6 e_g^0)$ can be made with the P charges being 1- which can be accommodated by forming P_4 rings with each P atom engaged in two $2c-2e^-$ P-P bonds. The band structure of this compound is considered to involve metal 3d, 4s, and 4p orbitals and

phosphorus 3s and 3p orbitals. The electronic structure consists of bands of filled M -P bonding and metal-based t_{2g} states at lower energy, and empty metal-based e_g and M -P antibonding states at higher energy.⁴⁵ These states are overlapped by bands of filled P-P bonding and empty P-P antibonding states.⁴⁵

In ternary skutterudites such as $\text{LaFe}_4\text{P}_{12}$, the rare-earth atoms can be considered to donate all of their valence electrons to the rest of the framework, thus creating $\text{La}^{3+}[\text{Fe}_4\text{P}_{12}]^{3-}$. If a P^{1-} state is assumed in analogy with the binary skutterudites, then the resultant average valence state of $\text{Fe}^{2.25+}$ implies that $\text{LaFe}_4\text{P}_{12}$ contains a partly filled t_{2g} band, with perhaps a single hole localized on one of the Fe atoms (i.e., three Fe^{2+} ($t_{2g}^6 e_g^0$) and one Fe^{3+} ($t_{2g}^5 e_g^0$) per $[\text{Fe}_4\text{P}_{12}]^{3-}$ unit).^{6, 45} Resistivity measurements confirm that $\text{LaFe}_4\text{P}_{12}$ behaves as a hole-doped metal that becomes superconducting below 4.1 K.^{178, 179} However, magnetic measurements and Mössbauer spectra show that only low-spin Fe^{2+} is present.¹⁸⁰⁻¹⁸² Band structure calculations suggest that the iron and phosphorus valence states may be closer to Fe^{2+} and $\text{P}^{11/12-}$, thereby implying that the hole is associated with one out of twelve P atoms.⁴⁵ The hole may reside in P-P nonbonding orbitals located close to the Fermi level (E_F).

$\text{CeFe}_4\text{P}_{12}$ was originally thought to contain tetravalent cerium (Ce^{4+} , $4f^0$), given the pronounced deviation of its cell parameter from the expected trend arising from the lanthanide contraction compared to other $RE\text{Fe}_4\text{P}_{12}$ members.³⁹ According to the assignment $\text{Ce}^{4+}[\text{Fe}_4\text{P}_{12}]^{4-}$, the $[\text{Fe}_4\text{P}_{12}]^{4-}$ (or $[\text{FeP}_3]^{1-}$) framework is isoelectronic with CoP_3 and should thus lead to similar material properties. Although electrical measurements confirm that $\text{CeFe}_4\text{P}_{12}$ is a small band gap semiconductor and magnetic measurements reveal a low magnetic susceptibility,¹⁸³ density functional calculations

argue for a trivalent state for cerium (Ce^{3+} , $4f^1$) and indicate that the energy gap really arises because of the important contribution of rare-earth 4f orbitals to bonding states near the Fermi level.⁵³ XANES supports the assignment of trivalent Ce.^{184, 185}

In this chapter, an experimental analysis of the electronic structure of the ternary phosphides $\text{LaFe}_4\text{P}_{12}$ and $\text{CeFe}_4\text{P}_{12}$ is presented using X-ray photoelectron spectroscopy (XPS) to access the valence states of all atoms during the same experiment. The RE, Fe, and P core-line spectra have been measured and interpreted in relation to the spectra of model compounds. The fitted valence band spectra of $\text{LaFe}_4\text{P}_{12}$ and $\text{CeFe}_4\text{P}_{12}$ are presented and compared to calculated band structures, which has permitted a detailed discussion of the bonding in these compounds, including the identification of Ce $4f^1$ states near the Fermi level.

6.2 Experimental

6.2.1 Synthesis

In accordance with previously reported methodology,¹⁸⁰ samples of $\text{LaFe}_4\text{P}_{12}$ and $\text{CeFe}_4\text{P}_{12}$ were prepared by direct reaction of the elements with excess red P and use of a Sn flux in sealed and evacuated fused-silica tubes (La, 99.9%, Alfa-Aesar; Ce, 99.9%, Cerac; Fe, 99.9%, Cerac; P, 99.995%, Cerac; Sn, 99.8%, Cerac). The La, Ce:Fe:P:Sn molar ratio was 1:4:20:50. The tubes were heated to 1223 K over 30 h, cooled to 1073 K over 10 h and held at this temperature for 1 week before being cooled to room temperature over 2 d. Once the reactions were complete, the product was carefully treated with dilute HCl (1:1) to remove the Sn flux as well as excess P and any binary phosphides or oxides that had formed. (*Caution:* some excess P may be transformed to the white allotrope, which is pyrophoric.) This treatment did not appear to decompose

the ternary phosphides, which are dark grey, polycrystalline (individual crystals were 0.05 – 0.10 mm in size), and air-stable. Powder X-ray diffraction (XRD) patterns, obtained on an Inel diffractometer equipped with a CPS 120 detector, confirmed that the samples consisted of the desired ternary phosphides, with trace amounts of elemental phosphorus.

6.2.2 XPS Analysis

All measurements were performed on a Kratos AXIS 165 spectrometer with a monochromatic Al K α X-ray source operating with a base pressure in the analytical chamber of 10^{-6} – 10^{-7} Pa. The resolution function of this instrument has been determined to be 0.4 eV based on analysis of the Co Fermi edge and the precision of the binding energies is estimated to be ± 0.1 eV.

Samples of LaFe₄P₁₂ and CeFe₄P₁₂ were ground and pressed onto C tape before being loaded into the instrument. Both samples were sputter-cleaned for nearly an hour with an Ar⁺ ion beam (4 kV, 10 mA) to remove surface contaminants (Sn, C, O, etc.). High-resolution spectra (La, Ce 3d; Fe 2p; P 2p; valence band) were then collected with energy envelopes ranging from 60 to 20 eV, a step size of 0.05 eV, a pass energy of 20 eV, a sweep time of 180 s and an analysis spot size of 700 \times 400 μ m. Since these compounds are electrically conducting, charge neutralization was not required during the spectroscopic measurements and charge correction was not applied in the data analysis. All results were analysed with use of the CasaXPS software package.¹¹⁰ To fit these high-resolution spectra, a Shirley-type function was used to remove the background, which arises largely from inelastic electron scattering. The extracted spectra were then

fitted with a combined Gaussian (70%) and Lorentzian (30%) line profile to account for spectrometer and life-time broadening, respectively.

To clarify the cerium valence state in $\text{CeFe}_4\text{P}_{12}$, several model compounds were also examined. The *RE* 3d and valence band spectra of CeF_3 (99.9%, Alfa-Aesar), CeF_4 (99.9%, Aldrich), LaP (prepared by direct reaction of the elements at 700 °C for 2 d, and sample purity confirmed by XRD), and LaF_3 (99.99%, Aldrich) were collected with similar parameters as above. Since these compounds are insulating, they were pressed into In foil to increase conductivity and were transported to the spectrometer under Ar to reduce reaction with the environment. The charge neutralizer was used (current = 1.7 A, charge balance = 1.8 V) during collection and the spectra were charge-corrected during data analysis by setting the adventitious C 1s binding energy to 284.8 eV.

6.2.3 Band Structure Calculations

Although several theoretical calculations have been previously performed on skutterudite-type compounds,^{45, 48-53} it was desirable to extract partial density of states profiles for the metal and phosphorus valence states to illustrate the fitting of the experimental valence band spectra. We reproduce a tight-binding extended Hückel band structure calculation on the $[\text{Fe}_4\text{P}_{12}]^{3-}$ substructure of $\text{LaFe}_4\text{P}_{12}$,⁴⁵ with the same parameters and 125 *k* points in the irreducible portion of the Brillouin zone, but showing the projections of the Fe and P orbital contributions over a wider energy window to draw an explicit comparison to the experimental valence band spectrum.

6.3 Results and Discussion

6.3.1 High-Resolution P 2p Spectra

Figure 6-1 shows the P 2p spectra of $\text{LaFe}_4\text{P}_{12}$ and $\text{CeFe}_4\text{P}_{12}$. Both spectra reveal P $2p_{3/2}$ binding energies (BE) of 129.3 eV, which is identical to that found in FeP and presented in Chapter 3, where a charge of -1.0 on the phosphorus atom was established through comparison with other Fe- and P-containing compounds with well-defined oxidation states. Homoatomic phosphorus-bonded units are present in the form of P_4 rings in $\text{REFe}_4\text{P}_{12}$ and zigzag chains in FeP, but whereas the P–P distances in $\text{LaFe}_4\text{P}_{12}$ ($2.288(2)$ – $2.356(2)$ Å)¹ are similar to a typical single P–P covalent bond length of 2.2 Å,³⁷ they are somewhat longer in FeP ($2.643(4)$ Å).³⁴ Nevertheless, it appears that in both cases, the prediction of a formal P^{1-} charge on the phosphorus atoms bound to two P neighbours, from a simple electron-counting scheme in which $2c-2e^-$ P–P bonds are assumed, is in good agreement with the charges extracted from the binding energies. Instead of P^{1-} , an alternative assignment of $\text{P}^{11/12-}$ has also been suggested,⁴⁵ but of course these charges are so similar that they cannot be distinguished by examining binding energies alone. Moreover, because the bonding is probably delocalized within the P_4 rings, it is perhaps more accurate to represent the charges as P_4^{4-} . As anticipated from the XRD pattern, the spectrum also shows the presence of unreacted elemental phosphorus, with a $2p_{3/2}$ binding energy of ~ 130.3 eV.

These results can be compared with those obtained from XPS studies of the binary skutterudite CoSb_3 presented in Chapter 7 and elsewhere.⁸⁰ The difference between the P $2p_{3/2}$ binding energy in $\text{REFe}_4\text{P}_{12}$ and in elemental P is substantially greater ($\Delta\text{BE} = \sim 1.0$ eV) than that between the Sb $3d_{5/2,3/2}$ binding energy in CoSb_3 and in

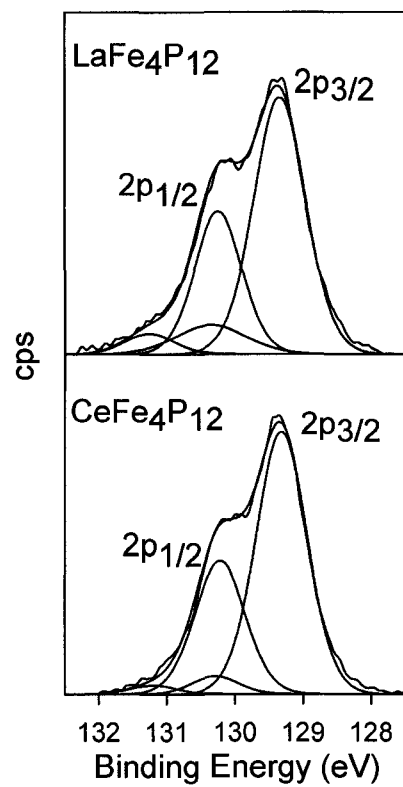


Figure 6-1 High-resolution P 2p XPS spectra of $\text{LaFe}_4\text{P}_{12}$ and $\text{CeFe}_4\text{P}_{12}$.

elemental Sb ($\Delta BE = 0.1\text{-}0.2$ eV). This observation can be attributed to the diminished electronegativity differences as phosphorus is replaced with antimony, and is consistent with the trend towards less ionic character in the Co–Sb bond compared to the Fe–P bond.

6.3.2 High-Resolution Fe 2p Spectra

The Fe 2p spectra of $\text{LaFe}_4\text{P}_{12}$ and $\text{CeFe}_4\text{P}_{12}$ are presented in Figure 6-2. In both spectra the Fe $2p_{3/2}$ signal appears as a single core line with asymmetric lineshapes skewed to higher binding energy. As indicated earlier, assignments of $\text{Fe}^{2.25+}$ or Fe^{2+} have been proposed from electron-counting schemes.^{6, 45} The assignment of $\text{Fe}^{2.25+}$ corresponds to mixed valency, with Fe^{2+} and Fe^{3+} present in the ratio 3:1, which should be manifested as two distinct Fe 2p signals with intensities in that same ratio. During a previous XPS study of the reduction of $\text{K}_3\text{Fe}(\text{CN})_6$, the $2p_{3/2}$ binding energy of low-spin Fe^{3+} was observed to be noticeably higher than that of low-spin Fe^{2+} .¹⁸⁶ When the compound was heavily reduced, so that only a small amount of Fe^{3+} remained, the $2p_{3/2}$ spectrum appeared to broaden with an apparent asymmetric tail to higher binding energy, similar to the $2p_{3/2}$ feature observed in Figure 6-2. However, the $2p_{1/2}$ spectrum of the reduced ferricyanide clearly showed two peaks, which arises from the presence of two distinct Fe valence states.¹⁸⁶ In contrast, as seen in Figure 6-2, the $2p_{1/2}$ signals for $\text{LaFe}_4\text{P}_{12}$ and $\text{CeFe}_4\text{P}_{12}$ are asymmetric and appear similar to the $2p_{3/2}$ signals, leading to the conclusion that only one Fe valence state is present in these compounds. Moreover, the Fe $2p_{3/2}$ binding energy (707.2 eV) is similar to that in FeS_2 (707.0 eV), which is well-known to contain low-spin Fe^{2+} .¹⁸⁷ It should also be noted that the spectra of low-spin Fe^{2+} compounds such as those shown here do not suffer the effects of multiplet

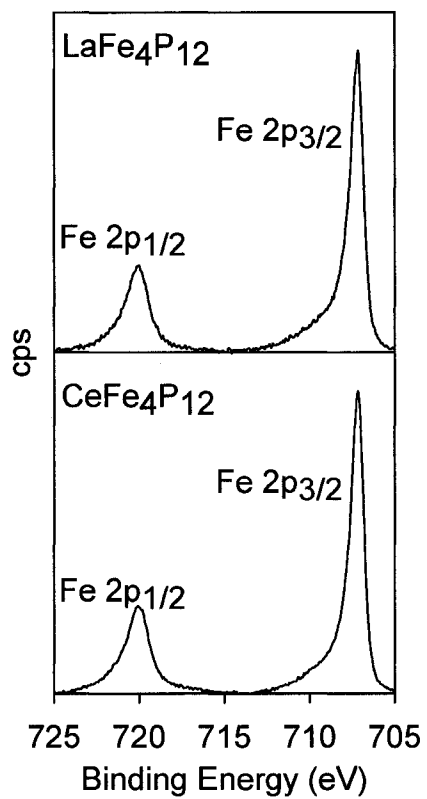


Figure 6-2 High-resolution Fe 2p XPS spectra of $\text{LaFe}_4\text{P}_{12}$ and $\text{CeFe}_4\text{P}_{12}$.

splitting, which tends to broaden the 2p spectra of high-spin Fe^{2+} compounds.⁸¹ The definitive finding of low-spin Fe^{2+} ($t_{2g}^6 e_g^0$) in $\text{LaFe}_4\text{P}_{12}$ and $\text{CeFe}_4\text{P}_{12}$ supports results obtained by Mössbauer spectroscopy.¹⁸⁰⁻¹⁸²

The origin of the asymmetric tail can be attributed to the Doniach and Šunjić processes that were described in Chapter 3. This type of lineshape arises when valence electrons, interacting with the core hole (produced after photoionization), are excited and scattered from filled states below the Fermi edge to a continuum of empty conduction states above.^{117, 118} This process is typically indicative of metal-metal bonding as is the case for the MnP-type compounds examined in Chapters 3-5, but the Fe-Fe distances exceed 3.9 Å in the skutterudite compounds discussed here. Calculations suggest that electronic conduction proceeds through bands near the Fermi level that arise from interactions between nonbonding or bonding orbitals on the P_4 rings and s,p orbitals on the transition-metal atoms.^{45, 49} The asymmetric lineshape may then perhaps reflect some delocalization of the metal electrons, which may account for the weak paramagnetism observed in these compounds.^{180, 188}

6.3.3 High-Resolution *RE* 3d Spectra

Figure 6-3 shows the *RE* 3d spectra for $\text{LaFe}_4\text{P}_{12}$ and $\text{CeFe}_4\text{P}_{12}$. Normally, as in most transition metals, the binding energy in the elemental metal is generally lower than in the oxidized species. Surprisingly, this is not the case in the *RE* spectra. For example, the $3d_{5/2}$ binding energy is 884 eV in Ce metal,^{189, 190} whereas it is 882 eV in CeCl_3 and CeO_2 .^{191, 192} This unusual behaviour may be traced to the poor screening of the nuclear charge offered by 4f electrons. Although the binding energy in *RE* spectra is not necessarily diagnostic of the valence state, the lineshape is quite characteristic of the

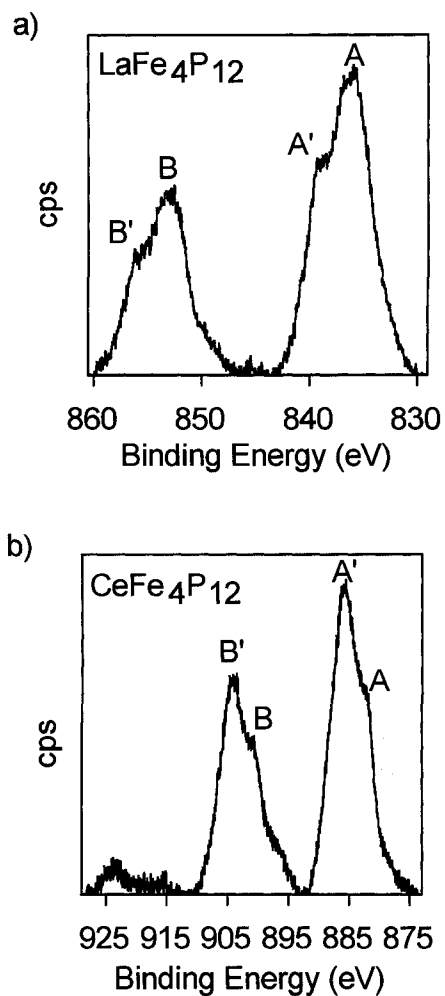


Figure 6-3 (a) High-resolution La 3d XPS spectrum of LaFe₄P₁₂ and (b) Ce 3d XPS spectrum of CeFe₄P₁₂. The 3d_{5/2} coreline is labelled *A* and the 3d_{3/2} coreline is labelled *B*. The most intense satellite peaks are labelled *A'* and *B'*.

valence state, especially for Ce compounds. The spectra of these rare-earth skutterudites can then be interpreted by making comparisons to those of model compounds.

For $\text{LaFe}_4\text{P}_{12}$, the binding energy of the La $3d_{5/2}$ core line (labelled *A* in Figure 6-3a) is 836.1 eV, similar to that in LaCl_3 (836 eV)¹⁹¹ but higher than in LaP (834.3 eV, Figure 6-4). The $3d_{5/2}$ lineshapes for all three compounds resemble each other, which leads to the unsurprising conclusion of a La^{3+} valence state. However, in addition to the core lines (labelled *A* and *B* for the $3d_{3/2}$ and $3d_{5/2}$ peaks, respectively), there are strong satellite peaks (labelled *A'* and *B'*), whose origins will be discussed below.

For $\text{CeFe}_4\text{P}_{12}$, assignments of Ce^{3+} or Ce^{4+} have been proposed.^{6, 39, 184, 185} CeF_3 and CeF_4 serve as appropriate comparisons, and their spectra are shown in Figure 6-5. As anticipated, the lineshapes differ markedly for Ce^{3+} and Ce^{4+} . There are more peaks in the Ce^{4+} spectrum because of the possibility for different final state 4f fillings ($4f^{0,1,2}$).¹⁹³ The spectrum of $\text{CeFe}_4\text{P}_{12}$ agrees well with that of CeF_3 , and has a $3d_{5/2}$ core-line binding energy (labelled *A* in Figure 6-3b) of 882.0 eV. This comparison confirms the presence of trivalent Ce in $\text{CeFe}_4\text{P}_{12}$.

In the 3d spectra of all of these rare-earth compounds, distinct satellite peaks appear at 3.5-4.0 eV above the $3d_{5/2}$ and $3d_{3/2}$ core lines. Several theories have been developed to explain the formation of such satellites. One theory, called the shake-up model, invokes a transition whereby a valence electron located on a metal centre is promoted to an empty state above the Fermi level following the photoionization event.¹⁹⁴ The cross-section of this satellite peak has been suggested to be influenced by the degree of overlap between the metal and ligand.¹⁹⁵ Greater orbital overlap between the ligand and metal allows for an increased density of electrons near the metal which are then able

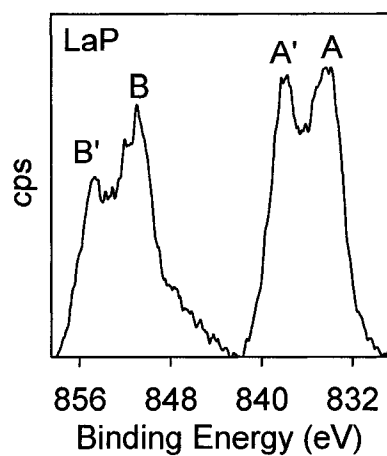


Figure 6-4 High-resolution La 3d XPS spectrum of LaP. The $3d_{5/2}$ and $3d_{3/2}$ corelines are labelled *A* and *B*, respectively. The most intense satellite peaks are labelled *A'* and *B'*.

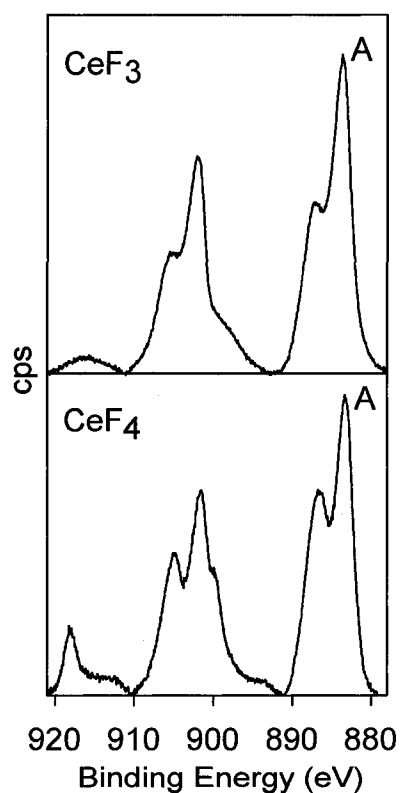


Figure 6-5 High-resolution Ce 3d XPS spectra of CeF_3 and CeF_4 , showing the difference between the Ce^{3+} and Ce^{4+} lineshapes. The $3d_{5/2}$ coreline is labelled *A* in each spectrum.

to screen the core-hole produced by the photoionization process. This enhanced screening allows for an increase in the cross-section for the promotion of an electron from a filled valence state on the metal to an empty metal-based conduction state. With highly electronegative ligands such as F, orbital overlap is poorer than with less electronegative ligands such as P, and the satellite intensity should diminish. For example, the intensity of the satellite peaks found in the $3d_{5/2}$ spectra of lanthanum trihalides, LaX_3 , decreases as the ligand is changed from I to F.¹⁹⁶ In the compounds containing La^{3+} , the satellite peak is found only ~ 3.5 eV above the core line. Although empty La 4f states located about 4–6 eV beyond the Fermi level exist,¹⁹¹ there are no filled La states within the valence band, so intraatomic shake-up can be ruled out as the cause of this satellite peak. In the compounds containing Ce^{3+} , there is a partially filled 4f state within the valence band ($4f^1$), so intraatomic shake-up cannot be ruled out as the source of the satellite.

A more reasonable model that can account for the presence of satellite peaks in the spectra of both the La^{3+} and Ce^{3+} compounds is ligand-to-metal charge-transfer shake-up.^{191, 195} This transition involves the promotion of a valence electron on a ligand to an empty state on the metal centre above the Fermi level, after the metal is photoionized and a core hole is produced.¹⁹⁵ These conditions are satisfied for both the La and Ce 3d spectra, where empty RE 4f states reside about 4–6 eV above the Fermi level and filled ligand states are present near the Fermi level.^{45, 50, 53} The cross-section for this process is again controlled by the degree of orbital overlap between the metal and ligand as well as the ability of the ligand valence electrons to relax towards the empty conduction states on the metal after production of the core-hole.¹⁹⁵ Less electronegative

ligands allow for easier relaxation of the valence electrons towards the metal centre and therefore the cross-section of the satellite is larger if less electronegative ligands are available rather than those having a larger electronegativity.¹⁹⁵ The satellite intensities and core line binding energies for $\text{LaFe}_4\text{P}_{12}$ (Figure 6-3a) and LaP (Figure 6-4) are not identical even though P atoms surround the La centres in both cases, because the coordination numbers and environments are different. The satellite peak is more intense in $\text{CeFe}_4\text{P}_{12}$ than in $\text{LaFe}_4\text{P}_{12}$ (Figure 6-3), which is consistent with the establishment of a greater orbital overlap arising from the presence of a $4f^1$ state within the valence band.

Because P and Fe atoms surround the *RE* atoms, it might be expected that, reciprocally, similar satellite peaks may be found in their spectra. Previous work has shown that if the ligand bonds to the metal through p orbitals, then the ligand electronic states will be less affected by the ligand-to-metal charge-transfer process and no satellite peak will appear.¹⁹⁵ Since the P atoms interact with the *RE* atoms largely through 3p orbitals, no satellite peak should appear in the P spectrum, as confirmed in Figure 6-1. If the Fe atoms interact significantly with the *RE* atoms through 3d orbitals, then a satellite peak would be expected, but none was observed (Figure 6-2). Such a satellite peak is predicted to be located above the core line at a binding energy much higher than is found in the *RE* spectra.¹⁹⁵ This is difficult to confirm by examining the P and Fe spectra, because strong energy loss occurs from interatomic effects such as plasmon loss and inelastic electron scattering, at energies in the range where these satellite peaks might be expected. All things considered, the ligand-to-metal charge-transfer shake-up model best accounts for the presence of satellite peaks observed in the La and Ce 3d spectra.

6.3.4 Valence Band Spectra

Valuable information about the bonding involved in solids can be gained by examining the occupation of the electronic states which can be derived from the valence band spectra. The interpretation of these spectra is aided by comparison with the density of states determined from band structure calculations. Below we illustrate how the spectrum of $\text{LaFe}_4\text{P}_{12}$ is analyzed through a simplified version of the fitting methodology that was successfully applied in Chapter 3 to the binary transition-metal phosphides, and then we extend the protocol to $\text{CeFe}_4\text{P}_{12}$.

The valence band spectrum of $\text{LaFe}_4\text{P}_{12}$ (Figure 6-6a) consists of three distinct regions: (i) a small doublet band from 15 to 8 eV, (ii) a broad band from 8 eV to the Fermi edge, and (iii) a narrow intense band, superimposed on the second region, from 3 eV to the Fermi edge. This spectrum closely resembles that of the binary skutterudite CoSb_3 .⁸⁰ Since the La atoms can be considered, to a first approximation, to merely donate their valence electrons to the rest of the structure, no La valence states are expected within the valence band. The total density of states curve (Figure 6-6b), determined from a tight-binding extended Hückel band structure calculation on the $[\text{Fe}_4\text{P}_{12}]^{3-}$ substructure, reproduces the general features seen in the valence band spectrum, bearing in mind that experimental effects such as lifetime broadening and photoionization cross-sections will introduce important differences in the observed intensities. Bonding within the remaining $[\text{Fe}_4\text{P}_{12}]^{3-}$ substructure then arises from the sharing of electrons between Fe and P atoms. One way to proceed with fitting is to assign features of the valence band spectrum to the contributing atomic orbitals that give rise to these electronic states in the solid. The projections of the P 3s, P 3p, and Fe 3d

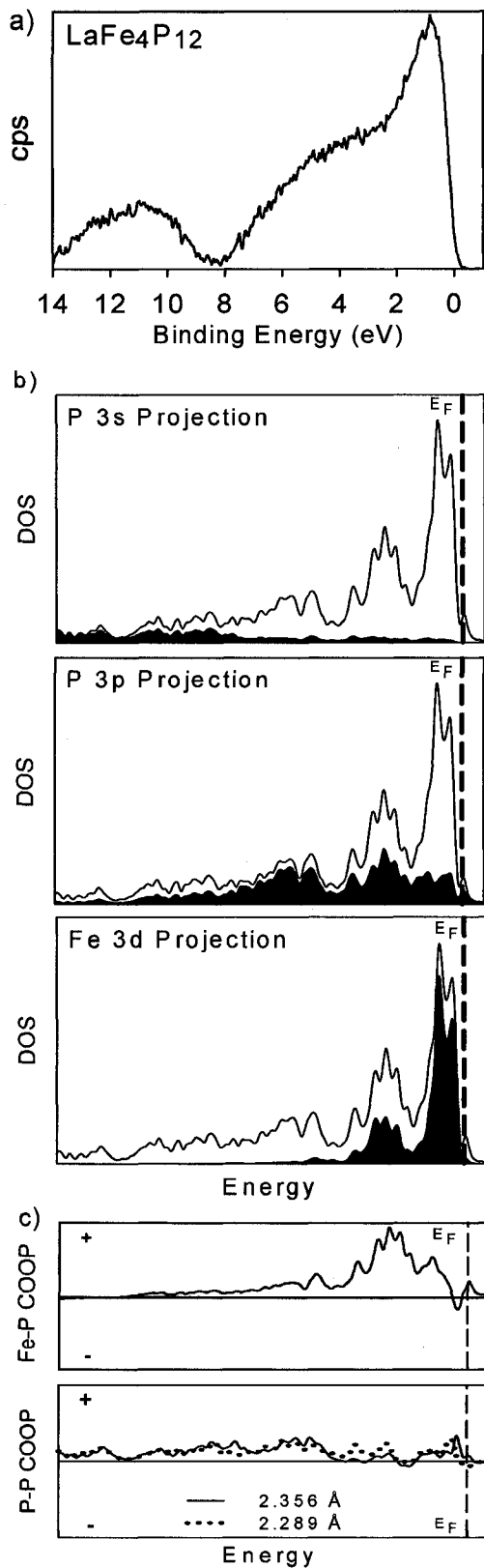


Figure 6-6 (a) Valence band spectrum of $\text{LaFe}_4\text{P}_{12}$. (b) Contributions of P 3s, P 3p, and Fe 3d orbitals (shaded regions) to the total density of states (line) for $\text{LaFe}_4\text{P}_{12}$. The dashed line marks the Fermi level. (c) Crystal orbital overlap population (COOP) curves for Fe-P and P-P contacts in $\text{LaFe}_4\text{P}_{12}$

contributions to the total density of states (Figure 6-6b) correspond closely to the three major binding energy regions identified respectively in the valence band spectrum. The electronic states can also be interrogated for their type of bonding character. The crystal orbital overlap population (COOP) curves (Figure 6-6c) indicate that Fe–P bonding states are constrained largely within an energy region close to the Fermi level, whereas P–P bonding states are spread out throughout the entire valence band.

On the basis of these assignments, the valence band spectrum for $\text{LaFe}_4\text{P}_{12}$ was fitted with a minimum number of peaks (Figure 6-7a). The binding energies, FWHM values, and peak areas of the component peaks are listed in Table 6-1. These values were refined by the procedure described in Chapter 3 (Section 3.3.4), and the goodness of the fit was monitored by the residual standard deviation (RSD) between the simulated and experimental spectra. A low RSD value implies a good fit. The doublet from 15 to 8 eV represents P 3s states and was fitted by two symmetric peaks having similar FWHM. The broad band from 8 eV to the Fermi edge was fitted by two P $3p_{3/2}$ states with rather large FWHM. A slightly better fit of this region can be achieved by invoking several pairs of $3p_{3/2}$ and $3p_{1/2}$ peaks in a fixed intensity ratio of 2:1 and an energy splitting similar to that observed in the P 2p core line spectra (0.9 eV), but as the electron counts extracted from both analyses as well as the RSD values are similar, this extra parameterization was not deemed justifiable. For example, in the $\text{LaFe}_4\text{P}_{12}$ spectrum, if a pair of P $3p_{3/2}$ and $3p_{1/2}$ peaks were used to represent each P 3p state, then a RSD of 2.7 was found whereas if only one P $3p_{3/2}$ peak was used, a RSD of 2.8 was observed. The presence of more than one P 3s or P 3p state is unlikely to be attributable to multielectron excitation processes, as these are normally not pronounced in valence band spectra.

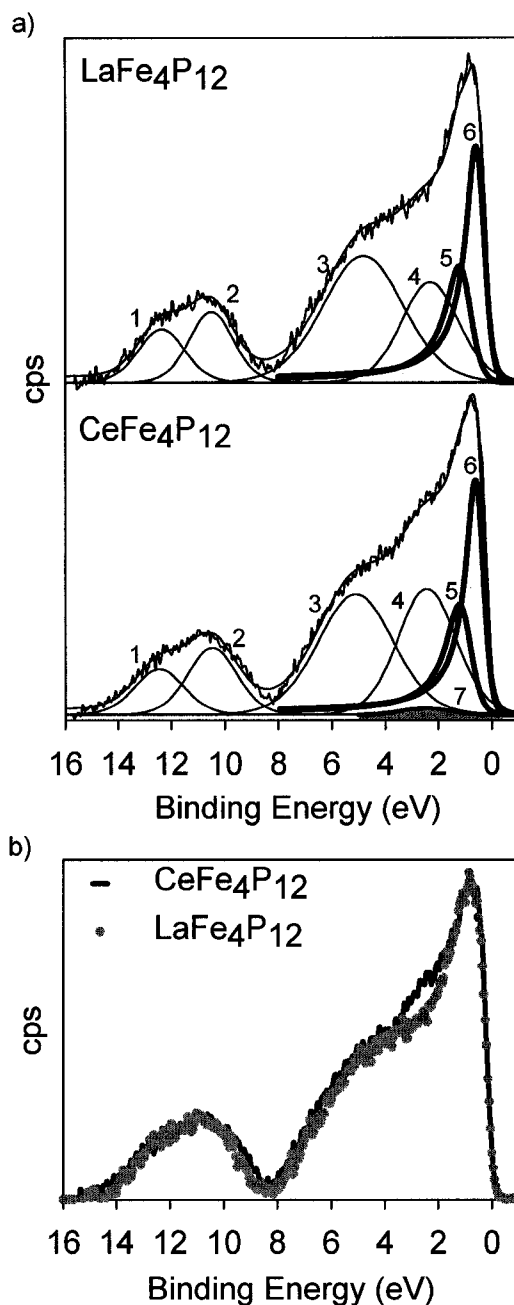


Figure 6-7 (a) Fitted valence band spectra of $\text{LaFe}_4\text{P}_{12}$ and $\text{CeFe}_4\text{P}_{12}$. The P peaks are represented by thin black lines and the asymmetric Fe 3d peaks are represented by thick black lines. The Ce 4f state centred at 2.5 eV in the $\text{CeFe}_4\text{P}_{12}$ spectrum is represented by a filled grey peak. The identity of each peak is provided in Table 6-1. (b) Valence band spectra from $\text{CeFe}_4\text{P}_{12}$ and $\text{LaFe}_4\text{P}_{12}$ overlaid on each other. The difference between the two spectra is apparent at 2.5 eV and is attributed to the presence of a Ce 4f component in the $\text{CeFe}_4\text{P}_{12}$ spectrum.

Table 6-1 Binding Energies (eV) of Component Peaks in Valence Band Spectra of $\text{LaFe}_4\text{P}_{12}$ and $\text{CeFe}_4\text{P}_{12}$ ^a

Peak	Assignment	$\text{LaFe}_4\text{P}_{12}$	$\text{CeFe}_4\text{P}_{12}$
1	P 3s A	12.4 (2.0) [8.9]	12.4 (2.2) [8.0]
2	P 3s B	10.5 (2.0) [11.1]	10.5 (2.2) [11.7]
3	P 3p _{3/2} A	4.8 (3.6) [36.4]	5.1 (3.3) [31.9]
4	P 3p _{3/2} B	2.3 (2.6) [20.6]	2.4 (2.6) [25.7]
5	Fe 3d _{3/2}	1.2 (1.0) [9.3]	1.2 (1.0) [8.6]
6	Fe 3d _{5/2}	0.6 (0.7) [13.8]	0.6 (0.7) [12.9]
7	Ce 4f _{7/2}		2.5 (2.0) [1.1]

^a FWHM values (eV) are indicated in parentheses while the peak areas, in percent, are indicated in square brackets.

A possible reason could be the distinction between the shorter (2.289 Å) and longer (2.356 Å) P–P bonds within the P₄ ring, which is not strictly square.³⁹ The inequivalence of these bonding states is manifested by a shift in energy in the P–P crystal orbital overlap population (COOP) curves in Figure 6-6c. A more enticing idea is that the two P 3p_{3/2} peaks represent states that are involved in the separate σ - and π - components of the P–P bonds within the P₄ ring.^{45, 49} Finally, the narrow band from 3 eV to the Fermi edge was fitted to two asymmetric peaks representing Fe 3d_{5/2} and 3d_{3/2} states with an intensity ratio of 3:2 and an energy splitting of 0.6 eV. The asymmetry of these peaks is similar to that found in the high-resolution Fe 2p core line spectra (Figure 6-2).

The valence band spectrum of CeFe₄P₁₂ is also shown in Figure 6-7a and can be fitted by component Fe and P peaks with similar energies and widths as in LaFe₄P₁₂. However, an important difference is the appearance of an increased band intensity centred near 2.5 eV in the valence band spectrum of CeFe₄P₁₂ that is absent in that of LaFe₄P₁₂, as can be seen more clearly by overlaying the two spectra in Figure 6-7b. We interpret this feature as arising from a Ce 4f¹ state located within the valence band, providing direct evidence for the presence of trivalent cerium. To support this interpretation, the valence band spectra of LaF₃ and CeF₃ were also recorded (Figure 6 - 8). A 4f signal was clearly observed in the spectrum of CeF₃ but not in LaF₃, at an energy (3.1 eV) similar to that for the 4f signal in CeFe₄P₁₂. Furthermore, the energy of the 4f¹ state (2.8 eV) obtained during a recent resonant photoemission study of CeFe₄P₁₂ is close to that found here.¹⁹⁷ Thus, in the valence band spectrum of CeFe₄P₁₂, this additional component was assigned to a Ce 4f_{7/2} peak (shown as the filled grey region in Figure 6-7a) positioned at 2.5 eV with a FWHM of 2.0 eV. These results are consistent

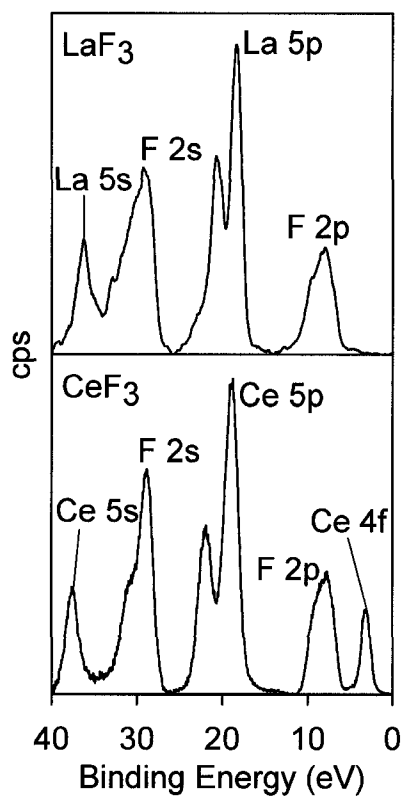


Figure 6-8 Valence band spectra of LaF_3 and CeF_3 . The Ce 4f peak at ~ 3.1 eV is apparent in the CeF_3 spectrum with no similar component being observed in the LaF_3 spectrum.

with predictions from density functional calculations, which show only empty 4f states in the conduction band for $\text{LaFe}_4\text{P}_{12}$ but filled 4f states in the valence band for $\text{CeFe}_4\text{P}_{12}$.^{50, 53} Moreover, in both cases, the sharpness of the Fermi edge in the valence band spectra is consistent with the location of the Fermi level lying just below the top of the valence band, as expected for these hole-doped materials.

In principle, the intensities of the component peaks in the fitted valence band spectra can be related to the electron populations of these states. However, the peak intensities (I) must be corrected for different photoionization cross-sections (σ) and inelastic mean free paths (IMFP, λ) for each state. These values are listed in Table 6-2. The normalized peak intensities (C_i) can then be calculated from Eq 6-1, which gives the fractional electron concentration for a given state.⁷⁵

$$C_i = \frac{I_i / (\sigma_i \lambda_i)}{\sum_{j=1}^n I_j / (\sigma_j \lambda_j)} \quad (6-1)$$

In this equation, $I_i / (\sigma_i \lambda_i)$ represents the corrected intensity of the peak under consideration and $\sum_{j=1}^n I_j / (\sigma_j \lambda_j)$ represents the sum of the corrected intensities from all of the peaks present in the valence band spectrum. The number of electrons in each state can then be determined by multiplying C_i by the total number of valence electrons (95 for $\text{LaFe}_4\text{P}_{12}$ and 96 for $\text{CeFe}_4\text{P}_{12}$). The electron populations and atomic charges are listed in Table 6-3. For $\text{LaFe}_4\text{P}_{12}$, charges of +1.7 for Fe and -0.8 for P are found. (A charge of +3 is assumed for La since no 4f states are occupied.) For $\text{CeFe}_4\text{P}_{12}$, charges of +2.6 for Ce, +2.1 for Fe, and -0.9 for P are found. With the charges in good agreement with the results deduced from the core line spectra, this type of population analysis serves as an

Table 6-2 Corrections Applied to Peak Intensities in Valence Band Spectra of LaFe₄P₁₂ and CeFe₄P₁₂^a

Atom	State	Photoionization cross-section, σ	IMFP, λ (Å)
Ce	4f _{7/2}	0.078	25.1
Fe	3d _{3/2}	0.0694	25.9
	3d _{5/2}	0.1017	
P	3s _{1/2}	0.1116	33.9
	3p _{3/2}	0.0708	

^a The P 3p_{3/2} cross-sections were corrected on the basis of comparison of experimental cross-sections determined by Brillson and Ceasar¹³⁰ to those calculated by Scofield.⁷³ All other cross-sections listed are those calculated by Scofield.⁷³ These cross-sections were determined for an excitation energy equal to that of Al K α x-rays.⁷³ The IMFP values were determined using the QUASESTM IMFP calculator.¹³¹

Table 6-3 Electron Populations in LaFe₄P₁₂ and CeFe₄P₁₂

State	LaFe ₄ P ₁₂	CeFe ₄ P ₁₂
P 3s A	5.7	5.1
P 3s B	7.0	7.5
P 3p A	36.5	32.3
P 3p B	20.7	26.1
Fe 3d	25.1	23.6
Ce 4f		1.4
Total number of e ⁻	95.0	96.0
Calculated charge per atom	+3 (La), ^a +1.7 (Fe), -0.8 (P)	+2.6 (Ce), +2.1 (Fe), -0.9 (P)

^a Assumed from analysis of the La 3d high-resolution spectrum.

independent check on the core line results and demonstrates the usefulness of fitting valence band spectra.

6.4 Conclusions

The rare-earth filled skutterudites $\text{LaFe}_4\text{P}_{12}$ and $\text{CeFe}_4\text{P}_{12}$ have been examined by XPS for the first time. Analysis of the binding energies and lineshapes in high-resolution core line spectra for La, Ce, Fe, and P supports the formulations $(\text{La}^{3+})(\text{Fe}^{2+})_4(\text{P}^{1-})_{12}$ and $(\text{Ce}^{3+})(\text{Fe}^{2+})_4(\text{P}^{1-})_{12}$, where the electron deficiency is represented by a hole in the valence band. The binding energies of the P $2p_{3/2}$ core lines are characteristic of anionic phosphorus, although the negative charge is probably delocalized within the P_4^{4-} ring. The Fe 2p spectra indicate the presence of only low-spin Fe^{2+} , as indicated by the narrow core lines observed. The asymmetric lineshapes in the Fe spectra suggest delocalization of the metal electrons via interaction with the P_4 rings. Characteristic lineshapes of core lines in the *RE* 3d spectra indicate the presence of La^{3+} and Ce^{3+} . Intense satellite peaks in these spectra are attributed to ligand-to-metal charge-transfer shake-up processes. The enhanced intensity of the satellite peak in the Ce 3d spectrum is consistent with greater orbital overlap that would be imparted by the presence of a 4f state located within the valence band of $\text{CeFe}_4\text{P}_{12}$ but not in $\text{LaFe}_4\text{P}_{12}$. This supports theoretical assertions about the importance of f-orbital hybridization in the bonding of these compounds. Direct evidence for an occupied Ce 4f state in $\text{CeFe}_4\text{P}_{12}$ is seen in its valence band spectrum at a binding energy around 2.5 eV, similar to that in CeF_3 . Comparison of the valence band spectra of $\text{LaFe}_4\text{P}_{12}$ and $\text{CeFe}_4\text{P}_{12}$ with theoretical density of states curves allows distinct energy regions of these spectra to be fitted with component peaks that can be identified with parent atomic orbitals. The atomic charges derived from an electron population

analysis of the intensities of these component peaks agree well with the formulations proposed above. This study provides a starting point for the more difficult analysis of other skutterudite-type compounds, particularly the antimonides, where electronegativity differences are considerably smaller than in the phosphides so valence state assignments will be even more challenging.

Chapter 7

Electronic Structure of the Antimonide and Phosphide Skutterudites $\text{LaFe}_4\text{Sb}_{12}$, $\text{CeFe}_4\text{Sb}_{12}$, CoSb_3 and CoP_3 Probed by X-ray Photoelectron Spectroscopy*

7.1 Introduction

In Chapter 6, X-ray photoelectron spectroscopy was applied to resolve some of the ambiguities about the electronic structure of skutterudites, particularly the rare-earth-filled phosphides $\text{LaFe}_4\text{P}_{12}$ and $\text{CeFe}_4\text{P}_{12}$. The interpretation of XPS spectra of intermetallic compounds, especially those containing heavier elements such as the rare earths, is still not well developed. Although these phosphides do not represent practical candidates for thermoelectric materials, they were chosen for the initial study to establish a point of reference for assigning valence states. In the more relevant antimonides $\text{REFe}_4\text{Sb}_{12}$, electronegativity differences are smaller and the interpretation of XPS spectra was anticipated to be considerably more challenging.

The skutterudites represent an extensive class of compounds that originally referred to binary transition-metal pnictides MPn_3 ($M = \text{Co, Rh, Ir}$; $\text{Pn} = \text{P, As, Sb}$) that adopt the same structure as the mineral CoAs_3 .^{41, 42} Jeitschko and Braun later extended them to include the ternary rare-earth-filled derivatives $\text{REM}_4\text{Pn}_{12}$ ($\text{RE} = \text{rare earth}$; $M = \text{Fe, Ru, Os}$; $\text{Pn} = \text{P, As, Sb}$).^{39, 46, 198} Their crystal structure was described in Section 1.4.2 of Chapter 1 (see Figure 1-9) and consists of a network of corner-sharing transition-

*A version of this chapter has been published. Reproduced with permission from Grosvenor, A. P.; Cavell, R. G.; Mar, A. *Phys. Rev. B* **2006**, 74, 125102/1-10. Copyright (2006) by the American Physical Society.

metal-centred octahedra, which undergo a tilting distortion to form nearly square Pn_4 rings and large dodecahedral cages that are filled by RE atoms in the ternary compounds. Skutterudites, especially the antimonides, are most widely acclaimed for their promise as improved thermoelectric materials, which require the incongruous alliance of good electrical conductivity and poor thermal conductivity.^{177, 199} Unfilled variants, such as $CoSb_3$, were initially targeted as candidates, but attention has shifted to the filled variants, such as $La(Fe_3Co)Sb_{12}$, because of the realization that the thermal conductivity could be reduced further by addition of RE .²⁰

The binary compounds are interesting in their own right given the wealth of unusual transport and magnetic properties displayed.⁶ Early bonding considerations predicted that the binaries MPn_3 would be diamagnetic semiconductors, in accordance with a formulation involving low-spin octahedral M^{3+} ($t_{2g}^6 e_g^0$) and closed-shell Pn^{1-} species each engaged in two 2 centre – 2 electron ($2c-2e^-$) $Pn-Pn$ bonds.^{39, 47} Experimental and theoretical studies generally indicated the existence of a very narrow to zero band gap, but these conclusions were not always definitive.^{45, 47-52, 80, 200-202} For CoP_3 , the existence of a band gap was suggested by electrical and optical measurements,⁴⁷ but there is disagreement among calculations.^{49, 50, 201} There seems to be consensus that $CoSb_3$ behaves as a narrow gap semiconductor.^{47, 48, 51, 200, 202} The same simple bonding arguments can be extended to the ternary skutterudites such as $REFe_4P_{12}$. Because they have fewer valence electrons compared to the previous binaries to achieve a closed-shell configuration, these ternaries were suggested to be hole-doped and to contain mixed-valent Fe atoms in accordance with the formulation $RE^{3+}[Fe_4P_{12}]^{3-}$.³⁹ However, the presence of exclusively low-spin Fe^{2+} in $REFe_4P_{12}$

(including $\text{CeFe}_4\text{Sb}_{12}$) has since been supported by magnetic measurements, Mössbauer spectroscopy, theoretical calculations, and by the XPS study presented in Chapter 6.^{45, 180, 182} Most $\text{REM}_4\text{Pn}_{12}$ compounds are metallic but a few are small band gap semiconductors.^{6, 20, 45, 50, 53, 188, 199, 203-210} Notably, the semiconducting behaviour of $\text{CeFe}_4\text{P}_{12}$ was initially attributed to the presence of Ce^{4+} , rendering the $[\text{Fe}_4\text{P}_{12}]^{4-}$ framework isoelectronic to binaries such as CoP_3 .³⁹ However, a trivalent cerium state ($4f^1$) has since been implicated in numerous investigations of $\text{CeFe}_4\text{Pn}_{12}$ (including $\text{CeFe}_4\text{P}_{12}$, which was discussed in Chapter 6).^{53, 184, 185, 197, 205, 206}

In this chapter, detailed interpretations of the XPS spectra of $\text{LaFe}_4\text{Sb}_{12}$, $\text{CeFe}_4\text{Sb}_{12}$, CoSb_3 , and CoP_3 are presented. Both high-resolution core-line spectra and valence band spectra are examined with an aim to determine atomic charges and to understand how the nature of bonding differs between the phosphides and antimonides. Although XPS measurements of CoSb_3 have been recently reported,⁸⁰ no remarks were offered on the distinctive satellite structure that appears in its Co $2p_{3/2}$ spectrum. We suggest an explanation for this feature and we demonstrate how it can be related to the population of Co states within the valence band across a series of Co-containing compounds. With the aid of calculated band structures, we attempt to fit the valence band spectra of these antimonide skutterudites through a procedure that was developed for transition-metal phosphides in Chapters 3 and 6, showing that the experimental analysis of the electronic structure of intermetallic compounds with small electronegativity differences can be performed.

7.2 Experimental

7.2.1 Synthesis

Starting materials were powders of La (99.9%, Alfa-Aesar), Ce (99.9%, Cerac), Fe (99.9%, Cerac), Co (99.999%, Spex), Sb (99.999%, Alfa-Aesar), and P (99.995%, Cerac). Stoichiometric mixtures of the elements were placed in fused-silica tubes that were carbon-coated through pyrolysis of acetone. This treatment helps minimize adventitious reactions of the active metals with the silica tube. Sample purity was assessed from powder X-ray diffraction (XRD) patterns collected on an Inel diffractometer equipped with a CPS 120 detector.

Samples of $\text{LaFe}_4\text{Sb}_{12}$ and $\text{CeFe}_4\text{Sb}_{12}$ were prepared according to an optimized heating program reported previously.¹⁹⁹ The tubes were heated to 873 K over 10 h and held there for 3 h, heated to 1323 K over 12 h and held there for >40 h, and quenched in water. Further annealing at 973 K for >30 h resulted in high-purity products, with only trace amounts of FeSb_2 . Samples of CoSb_3 and CoP_3 were prepared in the presence of a few grains of iodine. The tubes were heated to 1023 K over 30 h and held at this temperature for 1 week, and then quenched in water. Only trace amounts of unreacted pnictogen were detected in the products. Although air-stable, all compounds were stored in a glove box under Ar to preserve pristine surfaces for XPS analysis.

7.2.2 XPS Analysis

All measurements were performed on a Kratos AXIS 165 spectrometer with a monochromatic Al $K\alpha$ X-ray source and a base pressure in the analytical chamber of 10^{-6} – 10^{-7} Pa. The resolution function of this instrument has been determined to be 0.4–

0.5 eV on the basis of analysis of the Co and Fe Fermi edges and the precision of the binding energies is $\sim\pm 0.1$ eV.

Samples of $\text{LaFe}_4\text{Sb}_{12}$, $\text{CeFe}_4\text{Sb}_{12}$, CoSb_3 , and CoP_3 were ground under Ar and pressed onto In foil before being transferred to the instrument under Ar to reduce surface oxidation. They were sputter-cleaned for nearly 1 h with an Ar^+ ion beam (4 kV, 10 mA) to remove surface contaminants (e.g., C, O, I). Spectra collected throughout the sputter-cleaning process showed no changes except for reduction of the amount of surface oxide, confirming that the sputtering process did not appreciably alter the composition of the studied compounds. For example, the Co:Sb ratio in CoSb_3 determined by analysis of survey spectra was 1:2.5 before sputtering and 1:3.1 after sputtering was complete, indicating that the elemental concentration in these samples was not significantly changed by the sputtering process. High-resolution spectra (La, Ce 3d; Fe 2p; Co 2p; Sb 3d; P 2p; valence band) were then collected with energy envelopes ranging from 60 to 20 eV, a step size of 0.05 eV, a pass energy of 20 eV, a sweep time of 180 s, and an analysis spot size of $700 \times 400 \mu\text{m}$. Because these compounds are electrically conducting, charge neutralization was not required during the spectroscopic measurements and charge correction was not applied in the data analysis. The C 1s binding energy from adventitious C was equal to the accepted value of 284.8 eV throughout, further indicating that charging was not a factor. All results were analysed with use of the CasaXPS software package.¹¹⁰ To fit these high-resolution spectra, a Shirley-type function was used to remove the background, which arises largely from inelastic electron scattering. The extracted spectra were then fitted with a combined Gaussian (70%) and Lorentzian (30%) line profile to account for spectrometer and life-time broadening, respectively.

The Sb 3d spectra of the $REFe_4Sb_{12}$ compounds indicated the presence of a small amount of Sb oxide that was not removed by Ar^+ sputtering, and the Pn spectra of $CoPn_3$ indicated the presence of a small amount of oxidized Sb or unreacted P.

7.2.3 Band Structure Calculations

To examine the bonding and distribution of states within the valence band, an extended Hückel tight-binding band structure calculation was performed for CoP_3 with 125 k -points in the irreducible portion of the Brillouin zone with use of the EHMACC suite of programs.^{112, 113} The atomic parameters (valence shell ionization potentials H_{ii} (eV) and orbital exponents ζ_i) were as follows. For Co 4s, $H_{ii} = -7.8$, $\zeta_i = 2.0$; for Co 4p, $H_{ii} = -3.8$, $\zeta_i = 2.0$; for Co 3d, $H_{ii} = -9.7$, $\zeta_{i1} = 5.55$, $c_1 = 0.558$, $\zeta_{i2} = 1.9$; $c_2 = 0.668$; for P 3s, $H_{ii} = -18.6$, $\zeta_i = 1.84$; for P 3p, $H_{ii} = -14.0$, $\zeta_i = 1.45$. This calculation closely reproduces a previously reported one, but we extract the partial density of states curves to demonstrate the procedure for fitting the experimental valence band spectra.²⁰¹

7.3 Results and Discussion

7.3.1 High-Resolution Sb 3d and P 2p Spectra

Figure 7-1 shows the Sb 3d spectra for $LaFe_4Sb_{12}$, $CeFe_4Sb_{12}$, and $CoSb_3$, and the P 2p spectrum for CoP_3 . Although the most fundamental use of XPS spectra is to correlate binding energies with oxidation states, its application to intermetallic compounds has not been widespread and greater difficulties are faced in trying to find reference compounds for comparison.

In CoP_3 , the P $2p_{3/2}$ binding energy of 129.3 eV is markedly lower than that in elemental phosphorus (130.0 eV),¹¹⁶ and on a scale developed in Chapter 3 for a series of

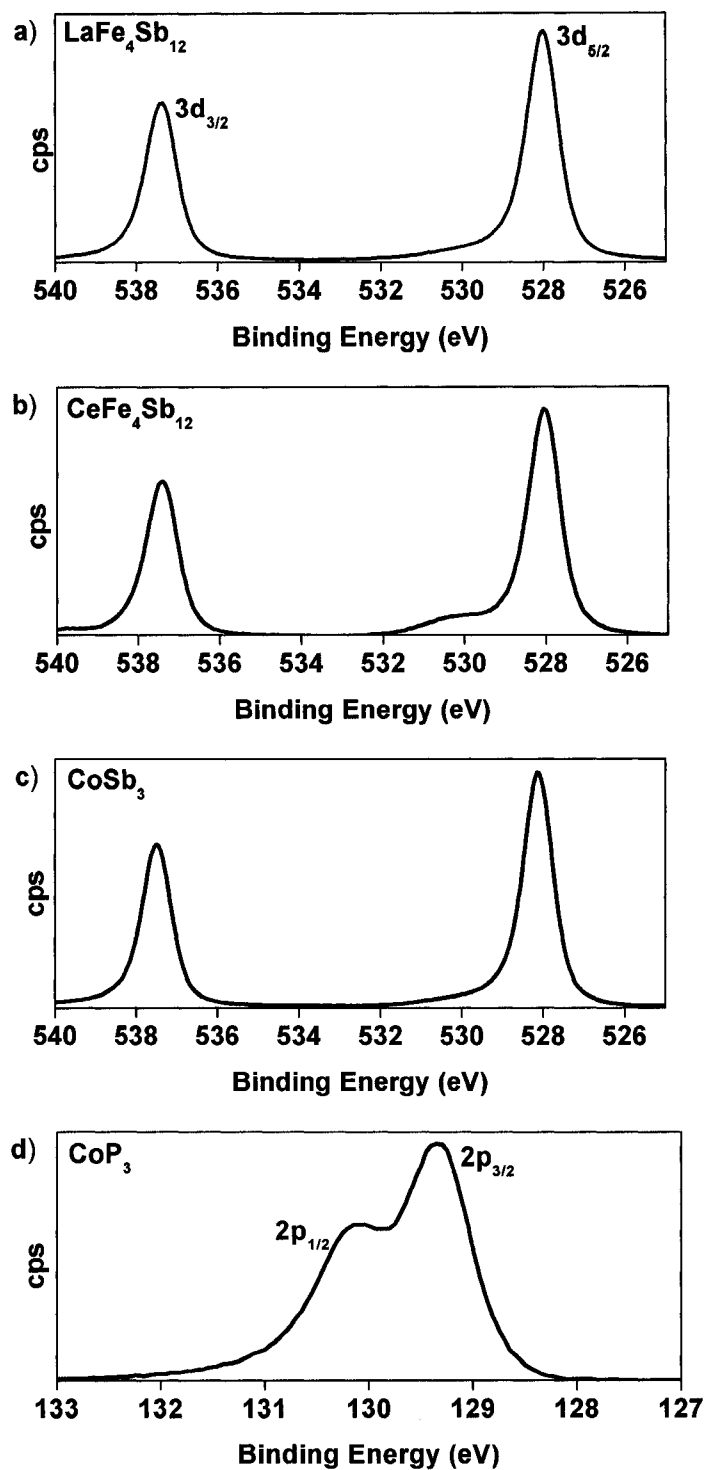


Figure 7-1 High-resolution Sb 3d spectra of (a) $\text{LaFe}_4\text{Sb}_{12}$, (b) $\text{CeFe}_4\text{Sb}_{12}$, (c) CoSb_3 , and (d) P 2p spectrum of CoP_3 . The low intensity satellite peak located above the Sb $3d_{5/2}$ core line is attributed to the presence of a small amount of Sb oxide not removed during sputtering. A small concentration of unreacted P was also observed in the P 2p spectrum from CoP_3 .

transition-metal monophosphides *MP*, it corresponds to the presence of anionic phosphorus with an approximate charge of -1.0 (see Figure 3-3). From charge neutrality, this implies a charge of $+3.0$ on the Co atoms. Although these charges agree fortuitously with the simple ionic model proposed earlier, care must be exercised in interpreting these charges too literally, as cautioned elsewhere.⁵³

In the antimonides, the Sb $3d_{5/2}$ binding energies of 528.0 eV for both $\text{LaFe}_4\text{Sb}_{12}$ and $\text{CeFe}_4\text{Sb}_{12}$ and 528.1 eV for CoSb_3 are only slightly lower than that in elemental antimony (528.2 eV).¹¹⁶ A comparison to binding energies in other Sb-containing compounds¹¹⁶ suggests Sb charges of -0.4 in $\text{LaFe}_4\text{Sb}_{12}$ and $\text{CeFe}_4\text{Sb}_{12}$, and -0.1 in CoSb_3 . Again, from charge neutrality, this implies charges of $+0.4$ for the Fe atoms in $\text{LaFe}_4\text{Sb}_{12}$ and $\text{CeFe}_4\text{Sb}_{12}$ (assuming RE^{3+}), and $+0.3$ for the Co atoms in CoSb_3 . These observations reflect the greater covalent character of the bonding that would be expected from reduced electronegativity differences in the antimonides.¹¹⁴ If we start from an ionic picture containing Sb^{1-} and then allow covalent bonding to occur, donation of electron density from filled Sb orbitals to empty metal orbitals tends to increase shielding of the metal nuclear charge and decrease shielding of the Sb nuclear charge, which results in an Sb $3d_{5/2}$ binding energy that is only slightly less than that of elemental Sb.

7.3.2 High-Resolution Fe and Co 2p Spectra

Figure 7-2 shows the Fe 2p spectra for $\text{LaFe}_4\text{Sb}_{12}$ and $\text{CeFe}_4\text{Sb}_{12}$, and the Co 2p spectra for CoSb_3 and CoP_3 . The observation of only one set of $2p_{3/2}$ and $2p_{1/2}$ signals indicates a single valence state, and the sharpness of these peaks along with the absence of multiplet splitting indicates a low-spin state for the metal atoms. This is consistent with proposals for the presence of only low-spin Fe^{2+} or Co^{3+} ($t_{2g}^6 e_g^0$). The asymmetry

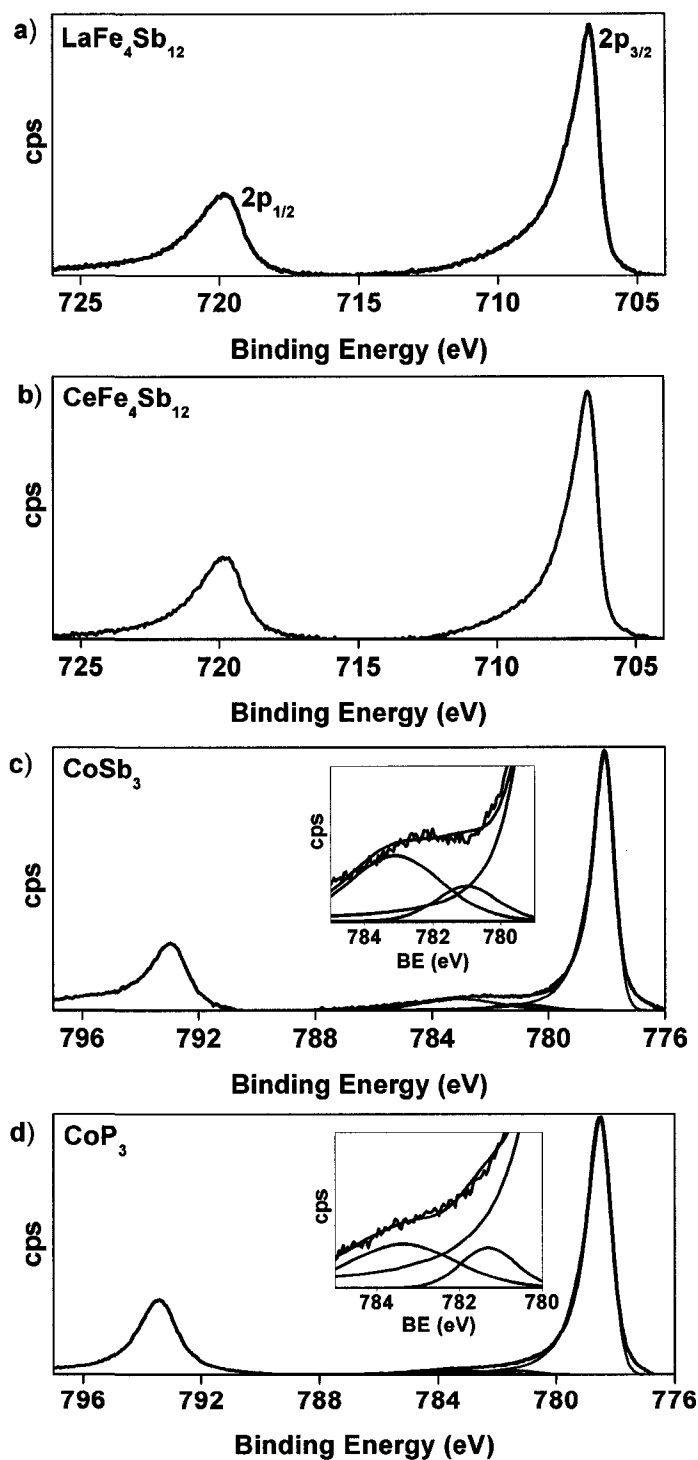


Figure 7-2 High-resolution Fe 2p spectra of (a) $\text{LaFe}_4\text{Sb}_{12}$ and (b) $\text{CeFe}_4\text{Sb}_{12}$; and Co 2p spectra of (c) CoSb_3 and (d) CoP_3 . The insets in (c) and (d) show the satellite peaks observed above the Co $2p_{3/2}$ peaks for CoSb_3 and CoP_3 .

of both the $2p_{3/2}$ and $2p_{1/2}$ peaks in these spectra is an interesting feature that was previously observed in Chapter 6 for $\text{LaFe}_4\text{P}_{12}$ and $\text{CeFe}_4\text{P}_{12}$. The asymmetric tail arises from the Doniach and Šunjić process that was described in Chapters 3 and 6.¹¹⁷ This process is typically observed in metals where metal-metal bonding occurs, but other sources of delocalization, such as that between the metal and pnictogen atoms, which may operate in these compounds, can also give rise to the asymmetric lineshape.

The Fe $2p_{3/2}$ binding energies of 706.7 eV for $\text{LaFe}_4\text{Sb}_{12}$ and 706.8 eV for $\text{CeFe}_4\text{Sb}_{12}$ are lower than in the phosphide analogues $\text{LaFe}_4\text{P}_{12}$ and $\text{CeFe}_4\text{P}_{12}$ (707.2 eV) and are essentially the same as that in Fe metal (706.8 eV).¹¹⁶ The Co $2p_{3/2}$ binding energies of 778.1 eV for CoSb_3 and 778.5 eV for CoP_3 can be compared to that in Co metal (778.1 eV).¹¹⁶ These comparisons illustrate the greater covalent character in the antimonides than in the phosphides, but the shifts in metal binding energy appear to be less sensitive to a change in the bonding character than in the pnictogen binding energy (Section 7.3.1). Nevertheless, the trends in the binding energy correlations with charge remain self-consistent whether the metal or pnictogen atoms are examined; for example, the greater positive Co charge found in CoP_3 compared to CoSb_3 can be inferred from either the Co or Pn binding energies.

A curious observation first noted by Anno *et al.*⁸⁰ in the XPS spectra for binary skutterudites (CoSb_3 , CoAs_3) is that the energy separation between the metal $2p_{1/2}$ and $2p_{3/2}$ peaks seems to be remarkably similar to that of the metal (Co), as is the case here. Normally, the energy separation between spin-orbit doublets can be assumed to be proportional to Z (atomic number) and $1/r^3$ (r = orbital radius).⁶⁰ Although the splittings in the Fe 2p (13 eV) and Co 2p peaks (15 eV) differ through the effect of Z , further

differences arising from changes in charge, and thus r , do not seem to be manifested. This may be the result of delocalization of the valence electrons on the metal, which is also the cause of the asymmetric lineshape. An alternative explanation suggests that the splitting in the core levels can be enhanced through coupling with stronger crystal field effects on the metal 3d band.²¹¹ The observed splittings are also similar to those in clean metal surfaces (Fe, 13.2 eV; Co, 14.9 eV). It appears that these crystal field interactions are small to a degree that they do not separate the 2p doublets any more than in the elemental metals.

7.3.3 Co 2p Satellite Structure

Distinct satellite peaks at higher binding energy than the core lines are observed in the Co 2p spectra of CoSb₃ and CoP₃, being especially visible for the 2p_{3/2} signal, as shown in the insets of Figures 7-2c and 7-2d. These satellites were observed previously in the spectra of Co metal and CoP presented in Chapter 3 (Section 3.3.3), and after additional REELS analysis on Co metal, an explanation involving plasmon loss instead of a two-core-hole theory was proposed. Below we reconsider each of the models to account for the satellite structure in CoSb₃ and CoP₃, and demonstrate that useful chemical information can be extracted from its analysis.

Plasmon loss can be described as the loss of kinetic energy of the photoelectron (increase in binding energy) arising from an oscillation of bound valence electrons.¹¹¹ Because the affected photoelectrons have lower kinetic energies, they appear as a satellite peak in the XPS spectrum with an apparently higher binding energy than the main core line. As in Co metal (Chapter 3), the appearance of two satellite peaks (Figure 7-2) can then be assigned to bulk (higher binding energy) and surface (lower binding energy)

plasmon losses. It should be noted that plasmon loss has also been observed to occur in Ni, Cr, and Fe.^{127, 163, 165} The Ni and Cr analysis was carried out using EELS,^{127, 163} whereas plasmon loss in Fe was observed by analysis of the 1s XPS core-line using a high energy Cu K X-ray source.¹⁶⁵ The Fe 2p_{3/2} peaks for REFe₄Sb₁₂ presented in Figures 7-2a and 7-2b do not show the presence of a plasmon loss peak, likely because the loss structure is overlapped by the more intense Fe core-line.¹⁶⁵

The two-core-hole theory was first introduced by Kotani and Toyozawa to account for the low intensity, high binding energy satellite peaks present in 3d spectra of La metal¹²⁴ and later to those in Co and Ni as well.^{119, 121, 212} This theory suggests that, after photoionization, the core hole present within an atom can influence the conduction states, causing them to be pulled below the Fermi edge (E_F). If the state pulled below E_F is empty, then a poorly screened final state is produced containing two holes: one within the core level and one within the valence band, the latter accounting for the observed satellite peak. If the state pulled below E_F contains an electron, then a well screened final state is produced in which excess energy is surrendered to the outgoing electron, giving it a higher kinetic energy (and an apparently lower binding energy).²¹² This final state appears as the strong core line (2p_{3/2} or 2p_{1/2} in the case of the Co spectra in Figure 7-2).

Although REELS spectra appear to corroborate the idea that the Co 2p satellite peaks result from plasmon loss (Chapter 3, Section 3.3.3), both models described above predict that the intensity of the satellite peak will depend on the occupancy of the metal valence states. In the plasmon loss model, the cross-section for plasmon oscillation events will increase if there are more valence electrons. In the two-core-hole theory, the cross-section for the production of a two-core-hole state will also increase with more

valence electrons; this poorly screened state, which accounts for the satellite peak, is stabilized as the occupancy of the valence states increases.

The relationship between satellite intensity and electron population can be verified. Earlier we inferred charges on the Co atoms in CoP_3 and CoSb_3 from the pnicogen core-line binding energies. Figure 7-3 shows a plot of the Co charges in these and other solids versus the ratio of the total satellite intensity ($I_{\text{satellite}}$) over the core-line intensity ($I_{\text{core-line}}$) in the Co 2p spectra. The plot confirms that the presence of more valence electrons (lower positive charge) on the Co atoms correlates with a greater satellite intensity (higher $I_{\text{satellite}}/I_{\text{core-line}}$). It illustrates convincingly how covalency acts to create true charges that are much less extreme than those based on oxidation state formalisms, and how delocalization of bonding electrons within the valence band becomes a significant factor in producing a charge reduction in CoSb_3 which accounts for the similarity of its satellite intensity to that of Co metal.

7.3.4 High-Resolution Rare-Earth 3d Spectra

Figure 7-4 shows the La 3d spectrum for $\text{LaFe}_4\text{Sb}_{12}$ and the Ce 3d spectrum for $\text{CeFe}_4\text{Sb}_{12}$. Judged by their similarity to other reference spectra, including the phosphides $\text{LaFe}_4\text{P}_{12}$ and $\text{CeFe}_4\text{P}_{12}$ presented in Chapter 6 (Figure 6-3), they are consistent with the presence of trivalent *RE*, a banal expectation for La compounds, but not so obvious for Ce compounds. The valence of cerium in skutterudites has been a source of debate,^{53, 184, 185} but comparison with previously recorded spectra of CeF_3 and CeF_4 (Figures 7-4c and 7-4d) shows conclusively that it is +3 in $\text{CeFe}_4\text{Sb}_{12}$, indicating the presence of a $4f^1$ state within the valence band.

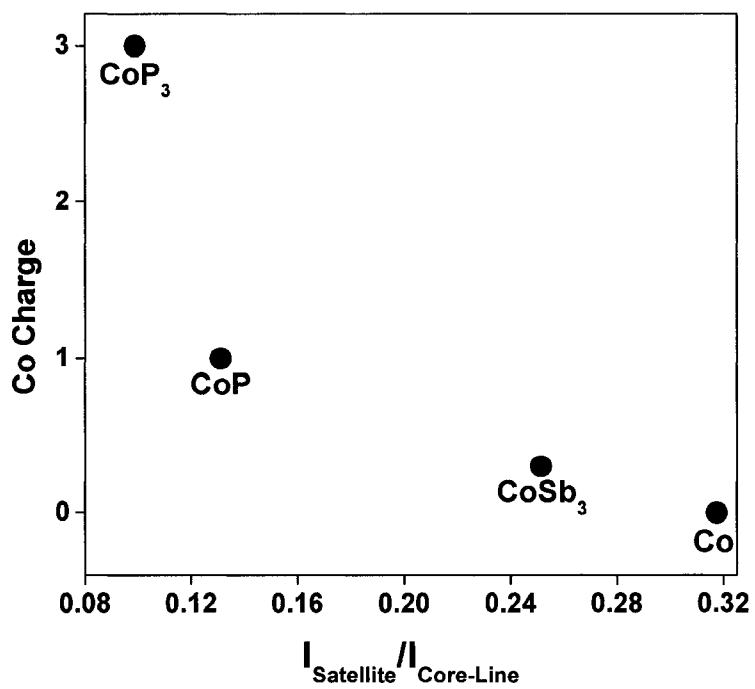


Figure 7-3 Correlation between Co charge and relative intensity of the Co 2p satellite in Co, CoSb_3 , CoP, and CoP_3 . The CoP charges were discussed in Chapter 3 while the Co charges in CoSb_3 and CoP_3 are from Section 7.3.1 of this chapter.

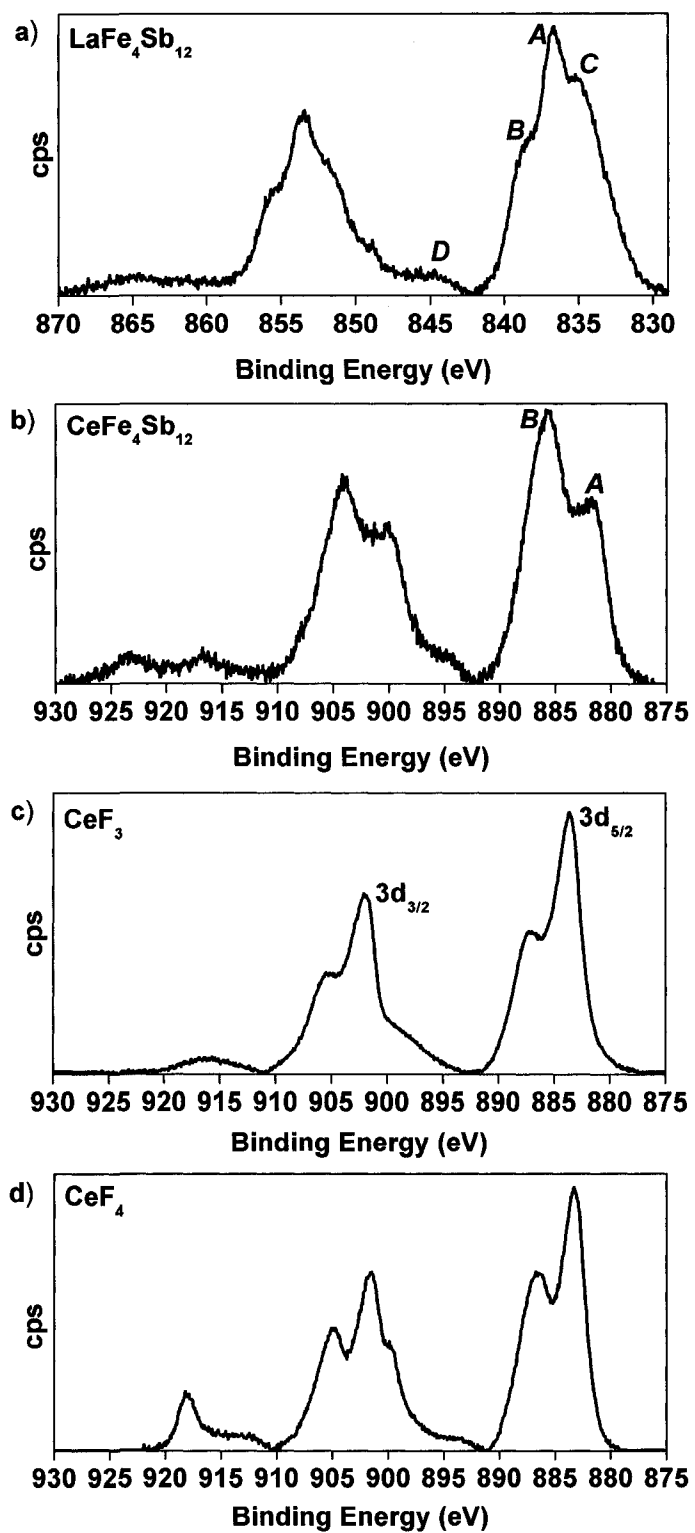


Figure 7-4 High-resolution rare-earth 3d spectra of (a) $\text{LaFe}_4\text{Sb}_{12}$ and (b) $\text{CeFe}_4\text{Sb}_{12}$, (c) CeF_3 , and (d) CeF_4 .

At higher binding energy to the main $3d_{5/2}$ core line (*A*), these spectra reveal satellite peaks (*B*) that were accounted for in Chapter 6 by a ligand-to-metal charge-transfer shake-up process. After an atom is excited and the photoelectron ejected, the relaxation of the electrons in the atom as a result of their response to the presence of a core-hole can precipitate a secondary process in which a valence electron on the ligand is also excited to empty conduction states localized on the rare earth.¹⁹⁴ The energy required to promote an electron from the ligand valence state to the empty conduction states on the rare earth is therefore not available to the photoelectron, causing it to appear in the spectrum with a higher binding energy (lower kinetic energy) than the core line. The empty 4f states are estimated to be 4–6 eV above the Fermi edge.¹⁹¹ The satellite peaks shown in Figure 7-4 are near this energy (2–4 eV), providing further support for the shake-up process. The cross-section for this process increases with greater overlap between ligand and rare-earth states, and with lower electronegativity of the ligand, which allows valence electrons to relax more readily from the ligand to the rare earth.¹⁹⁵ This is particularly evident in comparing the Ce 3d spectra, where the satellite intensity is more intense for $\text{CeFe}_4\text{Sb}_{12}$ than for $\text{CeFe}_4\text{P}_{12}$ (Figure 6-3).

Surprisingly, the opposite is true in the La 3d spectra of $\text{LaFe}_4\text{Sb}_{12}$ and $\text{LaFe}_4\text{P}_{12}$, but it is not immediately obvious why. Moreover, in addition to the shake-up satellite peak (*B*), there is another satellite peak (*C*) at lower binding energy to the main $3d_{5/2}$ core line (Figure 7-4a) in $\text{LaFe}_4\text{Sb}_{12}$ that was not observed in $\text{LaFe}_4\text{P}_{12}$. Here, the two-core-hole model described earlier (Section 7.3.3) can be invoked as a plausible explanation for this additional satellite. The assumption of partial covalent character of the La–Sb bonds may allow for the presence of electrons in the La 4f states. If, after production of a core

hole, a La conduction state containing an electron is pulled below E_F , then the La atom has a well screened final state in which this electron relinquishes its energy to the photoelectron. The photoelectron has an increased kinetic energy and appears below the core-line peak (*A*) on the binding energy scale. A similar satellite structure has been observed in the La 3d spectrum of LaSb and was also attributed to a two-core-hole-like process arising from partial filling of La 4f states.²¹³

The separation from the core line to this new satellite peak (*C*) is ~ 2 eV, the same as that to the shake-up peak (*B*), which is reasonable because both peaks arise from movement of electrons across the band gap. The two-core-hole theory also offers the possibility for an empty La conduction state to be pulled below E_F , forming a poorly screened final state containing two holes (one within the core and one within the valence levels).¹²⁴ This final state leads to the generation of a photoelectron having a higher binding energy than the core line. Accordingly, yet another satellite peak (*D*) can be found between the $3d_{5/2}$ shake-up satellite and the $3d_{3/2}$ states in the spectrum of $\text{LaFe}_4\text{Sb}_{12}$ (Figure 7-4a). In contrast, the two-core-hole satellite structure is absent in the spectrum of $\text{CeFe}_4\text{Sb}_{12}$ (Figure 7-4b). If trivalent Ce is assumed, the $4f^1$ state may already be substantially involved in bonding states in the valence band below E_F , and as such would be unable to participate in two-core-hole processes.

Returning to the question of why the shake-up peak in the La 3d spectrum is more intense in $\text{LaFe}_4\text{P}_{12}$ than in $\text{LaFe}_4\text{Sb}_{12}$, we offer the simplest explanation that the two-core-hole and shake-up processes are competitive, given that both involve either the promotion or demotion of electrons across the band gap. With the La-P bond in $\text{LaFe}_4\text{P}_{12}$ probably having significant ionic character, the La 4f states do not mix well

with the P states and remain essentially empty, so that only shake-up processes are likely to occur.

7.3.5 Valence Band Spectra

Although theoretical band structures determined using more rigorous methods (e.g., DFT, LMTO) are now available for many skutterudites,^{45, 48-53, 200-202, 204, 207} we reproduce here the results of a simple calculation on CoP_3 that suffices to illustrate how the experimental valence band spectra can be fitted to component states.²⁰¹ Figure 7-5 shows that the observed valence band spectrum of CoP_3 matches very well to the calculated density of states (DOS) curve. As assigned from the projections of the DOS curve, the spectrum shows a P 3s band at high binding energy, followed by a very broad P 3p band that ends well before E_F , and an intense narrow Co 3d band just below E_F . Analysis of overlap population curves (not shown) indicates that Co–P bonding occurs throughout the upper portion of the valence band whereas P–P bonding occurs in the lower portion of the valence band.

Figure 7-6 shows the valence band spectra for CoSb_3 , CoP_3 , $\text{LaFe}_4\text{Sb}_{12}$, and $\text{CeFe}_4\text{Sb}_{12}$, fitted on the basis of the assignments above, through a methodology that was applied to phosphides in Chapters 3 and 6. The CoSb_3 spectrum compares well to those previously reported.^{51, 80} In general, the valence band in the antimonide skutterudites (CoSb_3 , $\text{LaFe}_4\text{Sb}_{12}$, $\text{CeFe}_4\text{Sb}_{12}$) is not as wide as in the corresponding phosphides (CoP_3 , $\text{LaFe}_4\text{P}_{12}$, $\text{CeFe}_4\text{P}_{12}$), in agreement, for example, with calculations on $\text{CeFe}_4\text{Sb}_{12}$ and $\text{CeFe}_4\text{P}_{12}$.⁵³ In the spectra of the antimonides, the Sb 5s states occur in the lower portion of the valence band but both Sb 5p and Fe 3d states are clustered together in the upper portion of the valence band. The difference between the spectra of $\text{LaFe}_4\text{Sb}_{12}$ and

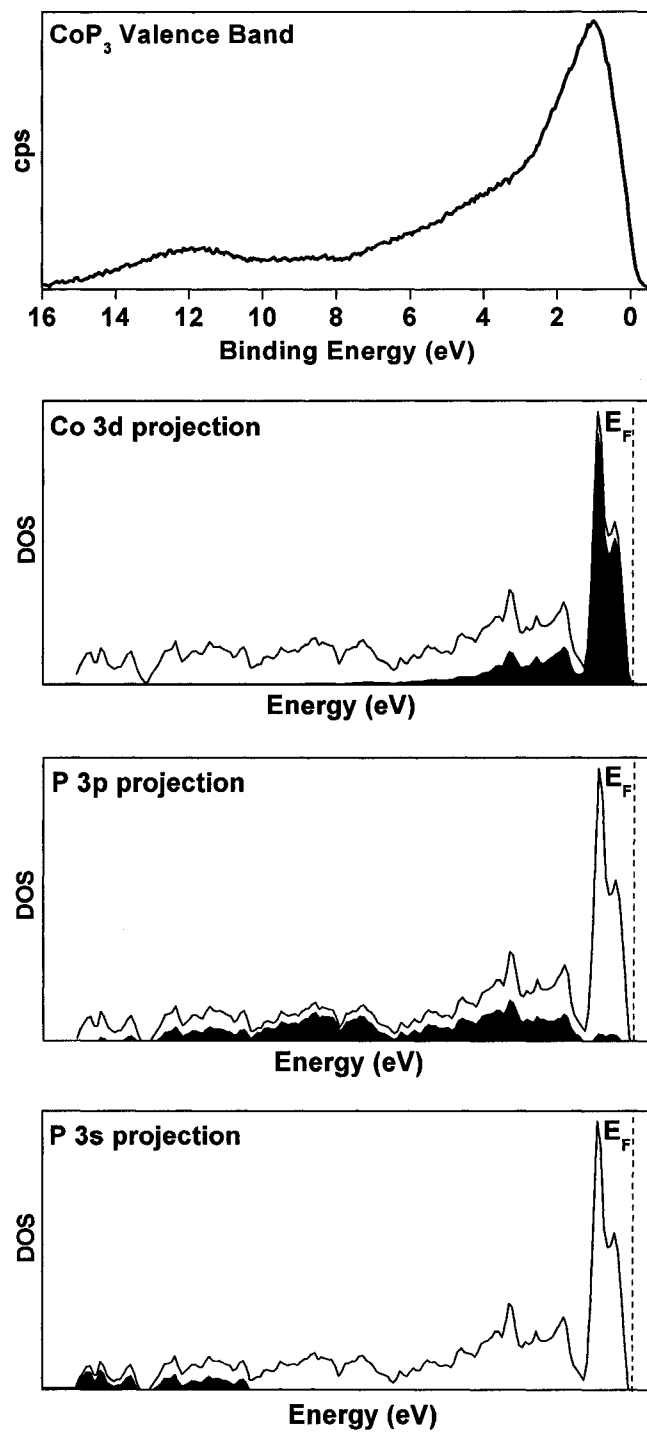


Figure 7-5 Valence band spectrum of CoP₃ compared with the Co 3d, P 3p, and P 3s projections of the density of states. The Fermi edge (E_F) is indicated in each of the projections.

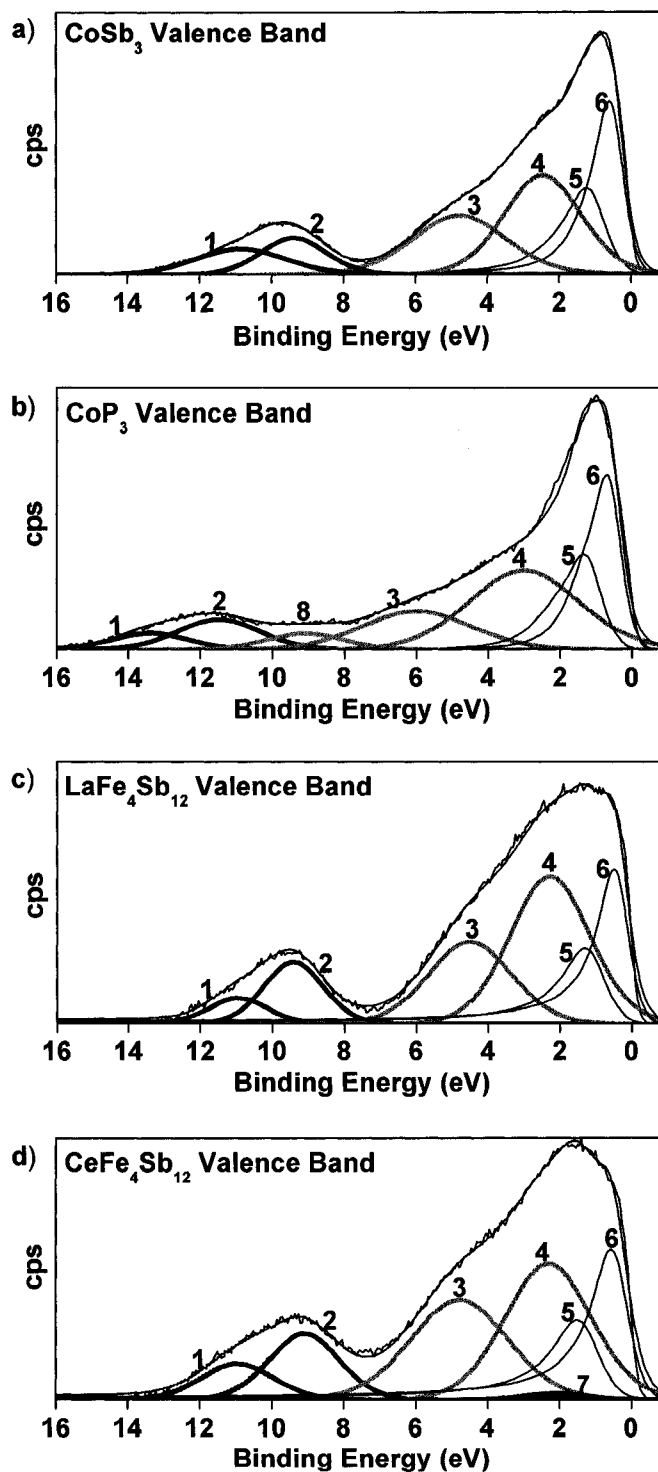


Figure 7-6 Fitted valence band spectra of (a) CoSb₃, (b) CoP₃, (c) LaFe₄Sb₁₂, and (d) CeFe₄Sb₁₂. The identity, energies, and FWHM of the peaks used to fit the spectra are shown in Table 7-1. The thick black lines represent *Pn ns* peaks, the thick grey lines represent *Pn np* peaks, and the thin black asymmetric lines represent the *M 3d_{3/2,5/2}* peaks. The Ce 4*f* state in CeFe₄Sb₁₂ is represented by a filled black peak centred at ~2 eV.

CeFe₄Sb₁₂ is difficult to detect, but if they are overlaid (Figure 7-7), a higher intensity is apparent near 2 eV in the case of CeFe₄Sb₁₂. We interpret this feature as arising from the presence of a Ce 4f¹ state, at an energy similar to that found in CeFe₄P₁₂ (2.5–2.8 eV)¹⁹⁷ in Chapter 6 (Figure 6-7) and in agreement with density functional calculations which locate it near E_F just below the top of the Fe 3d band.⁵³

Table 7-1 lists the binding energies, FWHM, and peak areas of the component peaks used to fit the valence band spectra. The widths and energies were refined as described in Chapter 3 (Section 3.3.4), and the goodness of the fit was monitored by the RSD between the simulated and experimental spectra with a low RSD indicating a good fit. The asymmetric lower region was fitted by two pnictogen *ns* peaks, and correspondingly the upper region of the valence band was fitted by two pnictogen *np* peaks, which overlap with the transition-metal 3d_{5/2} and 3d_{3/2} spin-orbit doublet peaks placed at the edge closest to E_F. The asymmetry of the *Pn ns* peak may be caused by the presence of *Pn–Pn* bonds of differing length^{39, 42} as well as the overlap of *Pn–Pn* and metal–*Pn* states. The spectrum of CoP₃ shows additional intensity in the region between the P 3s and lower binding energy P 3p peaks, requiring a third P 3p peak to properly fit this region. In the spectrum of CeFe₄Sb₁₂, a Ce 4f peak was centred at ~2 eV.

The electron populations of the component states in the fitted valence band spectra can be determined from the peak intensities I_i , corrected for different photoionization cross-sections (σ) and inelastic mean free paths (IMFP, λ) (Table 7-2), and normalized to give a fractional electron concentration C_i according to:

$$C_i = [I_i / (\sigma_i \lambda_i)] / [\sum_{j=1}^n I_j / (\sigma_j \lambda_j)].^{75}$$
 Multiplying C_i by the total number of valence electrons (24 for CoSb₃, CoP₃; 95 for LaFe₄Sb₁₂; 96 for CeFe₄Sb₁₂) gives the number of

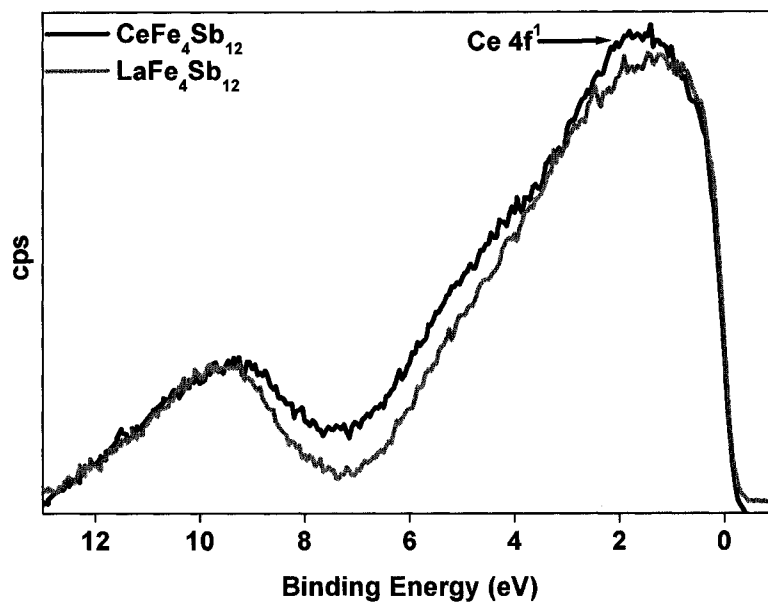


Figure 7-7 Overlapped valence band spectra of $\text{LaFe}_4\text{Sb}_{12}$ and $\text{CeFe}_4\text{Sb}_{12}$ showing the position of the $\text{Ce } 4f^1$ state.

Table 7-1 Binding energies (eV) of component peaks in valence band spectra of CoSb_3 , CoP_3 , $\text{LaFe}_4\text{Sb}_{12}$, and $\text{CeFe}_4\text{Sb}_{12}$.^a

Peak	Assignment	CoSb_3	CoP_3	$\text{LaFe}_4\text{Sb}_{12}$	$\text{CeFe}_4\text{Sb}_{12}$
1	$Pn \text{ } ns \text{ } A$	10.9 (2.9) [9.1]	13.4 (2.5) [5.0]	11.0 (1.9) [5.0]	10.9 (2.3) [7.0]
2	$Pn \text{ } ns \text{ } B$	9.4 (2.1) [9.4]	11.5 (2.7) [9.6]	9.4 (2.0) [12.2]	9.1 (2.3) [12.4]
3	$Pn \text{ } np_{3/2} \text{ } A$	4.8 (3.1) [21.7]	6.0 (3.6) [16.3]	4.5 (2.7) [22.2]	4.8 (3.2) [26.3]
4	$Pn \text{ } np_{3/2} \text{ } B$	2.5 (2.5) [30.1]	3.0 (3.6) [33.6]	2.3 (2.6) [38.1]	2.3 (2.8) [31.7]
5	$M \text{ } 3d_{3/2}$	1.2 (1.2) [11.9]	1.3 (1.1) [12.2]	1.3 (1.2) [9.1]	1.5 (1.3) [8.7]
6	$M \text{ } 3d_{5/2}$	0.6 (0.9) [17.8]	0.7 (0.9) [18.2]	0.5 (0.9) [13.6]	0.6 (1.1) [13.0]
7	$\text{Ce } 4f_{7/2}$				2.1 (2.0) [1.1]
8	$Pn \text{ } np_{3/2} \text{ } C$		9.1 (2.6) [4.9]		

^a FWHM values (eV) are indicated in parentheses and the peak areas, in percent, are indicated in square brackets.

Table 7-2 Corrections applied to peak intensities in valence band spectra of CoP_3 , CoSb_3 , $\text{LaFe}_4\text{Sb}_{12}$, and $\text{CeFe}_4\text{Sb}_{12}$.^a

Atom	State	Photoionization cross-section, σ	IMFP, λ (Å)
Ce	4f _{7/2}	0.078	25.1
Co	3d _{3/2}	0.1082	24.0
	3d _{5/2}	0.1582	
Fe	3d _{3/2}	0.0694	25.9
	3d _{5/2}	0.1017	
P	3s _{1/2}	0.1116	33.9
	3p _{3/2}	0.0708	
Sb	5s _{1/2}	0.1085	30.4
	5p _{3/2}	0.0747	

^a The P 3p_{3/2} cross-sections were corrected on the basis of comparison of experimental cross-sections determined by Brillson and Ceasar¹³⁰ to those calculated by Scofield.⁷³ All other cross-sections listed are those calculated by Scofield.⁷³ These cross-sections were determined for an excitation energy equal to that of Al K α X-rays.⁷³ The IMFP values were determined using the QUASESTM IMFP calculator and a kinetic energy of 1485 eV.¹³¹ These values are calculated assuming that the material only contains the element of interest and are considered estimates when applied to materials containing multiple elements in the simple calculation presented here.

Table 7-3 Electron populations in CoSb₃, CoP₃, LaFe₄Sb₁₂ and CeFe₄Sb₁₂.^a

State	CoSb ₃	CoP ₃	LaFe ₄ Sb ₁₂	CeFe ₄ Sb ₁₂
<i>Pn ns</i> A	1.8	0.9	3.4	4.9
<i>Pn ns</i> B	1.8	1.7	8.2	8.6
<i>Pn np</i> A	6.1	4.5	22.1	26.6
<i>Pn np</i> B	8.4	9.3	38.0	32.1
<i>Pn np</i> C		1.3		
<i>M</i> 3d	5.9	6.3	23.2	22.5
Ce 4f				1.3
Total number of e ⁻	24	24	95	96
Calculated charge per atom	+3.1 (Co), -1.0 (Sb)	+2.7 (Co), -0.9 (P)	+3 (La), +2.2 (Fe), -1.0 (Sb)	+2.7 (Ce), +2.4 (Fe), -1.0 (Sb)

^a The La charge was assumed from analysis of the La 3d high-resolution spectrum.

electrons in each state, from which atomic charges can be deduced (Table 7-3). Not only does this partitioning process of the electron populations provide further support for trivalent Ce in $\text{CeFe}_4\text{Sb}_{12}$, it also reproduces the familiar charges predicted from simple electron counting models, viz., the expectation of Co^{3+} and Fe^{2+} species (d^6), and anionic Pn^{1-} . These values are consistent with the results determined earlier from analysis of the core-line spectra, which tends to give charges that are less extreme but more discriminated. For example, whereas Sb charges of -0.4 for $\text{REFe}_4\text{Sb}_{12}$ and -0.1 for CoSb_3 result from analysis of the Sb 3d core-line spectra, they are all found to be -1.0 from analysis of the valence band spectra. The core-line analysis is more sensitive to true differences in covalency in individual bonds to a given atom.

7.4 Conclusions

The measured XPS spectra of $\text{LaFe}_4\text{Sb}_{12}$, $\text{CeFe}_4\text{Sb}_{12}$, CoSb_3 and CoP_3 has provided insights into their electronic structure. High-resolution core-line spectra of the pnictogen atoms confirmed that the decrease in electronegativity from P to Sb produces a shift of binding energy that reflects the lower ionicity of bonds to these atoms. Such a shift is less apparent in the metal 2p spectra, where delocalization of electron density tends to temper effects on the shielding of the nuclear charge and also induces a strong peak asymmetry. A plasmon loss satellite peak is observed in the Co 2p spectra of these and other Co compounds whose relative intensity increases as the Co 3d band occupancy increases. This interesting relationship may serve as a broader basis for quantifying Co charges on other Co-containing compounds. The presence of trivalent *RE* was confirmed in the $\text{REFe}_4\text{Sb}_{12}$ compounds, as was determined previously in the phosphide analogues. The La 3d spectrum of $\text{LaFe}_4\text{Sb}_{12}$ contains two types of satellite peaks, arising from

ligand-to-metal charge-transfer shake-up and from two-core-hole processes, both of which are final state effects whereby electrons are promoted from or demoted to states in the valence band. In contrast, only a shake-up satellite peak is found in the Ce 3d spectrum of $\text{CeFe}_4\text{Sb}_{12}$; a two-core-hole process is thwarted by the presence of a Ce 4f¹ state in the valence band involved in bonding, so that no electrons are available in 4f states above E_F that can undergo this process. Neither is the two-core-hole process active in the phosphide $\text{LaFe}_4\text{P}_{12}$ because the La–P bonds are too ionic to allow conduction electrons to populate La 4f states. Fitting of the valence band spectra supports the formulations $(\text{Co}^{3+})(\text{Pn}^{1-})_3$ and $(\text{RE}^{3+})(\text{Fe}^{2+})_4(\text{Sb}^{1-})_{12}$ (electronically balanced by a hole in the valence band), consistent with previous electrical, magnetic and Mössbauer measurements, and with theoretical models. The presence of Ce^{3+} in $\text{CeFe}_4\text{Sb}_{12}$ was confirmed by a 4f peak at ~ 2 eV in the valence band spectrum, but this observation was more difficult to make than in the previous case of $\text{CeFe}_4\text{P}_{12}$ because it is obscured by the greater mixing of states in the more covalent antimonide.

Chapter 8

Analysis of the Electronic Structure of $\text{Hf}(\text{Si}_{0.5}\text{As}_{0.5})\text{As}$ by X-ray Photoelectron and Photoemission Spectroscopy*

8.1 Introduction

Throughout this thesis, photoelectron spectroscopy has been applied to assess the electronic character of atoms in solid state compounds where true charges may not be as extreme as implied by simple electron-counting formalisms. Nevertheless, through proper interpretation, it is possible to extract information from valence band spectra that can be related to these charges, as was successfully demonstrated in Chapters 3, 6, and 7 for several phosphides and antimonides. Here we describe the synthesis, crystal structure, and physical properties of a new ZrSiS-type compound, $\text{Hf}(\text{Si}_{0.5}\text{As}_{0.5})\text{As}$, an end-member of the solid solution $\text{Hf}(\text{Si}_x\text{As}_{1-x})\text{As}$ ($0.5 \leq x \leq 0.7$), and examine its electronic structure through XPS and PES (photoemission spectroscopy). In the previous chapters, we have studied compounds containing anion-anion bonding of group 15 elements (P, As, Sb), here we extend our analysis to a compound which contains isolated As atoms as well as As atoms involved in homoatomic As-As bonding and heteroatomic As-Si bonding.

Many compounds of the form MAB crystallize in the tetragonal structure type known most commonly as the PbFCI- or ZrSiS-type, an ordered ternary variant of the

A version of this chapter has been published. Reproduced with permission from Grosvenor, A. P.; Cavell, R. G.; Mar, A.; Blyth, R. I. R. *J. Solid State Chem.* **2007, *180*, 2670-2681. Copyright (2007) by Elsevier.*

Cu_2Sb -type adopted by metal-rich compounds.^{54, 55} As indicated in Chapter 1 (Section 1.4.3), they can be distinguished by the quantity Δ , the electron deficiency experienced by A and B (after full electron transfer from M) with respect to each attaining an octet.⁵⁶ The PbFCI-type designates normal valence compounds where M provides sufficient electrons so that A and B each have an octet ($\Delta = 0$, as in $\text{Pb}^{2+}\text{F}^{1-}\text{Cl}^{1-}$) while the anions in ZrSiS-type compounds must participate in homoatomic bonding to fulfill their octets, as in $\text{Zr}^{4+}\text{Si}^2-\text{S}^{2-}$ ($\Delta = 2$) where polyanionic Si–Si bonding is present.⁵⁷ The ZrSiS-type structure is possessed by many compounds MAB where M is an early transition metal or f-block element (e.g., Zr, Hf, La, Ce) and A and B are heavier p-block elements (e.g., Si, Ge, As, Sb, S, Se, Te).⁵⁴

Electrical and magnetic measurements of ZrSiS-type compounds have revealed diverse properties, including metallic ($\text{ZrAs}_{1.4}\text{Se}_{0.5}$),⁵⁸ semimetallic (ThPS),²¹⁴ semiconducting ($\text{SmTe}_{1.8}$),²¹⁵ ferromagnetic (MnAlGe),²¹⁶ antiferromagnetic ($\text{USn}_{0.5}\text{Sb}_{1.5}$),²¹⁷ and paramagnetic (CeSbTe)²¹⁸ behaviour. Although spectroscopic studies can also yield valuable information about electronic structure, to our knowledge they have not been made for ZrSiS-type compounds and have been sparse for the related metal-rich Cu_2Sb -type binary compounds. Cu_2Sb itself was initially proposed to be antiferromagnetic,²¹⁹ but NMR spectroscopy indicated that it is diamagnetic,²²⁰ a result later confirmed by further magnetic measurements.²²¹ M_2As (M = Cr, Mn, Fe), Mn_2Sb , and MnAlGe have been examined by photoelectron spectroscopy performed using a laboratory X-ray (XPS), ultraviolet (UPS), or synchrotron radiation source (PES),^{216, 222, 223} In Mn_2Sb , the valence states of the Mn and Sb sites could be probed separately by adjusting the X-ray energy, thus altering their photoemission cross-

sections.²²² Further, the two structurally and magnetically inequivalent Mn sites could be distinguished by the higher binding energy of those atoms that have 3d states positioned at the Fermi edge and participate in metal-metal bonding.²²²

In this chapter, we have investigated the new compound $\text{Hf}(\text{Si}_{0.5}\text{As}_{0.5})\text{As}$. By analyzing the measured valence band spectra with the aid of band structure calculations, we have evaluated the charges of the constituent atoms and related them to the bonding in this compound. This has led to important implications about the electronic structure of ZrSiS-type compounds in general.

8.2 Experimental

8.2.1 Synthesis

Powders of Hf (99.6% (excluding 2–4% Zr); Alfa-Aesar), Si (99.99%; Alfa Inorganics), and As (99.9998%; Alfa Inorganics) in the molar ratio 1:0.5:1.5 were sealed in evacuated fused-silica tubes. The samples were heated to 873 K over 12 h, held at this temperature for 3 d, heated to 1173 K over 24 h, and annealed at this temperature for 1–4 weeks. After annealing, the samples were quenched in water. Addition of I_2 (Anachemia) to the reaction as a chemical vapour transport agent (CVT) yielded needle- or plate-shaped crystals depending on the annealing time at 1173 K. SEM-EDX analysis on a Hitachi S-2700 SEM (20 kV beam voltage) revealed that the composition of these crystals was $\text{HfSi}_{0.5(1)}\text{As}_{1.5(1)}$. Powder X-ray diffraction patterns obtained on an Inel diffractometer equipped with a CPS 120 detector indicated >95% purity of the desired phase, with the remaining <5% mostly containing HfO_2 . Use of initial reaction temperatures higher than 873 K led to reaction of Hf with the tube to form larger quantities of HfO_2 . When only Hf and As (in either 1:1 or 3:2 ratios) were reacted in a

fused-silica tube at 1173 K in the presence of I_2 , $Hf(Si_{0.5}As_{0.5})As$ as well as large quantities of HfO_2 and occasionally minor amounts of $HfAs_2$ were produced due to reaction with the tube.

8.2.2 Structure Determination

Single-crystal X-ray diffraction data were collected on a Bruker Platform / SMART 1000 CCD diffractometer at 295 K using ω scans. Structure solution and refinement were carried out with use of the SHELXTL (version 6.12) software package.²²⁴ Face-indexed numerical absorption corrections were applied. The centrosymmetric space group $P4/nmm$ was chosen and initial atomic positions were found by direct methods. Occupying the $2a$ site exclusively with As atoms led to large displacement parameters. If Si and As were assumed to be disordered within this site, the refined occupancies converged to 0.52(1) Si and 0.48(1) As and the displacement parameters became more reasonable. The absence of supercell reflections suggests that Si and As are randomly distributed in this site. The other sites were well-behaved.

Atomic positions were standardized with the program STRUCTURE TIDY.²²⁵ Crystal data and further details of the data collection are given in Table 8-1, final values of the positional and displacement parameters are given in Table 8-2, and interatomic distances are listed in Table 8-3. Further data, in CIF format, have been sent to Fachinformationszentrum Karlsruhe, Abt. PROKA, 76344 Eggenstein-Leopoldshafen, Germany, as supplementary material No. CSD-418329 and can be obtained by contacting FIZ (quoting the article details and the corresponding CSD numbers).

Table 8-1 Crystallographic data for Hf(Si_{0.5}As_{0.5})As

Formula	Hf(Si _{0.52(1)} As _{0.48(1)})As
Formula mass (amu)	304.92
Space group	<i>P4/nmm</i> (No. 129)
<i>a</i> (Å)	3.6410(5)
<i>c</i> (Å)	8.155(1)
<i>V</i> (Å ³)	108.10(3)
<i>Z</i>	2
ρ_{calcd} (g cm ⁻³)	9.367
Crystal dimensions (mm)	0.51 × 0.27 × 0.03
Radiation	Graphite monochromated Mo <i>K</i> α, $\lambda = 0.71073$ Å
μ (Mo <i>K</i> α) (mm ⁻¹)	70.83
Transmission factors	0.006–0.121
2θ limits	5.00° ≤ 2θ(Mo <i>K</i> α) ≤ 65.82°
Data collected	−5 ≤ <i>h</i> ≤ 5, −5 ≤ <i>k</i> ≤ 5, −12 ≤ <i>l</i> ≤ 12
No. of data collected	1449
No. of unique data, including $F_o^2 < 0$	153
No. of unique data, with $F_o^2 > 2\sigma(F_o^2)$	153
No. of variables	11
$R(F)$ for $F_o^2 > 2\sigma(F_o^2)$ ^a	0.028
$R_w(F_o^2)$ ^b	0.068
Goodness of fit	1.306
($\Delta\rho$) _{max} , ($\Delta\rho$) _{min} (e Å ⁻³)	3.60, −2.85

$$^a R(F) = \frac{\sum ||F_o| - |F_c||}{\sum |F_o|}$$

$$^b R_w(F_o^2) = \left[\frac{\sum [w(F_o^2 - F_c^2)^2]}{\sum w F_o^4} \right]^{1/2}; w^{-1} = \left[\sigma^2(F_o^2) + (0.0419p)^2 + 0.2623p \right]$$

$$\text{where } p = \left[\max(F_o^2, 0) + 2F_c^2 \right] / 3.$$

Table 8-2 Atomic coordinates and equivalent isotropic displacement parameters for Hf(Si_{0.5}As_{0.5})As

Atom	Wyckoff position	Occupancy	<i>x</i>	<i>y</i>	<i>z</i>	<i>U</i> _{eq} (Å ²) ^a
Hf	2 <i>c</i>	1	¼	¼	0.25606(6)	0.0092(3)
Si/As1	2 <i>a</i>	0.52(1)/0.48(1)	¾	¼	0	0.0114(6)
As2	2 <i>c</i>	1	¼	¼	0.6148(2)	0.0086(4)

^a *U*_{eq} is defined as one-third of the trace of the orthogonalized *U*_{*ij*} tensor.

Table 8-3 Selected interatomic distances (Å) in Hf(Si_{0.5}As_{0.5})As^a

Hf-As2 (×4)	2.7545(6)
Hf-As2	2.852(1)
Hf- <i>X</i> (×4)	2.8260(5)
<i>X</i> - <i>X</i> (×4)	2.5746(4)

^a *X* represents the disordered site containing 0.5 Si and 0.5 As1.

8.2.3 Property Measurements

The electrical resistivity along the length of a flat needle-shaped crystal (corresponding to the symmetry-equivalent [100] or [010] directions, or the in-plane resistivity, ρ_{ab}) having dimensions $1.9 \times 0.2 \times 0.1$ mm was measured from 2 to 300 K by standard four-probe techniques on a Quantum Design PPMS system equipped with an ac transport controller (Model 7100). The current was 100 μ A and the frequency was 16 Hz. Measurement of the out-of-plane resistivity ρ_c was precluded by the habit and dimensions of the available crystals. The magnetic susceptibility was measured on a ground sample of the crystals (~ 100 mg) from 2 to 300 K on a Quantum Design 9T-PPMS dc magnetometer/ac susceptometer under a 10 kOe field. The susceptibility was corrected for contributions from the holder and the core diamagnetism of the sample.

8.2.4 X-ray Photoelectron Spectroscopy (XPS)

XPS measurements were made on a Kratos AXIS 165 spectrometer fitted with a monochromatic Al K α X-ray (1486.7 eV) source. The resolution of this instrument has been determined to be 0.4 eV. The typical precision of binding energies (BE) in this instrument is better than ± 0.1 eV and the area analyzed was $\sim 700 \times 400 \mu\text{m}^2$.

Plate-shaped crystals (each with surface area $> 1 \times 1 \text{ mm}^2$) were affixed onto a Cu sample holder by C tape. The samples were connected with silver paint (DuPont Electronics) directly to the Cu holder, ensuring electrical contact with ground to minimize charging effects. After being loaded into the spectrometer, the samples were cleaned by Ar⁺ ion sputtering (4 kV accelerating voltage, 1–10 mA current) to reduce the concentration of surface oxides and other contaminants (e.g., C, I) present. Different currents were used to evaluate whether preferential sputtering of the light elements or

reduction occurred. Neither effect was observed and survey spectra from multiple samples indicated the composition of the surface was $\text{HfSi}_{0.6(1)}\text{As}_{1.3(2)}$, which agrees with the bulk composition when the accuracy of the measurement is considered. The samples were not annealed after sputter-cleaning because the constituent elements (particularly Hf, but also Si) were found to be quite reactive in the vacuum chamber of the spectrometer at room temperature, even though the base pressure was $\sim 10^{-7}$ Pa, producing small amounts of surface oxide over time. This phenomenon has also been observed during XPS studies of Hf metal.²²⁶ Annealing would only enhance this contamination and so was not performed. High-resolution spectra of the As 3d, Si 2p, and Hf 4f core lines and of the valence band were collected with a pass energy of 20 eV, a step size of 0.05 eV, a sweep time of 180 s, and an energy envelope of 10–20 eV. All spectra were analysed with the CasaXPS software program.¹¹⁰ During data analysis, the samples were calibrated using the C 1s line arising from adventitious C with a fixed value of 284.8 eV. Because As Auger signals overlap the C 1s line in this system, the calibration was checked by setting the maximum of the first derivative of the valence band on the low BE side of the spectrum to 0 eV, which represents the Fermi edge. This is an accepted calibration method for metallic compounds such as the one under study.¹³⁴ A Shirley-type function was applied to remove the background arising from energy loss and spectra were fitted using a combined Gaussian (70%) and Lorentzian (30%) line profile. For comparison purposes, the Hf 4f spectrum from Hf metal (99.5% (excluding 3% Zr); Alfa-Aesar) was also collected using the same sample preparation and XPS settings discussed above.

8.2.5 Photoemission Spectroscopy (PES)

Valence band photoemission spectra at different X-ray excitation energies (from 500 to 255 eV) were collected at the Canadian Light Source (CLS) in Saskatoon, Saskatchewan, using the spherical grating monochromator (SGM) undulator beamline, 11-ID.1,¹⁵³ and a Scienta 100 hemispherical analyser equipped with a channel plate detection system. Changing the excitation energies modulates the photoionization cross-section and separates the valence contributions arising from Hf, As, and Si. The monochromatized photon flux of this beamline is $\sim 10^{12}$ photons/second at 250 eV and 5×10^{12} photons/second at 500 eV. An aggregate of needle-shaped crystals was mounted on the sample holder with TorrSeal epoxy. Because the sample is insulated by the epoxy, it was connected with C tape to the grounded stage to reduce charging effects. After curing, the sample was loaded into the introduction chamber attached to the analytical chamber of the spectrometer. Once a suitable pressure was achieved in the introduction chamber ($\sim 10^{-7}$ Pa), the sample was scraped *in situ* in the introduction chamber using glass paper to produce a clean surface appropriate for photoemission experiments and then transferred to the analysis chamber. The cleanliness of the sample was monitored by examining the Hf 4f spectrum. The valence band spectra were measured with a pass energy of 100 eV, an energy step size of 0.02 eV, and a dwell time of 33 ms. At 500 eV, the overall resolution, including analyser and beamline contributions, was ~ 0.16 eV, measured using the Fermi edge of a clean Au sample. The beamline exit setting used, 20 μm , gives a spot size on the sample of $\sim 1 \text{ mm} \times 80 \mu\text{m}$. Resonant photoemission was performed by examining the valence band with an excitation energy equal to the Hf N_3 ($4p_{3/2}$) absorption peak (384 eV), which was determined by collecting a total electron

yield (TEY) X-ray absorption spectrum, compared to that obtained with an excitation energy just below the absorption edge (360 eV). To directly compare the spectra, all signal intensities were normalized to the incident photon flux. Because the sample is metallic, all valence band spectra were aligned by setting the maximum in the first derivative of the low binding energy side of the spectra to be equal to 0 eV (Fermi edge).

8.2.6 Band Structure Calculations

To help interpret the valence band spectra, tight-binding linear muffin-tin orbital band structure calculations were performed within the atomic spheres approximation (TB-LMTO ASA).⁴⁰ Contributions from the Si 3s, 3p; As 4s, 4p; and Hf 5d orbitals to the density of states were extracted. Because mixed occupancy is problematic to treat, three ordered models were considered in which the disordered site is occupied by: (i) As atoms only (“HfAs₂”), (ii) Si atoms only (“HfSiAs”), or (iii) alternating Si and As atoms with only heteroatomic Si–As bonding present (“Hf(Si_{0.5}As_{0.5})As”). In the last model, the space group was chosen to be $P\bar{4}m2$ (No. 115) and the atomic positions were: Hf, 2g ($\frac{1}{2}$, 0, -0.2651); Si, 1b ($\frac{1}{2}$, $\frac{1}{2}$, 0); As1, 1a (0, 0, 0); As2, 2g ($\frac{1}{2}$, 0, 0.3851). The calculations were performed with 245 *k* points in the irreducible portion of the Brillouin zone for the first model and 1152 *k* points for the other two models.

8.3 Results and Discussion

8.3.1. Synthesis and Crystal Structure

Hf(Si_{0.5}As_{0.5})As is a new ZrSiS-type representative, augmenting the three other examples, ZrSi_{0.7}Sb_{1.3}, ZrGeSb, and HfGeSb,^{57, 227} known in the ternary systems (Zr, Hf)–(Si, Ge)–(As, Sb). As in the synthesis of other Si-containing compounds of this structure type,^{54, 57} Hf(Si_{0.5}As_{0.5})As can also be formed through a deleterious reaction of

Hf and As with the fused-silica tube at high temperature. The nonstoichiometry suggests the possibility of a phase width, which was investigated by carrying out a series of reactions with compositions $\text{Hf}(\text{Si}_x\text{As}_{1-x})\text{As}$ ($0.1 \leq x \leq 1$). Powder XRD analysis established a small homogeneity range of $0.5 \leq x \leq 0.7$ where single-phase $\text{Hf}(\text{Si}_x\text{As}_{1-x})\text{As}$ was formed. Below $x = 0.5$, HfAs_2 and $\text{Hf}(\text{Si}_{0.5}\text{As}_{0.5})\text{As}$ were formed, whereas above $x = 0.7$, $\text{Hf}(\text{Si}_{0.7}\text{As}_{0.3})\text{As}$ was found with Si and HfAs. The cell parameters, calculated using the program UNITCELL,²²⁸ range from $a = 3.6279(6)$ Å and $c = 8.135(2)$ Å for $\text{Hf}(\text{Si}_{0.5}\text{As}_{0.5})\text{As}$ to $a = 3.6115(5)$ Å and $c = 8.160(2)$ Å for $\text{Hf}(\text{Si}_{0.7}\text{As}_{0.3})\text{As}$.

The ZrSiS -type structure adopted by MAB compounds such as $\text{Hf}(\text{Si}_{0.5}\text{As}_{0.5})\text{As}$, shown in Figure 8-1, can be described in terms of a stacking of square nets, those containing the A (Si/As1) atoms being twice as dense as those containing the M (Hf) or B (As2) atoms. The distances within the denser square net ($2.5746(4)$ Å) are indicative of weak bonding, whereas those within the other nets ($3.6410(5)$ Å, equal to the a parameter) are too far to be significant. The disorder of Si and As atoms within the A net implies that Si–Si, Si–As, and As–As bonding are operative. The Hf atoms are nine-coordinate, at the centres of monocapped square antiprisms connected in a head-to-head and tail-to-tail configuration. The distance to the capping atom ($2.852(1)$ Å) is only slightly longer than to the other atoms ($2.7545(6)$ – $2.8260(5)$ Å), implying strong bonding along all directions in the structure.

Size effects account for some of the structural features in $\text{Hf}(\text{Si}_{0.5}\text{As}_{0.5})\text{As}$. Si and As have sufficiently similar sizes (metallic radii $R_1 = 1.17$ Å for Si, 1.21 Å for As)³⁷ that they readily disorder within the denser A net, but the less dense B net contains

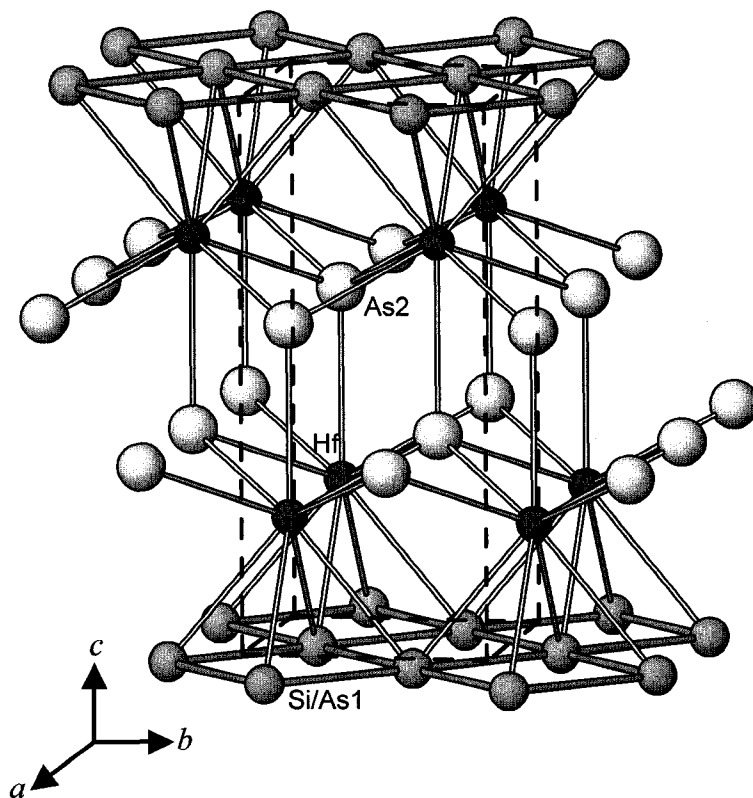


Figure 8-1 Structure of $\text{Hf}(\text{Si}_{0.5}\text{As}_{0.5})\text{As}$ viewed down the a direction. Like other MAB compounds with the ZrSiS -type structure, it consists of a stacking of nets of M (Hf), A (Si/As1), and B (As2) atoms.

exclusively the slightly larger As atoms. An analogous type of disorder has been observed previously in $\text{Zr}(\text{Si}_{1-x}\text{As}_x)(\text{As}_y\text{Te}_{1-y})$.⁵⁴ As seen above in the trends in cell parameters, as the larger As atoms are substituted for Si in the denser square net on going from $\text{Hf}(\text{Si}_{0.7}\text{As}_{0.3})\text{As}$ to $\text{Hf}(\text{Si}_{0.5}\text{As}_{0.5})\text{As}$, the expansion of a is accompanied by a contraction in c , which is related to the relief of steric crowding as the Hf-centred square antiprisms become flattened to allow the capping atoms to approach more closely.⁵⁴ The absence or presence of this interaction with the capping ligand has been used to classify ZrSiS-type structures as 2D or 3D, respectively, the transition occurring at a critical c/a ratio of ~ 2.3 .⁵⁴ For $\text{Hf}(\text{Si}_x\text{As}_{1-x})\text{As}$ ($0.5 \leq x \leq 0.7$), the c/a ratios of 2.24–2.26 are lower than the critical value and consistent with a 3D structure.

Electronic effects also play an important role, through the optimization of homoatomic and heteroatomic bonding interactions within and between the square nets. In ZrSiS-type structures, electronic stabilization is favoured by placement of the less electronegative main-group element in the denser A net,⁵⁵ consistent with the observed structure of $\text{Hf}(\text{Si}_{0.5}\text{As}_{0.5})\text{As}$. In some cases, geometrical distortion of the square net occurs to maximize bonding, as in GdPS or $\text{SmTe}_{1.84}$,^{55, 215} but this does not happen in $\text{Hf}(\text{Si}_{0.5}\text{As}_{0.5})\text{As}$. The Si/As disorder in the $2a$ site spans only a narrow range (0.7:0.3 to 0.5:0.5) and the parent binary phases adopt structure types (HfSi_2 (ZrSi₂-type); HfAs_2 (PbCl₂-type))²²⁹ different from the ternary phase, satisfying two of the criteria invoked by the concept of differential fractional site occupancy (DFS) stabilization.²³⁰ Although cationic DFS-stabilized materials are now well known,^{230, 231} anionic DFS-stabilized materials such as $\text{Hf}(\text{Si}_{0.5}\text{As}_{0.5})\text{As}$ are still relatively rare.^{231, 232} The different structure type adopted by $\text{Hf}(\text{Si}_{0.5}\text{As}_{0.5})\text{As}$ can be attributed to a competition between the anion-

anion (Si–Si, As–As, Si–As) bond energies and the configurational (non-kinetic) entropy of the disordered site.²³⁰ The distances within the denser A net in Hf(Si_{0.5}As_{0.5})As are somewhat longer than typical Si–Si (2.3 Å) or As–As (2.4 Å) covalent bonds,³⁷ lowering the contribution of the bond enthalpy. However, the random distribution of Si and As atoms within this net raises the configurational entropy, providing a stabilization of the Gibbs free energy of the system.

8.3.2 Electrical and Magnetic Properties

Most ZrSiS-type compounds are expected to be metallic, as predicted by band structure calculations on this (*vide infra*) and related members.⁵⁵ The profile of the in-plane electrical resistivity (ρ_{ab}) for a single crystal of Hf(Si_{0.5}As_{0.5})As, shown in Figure 8-2a, confirms metallic behaviour. The resistivity values are relatively high ($\rho_{300\text{K}} = 1.9 \times 10^{-4} \text{ } \Omega \text{ cm}$) and the residual resistivity ratio ($\text{RRR} = \rho_{300\text{K}}/\rho_{2\text{K}} = 2.0$) is small, consistent with the high degree of disorder in this material. The magnetic susceptibility curve, shown in Figure 8-2b, indicates essentially temperature-independent Pauli paramagnetism ($\chi = 8 \times 10^{-4} \text{ emu/mol}$), with a slight upturn at low temperatures most likely arising from small amounts of paramagnetic impurities.

8.3.3 Electronic Structure

In Hf(Si_{0.5}As_{0.5})As, if Hf is assumed to transfer four valence electrons, the Si and As atoms together are still deficient by $\Delta = 2.5$ electrons relative to filled octets. The As atoms in the B net are too far apart (3.6410(5) Å) to be bonding and can be assigned to be isolated As³⁻ anions. A charge-balanced ionic formulation would thus be Hf⁴⁺(Si_{0.5}As_{0.5})¹⁻As³⁻, implying that anion-anion bonding must develop within the A net among the disordered Si and As atoms to complete their octets. Although the distances

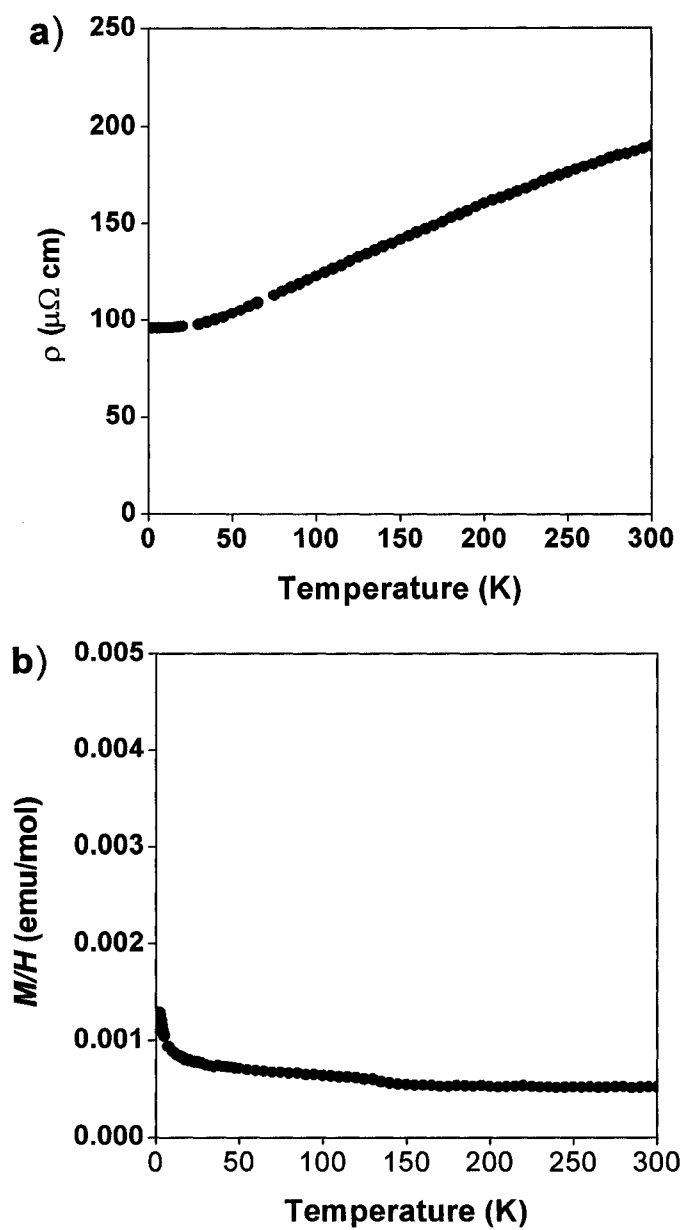


Figure 8-2 (a) Electrical resistivity (within the ab plane) and (b) magnetic susceptibility of Hf(Si_{0.5}As_{0.5})As.

within the A net (2.5746(4) Å) are smaller than those within the B net, they are certainly still too long to be considered $2c-2e^-$ Si-Si, Si-As, or As-As bonds (~ 2.4 Å).³⁷ These distances are instead consistent with multicentre bonding of fractional bond character. Within such hypervalent bonded square nets, the ideal electron count is six, corresponding to the presence of “one-electron bonds”.⁵⁵ This electron count is consistent with the charge assignment of As^{1-} but not quite with Si^{1-} ; however, a slight deviation is energetically permissible given that only nonbonding or weakly antibonding levels are affected. Although simple electron-counting schemes such as this are helpful in developing a first approximation to the electronic structure and can be remarkably successful in rationalizing bonding in complex solid-state structures, they overemphasize the degree of charge transfer that takes place. True charges are not expected to be as extreme as implied by these ionic formulations, and it is our goal to evaluate charges by experimental means and assess the validity of this approach.

8.3.3.1 As 3d and Si 2p XPS Spectra

The As 3d core-line spectrum of $Hf(Si_{0.5}As_{0.5})As$ is shown in Figure 8-3a. There is only one signal, split into a doublet representing the $3d_{5/2}$ and $3d_{3/2}$ spin-orbit coupled final states, which were fitted with two peaks each having a FWHM of ~ 0.9 eV in an intensity ratio equal to the theoretical value of 3:2. On the high BE side of the spectrum, the asymmetric lineshape may be attributed to contributions from As suboxides formed during the experiment (as has also been observed in surface studies of GaAs),²³³ or it may be related to the metallic nature of $Hf(Si_{0.5}As_{0.5})As$, as discussed below in the context of the Hf spectrum.

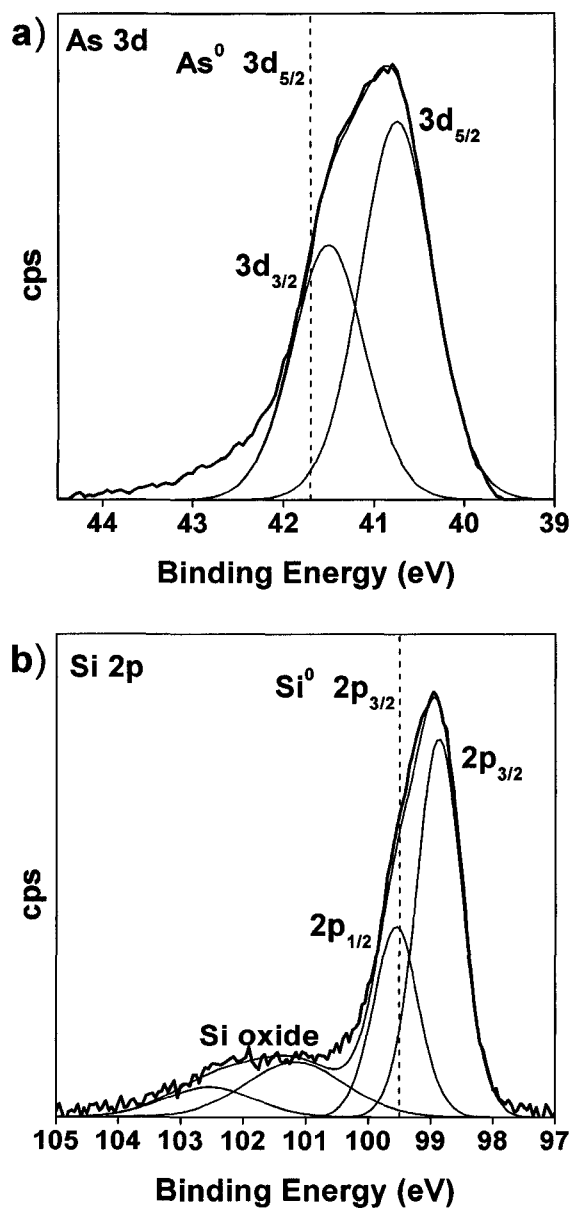


Figure 8-3 (a) As 3d and (b) Si 2p core-line spectra of $\text{Hf}(\text{Si}_{0.5}\text{As}_{0.5})\text{As}$, fitted with component peaks representing the spin-orbit coupled final states. The binding energy of elemental As or Si is marked by a vertical dashed line.

The BE of the As $3d_{5/2}$ peak is 40.8 eV, which is considerably lower than that in elemental As (41.7(2) eV, dashed line in Figure 8-3a),¹¹⁶ indicating that As is anionic in Hf(Si_{0.5}As_{0.5})As. In comparison to the BE of other As-containing compounds having known charges (e.g., As, As₂O₃, As₂O₅)¹¹⁶ and assuming a linear relationship, this value indicates an estimated As charge of approximately 1-. The presence of only one signal suggests that both As1 and As2 atoms adopt the same charge, contrary to the prediction made by the electron-counting scheme described above. The lower than expected charge implies significant covalent character in the Hf-As bonds and incomplete charge transfer from Hf to As. Caution must be exercised in interpreting charges derived from binding energies. Although binding energies are principally influenced by the charge on the atom of interest, they also depend on other factors such as the identity of the ligand, variations in the coordination environment, and final state relaxation effects.¹³⁴ For example, the As $3d_{5/2}$ BE is 45.3 eV in AsBr₃ and 47.1 eV in AsF₃,¹¹⁶ a substantial difference even though the nominal charge of As is 3+ in both compounds. Other analyses must therefore be performed, as described below, to substantiate the charge assignments derived from core-line binding energies.

The Si 2p core-line spectrum (Figure 8-3b) also shows one set of spin-orbit split peaks, representing the $2p_{3/2}$ and $2p_{1/2}$ final states, fitted with a FWHM of ~0.8 eV in an intensity ratio of 2:1. The Si $2p_{3/2}$ BE is 98.9 eV, about 0.6 eV lower than that in elemental Si (99.5(3) eV, dashed line in Figure 8-3b)¹¹⁶ and indicative of anionic Si. As before, binding energies were compared with other Si-containing compounds,¹¹⁶ resulting in an estimated Si charge of approximately 1- in Hf(Si_{0.5}As_{0.5})As. The Si $2p_{3/2}$ BE in Hf(Si_{0.5}As_{0.5})As is similar to that in TiSi₂.²³⁴ As well, the valence band spectrum

of TiSi_2 reveals occupied Ti 3d states,²³⁴ implying the Si charge is not as large as $2-$, as predicted by simple electron counting.

The smaller negative BE shift relative to the elements observed for the Si $2p_{3/2}$ line ($\Delta\text{BE} = 0.6$ eV) than for the As $3d_{5/2}$ line ($\Delta\text{BE} = 0.9$ eV) can be related to the difference in electronegativity between Si and As.³⁷ Because As is more electronegative, it attracts a greater amount of electron density from the neighbouring Hf and Si atoms, lowering the As 3d BE. On the other hand, because Si is less electronegative, the Hf–Si bonds are more covalent than the Hf–As bonds which reduces the screening of the Si nuclear charge by the valence electrons.

On the high BE side, the Si 2p spectrum (Figure 8-3b) also contains a component fitted by split $2p_{1/2}$ and $2p_{3/2}$ spin-orbit peaks, which may be attributed to Si oxides formed during data collection by reaction of the surface with residual oxygen in the vacuum chamber. Although the $2p_{3/2}$ BE of 101.2 eV is much lower than in bulk SiO_2 (103.5(3) eV),¹¹⁶ it is similar to that in Si suboxides observed during analysis of Si nanocrystals.^{235, 236} Only one set of broad spin-orbit split peaks was used to represent the Si suboxide component even though it is known that such oxides can have a variety of Si charges.²³⁶

8.3.3.2 Hf 4f XPS Spectra

The Hf 4f spectrum of $\text{Hf}(\text{Si}_{0.5}\text{As}_{0.5})\text{As}$ (Figure 8-4a) is compared with that of Hf metal (Figure 8-4b). Both spectra show two asymmetric spin-orbit coupled final states, $4f_{7/2}$ and $4f_{5/2}$, fitted by component peaks with a FWHM of ~ 0.7 – 0.8 eV in a fixed intensity ratio of 4:3. The asymmetric lineshapes are characteristic of not only metallic compounds (Chapter 3) but also small band-gap semiconductors that possess a

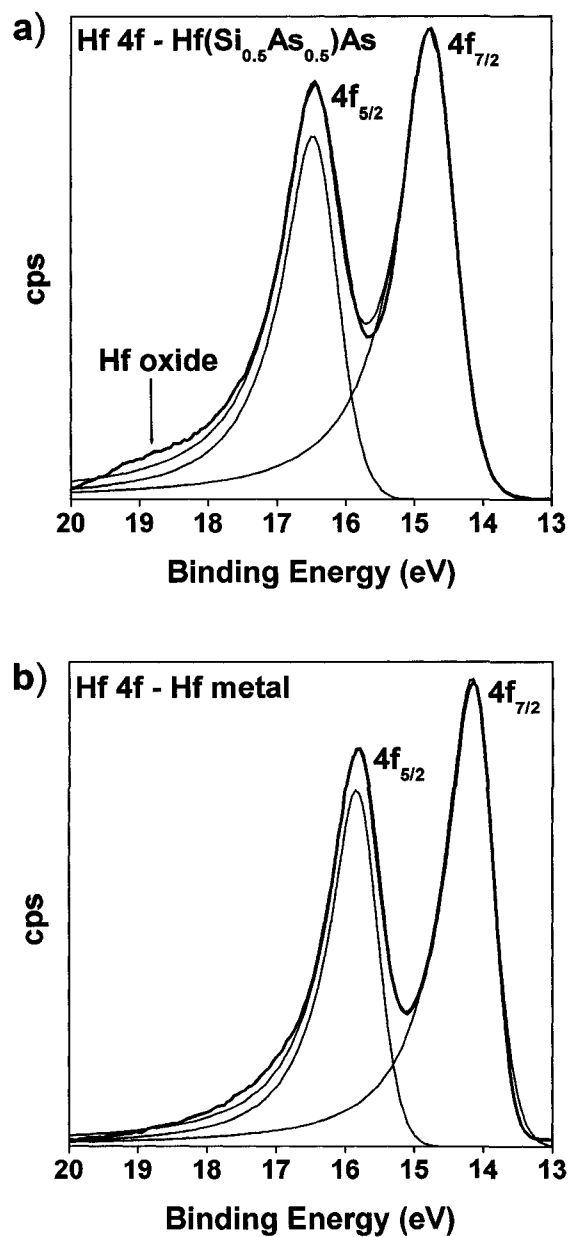


Figure 8-4 Hf 4f core-line spectra of (a) Hf(Si_{0.5}As_{0.5})As and (b) Hf metal, fitted with asymmetric component peaks representing the 4f_{7/2} and 4f_{5/2} final states.

delocalized electronic structure (Chapter 7). As described in earlier chapters, this asymmetry (first described by Doniach and Šunjić) arises when valence electrons, interacting with the core hole, are excited and scattered from filled states below the Fermi edge into empty conduction states.¹¹⁷ Metallic compounds, such as $\text{Hf}(\text{Si}_{0.5}\text{As}_{0.5})\text{As}$, have a continuum of states above the Fermi edge, so that an asymmetric tail comprising many closely spaced states is observed instead of a few distinct satellite peaks.¹¹⁸ In addition to the asymmetric peaks, other states at higher BE are seen in the spectra and may be attributed, as in the case of the Si 2p spectrum above, to small amounts of metal suboxide contamination. Sputter-cleaned Hf metal shows the same behaviour.²²⁶

The Hf $4f_{7/2}$ BE is 14.8 eV in $\text{Hf}(\text{Si}_{0.5}\text{As}_{0.5})\text{As}$, higher than in Hf metal (14.2 eV) and consistent with cationic Hf. The magnitude of this shift is smaller than expected for a Hf charge of 4+ (obtained from simple electron counting). For comparison, the measured Hf $4f_{7/2}$ BE for HfO_2 (Alfa-Aesar) is 16.7 eV. The delocalized electronic structure of $\text{Hf}(\text{Si}_{0.5}\text{As}_{0.5})\text{As}$, which is metallic, gives rise to very effective screening of the Hf nuclear charge, complicating the assignment of the Hf atomic charge solely on the basis of a BE analysis.

8.3.3.3 Valence Band XPS Spectra and LMTO Band Structure Calculations

When the core-line binding energy shifts do not give definitive information about valence states and when covalent bonding is significant, analysis of the valence band spectra can provide useful insight about the electronic structure, as was shown in Chapters 3, 6, and 7 for other intermetallic compounds. The valence band spectrum of $\text{Hf}(\text{Si}_{0.5}\text{As}_{0.5})\text{As}$ is shown in Figure 8-5, with its components labelled from 1 to 4. To interpret these components, the spectrum can be compared with band structures

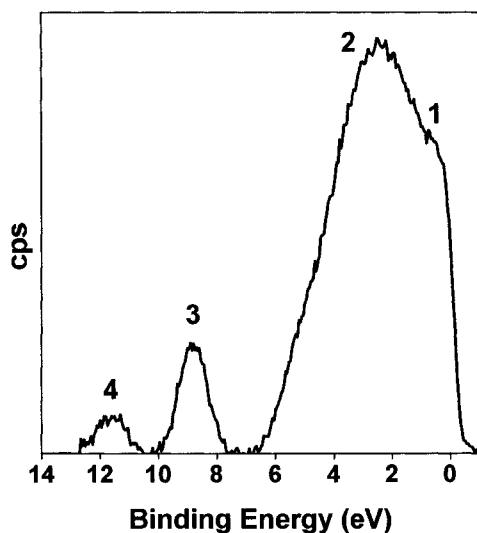


Figure 8-5 XPS valence band spectrum of $\text{Hf}(\text{Si}_{0.5}\text{As}_{0.5})\text{As}$ collected using $\text{Al K}\alpha$ X-rays.

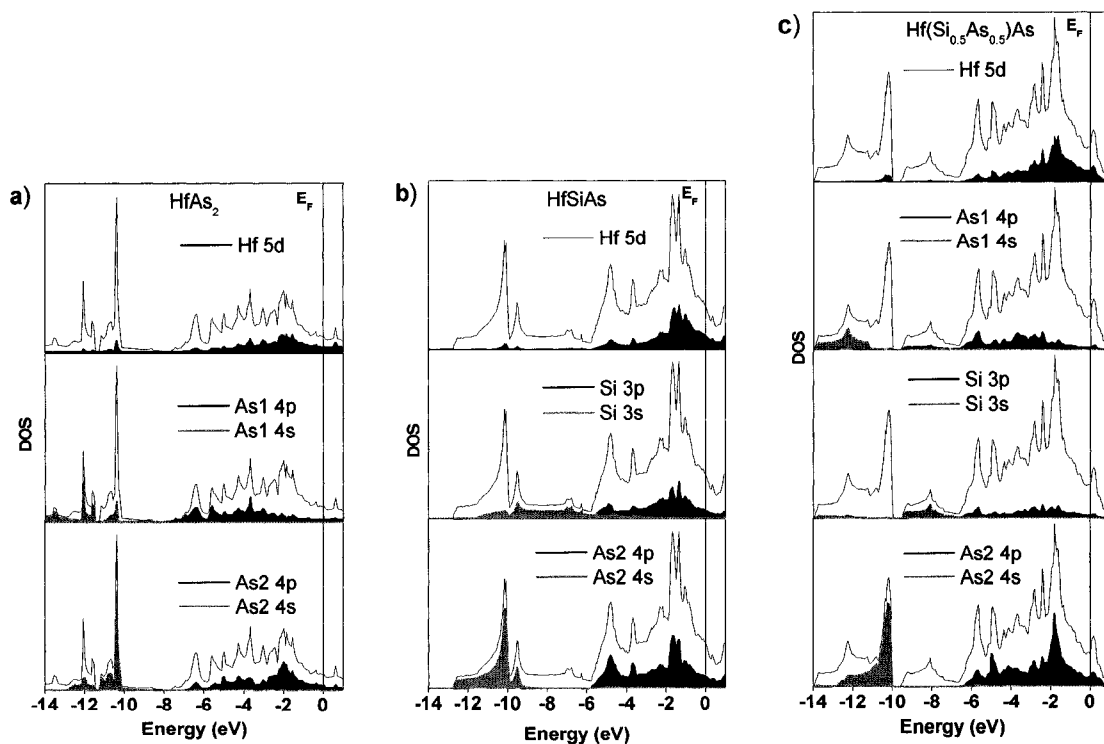


Figure 8-6 Band structures of (a) HfAs_2 , (b) HfSiAs , and (c) $\text{Hf}(\text{Si}_{0.5}\text{As}_{0.5})\text{As}$. The projections of different states are shown by the shaded regions and the total density of states by the thin line.

calculated for three ordered models differing in the occupancy of the disordered site and thereby the type of bonding interactions present in the denser square net: (i) “HfAs₂” (As–As bonding only), (ii) “HfSiAs” (Si–Si bonding only), and (iii) “Hf(Si_{0.5}As_{0.5})As” (Si–As bonding only) (Figure 8-6). All three models reproduce the general features of the valence band spectrum, if variations in the photoionization cross-sections of different elements, which affect intensities,⁷⁴ are taken into consideration.

The low intensity shoulder in Figure 8-5 (component 1) is located at the Fermi edge (0 eV), consistent with the metallic nature of this compound. The band structures reveal occupied Hf 5d states in the valence band, arguing against the presence of Hf⁴⁺. The intense broad peak (component 2) represents As 4p and Si 3p states. The low BE part of this peak originates from As₂ 4p states of the less dense square net, whereas the high BE part originates from Si 3p and As₁ 4p states of the denser square net. The difference in energy arises because stronger bonding interactions in the denser square net stabilize the Si/As₁ states (thus increasing their BE). If only Si–As bonding is active in this square net, the Si 3s states lie higher in energy than the As₂ 4s states (Figure 8-6c) but introduction of Si–Si bonding shifts the Si 3s states to lower energy so that they overlap the As₂ 4s states (Figure 8-6b). Thus, component 3 in Figure 8-5 is assigned to have contributions from both Si 3s and As₂ 4s states. Finally, component 4 is unambiguously assigned to arise from As₁ 4s states, which occur at the deepest energies in the band structures (Figures 8-6a and 8-6c).

8.3.3.4 Photoemission Spectroscopy (PES)

In Figure 8-5, the sharpness of the low BE shoulder (component 1) representing Hf 5d states suggests that only a single Hf 5d_{5/2} peak instead of a spin-orbit doublet (5d_{5/2}

and $5d_{3/2}$) is present in this region. This feature was investigated further with resonant PES conducted on the SGM beamline at the CLS. Resonant photoemission exploits optically allowed ($\Delta l = \pm 1$) transitions from a core level to a partially occupied band. If the occupancy of the Hf 5d band is N , then at photon energies where a Hf 4p core level electron can be excited into an empty 5d state, two possible photoemission processes can co-exist. In addition to the “normal” photoemission process, $4p^6 5d^N + h\nu \rightarrow 4p^6 5d^{N-1} + e^-$, the $5d^{N+1}$ excited state that can also be reached with appropriately selected photon energies can decay via an autoionization process: $4p^6 5d^N + h\nu \rightarrow 4p^5 5d^{N+1} \rightarrow 4p^6 5d^{N-1} + e^-$. The final state of this process is the same as that in the normal photoemission process, i.e., single ionization, not the double ionization produced by a normal Auger decay, and by conservation of energy the emitted electrons have the same kinetic energy as those of the “normal” photoemission process. The practical result is an increase in the 5d photoemission signal at photon energies corresponding to allowed 4p–5d transitions. The effect is well known, and very large, for 4d→4f transitions in lanthanide materials,^{237, 238} but is also observed as a smaller, but significant, effect for other allowed transitions, e.g., 3p→3d in Ti and 4f→5d in Ir.^{239, 240}

Figure 8-7 shows the resonant photoemission spectra of Hf(Si_{0.5}As_{0.5})As collected using an excitation energy of 384 eV (equal to the Hf N₃ (4p_{3/2}) absorption peak as determined by a X-ray absorption measurement) and 360 eV (below the Hf N₃ absorption edge). The region of the valence band spectra shown represents where the Hf 5d and As₂ 4p states were proposed to reside, based on comparison of Figure 8-5 to Figure 8-6. As can be seen, the peak found at the Fermi edge (0 eV) is enhanced when the excitation energy is increased from 360 eV to 384 eV, providing further evidence that it represents a

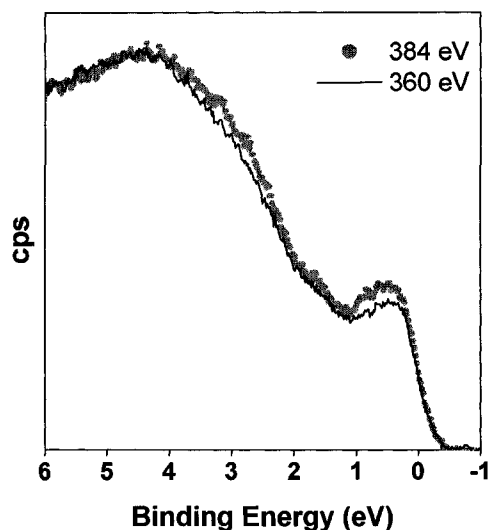


Figure 8-7 Resonant PES spectra of Hf(Si_{0.5}As_{0.5})As collected using an excitation energy equal to the Hf N₃ (4p_{3/2}) absorption edge (384 eV) and one just below the absorption edge (360 eV). The spectral intensities have been normalized to account for differences in incident photon flux.

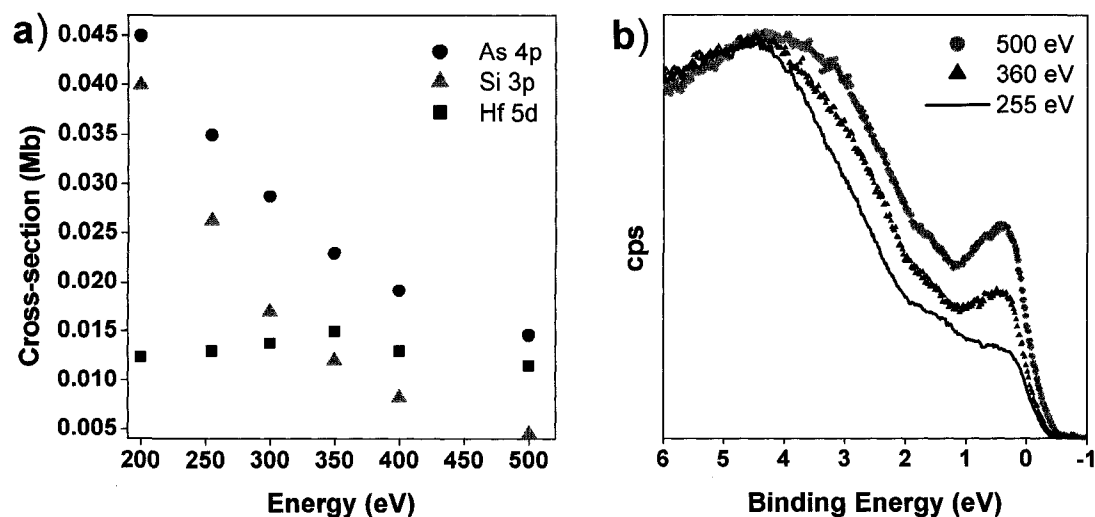


Figure 8-8 (a) Variation in the Hf 5d, As 4p, and Si 3p photoionization cross-sections from 250 eV to 500 eV⁷⁴ and (b) PES valence band spectra collected using excitation energies equal to 255 eV, 360 eV, and 500 eV. The spectra have been normalized to the As 4p peak.

Hf 5d state. Between 4 and 1 eV, there is also a small enhancement, implying contributions of the Hf 5d band in this region. The enhancement is not as large as would be expected if the excitation energy were equal to that of the 5p absorption edge, because the lifetime of the autoionization decay process experienced here is longer than that of a Coster-Kronig decay process.⁶⁰ Nevertheless, the increase in the Hf 5d intensity is greater than would be expected on the basis of only the difference in Hf 5d and As 4p photoionization cross-sections at the two energies.⁷⁴

The valence contributions in $\text{Hf}(\text{Si}_{0.5}\text{As}_{0.5})\text{As}$ were further assessed by varying the excitation energy, which changes the orbital photoemission cross-sections (Figure 8-8a) of different elements, allowing them to be identified. Valence band spectra collected at different excitation energies ranging from 500 to ~250 eV are shown normalized to the As2 4p intensity (Figure 8-8b). Although the surface was scraped in vacuum, a small amount of surface oxide was present, limiting our ability to examine the As1 4p/Si 3p and As 4s/Si 3s components. However, the region from 0 to 6 eV was unobscured, permitting identification of the Hf 5d and As2 4p states. As the excitation energy was changed from 500 to 255 eV, the intensity of the Hf 5d peak located at the Fermi edge diminishes significantly compared to the As2 4p peak, in accordance with the variation in cross-sections (Figure 8-8a). The reduction in intensity indicates that the region from 4 to 0 eV has contributions from Hf 5d states, in agreement with the resonant photoemission results. If the feature located at the Fermi edge is identified to be the Hf 5d_{5/2} peak, then the higher BE signal can be assigned to be the 5d_{3/2} peak (i.e., a Hf 5d spin-orbit doublet is observed). These results provide further evidence against a Hf^{4+} species.

8.3.3.5 Fitting of the Valence Band Spectrum

The core-line binding energies indicate charges of 1– for Si and As, and the valence band spectra (XPS and PES) indicate a charge of 2+ for Hf, as implied by the presence of occupied Hf 5d states and by charge balance with the anions. These charge assignments can be tested further by fitting the valence band spectrum. In Chapters 3, 6, and 7, this type of analysis was proven useful in extracting the atomic charges in other intermetallic compounds. As shown in Figure 8-9, the valence band spectrum was fitted with component peaks (labelled 1 to 6) representing the different states identified by PES and the band structure calculations. The widths and energies were refined as described in Chapter 3 (Section 3.3.4), and the goodness of the fit was monitored by the RSD between the simulated and experimental spectra with a low RSD indicating a good fit. Peaks 1 and 2 represent the Hf 5d_{5/2} and 5d_{3/2} spin-orbit doublet, fitted with asymmetric lineshapes in accordance with similar profiles observed in the Hf 4f spectrum (Figure 8-4a) and consistent with what has been observed in the valence band spectra of other transition metals (Chapter 3). The peak splitting was determined to be ~1 eV on the basis of the PES spectra (Figure 8-8b). Peak 3 represents the As 2p component. Peak 4 represents the Si 3p and As1 4p components. Because the separation between the spin-orbit split states, $np_{3/2}$ and $np_{1/2}$, is small, only a single peak was used to simplify the fitting of the np states. Peak 3 is more intense than peak 4 because the cross-section for As 4p is larger than for Si 3p when an excitation energy equal to that of Al K α X-rays is used (Table 8-4); ultimately, the difference in peak intensity depends on the ratio of As2 to As1 atoms, 2:1. Peak 5 represents both As2 4s and Si 3s states, and peak 6 represents

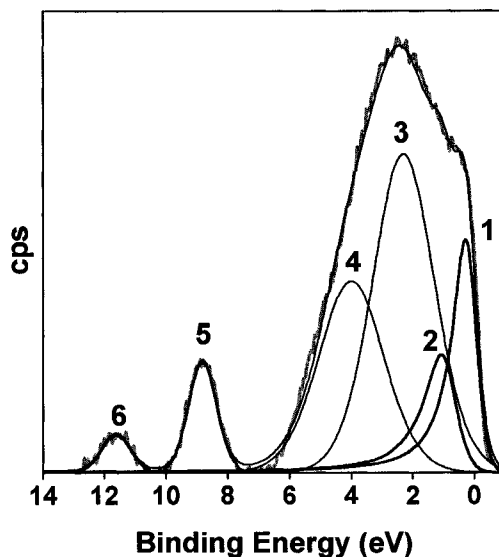


Figure 8-9 Fitted XPS valence band spectrum of $\text{Hf}(\text{Si}_{0.5}\text{As}_{0.5})\text{As}$ collected using $\text{Al K}\alpha$ X-rays. The assignments of the peaks labelled from 1 to 6 are discussed in the text and listed in Table 8-5. The experimental spectrum is represented by a thick grey line and the fitted envelope (simulated spectrum) by a thin black line.

Table 8-4 Atomic photoelectron cross-sections (σ)^{a,b}

Reference	74	73
Hf 5d	0.0024	0.0733
Si 3p	0.00017 (0.071)	0.0070 (0.095)
Si 3s	0.0010 (0.42)	0.0808 (1.10)
As 4p	0.0018 (0.75)	0.06045 (0.825)
As 4s	0.0017 (0.71)	0.1357 (1.85)

^a The cross-sections from reference 74 are in units of mega-barns (Mb) whereas the cross-sections from reference 73 are proportional to the C 1s cross-section of 13,600 barns.

^b The ratios of the cross-sections relative to the Hf 5d value are provided in parentheses. Between the two sets of values, only the magnitudes of the *ns* cross-sections relative to the Hf 5d cross-sections differ significantly.

the As1 4s state, on the basis of comparing the valence band spectrum to the band structure calculations (Figure 8-6).

The fitted peak areas can then be related to the total electron population in Hf(Si_{0.5}As_{0.5})As, yielding cation and anion charges. To do this, the intensities must first be corrected for variations in cross-section (σ) and inelastic mean free path (IMFP, λ):⁷⁵

$$C_i = \frac{I_i / (\sigma_i \lambda_i)}{\sum_{j=1}^n I_j / (\sigma_j \lambda_j)} \quad (8-1)$$

Because all observed photoelectron kinetic energies are similar throughout the valence band region, Eq 8-1 can be simplified to Eq 8-2 on the assumption that the IMFP values will be the same for all states:

$$C_i = \frac{I_i / (\sigma_i)}{\sum_{j=1}^n I_j / (\sigma_j)} \quad (8-2)$$

Here, I_i / σ_i represents the intensity of the peak for a given atomic component under consideration and $\sum_{j=1}^n I_j / \sigma_j$ represents the sum of all the corrected peak intensities in the complete valence band spectrum. (This method is a further simplified version of that initially proposed in Chapter 3.) Peak 4 was adjusted assuming a 1:1 ratio of Si 3p to As1 4p states, whereas peak 5 was adjusted assuming a 2:1 ratio of As2 4s to Si 3s states. Following Eq 8-2, the corrected and normalized component areas (C_i) were multiplied by the total valence electron population, which is 13.5 in the case of Hf(Si_{0.5}As_{0.5})As, to yield atomic charges. Two different sets of cross-sections were used (Table 8-4). The calculated electron populations per peak and the resulting average atomic charges

Table 8-5 Electron population of valence states in Hf(Si_{0.5}As_{0.5})As calculated using Eq 8 -2 and a total valence electron population of 13.5 e⁻.^a

State	Sample 1		Sample 2	
Cross-section (σ) reference	74	73	74	73
Hf 5d (peaks 1, 2)	1.5 [18.2]	1.8	1.9 [23.1]	2.3
As2 4p (peak 3)	5.1 [44.4]	5.2	4.8 [41.6]	4.9
As1 4p / Si 3p (peak 4)	5.8 [28.2]	6.0	5.8 [27.6]	5.8
As2 4s / Si 3s (peak 5)	0.9 [6.9]	0.4	0.8 [6.1]	0.4
As1 4s (peak 6)	0.2 [2.3]	0.1	0.2 [1.5]	0.1
Total Hf charge	2.5+	2.2+	2.1+	1.7+
Total anion charge [(Si _{0.5} As _{0.5})As]	2.5-	2.2-	2.1-	1.7-
Average charges ^b	2.1+ [Hf], 2.1- [(Si _{0.5} As _{0.5})As]			

^a The total peak areas of the peaks used to fit different states in the spectra are listed in square brackets.

^b Scaling of the *ns* cross-sections from Table 4 such that both sets are similar did not alter the calculated charges to any appreciable degree (<0.1).

determined from the spectrum shown in Figure 8-9 and from a second sample (not shown) are given in Table 8-5. These charges suggest the formulation $\text{Hf}^{2+}[(\text{Si}_{0.5}\text{As}_{0.5})\text{As}]^{2-}$, consistent with the values deduced earlier through analysis of the As 3d and Si 2p binding energies. Moreover, it appears that both As1 and As2 have the same charge of 1-, in agreement with the observation of a single set of spin-orbit split As 3d peaks (Figure 8-3a).

8.4 Conclusions

The metallic and Pauli-paramagnetic compound $\text{Hf}(\text{Si}_{0.5}\text{As}_{0.5})\text{As}$ is a new representative of the MAB series adopting the ZrSiS-type structure, exhibiting substitutional disorder of Si and As atoms within the denser square net of A atoms so that a narrow homogeneity range is possible in $\text{Hf}(\text{Si}_x\text{As}_{1-x})\text{As}$ ($0.5 \leq x \leq 0.7$). It augments the few examples of anionic DFSO-stabilized materials now known. XPS core-line binding energy shifts in the Si 2p and As 3d spectra suggest the presence of anionic Si^{1-} and As^{1-} . The Hf 4f spectrum showed an asymmetric lineshape to higher BE, indicative of electronic delocalization, which enhances screening of the nuclear charge and attenuates the BE shift making it difficult to determine the Hf charge. By comparison to band structure calculations, the valence band spectrum was decomposed into Hf 5d states at the Fermi edge, followed by As1, As2, and Si *np* and *ns* states. Valence band spectra collected at different excitation energies as well as resonant PES measurements revealed that Hf 5d_{5/2} and 5d_{3/2} spin-orbit doublet peaks were present in the uppermost region, nearest to the Fermi edge. With the different component states now identified and fitted in the valence band spectrum, their electron populations were calculated to yield the formulation $\text{Hf}^{2+}[(\text{Si}_{0.5}\text{As}_{0.5})\text{As}]^{2-}$. This charge assignment differs substantially from

that predicted by a simple electron-counting scheme, $\text{Hf}^{4+}(\text{Si}_{0.5}\text{As}_{0.5})^{1-}\text{As}^{3-}$, in which full electron transfer from Hf is assumed. Because X-ray spectroscopy provides an experimental probe and a more realistic evaluation of atomic charges, these results lead to the conclusions that: (i) MAB compounds with the ZrSiS-type structure, in general, possess substantial covalent bonding character, (ii) their metallic behaviour largely originates from hybridization of states from the atoms in the less dense square nets of M and B atoms, and (iii) the charges of the A and B atoms are similar despite their chemical inequivalence.

Chapter 9

Summary and Conclusions

9.1 X-ray Spectroscopy of Intermetallic Compounds

The bonding and charge distributions in intermetallic compounds have been examined by X-ray spectroscopy. Such techniques (XPS and XAS) have not been commonly applied to these types of compounds. This can be traced to the fact that shifts in binding or absorption energy are often small because of the covalent nature of the bonding and that earlier spectrometers lacked the resolution and precision to compare samples whose energy shifts were only a few tenths of an eV. Most previous XPS studies have focused on ionic compounds, where the BE shifts substantially as the oxidation state and coordination environment is changed (cf. Figure 2-6), facilitating interpretation of results. With the advent of better instrumentation, small variations in energy in intermetallic compounds can now be examined. More sophisticated spectral interpretations (e.g., examination of the Co $2p_{3/2}$ satellite intensity and fitting of valence band spectra) have also been developed to complement the binding energy and absorption energy analyses.

9.1.1 MnP-type Compounds

The charge distribution in binary MnP-type compounds can be formulated as $M^{1+}P^{1-}$ or $M^{3+}P^{3-}$, if P–P bonding is included or neglected, respectively. The core-line BE shifts and valence band spectra support the charge formulation of $M^{1+}P^{1-}$, in which $2c - 2e^-$ P-P bonds extend in zigzag chains (Chapter 3). The P $2p_{3/2}$ BE decreases gradually from CoP to CrP, as the M –P bond becomes more ionic (M becomes less electronegative) with the enhanced electron density on P leading to greater screening of the P photoemission site. These shifts were also interpreted with a charge potential model (Chapters 4 and 5), which takes into account interatomic and intraatomic effects.

The most appropriate electronegativity scale to interpret BE shifts is based on the Allred-Rochow definition:¹¹⁴

$$\chi = 0.359 \frac{Z_{eff}}{r^2} + 0.744 \quad (9-1)$$

Z_{eff} is the effective nuclear charge (reduced from the full nuclear charge through screening by electrons), r is the atomic radius, and the constants are included to scale to the more familiar Pauling electronegativities.¹¹⁴ Although differences in Allred-Rochow electronegativities accounted well for the BE shifts, some discrepancies were found. In particular, As is more electronegative than P on the Allred-Rochow scale,¹¹⁴ but the Co $2p_{3/2}$ BE shifts in $CoPn_3$ ($Pn = P, As, Sb$) could only be interpreted sensibly if the reverse were true (Chapter 5). That is, As is intermediate in electronegativity between P and Sb, consistent with the general trend of decreasing electronegativity down a group in the periodic table. The discrepancy may arise because Z_{eff} for As in Eq 9-1 is overestimated

by Slater's rules,¹⁷⁶ with the screening coefficient being too high for the As 3d electrons. Care must be exercised in using electronegativity values to interpret shifts in energy. As an experimental technique, XPS (and by extension, XAS) can be exploited to verify relative electronegativity values.

When a more electronegative metal (M) substitutes for a less electronegative one (M') in MnP-type compounds ($M_{1-x}M'_xP$), the P 2p_{3/2} BE and K-edge absorption energies decrease because the interatomic screening of the P photoemission site is reduced. In the first ever study to examine next-nearest neighbour effects in transition-metal phosphides (Chapter 4), the variation in the Madelung potential term arises from charge transfer from M' to M within the metal-metal bonding network in the MnP-type structure. The energy shifts were also interpreted on the basis of electronegativity differences, through a simplified version of the charge potential model (Eq 4-3). Between samples, the difference in the intraatomic term ($k\Delta q_i$) is $\chi_P - [(1-x)\chi_M + x\chi_{M'}]$ and the difference in the interatomic term ($\Delta\Sigma_{j\neq i} q_j/r_{ij}$), arising from $M' \rightarrow M$ charge transfer, is $\frac{(1-x)}{2}(\chi_M - \chi_{M'})$. This model helps explain how variations in charge transfer and in covalent bonding character affect binding and absorption energies. Although this equation can only account for relative differences in energy, it accurately predicts the P 2p_{3/2} BEs and K-edge absorption energies for a wide range of $M_{1-x}M'_xP$ compounds. (After data were collected on binary MP and ternary $Mn_{1-x}V_xP$ compounds, the P 2p_{3/2} BEs for $Co_{1-x}Mn_xP$ and $Co_{1-x}V_xP$ were predicted and confirmed by experiment.) Variations in intra- and interatomic screening of the P photoemission and absorption site were also examined in mixed arsenide phosphides ($MAs_{1-y}P_y$) with the MnP-type

structure (Chapter 5). Here, the P and As charges are influenced by As \rightarrow P charge transfer within the *Pn-Pn* bonding network found in this structure type. As in $M_{1-x}M'_xP$, next-nearest neighbour effects in the $MA_{1-y}P_y$ compounds affect the P $2p_{3/2}$ BEs and K-edge absorption energies.

These results show that the electronic structure of MnP-type compounds is widely tuneable, and imply that the catalytic activity of CoP could be modified by partial substitution of the Co or P atoms. Although the mechanism by which CoP removes S or N from petrochemicals is still unknown, it can be extrapolated by analogy with that of Ni_2P . In hydrodesulfurization (HDS) reactions, model compounds like thiophene (C_4H_4S) can adsorb to Ni_2P , and in the presence of $H_{2(g)}$, at an appropriate temperature, butadiene ($C_4H_{6(g)}$) and $H_2S_{(g)}$ are produced.⁹ During the initial stages of the reaction, thiophene adsorbs to the surface by interaction of the S and Ni atoms with the organic molecule oriented parallel to the surface.⁹ The P atoms may also play a role by weak back-bonding with the C atoms in C_4H_4S and by acting as the adsorption site of $H_{2(g)}$ which dissociates.⁹ If CoP participates in a similar mechanism, then its catalytic activity could be increased through the slight substitution of As for P atoms. Such a substitution would lower the positive charge on the Co atoms, making it resemble Ni in Ni_2P (compared to CoP) and increase the negative charge on the P atoms, enhancing their ability to back-bond to the petroleum feedstock. The lower positive charge on the Co atoms might limit the ability of S to bond strongly with the Co atoms, reducing the possibility of the surface being poisoned which partially accounts for the low HDS conversion ratio in CoP relative to Ni_2P .⁸

9.1.2 CoAs₃-type Compounds (Skutterudites)

Binary and rare-earth filled skutterudites were examined in Chapters 6 and 7 by XPS, primarily to verify atomic charges, which remained ambiguous in the literature.^{6, 39, 45, 184, 185, 197} The charge formulations $\text{Co}^{3+}(\text{Pn}^{1-})_3$ and $\text{RE}^{3+}(\text{Fe}^{2+})_4(\text{Pn}^{1-})_{12}$ were established from core-line and valence band spectra. The electron deficiency in the RE-containing compounds has been proposed to be represented as a hole in the valence band,⁴⁴ localized largely on either the Fe or P atoms.⁴⁵ Only one set of Fe 2p spin-orbit coupled peaks were observed, indicating one Fe charge state. This would suggest that the hole resides on the P atoms but, as the difference in BE between P atoms having an average charge of 11/12- or 1- would be within the precision of the instrument ($\sim\pm 0.1$ eV), we were unable to confirm this.

The valence of Ce in $\text{CeFe}_4\text{Pn}_{12}$ has been an ongoing question.^{6, 39, 184, 185, 197} Comparison of the Ce 3d spectra to those of model compounds favours the assignment of Ce^{3+} , as verified by the presence of a Ce 4f¹ state in the valence band spectra. The peak was particularly evident in the $\text{CeFe}_4\text{P}_{12}$ valence band spectrum, but was more difficult to observe in $\text{CeFe}_4\text{Sb}_{12}$ because of its more covalent bonding character.

The evolution of bonding character was apparent between the phosphide and antimonide skutterudites. In CoP_3 and $\text{REFe}_4\text{P}_{12}$, whose bonds have some ionic character, the P 2p_{3/2} BE shifts significantly (~ 0.7 eV) relative to that in elemental phosphorus. In contrast, in CoSb_3 and $\text{REFe}_4\text{Sb}_{12}$, whose bonds are more covalent, the Sb 3d_{5/2} BE is only slightly lower (by ~ 0.1 to 0.2 eV) than in elemental antimony. The less pronounced BE shift stems from the reduced screening of the nuclear charge of Sb (compared to that of P). Intermetallic antimonides may thus be at the limit of

applicability for XPS given these small shifts, at the limits of instrumental resolution. Extrapolating to other intermetallic compounds, BE shifts may be unobservable if the electronegativity differences are smaller than ~ 0.2 . The differences in BE shift observed for P vs. Sb (and As) containing compounds (when the coordinating metal is the same) suggests that these shifts in BE (relative to the element) may be used as a measure of the degree of covalency (or ionicity) of a metal-anion bond. Such a method would be more accurate than that proposed by Pauling in which the difference in electronegativity is used,³⁷ particularly as some discrepancies in electronegativity values exist.

9.1.3 Hf(Si_{0.5}As_{0.5})As

The new compound Hf(Si_{0.5}As_{0.5})As described in Chapter 8 is one end-member of the phase Hf(Si_xAs_{1-x})As ($0.5 \leq x \leq 0.7$), which adopts the ZrSiS-type structure. If $2c-1e^-$ $X-X$ bonds (X represents the disordered site containing As and Si atoms) and an ionic model are assumed, the charge formulation $\text{Hf}^{4+}(\text{Si}_{0.5}\text{As}_{0.5})^{1-}\text{As}^{3-}$ results. However, the shifts in Si 2p and As 3d BEs do not support this assignment. Moreover, occupied Hf 5d states are found in the XPS valence band spectrum, when interpreted with the aid of the calculated density of states. Photoemission spectroscopy (PES) confirmed that Hf 5d states were present in the uppermost portion of the valence band spectrum, near the Fermi edge. This analysis was performed by examining how the peak intensities vary with photoelectron cross-section as well as by resonant PES, a powerful technique to distinguish the different states present in valence band spectra.

To determine the true charges, a fitting was applied to the XPS valence band spectrum. To our knowledge, this is the first time that such a fitting has been applied to extract atomic charges from valence band spectra. This method was developed in

Chapter 3, giving charges in MnP-type compounds to be $M^{1+}P^{1-}$, in agreement with the core-line XPS results. The original fitting method proposed in Chapter 3 required the valence spectra to be fitted by spin-orbit coupled doublet peaks, with the intensities being corrected for both the inelastic mean free path (IMFP, calculated for the element), and photoionization cross-section. A similar but slightly simpler method was used in Chapters 6 and 7 to examine CoAs_3 -type compounds. For the case of $\text{Hf}(\text{Si}_{0.5}\text{As}_{0.5})\text{As}$, the fitting method was further simplified so that only one peak was used to approximate both spin-orbit coupled final states (except for the case of the Hf 5d states). It was also realized that the photoelectrons excited from different valence states would have similar kinetic energies and therefore similar IMFP values, so this variable was removed from the equation (Eq 8-2). This simplified method of fitting the valence band led to the new charge formulation of $\text{Hf}^{2+}[(\text{Si}_{0.5}\text{As}_{0.5})\text{As}]^{2-}$, which agreed, at least qualitatively, with the core-line XPS and PES results. To properly fit the valence band spectra in Chapters 3 and 6 to 8, it is important to compare the spectra to the calculated total and partial density of states. This fitting method may be limited when examining compounds having fairly covalent bonds as the energy separation between different valence states is small.

Although electron counting, using an ionic model, led to charges that agreed, perhaps fortuitously, with experimental values found in the MnP-type and skutterudite compounds, it failed in the case of $\text{Hf}(\text{Si}_{0.5}\text{As}_{0.5})\text{As}$. This discrepancy arises from the highly covalent bond character in $\text{Hf}(\text{Si}_{0.5}\text{As}_{0.5})\text{As}$, as well as the delocalization of the valence electron density. The analyses presented in Chapter 8 shows that when examining new compounds, experimental techniques such as X-ray spectroscopy must be used to verify predicted charges.

9.1.4 Charges of Anions Involved in Homo- or Hetero-Atomic Anion-Anion Bonds

The structures examined here contain polyanionic bonding networks. In the MnP- and CoAs₃-type structures, each anion is two-bonded to other anions at distances consistent with covalent 2c-2e⁻ bonds, so that each anion is assigned a charge of 1-. This is represented in Figure 9-1 in the form of Lewis dot diagrams. In the ZrSiS-type structure adopted by Hf(Si_{0.5}As_{0.5})As, there are square nets of disordered Si and As atoms, at longer distances consistent with hypervalent 2c-1e⁻ bonds (Figure 9-1c). To fulfill their octets, the As (labelled As1 in Figure 8-1) and Si atoms should acquire charges of 1- and 2-, respectively, but this does not appear to be the case with the Si charge found to be only 1- based on XPS analysis. The differences between the charges proposed by electron counting, using an ionic model, and those determined experimentally can be traced to the polar-covalent bonding found in this structure type, as well as the others investigated in this thesis. Pauling's correlation of the difference in electronegativity with ionic character implies that the Hf-Si, Hf-As, and Si-As bonds contain less than 20 % ionic character.³⁷ The above discussion further indicates that the use of an ionic model to predict charges in polar-covalently bonded compounds is insufficient, necessitating the use of experimental techniques such as X-ray spectroscopy. Within the valence band spectrum of Hf(Si_{0.5}As_{0.5})As, the upper portion (from 6-0 eV), near the Fermi edge, contains Hf 5d, As 4p and Si 3p states with anti-bonding anion-anion states present close to the Fermi edge. Because of this, the partial depletion of the Si 3p anti-bonding states, resulting in a charge of 1- rather than 2-, may actually strengthen the Si-As/Si bonds in the disordered site with the resulting valence states

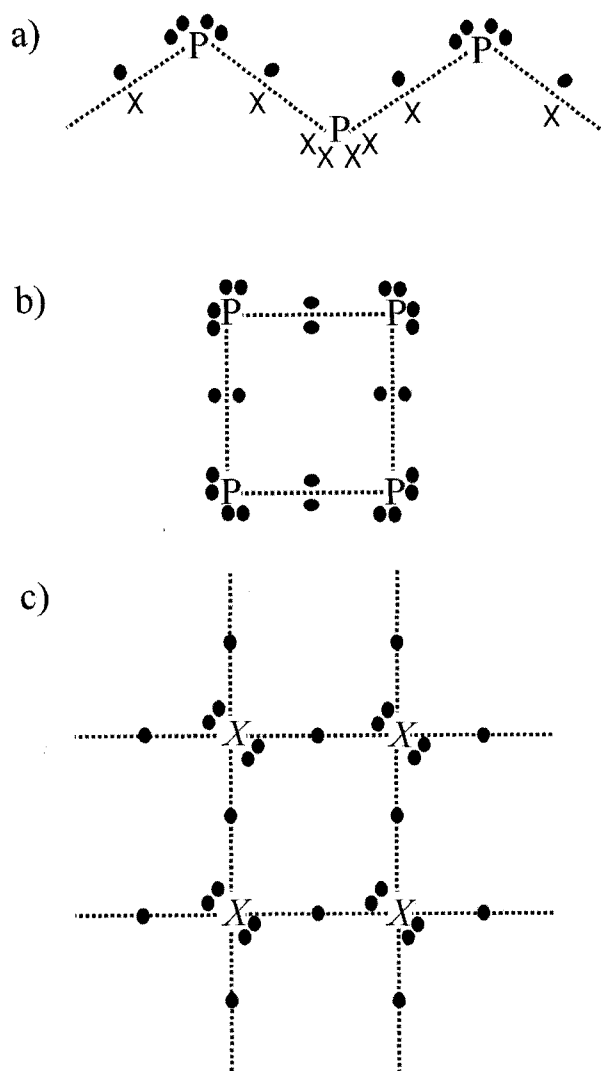


Figure 9-1 Lewis dot diagrams of the P-P bonding network present in MnP-type (a) and CoAs₃-type (b) compounds. In both cases, $2c-2e^-$ P-P bonding is considered with the remaining electrons required to complete the octet of P coming from the more electropositive *M* atoms (not shown). Based on this model, each P atom has six valence electrons and therefore a charge of 1-. The anion-anion bonding environment in Hf(Si_{0.5}As_{0.5})As is presented in (c). The disordered site containing Si or As atoms is represented as *X* with these atoms being involved in $2c-1e^-$ *X-X* bonds and based on electron counting, each *X* atom would have six valence electrons resulting in Si and As charges of 2- and 1-, respectively. The electrons in (a) are represented as either ● or x to indicate to which P atom they are associated, whereas in (b) and (c) the electrons are only represented as ●. The bond between two atoms (P or *X*) is shown as a dashed line.

being stabilized by the delocalized nature of the valence band, as well as the metallic character of this compound.

9.2 Metal Spectra in MnP-type and CoAs₃-type Compounds

To examine the charge environment of the transition metals in the MnP-type and skutterudite compounds, the *M* 2p XPS spectra were collected. Unlike for the anions, the shifts in BE relative to that of the elemental metal or other model compounds were often so small that little information could be extracted. This occurs because of the well-screened nature of both the initial and final states of the metal atoms resulting from the delocalized valence states. The delocalization arises from the metallic or nearly metallic nature of these materials and *M-M* bonds, especially in the MnP-type compounds. To further examine the charge and bonding environments of the metal atoms, more sophisticated analyses were thus necessary.

In the Co 2p_{3/2} spectra, a satellite peak was observed at slightly higher binding energy than the main core-line. On the basis of REELS analysis of Co metal (Chapter 3), it was concluded that this satellite results from plasmon loss rather than the 2-core-hole phenomenon previously proposed.¹¹⁹ In Chapters 3 to 5 and 7, the intensity of this satellite peak was observed to become less intense as the Co 3d states are depleted and as the Co-anion bond becomes more ionic. This observation, the first of its kind for intermetallic compounds, generated considerably more information than just a BE analysis.

A recent XPS study of CoP₃ revealed a charge formulation of $\sim\text{Co}^{1+}(\text{P}_3)^{1-}$, which is different than the charges determined here, $\text{Co}^{3+}(\text{P}^{1-})_3$ (Chapter 7).²⁴¹ These revised charges neglect the diamagnetism of this compound, which implies a Co charge of 3+

when its octahedral coordination environment is considered (i.e., $d^6, t_{2g}^6 e_g^0$).⁴⁷ Further, although the Co 2p satellite intensity in CoP_3 observed in Chapter 7 was confirmed in this study, it was suggested to most likely result from 2-core hole rather than plasmon loss and that the satellite intensity should decrease with increasing occupancy of Co 3d states.²⁴¹ This last statement was based on observations made by Hillebrecht *et al.* that the Ni 2p satellite peak intensity (which is similar to that of Co) decreases in alloys when Ni is the most electronegative element (e.g., AlNi) and increases when Ni is the least electronegative element (e.g., NiAu).²⁴² This observation would suggest that the satellite intensity lowers with increasing occupation of the Ni 3d states.²⁴² However, examination of alloys (e.g., CuAu) and metal-metalloid intermetallics (e.g., AuIn_2) by other authors have shown that charge transfer in these compounds mostly occurs from the electropositive to the electronegative element via *ns* or *np* orbitals but that some back donation through *n-1d* orbitals may occur.²⁴³⁻²⁴⁵ This would indicate then that even though the electronegative metal is anionic, its *n-1d* states are less occupied than in the parent metal.²⁴³⁻²⁴⁵ Such an observation might explain the anomalous results obtained by Hillebrecht *et al.* In the Co containing intermetallic compounds studied in Chapters 3 to 5 and 7, the Co-*Pn* bonds principally involve Co 3d orbitals (with little or no involvement of 4s or 4p orbitals) so that the Co 2p satellite intensity should decrease as the 3d states are depopulated. (This was confirmed by XANES analysis in Chapters 4 and 5.) The above discussion indicates that further examinations of the satellite peak found in Co 2p XPS spectra of metallic and narrow band-gap compounds needs to be pursued. The nature of the satellite peak should be further investigated by theoretical and

experimental means as well as the reason for the non-linear decline in satellite intensity as the Co charge becomes more positive (see Figure 7-3).

In compounds that did not contain Co, XANES was used to augment the XPS analysis to examine the *M* charges. In the *M* L-edge XANES spectra, the peak intensity, which results from a 2p to 3d excitation, increases as the 3d states are depopulated (Chapter 5). In the *M* K-edge XANES spectra, the intensity of the quadrupolar ($1s \rightarrow 3d$) pre-edge peak also increases as the *M* 3d states are depopulated. As this peak results from a quadrupolar excitation, the coordination environment must be fixed when examining different compounds as the intensity is significantly affected when *M* 4p orbitals become important. This is because dipolar (e.g., $1s \rightarrow 4p$) excitations are considerably more intense than quadrupolar excitations.¹⁶⁹

9.3 XPS and XANES Results for Intermetallic Compounds

In the preceding sections we have shown that XPS (or PES) and XANES provides information about charge states, bonding-type, effect of the coordination environment, whether the material is a metal or semiconductor and bonding states in intermetallic compounds (Table 9-1). However, some information is still difficult to obtain from these techniques. Specifically, the charge on the metal atoms was particularly difficult to ascertain from only a BE (or absorption energy) analysis because of the well screened nature of these atoms stemming from the delocalized nature of the valence states. Therefore, evaluation of these charges will depend on the use of alternative methods. Mössbauer spectroscopy, which is indirectly sensitive to the electron density, especially in s orbitals closest to the nucleus, has been used to determine the charge states of Fe in the $REFe_4Pn_{12}$ compounds. These studies indicated that the Fe charge was uniform and

Table 9-1 Information obtained from intermetallic compounds (marked by X) using XPS and XANES

Feature	Relative charge ^a	Coordination environment		Metal/ semiconductor	Bonding states
		Ligand	CN		
XPS^b					
Anion (<i>Pn</i> , Si)	X	X			
BE					
Cation (<i>M/RE</i>)					
BE					
Lineshape	X	X		X	
Co 2p satellite peak	X			X	
Valence band spectrum	X			X	X
XANES					
Anion (<i>Pn</i>)	X	X			
Absorption energy					
Intensity	X				X
Cation (<i>M</i>)	X	X		X	
L-edge intensity ^c					
K-edge absorption energy					
K-edge pre-edge intensity	X		X		X

^aIncludes analysis of degree of covalent bonding.

^bThe features displayed in XPS are also observed using PES.

^cIncludes lineshape.

only 2+ rather than 2.25+ (3 Fe atoms having a charge of 2+ and one having a charge of 3+).¹⁸⁰⁻¹⁸² Although the presence of a single Fe charge was confirmed in Chapters 6 and 7 by the observation of only one set of Fe 2p spin-orbit peaks, these spectra did not provide any information on the magnitude of the charge. Mössbauer spectroscopy measures the γ -ray absorption of atoms via the excitation of nuclear states.²⁴⁶ The γ -ray source is the same as the atoms under study and only a few element isotopes are active, with the most studied isotope being ^{57}Fe .²⁴⁷ In the case of ^{57}Fe in $\text{REFe}_4\text{Pn}_{12}$, two peaks were observed in the spectrum, resulting from the presence of two final nuclear states with spin quantum numbers of $I=3/2$ and $1/2$. Taking into consideration the charges of the coordinating atoms and magnetism of the samples, these spectra indicate that only low-spin Fe^{2+} is present.¹⁸⁰⁻¹⁸² When the atoms under study have a magnetic moment, the nuclear states are split into many non-degenerate levels such that multiple peaks are observed in the Mössbauer spectra.²⁴⁷ These results further suggest that the hole located in the valence band of $\text{REFe}_4\text{Pn}_{12}$ must be present on the Pn atoms.

9.4 Future Spectroscopic Examinations of Intermetallic Compounds

Although many transition metal pnictides having different structures have been investigated by X-ray spectroscopy in this thesis, some questions remain unanswered. Besides the binary (MP) and ternary ($\text{M}_{1-x}\text{M}'_x\text{P}$, $\text{MAs}_{1-y}\text{P}_y$) phosphides that adopt the MnP-type structure and were investigated in Chapters 3 to 5, quaternary compounds also exist ($\text{M}_{1-x}\text{M}'_x\text{As}_{1-y}\text{P}_y$). At this point only $\text{Mn}_{1-x}\text{Cr}_x\text{As}_{1-y}\text{P}_y$ is known but it is likely that compounds containing other metals could be formed.^{30, 31} Because the energy shifts observed in both the $\text{M}_{1-x}\text{M}'_x\text{P}$ and $\text{MAs}_{1-y}\text{P}_y$ P 2p_{3/2} XPS and K-edge absorption spectra result partially from a next-nearest neighbour effect, it is of interest to determine if such a

shift occurs in $M_{1-x}M'_xAs_{1-y}P_y$ compounds. In this case, the shifts in energy compared to the parent $M_{1-x}M'_xP$ and $MAs_{1-y}P_y$ systems would probably be similar and therefore difficult to determine if both $M' \rightarrow M$ and $As \rightarrow P$ charge transfer effects modify the BEs and absorption energies. To examine these systems, it may be useful to use PES rather than XPS. The resolution function of the PES system located on the SGM beam-line at the CLS is lower than that found for the XPS instruments used in this thesis (0.16 eV compared to 0.4 eV). By collecting core-line PES spectra, narrower linewidths would be found (compared to XPS), possibly increasing the precision of the BEs.

Further studies of transition-metal pnictides should also include analysis of compounds having the formula M_2P . As indicated in Chapter 1, Ni_2P has a higher efficiency than CoP for removing S or N from petrochemicals. Currently, only a few studies have examined the electronic structure of some M_2P and M_2As compounds by either XPS or XAS.^{15, 223, 248, 249} Future studies, which have already begun in the Mar group, should examine mixed-metal pnictides of the form $M_{2-x}M'_xPn$ ($Pn=P, As$). Because significant $M-M$ bonding is present in M_2Pn compounds,²⁴ shifts in the Pn BEs and absorption energies resulting from next-nearest neighbour effects are expected. Such work would increase our knowledge of the electronic structure of these compounds and possibly lead to the development of more efficient HDS and HDN (hydrodenitrogenation) catalysts. The transition-metal pnictides listed above and studied in this thesis should also be tested for their HDS/HDN catalytic activity.

There is still a question remaining regarding how covalent the metal-anion bond can be to observe a shift in BE or absorption energy compared to the element. In Section 9.1.2 it was suggested that if the difference in electronegativity between the metal

and anion is below 0.2, then no shift in energy would be observed when the precision of the instrument is taken into consideration. This should be further tested by examining compounds containing more electronegative metals (e.g., Ni, Cu) and less electronegative anions (e.g., Bi, Ge) than those studied here.

It was recently observed in the Mar group that a Zr analog of $\text{Hf}(\text{Si}_x\text{As}_{1-x})\text{As}$ having the ZrSiS-type structure can be formed. This study should be extended to examine if shifts in the As 3d or Si 2p BEs are observed as the metal is changed. The possibility of forming mixed-metal compounds having the formula $M_{1-y}M'_y(\text{Si}_x\text{As}_{1-x})\text{As}$ should also be investigated as this would be the first case of a cationic and anionic DFSSO stabilized material. Although a considerable amount of work needs to be done to further our understanding of intermetallic compounds, the work presented in this thesis has significantly extended our knowledge of the information that can be obtained by use of X-ray spectroscopy.

References

- (1) Westbrook, J. H.; Fleischer, R. L., Eds. *Intermetallic Compounds: Principles and Practice, Volume 3 - Progress*; John Wiley & Sons, Ltd.: Chichester, 2002.
- (2) Hallman, E. D.; Brockhouse, B. N. *Can. J. Phys.* **1969**, *47*, 1117-1131.
- (3) Buchwald, V. F. *Handbook of Iron Meteorites, Volume 1: Iron Meteorites in General*; University of California Press: Berkeley, 1975.
- (4) Cavell, R. G.; Barnes, E. M.; Arboleda, P. H.; Cavell, P. A.; Feng, R.; Gordon, R. A.; Webb, M. A. *Am. Mineral.* **2004**, *89*, 519-526.
- (5) Oyama, S. T. *J. Catal.* **2003**, *216*, 343-352.
- (6) Sales, B. C. In *Handbook on the physics and Chemistry of Rare Earths*; K. A. Gschneidner, J.-C. Bunzli and V. K. Pecharsky, Eds.; Elsevier: Amsterdam, 2003; Vol. 33; pp 1-34.
- (7) Bulman, G. E.; Siivola, E.; Shen, B.; Venkatasubramanian, R. *Appl. Phys. Lett.* **2006**, *89*, 122117/1-3.
- (8) Wang, X.; Clark, P.; Oyama, S. T. *J. Catal.* **2002**, *208*, 321-331.
- (9) Liu, P.; Rodriguez, J. A.; Asakura, T.; Gomes, J.; Nakamura, K. *J. Phys. Chem. B* **2005**, *109*, 4575-4583.
- (10) Sawhill, S. J.; Layman, K. A.; Van Wyk, D. R.; Engelhard, M. H.; Wang, C.; Bussell, M. E. *J. Catal.* **2005**, *231*, 300-313.
- (11) Domashevskaya, E. P.; Terekhov, V. A.; Ugai, Ya. A.; Nefedov, V. I.; Sergushin, N. P.; Firsov, M. N. *J. Electron Spectrosc. Relat. Phenom.* **1979**, *16*, 441-453.
- (12) Myers, C. E.; Franzen, H. F.; Anderegg, J. W. *Inorg. Chem.* **1985**, *24*, 1822-1824.
- (13) Okuda, H.; Senba, S.; Sato, H.; Shimada, K.; Namatame, H.; Taniguchi, M. *J. Electron Spectrosc. Relat. Phenom.* **1999**, *101-103*, 657-660.
- (14) Shabanova, I. N.; Mitrochin, Y. S.; Terebova, N. S.; Nebogatikov, N. M. *Surf. Interface Anal.* **2002**, *34*, 606-609.
- (15) Kanama, D.; Oyama, S. T.; Otani, S.; Cox, D. F. *Surf. Sci.* **2004**, *532*, 8-16.
- (16) Perera, S. C.; Fodor, P. S.; Tsoi, G. M.; Wenger, L. E.; Brock, S. L. *Chem. Mater.* **2003**, *15*, 4034-4038.

- (17) Perera, S. C.; Tsoi, G.; Wenger, L. E.; Brock, S. L. *J. Am. Chem. Soc.* **2003**, *125*, 13960-13961.
- (18) Henkes, A.; Schaak, R. E. *Chem. Mater.* **2007**, *19*, 4234-4242.
- (19) Henkes, A. E.; Vasquez, Y.; Schaak, R. E. *J. Am. Chem. Soc.* **2007**, *129*, 1896-1897.
- (20) Nolas, G. S.; Morelli, D. T.; Tritt, T. M. *Annu. Rev. Mater. Sci.* **1999**, *29*, 89-116.
- (21) Miessler, G. L.; Tarr, D. A. *Inorganic Chemistry*; Prentice Hall: Englewood Cliffs, New Jersey, 1991.
- (22) Carter, R. L. *Molecular Symmetry and Group Theory*; John Wiley & Sons, Inc.: Toronto, 1998.
- (23) Aronsson, B.; Lundström, T.; Rundqvist, S. *Borides, Silicides and Phosphides*; Methuen, London, 1965.
- (24) Rundqvist, S. *Arkiv för Kemi* **1962**, *20*, 67-113.
- (25) Tremel, W.; Hoffmann, R.; Silvestre, J. *J. Am. Chem. Soc.* **1986**, *108*, 5174-5187.
- (26) Fjellvåg, H.; Kjekshus, A. *Acta Chem. Scand. Ser. A* **1984**, *38*, 563-573.
- (27) Fjellvåg, H.; Kjekshus, A. *Acta Chem. Scand. Ser. A* **1984**, *38*, 703-710.
- (28) Selte, K.; Kjekshus, A.; Oftedal, T. A.; Andressen, A. F. *Acta Chem. Scand. Ser. A* **1974**, *28*, 957-962.
- (29) Kanaya, K.; Abe, S.; Yoshida, H.; Kamigaki, K.; Kaneko, T. *J. Alloys Compd.* **2004**, *383*, 189-194.
- (30) Schünemann, J.-W.; Bärner, K.; Fjellvåg, H.; Kjekshus, A.; Eigemann, J.; Gmelin, E.; Sondermann, U. *Phys. State. Sol. A: applied research* **1988**, *110*, 141-154.
- (31) Fjellvåg, H.; Kjekshus, A.; Stolen, S.; Andresen, A. F. *Acta Chem. Scand. Ser. A* **1988**, *42*, 214-225.
- (32) Yanase, A.; Hasegawa, A. *J. Phys. C: Solid State Phys.* **1980**, *13*, 1989-1993.
- (33) Perkins, P. G.; Marwaha, A. K.; Stewart, J. J. P. *Theor. Chim. Acta* **1981**, *59*, 569-583.

- (34) Rundqvist, S.; Nawapong, P. C. *Acta. Chem. Scand.* **1965**, *19*, 1006-1008.
- (35) Hulliger, F. *Struct. Bonding* **1968**, *4*, 83-229.
- (36) Rundqvist, S. *Colloques Internationaux du Centre National de la Recherche Scientifique* **1967**, 85-90.
- (37) Pauling, L. *The Nature of the Chemical Bond, 3rd ed.*; Cornell University Press: Ithaca, NY, 1960.
- (38) Hoffmann, R. *Angew. Chem. Int. Ed. Engl.* **1987**, *26*, 846-878.
- (39) Jeitschko, W.; Braun, D. *Acta Crystallogr., Sect. B* **1977**, *33*, 3401-3406.
- (40) Andersen, O. K. *Phys. Rev. B* **1975**, *12*, 3060-3083.
- (41) Oftedal, I. *Zeitschrift für Kristallographie* **1928**, *66*, 517-546.
- (42) Rundqvist, S.; Errson, N.-O. *Ark. Kemi* **1968**, *30*, 103-114.
- (43) Kjekshus, A.; Rakke, T. *Acta Chem. Scand.* **1974**, *A28*, 99-103.
- (44) Sato, H.; Abe, Y.; Okada, H.; D., M. T.; Abe, K.; Sugawara, H.; Aoki, Y. *Phys. Rev. B* **2000**, *62*, 15125-15130.
- (45) Jung, D.; Whangbo, M.-H.; Alvarez, S. *Inorg. Chem.* **1990**, *29*, 2252-2255.
- (46) Braun, D. J.; Jeitschko, W. *J. Less-Common Met.* **1980**, *72*, 147-156.
- (47) Ackermann, J.; Wold, A. *J. Phys. Chem. Solids* **1977**, *38*, 1013-1016.
- (48) Singh, D. J.; Pickett, W. E. *Phys. Rev. B* **1994**, *50*, 11235-11238.
- (49) Llunell, M.; Alemany, P.; Alvarez, S.; Zhukov, V. P.; Vernes, A. *Phys. Rev. B* **1996**, *53*, 10605-10609.
- (50) Fornari, M.; Singh, D. J. *Phys. Rev. B* **1999**, *59*, 9722-9724.
- (51) Lefebvre-Devos, I.; Lassalle, M.; Wallart, X.; Olivier-Fourcade, T.; Monconduit, L.; Jumas, J. C. *Phys. Rev. B* **2001**, *63*, 125110-1-125110-7.
- (52) Kurmaev, E. Z.; Moewes, A.; Shein, R. R.; Finkelstein, L. D.; Ivanovskii, A. L.; Anno, H. *J. Phys.: Condens. Matter* **2004**, *16*, 979-987.
- (53) Nördstrom, L.; Singh, D. J. *Phys. Rev. B* **1996**, *53*, 1103-1108.

- (54) Wang, C.; Hughbanks, T. *Inorg. Chem.* **1995**, *34*, 5224-5229.
- (55) Tremel, W.; Hoffmann, R. *J. Am. Chem. Soc.* **1987**, *109*, 124-140.
- (56) Hulliger, F. *J. Less-Common Metals* **1968**, *16*, 113-117.
- (57) Lam, R.; Mar, A. *J. Solid State Chem.* **1997**, *134*, 388-394.
- (58) Schmidt, M.; Cichorek, T.; Niewa, R.; Schlechte, A.; Prots, Y.; Steglich, F.; Kniep, R. *J. Phys.: Condens. Matter* **2005**, *17*, 5481-5488.
- (59) Papoian, G. A.; Hoffmann, R. *Angew. Chem., Int. Ed.* **2000**, *39*, 2409-2448.
- (60) Briggs, D.; Seah, M. P., Eds. *Practical Surface Analysis, Vol.1: Auger and X-ray Photoelectron Spectroscopy, 2nd ed.*; Wiley: Chichester, 1990.
- (61) Siegbahn, K.; Nordling, C.; Fahlman, A.; Nordberg, R.; Hamrin, K.; Hedman, J.; Johansson, G.; Bergmark, T.; Karlsson, S.-E.; Lindgren, I.; Lindberg, B. *ESCA: Atomic, Molecular and Solid State Structure Studied by Means of Electron Spectroscopy*; Almqvist & Wiksells Boktryckeri AB: Uppsala, 1967.
- (62) Bernstein, J. *Secrets of the old one: Einstein, 1905*; Copernicus Books, New York, 2005.
- (63) Gerson, A. R.; Bredow, T. *Surf. Interface Anal.* **2000**, *29*, 145-150.
- (64) Brundle, C. R. *J. Vac. Sci. Technol.* **1974**, *11*, 212-224.
- (65) Kövér, L.; Novák, M.; Egri, S.; Cserny, I.; Berényi, Z.; Tóth, J.; Varga, D.; Drube, W.; Yubero, F.; Tougaard, S.; Werner, W. S. M. *Surf. Interface Anal.* **2006**, *38*, 569-573.
- (66) Jablonski, A.; Powell, C. J. *Phys. Rev. B* **1994**, *50*, 4739-4748.
- (67) Vulli, M. *Surf. Interface Anal.* **1981**, *3*, 67-71.
- (68) Tougaard, S. *J. Vac. Sci. Technol. A* **1990**, *8*, 2197-2203.
- (69) Tougaard, S. *Solid State Commun.* **1987**, *61*, 547-549.
- (70) Tanuma, S.; Powell, C. J.; Penn, D. R. *Surf. Interface Anal.* **2005**, *37*, 1-14.
- (71) Pfau, A.; Schierbaum, K. D. *Surf. Sci.* **1994**, *321*, 71-80.

- (72) Holgado, J. P.; Alvarez, R.; Munuera, G. *Appl. Surf. Sci.* **2000**, *161*, 301-315.
- (73) Scofield, J. H. *J. Electron Spectrosc. Relat. Phenom.* **1976**, *8*, 129-137.
- (74) Yeh, J. J.; Lindau, I. *At. Data Nucl. Data Tables* **1985**, *32*, 1-155.
- (75) Watts, J. F.; Wolstenholme, J. *An Introduction to Surface Analysis by XPS and AES*; Wiley: Rexdale, 2003.
- (76) Koopmans, T. *Physica* **1933**, *1*, 104-113.
- (77) Harris, D. C.; Bertolucci, D. *Symmetry and Spectroscopy: An Introduction to Vibrational and Electronic Spectroscopy*; Oxford University Press: Oxford, 1978.
- (78) Gupta, R. P.; Sen, S. K. *Phys. Rev. B* **1974**, *10*, 71-77.
- (79) Riviere, J. C. *Surface Analytical Techniques*; Oxford University Press, Oxford, 1990.
- (80) Anno, H.; Matsubara, K.; Caillat, T.; Fleurial, J.-P. *Phys. Rev. B* **2000**, *62*, 10737-10743.
- (81) Grosvenor, A. P.; Kobe, B. A.; Biesinger, M. C.; McIntyre, N. S. *Surf. Interface Anal.* **2004**, *36*, 1564-1574.
- (82) Bellhouse, E. M.; Mertens, A. I. M.; McDermid, J. R. *Mater. Sci. Eng. A* **2007**, *463*, 147-156.
- (83) Tougaard, S. *J. Vac. Sci. Technol. A* **2003**, *21*, 1081-1086.
- (84) Strohmeier, B. R. *Surf. Interface Anal.* **1990**, *15*, 51-56.
- (85) Hajati, S.; Coultas, S.; Blomfield, C.; Tougaard, S. *Surf. Sci.* **2006**, *600*, 3015-3021.
- (86) Sham, T. K.; Rivers, M. L. *Rev. Mineral. Geochem.* **2002**, *49*, 117-147.
- (87) Blewett, J. P. *Synchrotron Rad.* **1998**, *5*, 135-139.
- (88) Eberhardt, E., Ed. *Applications of Synchrotron Radiation: High-Resolution Studies of Molecules and Molecular Adsorbates on Surfaces*; Springer-Verlag: Berlin, 1995; Vol. 35.
- (89) Holmes, K. C.; Ronsenbaum, G. *J. Synchrtron Rad.* **1998**, *5*, 147-153.
- (90) Sasaki, T. *J. Synchrotron Rad.* **1998**, *5*, 140-146.

- (91) Bancroft, G. M. *Can. J. Chem.* **2004**, *82*, 1028-1042.
- (92) Attwood, D. *Soft X-ray and Extreme Ultraviolet Radiation*; Cambridge University Press: New York, 2000.
- (93) Wende, H. *Rep. Prog. Phys.* **2004**, *67*, 2105-2181.
- (94) Newville, M. "Fundamentals in XAFS," Consortium for Advanced Radiation Sources, University of Chicago: Chicago, 2004.
- (95) Koningsberger, D. C.; Mojet, B. L.; van Dorssen, G. E.; Ramkaer, D. E. *Top. Catal.* **2000**, *10*, 143-155.
- (96) Hähner, G. *Chem. Soc. Rev.* **2006**, *35*, 1244-1255.
- (97) Wong, J.; Lytle, F. W.; Messmer, R. P.; Maylotte, D. H. *Phys. Rev. B* **1984**, *30*, 5596-5610.
- (98) Fleet, M. E. *Can. Mineral.* **2005**, *43*, 1811-1838.
- (99) Rehr, J. J.; Albers, R. C. *Rev. Mod. Phys.* **2000**, *72*, 621-654.
- (100) Wei, S.-Q.; Sun, Z.-H.; Pan, Z.-Y.; Zhang, X.-Y.; Yan, W.-S.; Zhong, W.-J. *Nuclear Science and Techniques* **2006**, *17*, 370-388.
- (101) Farges, F.; Brown, G. E., Jr.; Rehr, J. J. *Phys. Rev. B* **1997**, *56*, 1809-1819.
- (102) Schroeder, S. L. M.; Moggridge, G. D.; Rayment, T.; Lambert, R. M. *J. Mol. Catal. A: Chem.* **1997**, *119*, 357-365.
- (103) Green, J. C.; Decleva, P. *Coord. Chem. Rev.* **2005**, *249*, 209-228.
- (104) Huber, E. E., Jr.; Ridgley, D. H. *Phys. Rev. [Sect.] A* **1964**, *135*, 1033-1040.
- (105) Okabayashi, J.; Tanaka, K.; Hashimoto, M.; Fujimori, A.; Ono, K.; Okusawa, M.; Komatsubara, T. *Phys. Rev. B* **2004**, *69*, 132411/1-132411/4.
- (106) Rundqvist, S. *Acta. Chem. Scand.* **1962**, *16*, 287-292.
- (107) Pearson, W. B. *The Crystal Chemistry and Physics of Metals and Alloys*; Wiley-Interscience: New York, 1972.
- (108) Noläng, B.; Eriksson, O.; Johansson, B. *J. Phys. Chem. Solids* **1990**, *51*, 1033-1046.

- (109) Scott, B. A.; Eulenberger, G. R.; Bernheim, R. A. *J. Chem. Phys.* **1968**, *48*, 263-272.
- (110) Fairley, N. *CasaXPS, version 2.3.9*; Casa Software Ltd.: Teighnmouth, Devon, UK, 2003 (www.casaxps.com).
- (111) Egerton, R. G.; Malac, M. *J. Electron Spectrosc. Relat. Phenom.* **2005**, *143*, 43-50.
- (112) Whangbo, M.-H.; Hoffmann, R. *J. Am. Chem. Soc.* **1978**, *100*, 6093-6098.
- (113) Hoffmann, R. *Solids and Surfaces: A Chemist's View of Bonding in Extended Structures*; VCH Publishers, New York, 1988.
- (114) Allred, A. L.; Rochow, E. G. *J. Inorg. Nucl. Chem.* **1958**, *5*, 264-268.
- (115) Tong, G. S. M.; Jeung, G. H.; Cheung, A. S.-C. *J. Chem. Phys.* **2003**, *118*, 9224-9232.
- (116) Wagner, C. D.; Naumkin, A. V.; Kraut-Vass, A.; Allison, J. W.; Powell, C. J.; Rumble, J. R., Jr. *NIST X-ray Photoelectron Spectroscopy Database, version 3.4 (web version)*; National Institute of Standards and Technology: Gaithersburg, MD, 2003 (srdata.nist.gov/xps).
- (117) Doniach, S.; Šunjić, M. *J. Phys. C: Solid State Phys.* **1970**, *3*, 285-291.
- (118) Hüfner, S. In *Photoemission in Solids II*; L. Ley and M. Cardona, Ed.; Springer-Verlag: Berlin, 1979.
- (119) Raaen, S. *Solid State Commun.* **1986**, *60*, 991-993.
- (120) Richardson, D.; Hisscott, L. A. *J. Phys. F: Metal Phys.* **1976**, *6*, L127-L134.
- (121) Hüfner, S. *Photoelectron Spectroscopy*; Springer-Verlag: Berlin, 1995.
- (122) Kemeny, P. C.; Shevchik, N. J. *Solid State Commun.* **1975**, *17*, 255-258.
- (123) Hüfner, S.; Wertheim, G. K. *Phys. Lett. A* **1975**, *51*, 299-300.
- (124) Kotani, A.; Toyozawa, T. *J. Phys. Soc. Jpn.* **1974**, *37*, 912-919.
- (125) Robins, J. L.; Swan, J. B. *Proc. Phys. Soc., London* **1960**, *76*, 857-869.
- (126) Misell, D. L.; Atkins, A. J. *J. Phys. C: Solid State Phys.* **1972**, *5*, 95-106.

- (127) Grosvenor, A. P.; Biesinger, M. C.; Smart, R. S.-C.; McIntyre, N. S. *Surf. Sci.* **2006**, *600*, 1771-1779.
- (128) Gorodetsky, D. A.; Melnik, Y. P.; Proskurin, D. P.; Sklyar, V. K.; Usenko, V. A.; Yas'ko, A. A. *Surf. Sci.* **1998**, *416*, 255-263.
- (129) Liang, K. S.; Chen, T. *Solid State Commun.* **1977**, *23*, 975-978.
- (130) Brillson, L. J.; Ceasar, G. P. *Surf. Sci.* **1976**, *58*, 457-468.
- (131) Tougaard, S. *QUASES-IMFP-TPP2M: Database for Calculation of IMFPs by TPP2M Formula, version 2.1*; QUASES-Tougaard Inc.: Odense, Denmark, 2000 (www.quases.com).
- (132) Selte, K.; Fjellvåg, H.; Kjekshus, A. *Acta Chem. Scand. Ser. A* **1979**, *33*, 391-395.
- (133) Fjellvåg, H.; Kjekshus, A. *Acta Chem. Scand. Ser. A* **1984**, *38*, 1-13.
- (134) Briggs, D. *Surface Analysis of Polymers by XPS and Static SIMS*; Cambridge University Press: Cambridge, 2005.
- (135) Mottana, A.; Marcellie, A.; Giuli, G.; Wu, Z.; Seifert, F.; Paris, E. *Phys. Chem. Miner.* **1996**, *23*, 227-228.
- (136) Clark, D. T.; Kilcast, D. *J. Chem. Soc. B: Phys. Org. Chem.* **1971**, 2243-2247.
- (137) Clark, D. T.; Feast, W. J.; Kilcast, D.; Musgrave, W. K. R. *J. Polym. Sci.: Polym. Chem. Ed.* **1973**, *11*, 389-411.
- (138) Meier, R. *J. Chem. Phys. Lett.* **1987**, *138*, 471-475.
- (139) Pijpers, A. P.; Donners, W. A. B. *J. Polym. Sci.: Polym. Chem. Ed.* **1985**, *23*, 453-462.
- (140) Meier, R. J.; Pijpers, A. P. *Theor. Chim. Acta* **1989**, *75*, 261-270.
- (141) Briggs, D.; Beamson, G. *Anal. Chem.* **1992**, *64*, 1729-1736.
- (142) Clark, D. T.; Thomas, H. R. *J. Polym. Sci.: Polym. Chem. Ed.* **1978**, *16*, 791-820.
- (143) van der Heide, P. A. W. *Surf. Sci.* **2001**, *490*, L619-L626.
- (144) van der Heide, P. A. W. *J. Electron. Spectrosc. Relat. Phenom.* **2006**, *151*, 79-91.

- (145) Shallenberger, J. R.; Cole, D. A.; Novak, S. W. *J. Vac. Sci. Technol. A* **1999**, *17*, 1086-1090.
- (146) Bouvet, D.; Clivaz, P. A.; Dutoit, M.; Coluzza, C.; Almeida, J.; Margaritondo, G.; Pio, F. *J. Appl. Phys.* **1996**, *79*, 7114-7122.
- (147) Salim, M. A.; Khattak, G. D.; Fodor, P. S.; Wenger, L. E. *J. Non-Cryst. Solids* **2001**, *289*, 185-195.
- (148) Chowdari, B. V. R.; Tan, K. L.; Chia, W. T.; Gopalakrishnan, R. *J. Non-Cryst. Solids* **1990**, *119*, 95-102.
- (149) Khattak, G. D.; Salim, M. A.; Wenger, L. E.; Gilani, A. H. *J. Non-Cryst. Solids* **2000**, *262*, 66-79.
- (150) Khattak, G. D.; Salim, M. A.; Al-Harhi, A. S.; Thompson, D. J.; Wenger, L. E. *J. Non-Cryst. Solids* **1997**, *212*, 180-191.
- (151) Andreassen, I. L.; Selte, K.; Kjekshus, A. *Acta Chem. Scand. Sect. A* **1977**, *31*, 421-422.
- (152) Denton, A. R.; Ashcroft, N. W. *Phys. Rev. A* **1991**, *43*, 3161-3164.
- (153) Regier, T.; Paulsen, J.; Wright, F.; Coulthard, I.; Tan, K.; Sham, T. K.; Blyth, R. I. *R. AIP Conf. Proc.* **2007**, *879*, 473-476.
- (154) Engemann, C.; Kohring, G.; Pantelouris, A.; Hormes, J.; Grimme, S.; Peyerimhoff, S. D.; Clade, J.; Frick, F.; Jansen, M. *Chem. Phys.* **1997**, *221*, 189-198.
- (155) Jiang, D. T.; Crozier, E. D. *Can. J. Phys.* **1998**, *76*, 621-643.
- (156) Thompson, A.; Attwood, D.; Gullikson, E.; Howells, M.; Kim, K.-J.; Kirz, J.; Kortright, J.; Lindau, I.; Peanetta, P.; Robinson, A.; Scofield, J.; Underwood, J.; Vaughan, D.; Williams, G.; Winick, H. *X-ray Data Booklet*; Lawrence Berkeley National Laboratory, University of California: Berkeley, 2001.
- (157) Ravel, B.; Newville, M. *J. Synchrotron Rad.* **2005**, *12*, 537-541.
- (158) Oswald, S.; Wirth, H. *Surf. Interface Anal.* **1999**, *27*, 136-141.
- (159) Cavell, R. G.; Sodhi, R. N. S. *J. Electron Spectrosc. Relat. Phenom* **1986**, *41*, 25-35.
- (160) Sodhi, R. N. S.; Cavell, R. G. *J. Electron Spectrosc. Relat. Phenom.* **1986**, *41*, 1-24.

- (161) Kotsis, K.; Staemmler, V. *Phys. Chem. Chem. Phys.* **2006**, *8*, 1490-1498.
- (162) Rössler, N.; Kotsis, K.; Staemmler, V. *Phys. Chem. Chem. Phys.* **2006**, *8*, 697-706.
- (163) Hagelin-Weaver, H. A. E.; Weaver, J. F.; Hoflund, G. B.; Salaita, G. N. *J. Alloys. Compd.* **2005**, *389*, 34-41.
- (164) Hagelin-Weaver, H. A. E.; Hoflund, G. B.; Minahan, D. M.; Salaita, G. N. *Appl. Surf. Sci.* **2004**, *235*, 420-448.
- (165) Moslemzadeh, N.; Beamson, G.; Tsakirooulos, P.; Watts, J. F. *Surf. Sci.* **2006**, *600*, 265-277.
- (166) Moslemzadeh, N.; Beamson, G.; Tsakirooulos, P.; Watts, J. F.; Haines, S. R.; Weightman, P. *J. Electron Spectrosc. Relat. Phenom.* **2006**, *152*, 129-133.
- (167) de Groot, F. M. F.; Pizzini, S.; Fontaine, A.; Hämäläinen, K.; Kao, C. C.; Hastings, J. B. *Phys. Rev. B* **1995**, *51*, 1045-1050.
- (168) de Groot, F. *Coord. Chem. Rev.* **2005**, *249*, 31-63.
- (169) Westre, T. E.; Kennepohl, P.; DeWitt, J. G.; Hedman, B.; Hodgson, K. O.; Solomon, E. I. *J. Am. Chem. Soc.* **1997**, *119*, 6297-6314.
- (170) Fjellvåg, H.; Kjekshus, A.; Zieba, A.; Foner, S. *J. Phys. Chem. Solids* **1984**, *45*, 709-718.
- (171) de Vries, A. H.; Hozoi, L.; Broer, R. *Int. J. Quantum Chem.* **2003**, *91*, 57-61.
- (172) Huheey, J. E.; Keiter, E. A.; Keiter, R. L. *Inorganic Chemistry: Principles of Structure and Reactivity*, 4th ed.; Harper Collins, New York, 1993.
- (173) Pfeiffer, G.; Rehr, J. J.; Sayers, D. E. *Phys. Rev. B* **1995**, *51*, 804-810.
- (174) Pantelouris, A.; Kuper, G.; Hormes, J.; Feldmann, C.; Jansen, M. *J. Am. Chem. Soc.* **1995**, *117*, 11749-11753.
- (175) Arcon, I.; Kolar, J.; Kodre, A.; Hanzel, D.; Strilic, M. *X-ray Spectrom.* **2007**, *36*, 199-205.
- (176) Slater, J. C. *Phys. Rev.* **1930**, *36*, 57-64.
- (177) Slack, G. A. In *CRC Handbook of Thermoelectrics*; D. M. Rowe, Ed.; CRC Press: Boca Raton, FL, 1995; pp 407-440.

- (178) Meisner, G. P. *Physica B* **1981**, *108*, 763-764.
- (179) Torikachvili, M. S.; Chen, J. W.; Calichaouch, Y.; Guertin, R. P.; McElfresh, M. W.; Rossel, C.; Maple, M. B.; Meisner, G. P. *Phys. Rev. B* **1987**, *36*, 8660-8664.
- (180) Grandjean, F.; Gérard, A.; Braun, D. J.; Jeitschko, W. *J. Phys. Chem. Solids* **1984**, *45*, 877-886.
- (181) Shenoy, G. K.; Noakes, D. R.; Meisner, G. P. *J. Appl. Phys.* **1982**, *53*, 2628-2630.
- (182) Long, G. J.; Hautot, D.; Grandjean, F.; Morelli, D. T.; Meisner, G. P. *Phys. Rev. B* **1999**, *60*, 7410-7418.
- (183) Meisner, G. P.; Torikachvili, M. S.; Yang, K. N.; Maple, M. B.; Guertin, R. P. *J. Appl. Phys.* **1985**, *57*, 3073-3075.
- (184) Xue, J. S.; Antonio, M. R.; White, W. T.; Soderholm, L. *J. Alloys Compd.* **1994**, *207/208*, 161-164.
- (185) Grandjean, F.; Long, G. J.; Cortes, R.; Morelli, D. T.; Meisner, G. P. *Phys. Rev. B* **2000**, *62*, 12569-12572.
- (186) Wallbank, B.; Johnson, C. E.; Main, I. G. *J. Electron Spect. Related Phenom.* **1974**, *4*, 263-269.
- (187) Nesbitt, H. W.; Muir, I. J. *Geochim. Cosmochim. Acta* **1994**, *58*, 4667-4679.
- (188) Danebrock, M. E.; Evers, C. B. H.; Jeitschko, W. *J. Phys. Chem. Solids* **1996**, *57*, 381-387.
- (189) Schlapbach, L.; Osterwalder, J.; Siegmann, H. C. *J. Less-Common Met.* **1982**, *88*, 291-297.
- (190) Schlapbach, L.; Osterwalder, J. *Solid State Commun.* **1982**, *42*, 271-274.
- (191) Park, K.-H.; Oh, S.-J. *Phys. Rev. B* **1993**, *48*, 14833-14842.
- (192) Dauscher, A.; Hilaire, L.; Le Normand, F.; Mueller, W.; Maire, G.; Vasquez, A. *Surf. Interface Anal.* **1990**, *16*, 341-346.
- (193) Kaindl, G.; Wertheim, G. K.; Shmiester, G.; Sampathkurman, E. V. *Phys. Rev. Lett.* **1987**, *58*, 606-609.
- (194) Imada, S.; Jo, T. *J. Phys. Soc. Jpn.* **1989**, *58*, 402-405.

- (195) Sarma, D. D.; Vishnu Kamath, P.; Rao, C. N. R. *Chem. Phys.* **1983**, *73*, 71-82.
- (196) Uwamino, Y.; Tsuge, A.; Ishizuka, T.; Yamatera, H. *Bull. Chem. Soc. Jpn.* **1986**, *59*, 2263-2267.
- (197) Ishii, H.; Miyahara, T.; Takayama, Y.; Obu, K.; Shinoda, M.; Lee, C.; Shiozawa, H.; Yuasa, S.; Matsuda, T. D.; Sugawara, H.; Sato, H. *Surf. Rev. Lett.* **2002**, *9*, 1257-1261.
- (198) Braun, D. J.; Jeitschko, W. *J. Solid State Chem.* **1980**, *32*, 357-363.
- (199) Sales, B. C.; Mandrus, D.; Chakoumakos, B. C.; Keppens, V.; Thompson, J. R. *Phys. Rev. B* **1997**, *56*, 15081-15089.
- (200) Sofo, J. O.; Mahan, G. D. *Phys. Rev. B* **1998**, *58*, 15620-15623.
- (201) Partik, M.; Lutz, H. D. *Phys. Chem. Minerals* **1999**, *27*, 41-46.
- (202) Koga, K.; Akai, K.; Oshiro, K.; Matsuura, M. *Phys. Rev. B* **2005**, *71*, 155119-1-155119-9.
- (203) Morelli, D. T.; Meisner, G. P. *J. Appl. Phys.* **1995**, *77*, 3777-3781.
- (204) Singh, D. J.; Mazin, I. I. *Phys. Rev. B* **1997**, *56*, R1650-R1653.
- (205) Gajewski, D. A.; Dilley, N. R.; Bauer, E. D.; Freeman, E. J.; Chau, R.; Maple, M. B.; Mandrus, D.; Sales, B. C.; Lacerda, A. H. *J. Phys.: Condens. Matter* **1998**, *10*, 6973-6985.
- (206) Ravot, D.; Lafont, U.; Chapon, L.; Tedenac, J. C.; Mauger, A. *J. Alloys Compd.* **2001**, *323-324*, 389-391.
- (207) Harima, H.; Takegahara, K. *Physica B* **2003**, *328*, 26-28.
- (208) Viennois, R.; Ravot, D.; Terki, F.; Hernandez, C.; Charar, S.; Haen, P.; Paschen, S.; Steglich, F. *J. Magn. Magn. Mater.* **2004**, *272-276*, E113-E114.
- (209) Bauer, E. D.; Chau, R.; Dilley, N. R.; Maple, M. B.; Mandrus, D.; Sales, B. C. *J. Phys.: Conds. Matter* **2000**, *12*, 1261-1267.
- (210) Viennois, R.; Charar, S.; Ravot, D.; Haen, P.; Mauger, A.; Bentien, A.; Paschen, S.; Steglich, F. *Eur. Phys. J. B* **2005**, *46*, 257-267.

- (211) Ley, L.; Pollak, R. A.; McFeely, F. R.; Kowalczyk, S. P.; Shirley, D. A. *Phys. Rev. B* **1974**, *9*, 600-621.
- (212) Nesbitt, H. W.; Legrand, D.; Bancroft, G. M. *Phys. Chem. Minerals* **2000**, *27*, 357-366.
- (213) Baer, Y.; Hauger, R.; Zürcher, C.; Campagna, M.; Wertheim, G. K. *Phys. Rev. B* **1978**, *18*, 4433-4439.
- (214) Wawryk, R.; Wojakowski, A.; Pietraszko, A.; Henkie, Z. *Solid State Commun.* **2005**, *133*, 295-300.
- (215) Park, S.-M.; Park, S.-J.; Kim, S.-J. *J. Solid State Chem.* **1998**, *140*, 300-306.
- (216) Kimura, A.; Suga, S.; Matsushita, T.; Kaneko, T.; Kanomata, T. *Solid State Commun.* **1993**, *85*, 901-905.
- (217) Tran, V. H.; Bukowski, Z.; Stepien-Damm, J.; Troć, R. *J. Solid State Chem.* **2006**, *179*, 1401-1406.
- (218) Wang, Y. C.; Poduska, K. M.; Hoffmann, R.; DiSalvo, F. J. *J. Alloys Compd.* **2001**, *314*, 132-139.
- (219) Yuzuri, M. *J. Phys. Soc. Jpn.* **1960**, *15*, 2007-2012.
- (220) Gupta, L. C.; Malik, S. K.; Vijayaraghavan, R. *Phys. Lett. A* **1968**, *28*, 255-256.
- (221) Vitkina, T. Z.; Zhigadlo, N. D.; Ryzhkovskii, V. M. *Cryst. Res. Technol.* **1988**, *23*, 945-948.
- (222) Kimura, A.; Suga, S.; Matsubara, H.; Matsushita, T.; Saitoh, Y.; Daimon, H.; Kaneko, T.; Kanomata, T. *Solid State Commun.* **1992**, *81*, 707-710.
- (223) Kimura, A.; Suga, S.; Matsushita, T.; Daimon, H.; Kaneko, T.; Kanomata, T. *J. Phys. Soc. Jpn.* **1993**, *62*, 1624-1633.
- (224) Sheldrick, G. M. *SHELXTL, version 6.12*; Bruker AXS Inc.: Madison, WI, 2001.
- (225) Gelato, L. M.; Parthe, E. *J. Appl. Crystallogr.* **1987**, *20*, 139-143.
- (226) Morant, C.; Galan, L.; Sanz, J. M. *Surf. Interface Anal.* **1990**, *16*, 304-308.
- (227) Dashjav, E.; Kleinke, H. *Z. Anorg. Allg. Chem.* **2002**, *628*, 2176.
- (228) Holland, T. J. B.; Redfern, S. A. T. *Mineral. Mag.* **1997**, *61*, 65-77.

- (229) Villars, P., Ed. *Pauling File Binaries Edition, version 1.0*; ASM International: Materials Park, OH, 2002.
- (230) Franzen, H. F.; Köckerling, M. *Prog. Solid State Chem.* **1995**, *23*, 265-289.
- (231) Kleinke, H. *Trends Inorg. Chem.* **2001**, *7*, 135-149.
- (232) Soheilnia, N.; Assoud, A.; Kleinke, H. *Inorg. Chem.* **2003**, *42*, 7319-7325.
- (233) Flinn, B. J.; McIntyre, N. S. *Surf. Interface Anal.* **1990**, *15*, 19-26.
- (234) Petö, G.; Zsoldos, E.; Gucci, L.; Schay, Z. *Solid State Commun.* **1986**, *57*, 817-819.
- (235) Renault, O.; Marlier, R.; Barrett, N. T.; Martinez, E.; Baron, T.; Gely, M.; De Salvo, B. *Surf. Interface Anal.* **2006**, *38*, 486-488.
- (236) Hessel, C. M.; Henderson, E. J.; Veinot, J. G. C. *J. Phys. Chem. C* **2007**, *111*, 6956-6961.
- (237) Thiel, C. W.; Cruguel, H.; Wu, H.; Sun, Y.; Lapeyre, G. J.; Cone, R. L.; Equall, R. W.; Macfarlane, R. M. *Phys. Rev. B* **2001**, *64*, 085107-1-085107-13.
- (238) Thompson, J.; Arima, V.; Zou, Y.; Fink, R.; Umbach, E.; Cingolani, R.; Blyth, R. I. *Phys. Rev. B* **2004**, *70*, 153104-1-153104-3.
- (239) Thomas, A. G.; Flavell, W. R.; Mallick, A. K.; Kumarasinghe, A. R.; Tsoutsou, D.; Khan, N.; Chatwin, C.; Rayner, S.; Smith, G. C.; Stockbauer, R. L.; Warren, S.; Johal, T. K.; Patel, S.; Holland, D.; Taleb, A.; Wiame, F. *Phys. Rev. B* **2007**, *75*, 035105-1-035105-12.
- (240) Thompson, J.; Arima, V.; Matino, F.; Berkebile, S.; Koller, G.; Netzer, F. P.; Ramsey, M. G.; Cingolani, R.; Blyth, R. I. *Synth. Met.* **2005**, *153*, 233-236.
- (241) Diplas, S.; Prytz, Ø.; Karlsen, O. B.; Watts, J. F.; Taftø, J. *J. Phys.: Condens. Matter* **2007**, *19*, 246216-1-246216-13.
- (242) Hillebrecht, F. U.; Fuggle, J. C.; Bennet, P. A.; Zolnierrek, Z.; Freiburg, C. *Phys. Rev. B* **1983**, *27*, 2179-2193.
- (243) Sham, T. K.; Hiraya, A.; Watanabe, M. *Phys. Rev. B* **1997**, *55*, 7585-7592.
- (244) Bzowski, A.; Sham, T. K.; Yiu, Y. M. *Phys. Rev. B* **1994**, *49*, 13776-13779.
- (245) Bzowski, A.; Yiu, Y. M.; Sham, T. K. *Phys. Rev. B* **1995**, *51*, 9515-9520.

- (246) Rees, L. V. C. *Mol. Sieves* **2004**, *4*, 517-543.
- (247) Bandyopadhyay, D. *Int. Mater. Rev.* **2006**, *51*, 171-208.
- (248) Li, Q.; Greig, D.; Matthew, J. A. D.; Shen, T. H.; Beamson, B. *Philos. Mag.* **2005**, *85*, 885-893.
- (249) Soo, Y. L.; Kioseoglou, G.; Huang, S.; Kim, S.; Kao, Y. H.; Takatani, Y.; Haneda, S.; Munkata, H. *J. Synchrotron Rad.* **2001**, *8*, 874-876.
- (250) Barrett, N.; Renault, O.; Damlencourt, J.-F.; Martin, F. *J. Appl. Phys.* **2004**, *96*, 6362-6369.
- (251) Wilk, G. D.; Wallace, R. M.; Anthony, J. M. *Appl. Phys. Rev.* **2001**, *89*, 5243-5275.
- (252) Panchaipetch, P.; Pant, G.; Quevedo-Lopez, M.; Zhang, H.; El-Bouanani, M.; Kim, M. J.; Wallace, R. M.; Gnade, B. E. *Thin Solid Films* **2003**, *425*, 68-71.
- (253) Opila, R. L.; Wilk, G. D.; Alam, M. A.; van Dover, R. B.; Busch, B. W. *Appl. Phys. Lett.* **2002**, *81*, 1788-1790.
- (254) Speer, J. A.; Cooper, B. J. *Am. Mineral.* **1982**, *67*, 804-808.
- (255) Grosvenor, A. P.; Kobe, B. A.; McIntyre, N. S. *Surf. Sci.* **2004**, *572*, 217-227.
- (256) Quevedo-Lopez, M. A.; El-Bouanani, M.; Kim, M. J.; Gnade, B. E.; Wallace, R. M.; Viokay, M. R.; Li-Fatou, A.; Bevan, M. J.; Colombo, L. *Appl. Phys. Lett.* **2002**, *81*, 1609-1611.

Appendix 1

Supplementary Data for Chapter 4

Table A1-1 Full width at half maximum (FWHM), in degrees, for strongest reflections in $\text{Mn}_{1-x}\text{V}_x\text{P}$ and MnP

Sample	x in $\text{Mn}_{1-x}\text{V}_x\text{P}$	011	111	211
MnP	0	0.14°	0.14°	0.17°
$\text{Mn}_{0.95}\text{V}_{0.05}\text{P}$	0.05	0.14°	0.15°	0.18°
$\text{Mn}_{0.85}\text{V}_{0.15}\text{P}$	0.15	0.12°	0.12°	0.12°
$\text{Mn}_{0.75}\text{V}_{0.25}\text{P}$	0.25	0.11°	0.13°	0.14°
$\text{Mn}_{0.60}\text{V}_{0.40}\text{P}$	0.40	0.13°	0.11°	0.14°

Table A1-2 P $2p_{3/2}$ binding energies (eV) from measurements for separate $\text{Mn}_{1-x}\text{V}_x\text{P}$ samples or at separate times for $\text{Co}_{1-x}\text{V}_x\text{P}$ and $\text{Co}_{1-x}\text{Mn}_x\text{P}$ samples.^a

Sample	x in $M_{1-x}M'_x\text{P}$	Run 1	Run 2
$\text{Mn}_{0.95}\text{V}_{0.05}\text{P}$	0.05	128.96	129.03
$\text{Mn}_{0.85}\text{V}_{0.15}\text{P}$	0.15	128.95	129.04
$\text{Mn}_{0.75}\text{V}_{0.25}\text{P}$	0.25	128.92	129.02
$\text{Mn}_{0.60}\text{V}_{0.40}\text{P}$	0.40	128.93	128.99
$\text{Co}_{0.90}\text{V}_{0.10}\text{P}$	0.10	129.15	129.10
$\text{Co}_{0.80}\text{V}_{0.20}\text{P}$	0.20	129.15	129.11
$\text{Co}_{0.40}\text{Mn}_{0.60}\text{P}$	0.60	129.28	129.28

^a The reliability of the P $2p_{3/2}$ BEs was assessed by examining the change in BE between the Run 1 and Run 2 values for each sample in the series. The average difference in BE was found to be 0.06 ± 0.03 eV which corresponds to a precision of better than ± 0.10 eV.

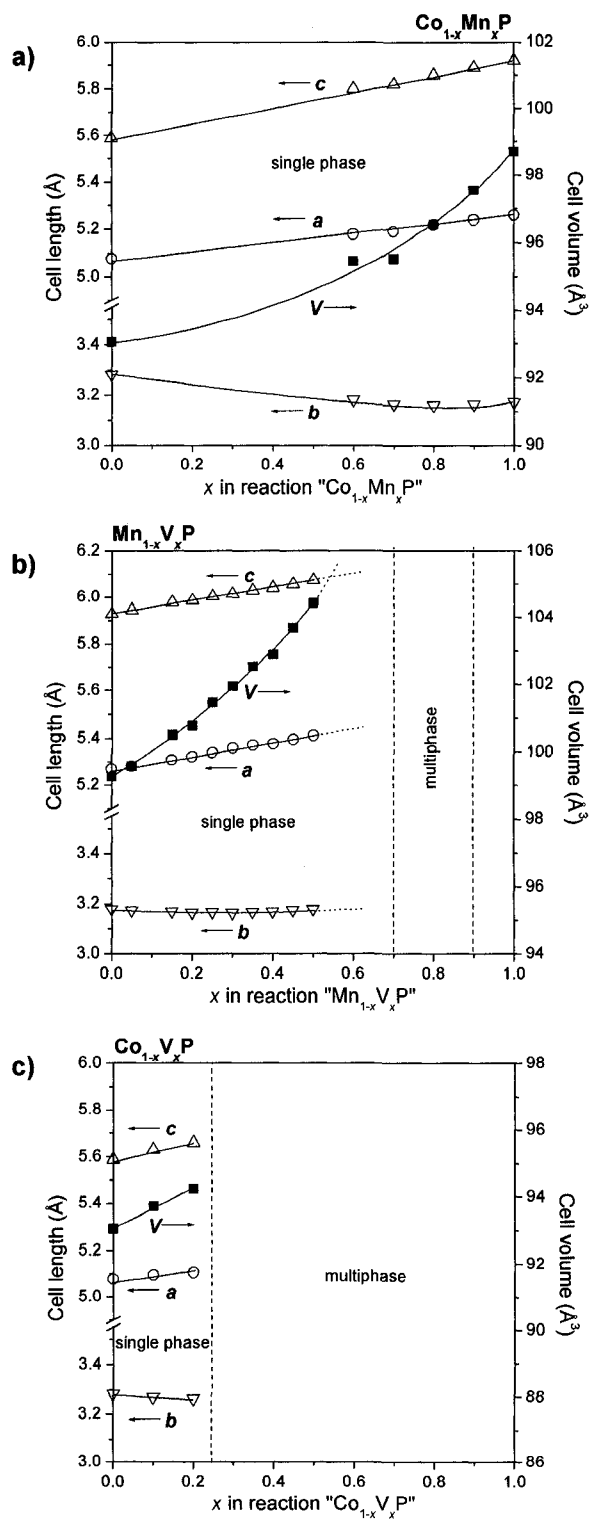


Figure A1-1 Plot of cell parameters vs. x for MnP-type phases observed in reactions with nominal composition (a) $Co_{1-x}Mn_xP$, (b) $Mn_{1-x}V_xP$, and (c) $Co_{1-x}V_xP$, with single-phase regions indicated.

Appendix 2

Supplementary Data for Chapter 5

Table A2-1 P $2p_{3/2}$ binding energies (eV) from measurements for separate $MAs_{1-y}P_y$ samples or for the same $MAs_{1-y}P_y$ sample but collected at different times.^a

Sample	y in $MAs_{1-y}P_y$	Run 1	Run 2	Run 3
CoAs _{0.10} P _{0.90}	0.90	129.34	129.34	129.30
CoAs _{0.25} P _{0.75}	0.75	129.35	129.34	
CoAs _{0.50} P _{0.50}	0.50	129.39	129.34	
CoAs _{0.75} P _{0.25}	0.25	129.40		
FeAs _{0.10} P _{0.90}	0.90	129.20	129.17	129.14
FeAs _{0.25} P _{0.75}	0.75	129.24	129.19	
FeAs _{0.50} P _{0.50}	0.50	129.24	129.20	
FeAs _{0.75} P _{0.25}	0.25	129.28	129.29	
FeAs _{0.90} P _{0.10}	0.10	129.33	129.31	
CrAs _{0.10} P _{0.90}	0.90	128.99	128.98	
CrAs _{0.75} P _{0.25}	0.25	129.06	129.05	

^aThe reliability of the P $2p_{3/2}$ BEs was assessed by examining the change in BE between the Run 1 and Run 2 values for each sample in the series. The average difference in BE was found to be 0.02 ± 0.02 eV which corresponds to a precision of $\sim \pm 0.05$ eV for this data set.

Appendix 3

ARXPS Study of the Ion Mobility Through $(\text{HfO}_2)_x(\text{SiO}_2)_{1-x}$ Formed on Air-Exposed $\text{Hf}(\text{Si}_{0.5}\text{As}_{0.5})\text{As}^*$

A3.1 Introduction

In the drive towards smaller devices in the semiconductor industry, alternatives for Si-based materials are being sought,^{250, 251} including high dielectric materials such as Hf-containing silicates.^{250, 252} Often formulated as $(\text{HfO}_2)_x(\text{SiO}_2)_{1-x}$, these silicates can be formed at the interface when a layer of HfO_2 is deposited and annealed on a SiO_2/Si substrate.^{250, 253} They can also be formed by reaction of HfSi_2 with oxygen.²⁵² Because diffusion of elements into other parts of a semiconductor device may hinder performance, it is important to understand the mobility of constituent atoms in these silicates.²⁵¹

In Chapter 8 we identified the new ternary compound $\text{Hf}(\text{Si}_{0.5}\text{As}_{0.5})\text{As}$, which is metallic and represents one end-member of the phase $\text{Hf}(\text{Si}_x\text{As}_{1-x})\text{As}$ with a homogeneity range of $0.5 \leq x \leq 0.7$. It adopts the prevalent ZrSiS -type structure, which is built up from a stacking of square nets, with those nets containing the disordered Si/As1 atoms being twice as dense as those containing the Hf or As2 atoms (Figure 8-1). From analysis based on laboratory XPS and photoemission spectroscopy using synchrotron radiation, a charge formulation of $\text{Hf}^{2+}((\text{Si}_{0.5}\text{As}_{0.5})\text{As})^{2-}$ was proposed in Chapter 8.

**A version of this chapter has been published. Reproduced with permission from Grosvenor, A. P.; Cavell, R. G.; Mar, A. Surf. Interface Anal. 2008, 40, 490-494. Copyright (2008) by John Wiley & Sons Limited.*

We report here a kinetic study of the oxidation of $\text{Hf}(\text{Si}_{0.5}\text{As}_{0.5})\text{As}$ in air at room temperature, which results in $(\text{HfO}_2)_x(\text{SiO}_2)_{1-x}$ as the predominant product. By use of angle-resolved X-ray photoelectron spectroscopy (ARXPS), the mobility of constituent atoms has been examined as they diffuse through the silicate layer. This information is required to evaluate $(\text{HfO}_2)_x(\text{SiO}_2)_{1-x}$ as a practical semiconductor material.

A3.2 Experimental

$\text{Hf}(\text{Si}_{0.5}\text{As}_{0.5})\text{As}$ was prepared by reacting mixtures of Hf (99.6% (excluding 2–4% Zr), Alfa-Aesar), Si (99.99%, Alfa Inorganics), and As (99.9998%, Alfa Inorganics) powders in the molar ratio 1:0.5:1.5, which were sealed in evacuated fused-silica tubes along with a few grains of I_2 (Anachemia) acting as a chemical vapour transport agent. The tubes were heated to 873 K over 12 h, held at this temperature for 3 d, heated to 1173 K over 24 h, and held at this temperature for 1–4 weeks. To serve as a reference standard, HfSiO_4 was also synthesized by reacting equimolar amounts of HfO_2 (98%, Aldrich) and SiO_2 (silica gel, Aldrich) in the presence of excess Li_2MoO_4 flux (99.9%, Aldrich) at temperatures ranging from 1273 to 1500 K, in accordance with previous reports.²⁵⁴ The purity of these prepared samples was confirmed through powder X-ray diffraction patterns collected on an Inel powder diffractometer equipped with a CPS 120 detector.

The (001) surface of plate-shaped $\text{Hf}(\text{Si}_{0.5}\text{As}_{0.5})\text{As}$ crystals having areas $>1 \times 1 \text{ mm}^2$ was examined on a Kratos AXIS 165 X-ray photoelectron spectrometer with Al $K\alpha$ X-rays. The plates were placed in electrical contact with the copper sample holder via silver paint (DuPont Electronics). The surfaces were cleaned *in situ* by Ar^+ sputtering (4 kV, 10 mA) to remove O and C. Although annealing could not be carried out because

the surface is somewhat reactive in vacuum, the sputtering process did not appear to preferentially remove the lighter Si atoms or reduce any of the constituent atoms. ARXPS was performed at take-off angles ranging from 90° to 15° between the surface and detector. High-resolution spectra of the As 3d, Si 2p, Hf 4f, O 1s, and C 1s core lines were collected with a pass energy of 40 eV, a step size of 0.05 eV, and a sweep time of 180 s. The spectra were calibrated by fixing the C 1s line arising from adventitious C to 284.8 eV. All spectra were analysed with the CasaXPS software program.¹¹⁰

Three samples of Hf(Si_{0.5}As_{0.5})As, after being Ar⁺ sputter cleaned, were oxidized through exposure to the ambient atmosphere at room temperature (relative humidity of ~50%) over times ranging from 1 to 60 minutes. The overall oxide thickness, d , was determined by applying the Strohmeier equation to the Hf 4f spectra:⁸⁴

$$d = \lambda_o \sin \Theta \ln \left(\frac{N_m \lambda_m I_o}{N_o \lambda_o I_m} + 1 \right)$$

For either the HfSi_{0.5}As_{1.5} (m) or oxide layer (o), λ is the inelastic mean free path (IMFP) calculated with the TPP-2M equation,¹³¹ N is the volume density of atoms, and I is the peak area. To use this equation, the core-line spectrum analysed must contain components from the surface oxide and substrate layers and the assumption must be made that a distinct interface is present between the two,⁸⁴ which is not always the case.²⁵⁵

To assign the different components within the oxide layer formed, reference spectra for As₂O₃ (99.5%, Alfa-Aesar), SiO₂ (optical grade, ESCO products), and HfSiO₄ were collected under similar conditions as noted above, with a charge neutralizer ($I = 1.7$ A, $V = 1.8$ V) applied to reduce charging effects.

A3.3 Results and Discussion

The Hf 4f, Si 2p, and As 3d spectra for clean Hf(Si_{0.5}As_{0.5})As and after exposing the surface to the atmosphere for 60 minutes (at take-off angles of 90° and 15°) are presented in Figure A3-1. All spectra were fitted by comparing the binding energies of the component peaks to those of standards collected here or elsewhere (Table A3-1).^{226, 250} Because Hf(Si_{0.5}As_{0.5})As is metallic, the Hf 4f component peak was fitted with an asymmetric lineshape, which arises from final state effects first described by Doniach and Šunjić and discussed in earlier chapters.¹¹⁷ In the clean surface, the spectra reveal some suboxides of Hf and Si that were formed from reaction with residual gases in the vacuum chamber. After exposure to the atmosphere, the signals from the substrate diminish substantially (particularly in the Hf 4f and Si 2p spectra), while several oxides are formed.

It is known that oxidation of HfSi₂ leads to the formation of hafnium silicates.²⁵² Similarly, the Hf 4f and Si 2p spectra show that oxidation of Hf(Si_{0.5}As_{0.5})As yields a predominant oxide layer having a Hf 4f_{7/2} BE of 17.7 eV and a Si 2p_{3/2} BE of 102.1 eV, which are slightly higher than in HfSiO₄ (Table A3-1). The intensity of both oxide peaks change in the same way as the take-off angle is varied, confirming that they belong to the same phase. Previous work in (HfO₂)_x(SiO₂)_{1-x} films has shown that as *x* increases, the Si 2p BE decreases and is always lower than in SiO₂, whereas the Hf 4f BE increases and is always higher than in HfO₂.²⁵³ These shifts are caused by a next-nearest neighbour interaction when the electronegative Si atoms are exchanged for the more electropositive Hf atoms.²⁵³ The oxide layer formed on Hf(Si_{0.5}As_{0.5})As has Si 2p and Hf 4f binding

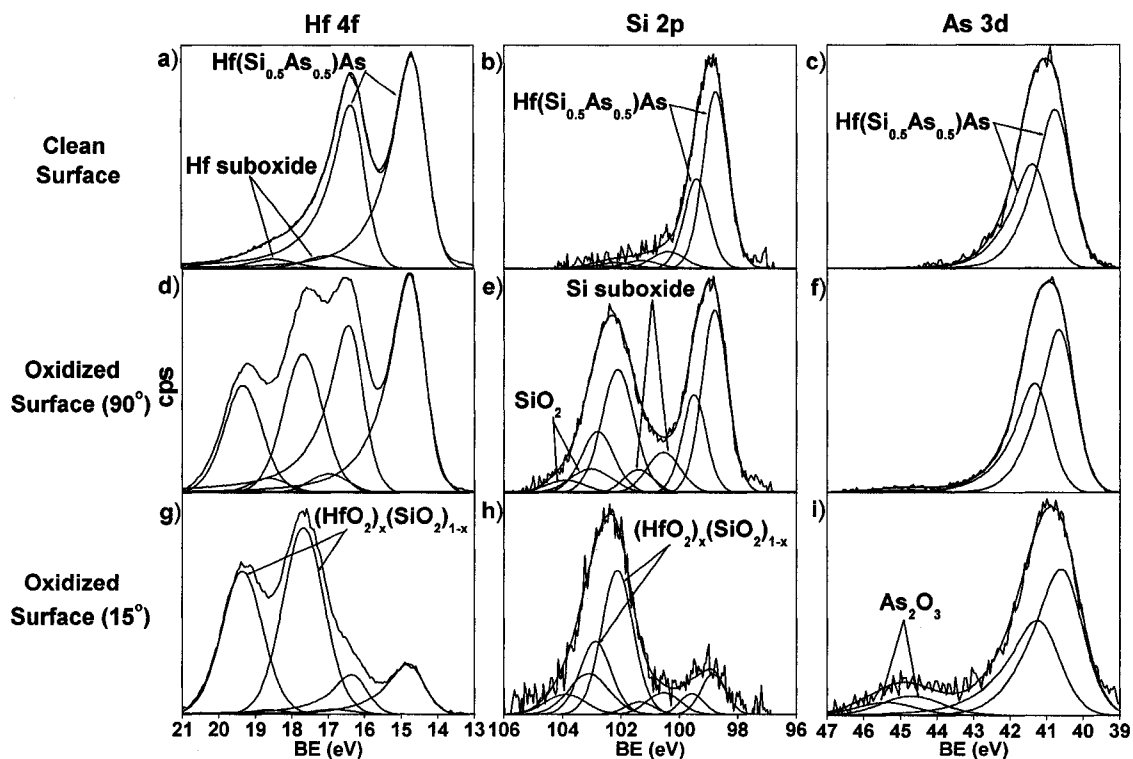


Figure A3-1 Core-line spectra of the Hf 4f, Si 2p, and As 3d components from clean $\text{Hf}(\text{Si}_{0.5}\text{As}_{0.5})\text{As}$ after Ar^+ sputter-cleaning (a–c), and after exposure to the atmosphere at a take-off angle of 90° (d–f) or 15° (g–i). All spectra were fitted with spin-orbit split component peaks as listed in Table A3-1.

Table A3-1 Binding energy values for the spin-up component peaks of the fitted Hf 4f, Si 2p, and As 3d spectra from air-exposed Hf(Si_{0.5}As_{0.5})As. The binding energies from standard compounds are provided for reference.

Component	Peak	Experimental BE (eV)	Standard BE (eV)
Hf(Si _{0.5} As _{0.5})As	Hf 4f _{7/2}	14.8	
	Si 2p _{3/2}	98.8	
	As 3d _{5/2}	40.7	
(HfO ₂) _x (SiO ₂) _{1-x} ^a	Hf 4f _{7/2}	17.7	17.1
	Si 2p _{3/2}	102.1	101.5
	O 1s	531.0	530.7
SiO ₂ ^b	Si 2p _{3/2}	103.0	103.0
	O 1s	532.5	532.5
As ₂ O ₃	As 3d _{5/2}	44.7	44.9
	O 1s	531.8	531.6
Hf suboxide ^c	Hf 4f _{7/2}	17.0	15–17 ¹⁰
Si suboxide	Si 2p _{3/2}	100.6	100–102 ¹

^a The BE values for the standard are from HfSiO₄.

^b The O 1s BE for SiO₂ also corresponds to that of adsorbed OH^{δ-}.²⁵⁵

^c Although one set of spin-orbit split peaks has been used to fit the Hf and Si suboxide components, normally multiple peaks corresponding to Hf⁽¹⁻³⁾⁺ and Si⁽¹⁻³⁾⁺ are used with a range of BE.^{226, 250}

energies that are similar to those for a film with composition $(\text{HfO}_2)_{0.35}(\text{SiO}_2)_{0.65}$,²⁵⁰ suggesting that its composition is also slightly Si-rich.

Besides $(\text{HfO}_2)_x(\text{SiO}_2)_{1-x}$, other oxidation products formed are suboxides of Si and Hf, and SiO_2 , whose evolution can be tracked as the take-off angle is lowered from 90° to 15° . In the Hf 4f spectra (Figures A3-1d and A3-1g), the intensity from the $(\text{HfO}_2)_x(\text{SiO}_2)_{1-x}$ component increases whereas the peak intensities from the Hf suboxide and the substrate decrease. The intensity for $\text{Hf}(\text{Si}_{0.5}\text{As}_{0.5})\text{As}$ decreases more rapidly than for Hf suboxide as the take-off angle is lowered. In the Si 2p spectra (Figures A3-1e and A3-1h), the signals from the $\text{Hf}(\text{Si}_{0.5}\text{As}_{0.5})\text{As}$, Si suboxide, and $(\text{HfO}_2)_x(\text{SiO}_2)_{1-x}$ components decrease whereas that from SiO_2 increases.

The As 3d spectrum of the clean substrate (Figure A3-1c) shows an asymmetric lineshape, similar to that observed in the Hf 4f spectrum (Figure A3-1a). After exposure to the atmosphere, the spectrum collected at a take-off angle of 90° (Figure A3-1f) shows a small amount of oxide, assigned to be As_2O_3 on the basis of its binding energy (Table A3-1). Lowering the take-off angle enhances this signal significantly, indicating that As_2O_3 is at the surface (Figure A3-1i). It appears that considerably less As_2O_3 is formed than the Hf- and Si-containing oxides, but this is difficult to quantify because the As 3d signal from the substrate is overlapped by the broad Hf $5p_{1/2}$ signal from $(\text{HfO}_2)_x(\text{SiO}_2)_{1-x}$. Similar to the Hf 4f results, the intensity of the Hf $5p_{1/2}$ peak is expected to increase significantly as the take-off angle is lowered, further restricting the ability to compare the As 3d intensity from As_2O_3 to that from $\text{Hf}(\text{Si}_{0.5}\text{As}_{0.5})\text{As}$.

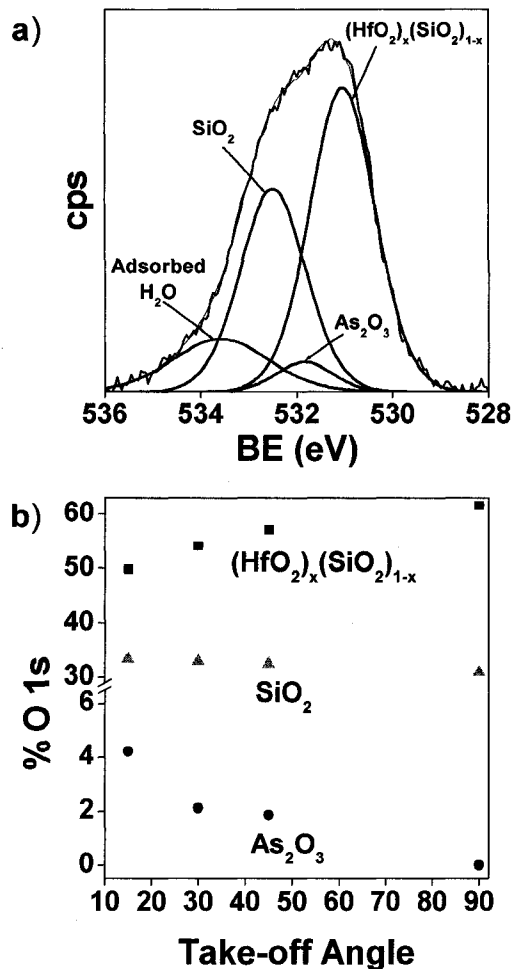


Figure A3-2 (a) O 1s spectrum from air-exposed Hf(Si_{0.5}As_{0.5})As surface at a take-off angle of 15°. The spectrum was fitted with component peaks as listed in Table A3-1. The component identified as adsorbed H₂O has a BE similar to a previous value.²⁵⁵ (b) Plot of O 1s component peak intensities versus take-off angle. The adsorbed H₂O signal has not been included for simplicity.

The O 1s spectrum from the oxidized surface collected at a take-off angle of 15° is shown in Figure A3-2a, with various components indicated. The percent concentration of each component is plotted versus the take-off angle in Figure A3-2b. As the take-off angle decreases, so that the measurement becomes more surface-sensitive, the $(\text{HfO}_2)_x(\text{SiO}_2)_{1-x}$ concentration decreases whereas the SiO_2 and As_2O_3 concentrations increase. Suboxides of Hf and Si have not been included in this analysis because their signals would be weak and because suitable standards are unavailable for comparison of O 1s BE values. Nevertheless, the earlier analysis of the Hf and Si spectra indicates that these suboxides are present at the oxide-substrate interface. Above the suboxides is $(\text{HfO}_2)_x(\text{SiO}_2)_{1-x}$, and then at the air-oxide interface are SiO_2 and As_2O_3 . The amount of SiO_2 is difficult to quantify because its O 1s signal overlaps that for adsorbed OH^δ^- ,²⁵⁵ which is expected to be found at the surface. Figure A3-3 shows a schematic of the oxide layer formed on $\text{Hf}(\text{Si}_{0.5}\text{As}_{0.5})\text{As}$. For simplicity, the different oxides formed are depicted as separate layers, but it is more likely that some overlap occurs.

These results imply that oxidation of $\text{Hf}(\text{Si}_{0.5}\text{As}_{0.5})\text{As}$ proceeds by diffusion of cations, with Si and As being much more mobile than Hf in the oxide film. This model is consistent with the observation that the $(\text{HfO}_2)_x(\text{SiO}_2)_{1-x}$ layer is Si-rich even though the $\text{Hf}(\text{Si}_{0.5}\text{As}_{0.5})\text{As}$ substrate has a Hf:Si ratio of 2:1, and with the presence of both Si and As binary oxides on the surface of the film. Previous SIMS studies have shown that As and P atoms can diffuse through a hafnium silicate film, within grain boundaries formed during crystallization when the film is annealed at 1273–1323 K.²⁵⁶ In contrast, they do not diffuse through a N-substituted hafnium silicate film, which remains amorphous and provides no grain boundaries for diffusion.²⁵⁶ Because the $(\text{HfO}_2)_x(\text{SiO}_2)_{1-x}$ layer on

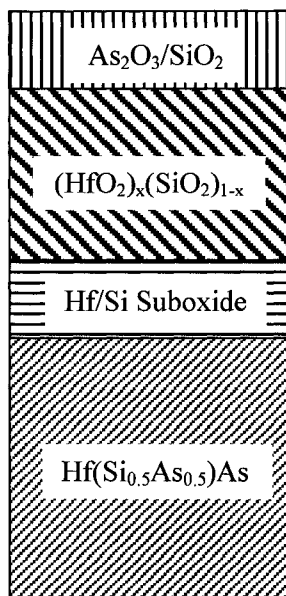


Figure A3-3 Schematic representation of the oxide film formed on $\text{Hf}(\text{Si}_{0.5}\text{As}_{0.5})\text{As}$ after exposure to the ambient atmosphere for 60 minutes at room temperature.

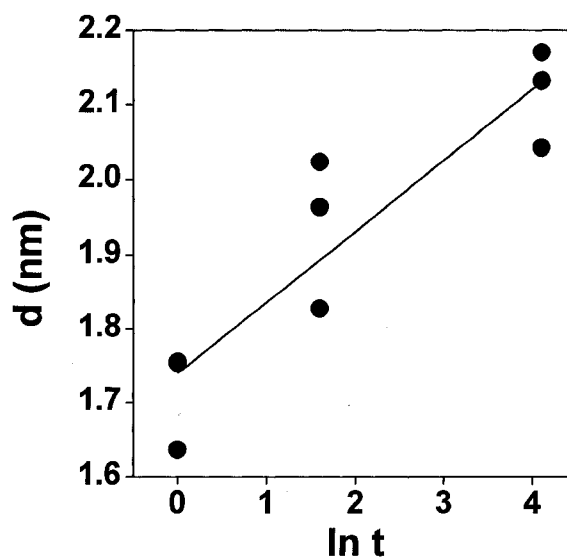


Figure A3-4 Logarithmic kinetics of the oxidation of $\text{Hf}(\text{Si}_{0.5}\text{As}_{0.5})\text{As}$ after exposure to the atmosphere for 1, 5, and 60 minutes. Three samples were exposed to the atmosphere for each oxidation time studied. The thicknesses, d , were calculated using the Strohmeyer equation and the following parameters: $N_m/N_o = 0.7$, $\lambda_o = 24.9 \text{ \AA}$, $\lambda_m = 25.6 \text{ \AA}$, $\Theta = 90^\circ$.

Hf(Si_{0.5}As_{0.5})As was formed at room temperature and is thus likely amorphous, the grain boundary pathway can be precluded. Instead, the Si and As atoms probably diffuse through the (HfO₂)_x(SiO₂)_{1-x} layer via vacancies, in the form of defects and interstitial spaces. In the N-substituted hafnium silicate film discussed above, the exchange of O with larger N atoms may act to block these pathways for As and P diffusion.

The reactivity of Hf(Si_{0.5}As_{0.5})As to air was further examined by investigating its oxidation kinetics. Since the hafnium silicate represents the major component, the overall composition of the oxide film was approximated as HfSiO₄ and its thickness was calculated by applying the Strohmeier equation to the Hf 4f spectra. As shown in Figure A3-4, the thickness follows a logarithmic dependence, indicating that the oxide film formed acts as a passive layer. If the assumption is made that the oxide film is slightly Si-rich, the calculated thicknesses become only slightly greater (by ~0.2 nm).

A3.4 Conclusions

The air oxidation of Hf(Si_{0.5}As_{0.5})As results in the formation of suboxides of Hf and Si at the oxide-substrate interface, followed by a Si-rich (HfO₂)_x(SiO₂)_{1-x} layer, and then SiO₂ and As₂O₃ at the air-oxide interface. The diffusion of Si and As atoms through these amorphous oxide layers formed at room temperature probably occurs not through grain boundaries but rather via vacancies as the primary pathway. This material, Hf(Si_{0.5}As_{0.5})As, is not viable for use in semiconductor devices because of its metallic nature and the high concentration of As, which is toxic. However, the study of its oxidation behaviour indicates that further work is necessary to reduce the ability of atoms to diffuse through hafnium silicates. The formation of the oxide layer on Hf(Si_{0.5}As_{0.5})As, which is passive, follows logarithmic kinetics.